

UNIVERSIDADE FEDERAL DE UBERLÂNDIA

INSTITUTO DE QUÍMICA

Programa de Pós-Graduação em Química

Laboratório de Fotoquímica e Ciência dos Materiais (LAFOT-CM)

MARCOS EDUARDO GOMES DO CARMO

From Molecular to Hybrid Covalent Organic Framework catalysts: Rational Design of Catalytic Platforms for Photocatalytic and Electrocatalytic CO_2 Reduction

Uberlândia - MG

2026

MARCOS EDUARDO GOMES DO CARMO

From Molecular to Hybrid Covalent Organic Framework catalysts: Rational Design of Catalytic Platforms for Photocatalytic and Electrocatalytic CO_2 Reduction

Tese apresentada ao Programa de Pós-Graduação em Química da Universidade Federal de Uberlândia, na área de concentração Química Inorgânica, como requisito para obtenção do título de Doutor em Química.

Orientador: Prof. Dr. Antonio Otavio de Toledo Patrocinio

Uberlândia - MG

2026

Ficha Catalográfica Online do Sistema de Bibliotecas da UFU
com dados informados pelo(a) próprio(a) autor(a).

C287
2026

Carmo, Marcos Eduardo Gomes do, 1998-
From Molecular to Hybrid Covalent Organic Framework catalysts: Rational Design of Catalytic Platforms for Photocatalytic and Electrocatalytic CO2 Reduction [recurso eletrônico] / Marcos Eduardo Gomes do Carmo. - 2026.

Orientador: Antonio Otavio de Toledo Patrocinio.
Tese (Doutorado) - Universidade Federal de Uberlândia, Pós-graduação em Química.
Modo de acesso: Internet.
DOI http://doi.org/10.14393/ufu.te.2026.703
Inclui bibliografia.

1. Química. I. Patrocinio, Antonio Otavio de Toledo,1983-, (Orient.). II. Universidade Federal de Uberlândia. Pós-graduação em Química. III. Título.

CDU: 54

Bibliotecários responsáveis pela estrutura de acordo com o AACR2:
Gizele Cristine Nunes do Couto - CRB6/2091
Nelson Marcos Ferreira - CRB6/3074

UNIVERSIDADE FEDERAL DE UBERLÂNDIA
Coordenação do Programa de Pós-Graduação em Química
Av. João Naves de Ávila, 2121, Bloco 5I - Bairro Santa Mônica, Uberlândia-MG, CEP 38400-902
Telefone: (34) 3239-4385 - www.cpgquimica.iq.ufu.br - cpgquimica@ufu.br

ATA

Programa de Pós-Graduação em:	Química				
Defesa de:	Tese de Doutorado Acadêmico, 189, PPGQUI				
Data:	Quatro de setembro de dois mil e vinte e seis	Hora de início:	13h	Hora de encerramento:	17:07
Matrícula do Discente:	12223QMI004				
Nome do Discente:	Marcos Eduardo Gomes do Carmo				
Título do Trabalho:	From Molecular to Hybrid Covalent Organic Framework catalysts: Rational Design of Catalytic Platforms for Photocatalytic and Electrocatalytic CO2 Reduction				
Área de concentração:	Química				
Linha de pesquisa:	Química Bioinorgânica, Fotoquímica e Fotobiologia				
Projeto de Pesquisa de vinculação:	Estudos espectroeletroquímicos de fotocatalisadores híbridos para aplicações em conversão de energia solar em combustíveis				
ODS 7, 11 e 13	ODS 7 - Energia limpa e acessível: garantir acesso à energia barata, confiável, sustentável e renovável para todos. ODS 11 - Cidades e comunidades sustentáveis: tornar as cidades e os assentamentos humanos inclusivos, seguros, resilientes e sustentáveis. ODS 13 - Ação contra a mudança global do clima: tomar medidas urgentes para combater a mudança climática e seus impactos.				

Reuniu-se, por webconferência, no *link*: https://teams.microsoft.com/meet/23767647552702?p=Eq5p8VG8a4YmtPsg0U, a Banca Examinadora, designada pelo Colegiado do Programa de Pós-graduação em Química, assim composta: Professores Doutores: **André Luiz Bogado**, da Universidade Federal de Uberlândia; **Susana Ines Cordoba de Torresi,** da Universidade de São Paulo; **Pablo Sebastian Fernandez**, da Universidade Estadual de Campinas; **Rose Maria Carlos**, da Universidade Federal de São Carlos, e **Antonio Otavio de Toledo Patrocinio**, orientador do candidato.

Iniciando os trabalhos o presidente da mesa, **Dr. Antonio Otavio de Toledo Patrocinio**, apresentou a Comissão Examinadora e o candidato, agradeceu a presença do público, e concedeu ao Discente a palavra para a exposição do seu trabalho. A duração da apresentação do Discente e o tempo de arguição e resposta foram conforme as normas do Programa.

A seguir o senhor(a) presidente concedeu a palavra, pela ordem sucessivamente, aos(às) examinadores(as), que passaram a arguir o(a) candidato(a). Ultimada a arguição, que se desenvolveu

dentro dos termos regimentais, a Banca, em sessão secreta, atribuiu o resultado final, considerando o(a) candidato(a):

Aprovado.

Esta defesa faz parte dos requisitos necessários à obtenção do título de Doutor.

O competente diploma será expedido após cumprimento dos demais requisitos, conforme as normas do Programa, a legislação pertinente e a regulamentação interna da UFU.

Documento assinado eletronicamente por **Antonio Otavio de Toledo Patrocínio**, **Professor(a) do Magistério Superior**, em 04/09/2026, às 17:08, conforme horário oficial de Brasília, com fundamento no art. 6º, § 1º, do Decreto nº 8.539, de 8 de outubro de 2015.

Documento assinado eletronicamente por **Andre Luiz Bogado**, **Professor(a) do Magistério Superior**, em 04/09/2026, às 17:08, conforme horário oficial de Brasília, com fundamento no art. 6º, § 1º, do Decreto nº 8.539, de 8 de outubro de 2015.

Documento assinado eletronicamente por **ROSE MARIA CARLOS**, **Usuário Externo**, em 05/09/2026, às 07:34, conforme horário oficial de Brasília, com fundamento no art. 6º, § 1º, do Decreto nº 8.539, de 8 de outubro de 2015.

Documento assinado eletronicamente por **PABLO SEBASTIAN FERNANDEZ**, **Usuário Externo**, em 07/09/2026, às 12:18, conforme horário oficial de Brasília, com fundamento no art. 6º, § 1º, do Decreto nº 8.539, de 8 de outubro de 2015.

Documento assinado eletronicamente por **SUSANA INES CORDOBA DE TORRESI**, **Usuário Externo**, em 09/09/2026, às 10:32, conforme horário oficial de Brasília, com fundamento no art. 6º, § 1º, do Decreto nº 8.539, de 8 de outubro de 2015.

A autenticidade deste documento pode ser conferida no site https://www.sei.ufu.br/sei/controlador_externo.php?acao=documento_conferir&id_orgao_acesso_externo=0, informando o código verificador **7465094** e o código CRC **78F2DE41**.

Referência: Processo nº 23117.045083/2026-00 SEI nº 7465094

Aos meus pais, por todo o amor, apoio e confiança. Esta conquista também é de vocês.

Acknowledgements

The completion of this thesis marks the end of a journey shaped by countless learning experiences, challenges, opportunities, and the support of many people who have been part of my academic and personal life. I am deeply grateful to everyone who, in different ways, contributed to making this work possible.

My sincere thanks go to all the teachers and professors who have been part of my educational and academic journey, from elementary school through my undergraduate, master's, and PhD studies. Thank you for your guidance, encouragement, and the opportunities that helped shape my career.

I would like to express my deepest gratitude to my advisor, Prof. Dr. Antonio O. T. Patrocinio, for the trust he placed in me throughout all these years, for his guidance, scientific mentorship, the freedom to pursue new ideas, and the opportunities that were fundamental to my development as a researcher.

I am especially grateful for the opportunity to undertake research internships abroad, experiences that profoundly transformed both my scientific and personal development. I would like to sincerely thank Professor Dr. Thomas Bein and Dr. Jenny Schnider at Ludwig-Maximilians-Universität München (LMU) for welcoming me into their research group, for their trust, patience, guidance, and the opportunity to work in an outstanding scientific environment. I am also grateful to all the members of the group, especially Dr. Laura Spies, for her collaboration and generosity in sharing her knowledge throughout our collaboration, which had a profound impact on my scientific perspective and personal growth during my PhD. journey.

I am deeply grateful to Professor Dr. Gerald J. Meyer at the University of North Carolina at Chapel Hill (UNC) for welcoming me into his research group, for his guidance, for involving me in his research activities, literature discussions, and group seminars, providing invaluable scientific discussions, and for the opportunity to broaden my perspective on research and science. I also thank my lab mates and staff members of the group, especially Dr. Renato Sampaio, for their support, collaboration and knowledge exchange during my time in the United States.

To my lab mates and professors at LAFOT-CM, thank you for the daily companionship, the scientific discussions, the collaborations, the support, and the countless exchanges of knowledge throughout my PhD.

I would also like to acknowledge the opportunity to supervise undergraduate students during my PhD and extend my sincere gratitude to all of them for being part of this journey.

Special thanks to Gabrielly Moreira and Vanessa Silva, two remarkable and determined undergraduate students with whom I had the privilege of working closely. Their enthusiasm, dedication, and curiosity made this experience deeply rewarding. Although they may not realize it, they constantly challenged me to become a better researcher and mentor, teaching me how to guide scientific work, approach problems with greater patience and creativity, and communicate research more effectively. Most importantly, they showed me that mentorship can grow into genuine friendship, and I am truly grateful for everything I learned from them along the way.

I am profoundly grateful to my parents, Clever and Fabiana, and to my siblings, Kamilly and Thiago, for supporting my decisions and my journey with unconditional love, trust, and encouragement. Everything I have achieved is rooted in the values and unwavering support you have always given me.

I am especially grateful to my girlfriend, Amanda, for being by my side throughout every single stage of my PhD journey. Thank you for your constant support, encouragement, patience, and, above all, for always believing that I could go further. You gave me strength, confidence, and perspective whenever I needed them most.

To my friends James Michael, Gustavo Buzi, Thiago Felipe, thank you for always being present, even from away, sharing moments of achievement, joy, and also difficult times. Knowing that I could always count on you made all the difference.

To all the Grego group, a long friendship that began in the laboratory during my master's years and has remained one of the greatest gifts of this academic journey. Thank you for the countless conversations, laughter, support and celebrations. Our friendship has gone far beyond research, and I am incredibly grateful to have shared this journey with such remarkable people.

Finally, I gratefully acknowledge the financial support provided by CNPq, CAPES, FAPEMIG, and the Alexander von Humboldt Foundation, which made this research possible.

The most dangerous worldviews are the worldviews of those who have never viewed the world.

Alexander von Humboldt

RESUMO

A conversão seletiva de CO_2 em combustíveis é um dos principais desafios da conversão sustentável de energia. Esta tese estabelece princípios de design para sistemas catalíticos moleculares e híbridos aplicados à redução foto- e eletrocatalítica de CO_2, integrando precisão molecular e arquiteturas catalíticas porosas.

Estudos mecanísticos com complexos de Re(I) tricarbonílico, combinando espectroeletroquímica e espectroscopia *in situ*, evidenciaram intermediários catalíticos e a principal rota de desativação na conversão fotocatalítica de CO_2 em CO. Esses resultados orientaram a imobilização de Re(I) em Covalent Organic Frameworks (COFs) baseados em bipiridina, preservando o mecanismo molecular de redução e aumentando a estabilidade operacional pelo isolamento dos sítios catalíticos. Análises por STEM-HAADF revelaram a distribuição atomicamente ordenada dos centros de Re(I) na estrutura do COF, confirmando arquiteturas catalíticas de sítios isolados.

Essa estratégia foi estendida à eletroredução de CO_2 por meio da incorporação de complexo tricarbonílico de Mn(I) em estruturas porosas baseadas em bipiridina. O eletrocatalisador híbrido foi implementado com sucesso em um eletrolisador *zero-gap* sem católito, evidenciando o potencial de catalisadores híbridos e porosos para tecnologias escalonáveis de conversão de CO_2. Além disso, centros catalíticos complementares foram integrados em uma única estrutura porosa para promover a conversão sequencial de CO_2 em CO e, posteriormente, em CH_3OH, fornecendo evidências preliminares de catálise em cascata com múltiplos sítios ativos.

De modo geral, este trabalho estabelece princípios de design para catalisadores moleculares e híbridos, integrando entendimento mecanístico e engenharia de estruturas porosas. Esses resultados fornecem uma base para o desenvolvimento de materiais catalíticos mais eficientes e seletivos para a conversão de CO_2 em combustíveis de maior complexidade molecular.

Palavras-chave: redução de CO_2, Covalent Organic Frameworks, estudos mecanísticos, catalisadores de sítios isolados, catalisadores em cascata.

ABSTRACT

The selective conversion of CO_2 into energy-rich fuels is a major challenge in sustainable energy conversion. This thesis investigates the rational design of molecular and hybrid catalysts for photo- and electrocatalytic CO_2 reduction, establishing design principles that progress from molecular catalyst engineering to multifunctional porous catalytic architectures.

Mechanistic studies on Re(I) tricarbonyl molecular catalysts, combining spectroelectrochemistry and *in-situ* spectroscopy experiments, enabled the identification of key catalytic intermediates and deactivation pathways involved in the CO_2-to-CO photocatalytic cycle. These insights guided the immobilization of Re(I) catalytic centers within bipyridine-based Covalent Organic Frameworks (COFs), where the molecular reduction mechanism was preserved while operational stability was significantly enhanced through spatial isolation of the catalytic sites. STEM-HAADF analysis resolved the atomically ordered distribution of Re(I) centers within the COF framework, providing direct structural evidence for site-isolated catalytic architectures.

The design strategy was extended to electrocatalytic CO_2 reduction through the incorporation of Mn(I) carbonyl complexes into porous bipyridine-based frameworks. The resulting hybrid catalyst was implemented in a catholyte-free zero-gap electrolyzer, evidencing the potential of molecularly defined porous catalysts for scalable CO_2 conversion technologies. Finally, complementary molecular catalytic centers were integrated within a single porous framework to promote sequential CO_2-to-CO-to-CH_3OH conversion, providing preliminary evidence for multi-site cascade catalysis and establishing a new strategy for the selective production of liquid fuels.

Overall, this work spans molecular ligand engineering, catalyst immobilization, framework engineering, scalable electrocatalytic systems, and multi-site cascade catalyst architectures. The mechanistic studies and framework engineering provides a foundation for the next generation of hybrid catalytic materials aimed at the efficient and selective conversion of CO_2 into valued fuels.

Key words: CO_2 reduction, Covalent Organic Frameworks, mechanistic studies, site-isolated catalysts, cascade catalysts.

LIST OF FIGURES

Figure 1. Percentual (a) and raw amount (b) of the global Total Energy Supply (TES) and by energy source between 1990 and 2023, according to the International Energy Agency (IEA) Red: Oil and oil products; Pink: Biofuels and waste; Brown: Coal and coal products; Blue: Hydropower; Grey: Natural gas; Orange: Nuclear; Green: Solar, wind, and other renewables.[3] 30

Figure 2. (a) The global surface temperature since 1850-1900. (b) Historical cumulative net anthropogenic CO_2 emissions per region from 1850 to 2019 in $GtCO_2$.(c) Atmospheric concentrations of several Greenhouse Gas (GHG) including the three major well-mixed GHGs CO_2, CH_4 and N_2O. (d) Global net anthropogenic GHG emissions include CO_2 from fossil fuel combustion and industrial processes (CO_2-FFI) (dark green); net CO_2 from land use, land-use change and forestry (CO_2-LULUCF) (green); CH_4; N_2O; and fluorinated gases (HFCs, PFCs, SF_6, NF_3) (light blue). Adapted from Climate Change 2023 Synthesis Report.[7] 31

Figure 3. Natural (left) and Artificial Photosynthetic (right) pathways. ... 34

Figure 4. Schematic representation of the main components of a photocatalytic CO_2 reduction system showing the roles of the photosensitizer/light harvester (PS), electron donor (D), catalyst (Cat) and photocatalyst (PCat). ... 35

Figure 5. Schematic representation of an electrochemical CO_2 reduction system. Adapted from Kuramochi.[20] 36

Figure 6. Representative metal complexes structures of some CO_2 catalysts.[20] 40

Figure 7. Most accepted reduction pathway for the *fac*-$Re(CO)_3(bpy)Cl$ catalyst. 42

Figure 8. Examples of monomer symmetry combination for producing different 2D Lattices (b) and some published lattices and morphologies of COFs (b).[64] 46

Figure 9. Covalent Organic Frameworks as stable platforms for making hybrid COFs CO_2 photocatalysts. 47

Figure 10. Oxidation process of the sacrificial donor BIH in the photochemical CO_2 reduction. PS stands for photosensitiser. 59

Figure 11. Chemical structures and abbreviations of the Re(I) catalysts. 60

Figure 12. The ^{1}H-NMR spectra of Re-pbiH (orange) and Re-bbzp (blue) in DMSO-d^6. 68

Figure 13. Absorption spectra (a) of the Re-pbiH (orange) and Re- bbzp (blue) in CH_3CN at 298 K as well as these emission spectrum (b) in CH_3CN at 298 K (solid lines) and butyronitrile at 77 K (dashed lines); λ_{exc} = 375 nm. Surface contours of the HOMO and LUMO orbitals for the Re-pbiH (c) and Re-bbzp (d) complexes. 69

Figure 14. Emission lifetimes measurements for Re-pbiH (a) and Re-bbzp (b) in in CH_3CN at 298 K. *Inset:* log(t) vs I plot of the decays. 71

Figure 15. Absorption spectra (A) and emission spectra (B) of pure Re-pbiH in CH_3CN and after addition of $HClO_4$ (acid). Emission decay (C) for Re-pbiH monitored at different wavelengths (C) and emission decay for Re-pbiH in CH_3CN and after addition of $HClO_4$ (acid) (D). 73

Figure 16. Cyclic voltammograms recorded, with a scan rate of 100 mV s^{-1} (solid line), and Square Wave Voltammograms measured at a frequency of 50 Hz (dashed line) for Re-pbiH (A) and Re-bbzp (B) complexes in argon-saturated 0.1 M $TBAPF_6/CH_3CN$. The arrow indicates the scan directions. 74

Figure 17. (a) Cyclic Voltammogram at 100 mV s^{-1} of scan rate (solid line) and Square Wave Voltammetry at 50 Hz of frequency (dashed line) for Re-bbzp complex. (b) and (c) are showing the SWV as a function of applied frequency (*f*) variation as well as its linear dependence along to the applied frequency for the first reduction process (n = 2.0), respectively. (d) and (e) are showing the SWV as a function of applied frequency (*f*) variation as well as its linear dependence along to the applied frequency for the second reduction process (n = 1), respectively. 75

Figure 18. (a) Cyclic Voltammogram at 100 mV s^{-1} of scan rate (solid line) and Square Wave Voltammetry at 50 Hz of frequency (dashed line) for *fac*-$Re(CO)_3(bpy)Cl$ complex. (b) and (c) are showing the SWV as a function of applied frequency (*f*) variation as well as its linear dependence along to the

applied frequency for the first reduction process (n = 2.0), respectively. (d) and (e) are showing the SWV as a function of applied frequency (*f*) variation as well as its linear dependence along to the applied frequency for the second reduction process (n = 1.0), respectively. 77

Figure 19. The *turnover number* (TON) for CO formation photocatalyzed by Re-pbiH (orange) and Re-bbzp (blue) complexes. Experiments were performed in CO_2-saturated 10 mL CH_3CN solutions containing 6.7 mmol L^{-1} of BIH and 0.03 mmol L^{-1} of photocatalysts (λ > 370 nm). 78

Figure 20. (a) *Turnover number* (TON) for CO formation mediated by Re-bbzp in CO_2-saturated CH_3CN containing BIH (6.7 mmol L^{-1}) and Re-bbzp (0.03 mmol L^{-1}) and the indicated H_2O concentrations (λ_{exc} > 370 nm). (b) *Turnover number* (TON) for CO formation using BIH and BID from which a kinetic isotope effect was extracted, KIE = 1.5. (c) Isodesmic reaction employed to estimate the pK_a of the protonated reduced Re-bbzp intermediate, using $BIH^{\bullet+}$ as the reference acid..... 81

Figure 21. DFT-optimized geometry of the two-electron- and one-proton-reduced Re-bbzp species featuring a CO_2 adduct intermediate..... 82

Figure 22. Infrared spectroelectrochemistry (IR-SEC) of Re-bbzp in 0.1 M $TBAPF_6/CH_3CN$ electrolyte for the first (E_p = –2.5 V *vs*. Fc^+/Fc) and second (E_p = –2.7 V vs. Fc^+/Fc) electron reduction process under Ar (A) and CO_2 (B) atmosphere. (C) Proposed reduction pathway for Re-bbzp complex (a) to species (b), (c) and (d) color-coded to the spectral assignments in (A) and (B). 83

Figure 23.IR-SEC of Re-bbzp in acetonitrile with Bu_4NPF_6 electrolyte for the first electron reduction process under Ar atmosphere (Δt = 15s)..... 84

Figure 24. IR-SEC of Re-bbzp in acetonitrile with Bu_4NPF_6 electrolyte for the first electron reduction process under CO_2 atmosphere (a) t < 15 s (b) t > 15 s. (Dt = 15s)..... 85

Figure 25. *In-situ*-FTIR- spectra measured over the indicated photolysis time for Re-bbzp in Ar-saturated (a and b) and CO_2-saturated (c and d) CH_3CN solutions containing excess BIH..... 86

Figure 26. kinetic monitoring for each species based their corresponding peaks (2025 (a), 2015 (c), 2005 (d) and 1800 cm^{-1} for (2c)) under Ar (A and B) and CO_2 (B and C) atmosphere. 88

Figure 27. Proposed photocatalytic cycle for Re-bbzp using BIH as electron donor in acetonitrile. 90

Figure 28. Schematic illustration of the operating principle of the photocatalytic CO_2 conversion (red balls: O, grey balls: C, white balls: H). 97

Figure 29. (a) Preparation of different ZnO nanostructures and (b) the determined conduction band (CB) and valence band (VB) potentials of ZnO microspheres (S-1), microflowers (S-2), and nanorods (S-3) *vs*. NHE (pH = 0) and (c) their respective photocatalytic activity towards CO evolution. Adapted with permission.[145] Copyright 2016, Springer Nature..... 104

Figure 30. (a) CH_4 evolution kinetics from CO_2 photoreduction over CuO prepared *via* solvothermal synthesis (CuO-Solv), co-precipitation (CuO-Prec), calcination method (CuO-Calc), and commercially acquired (CuO-Com). (b) Simplified scheme of the CO_2 photoreduction process on the CuO surface. Adapted with permission.[156] Copyright 2020, Elsevier. 105

Figure 31. Proposed pathways for CO_2 photoreduction over the acidic surface of Nb_2O_5. Reproduced with permission.[168] Copyright 2019, Elsevier. 107

Figure 32. Photocatalytic reduction of CO_2 with H_2O as a hole scavenger over In-doped TiO_2 photocatalyst. Adapted with permission.[195] Copyright 2015, Elsevier..... 114

Figure 33. Schematic representation of the energy band positions in MoS_2/TiO_2 heterojunction composites and corresponding photoinduced charge carrier processes. Adapted with permission.[182] Copyright 2019, Elsevier. 115

Figure 34. Proposed photoinduced electron transfer from the carbazole to the triazine moiety and the reaction pathway in the photoreduction of CO_2 (PET = Photoinduced Electron Transfer). Reproduced with permission.[238] Copyright 2020, John Wiley and Sons. 122

Figure 35. Schematic representation of 2D and 3D COF networks. (a) 2D COFs consist of 2D sheets in the x-y-plane, stacked through π-π interactions in the z-direction. (b) In 3D COFs, the covalent bonds extend in all three spatial directions, often with *n*-fold intercalation. 125

Figure 36. Proposed photocatalytic mechanism for the CO_2 reduction to CO using the Re(I)-decorated COF. Adapted with permission.[66] Copyright 2018, American Chemical Society..... 135

Figure 37. (a) Modified TFBD-Co-SA-COF and (b) proposed mechanism of the photocatalytic CO_2 reduction in the presence of TEOA as a hole scavenger. Adapted with permission.[285] Copyright 2021, American Chemical Society. ... 136

Figure 38. Schematic energy level diagram of a COF (TpPa-1) decorated with Ru nanoparticles for the conversion of CO_2 to formic acid. Adapted with permission.[289] Copyright 2021, Elsevier. 137

Figure 39. Schematic illustration of the charge carrier transfer in COF-318-TiO_2 under light illumination following the Z-scheme model. Adapted with permission.[248] Copyright 2020, John Wiley and Sons. 139

Figure 40. Synthesis route of the CTF-Py COF and the heterogeneous catalyst TiO_2@CTF-Py. Reproduced with permission.[294] Copyright 2021, Elsevier..... 140

Figure 41. (a) DFT-calculated adsorption energy of CO_2 and H_2O on $[Ni(bpy)_2]^0$ with and without PI-COF-TT (inset: activation of CO_2 by $[Ni(bpy)_2]$). (b) Proposed mechanism for the CO_2 photoreduction over PI-COF-TT. Reproduced with permission.[265] Copyright 2020, Royal Society of Chemistry..... 146

Figure 42. COF fragment reflecting the 2:1 ratio of bpy to Pyr. 157

Figure 43. a) Experimental and indexed Pawley-refined PXRD pattern of **bpyPyr** and b) its crystal structure showing the unit cell used for Pawley-refinement and its c) cross-sectional view. Lattice parameters: a = 28.201 Å, b = 28.226 Å, c = 7.282 Å, α = 103.2°, β = 104.3°, and γ = 81.7°. Powder refinement: R_p = 7.37%. 158

Figure 44. a) Experimental and indexed Pawley-refined PXRD pattern of **Re bpyPyr** and b) its crystal structure showing the unit cell used for Pawley-refinement and its c) cross-sectional view. The experimental PXRD spectrum contains 57% of the bpy sites covered with $Re(CO)_3Cl$ units while the crystal structure contains 50%. Lattice parameters: a = 28.201 Å, b = 28.226 Å, c = 7.282 Å, α = 103.2°, β = 104.3°, and γ = 81.7°. Powder refinement: R_p = 6.59%..... 160

Figure 45. a) Nitrogen sorption isotherms of **bpyPyr COF** and **RebpyPyr COF**. b) Pore size distribution and cumulative pore volume of **bpyPyr COF** and **Re bpyPyr COF**. c) CO_2 sorption isotherms at 273 K (0 °C), indicating enhanced affinity of **Re bpyPyr COF** for CO_2 (filled symbols: adsorption, open symbols: desorption). d-f) STEM-HAADF images of **Re bpyPyr COF** showing the highly

ordered Re sub-structure within the COF backbone: d) interlayer distance, e) In-plane lattice spacing, and f) magnified view of (e). The experimental data corresponds to 42% site occupation. 164

Figure 46. a) The UV-vis absorption spectra, b) Tauc plot analysis, c) PL spectra and d) normalized PL spectra (λ_{exc} = 375 nm) of **bpyPyr** and **RebpyPyr COFs.** 166

Figure 47. The CO production rate by **Re bpyPyr COFs** with 42-85% Re loadings over 8 hours under illumination with λ > 370 nm. d) Corresponding TON measured after 8 h. Experiments were performed in CO_2-saturated CH_3CN/TEOA (5:1) solutions. The TON were calculated by dividing the amount of CO produced by the actual amount of Re present during the photocatalytic experiments. .. 169

Figure 48. a) Photocatalytic CO production rates of **Re bpyPyr COF (42% occupancy of bpy sites)** using TEOA versus BIH as SEDs. b) Impact of protic additives such as 0.05 mM water and 0.50 mM phenol on the CO production rates. . All experiments were performed in CO_2-saturated CH_3CN/TEOA (5:1) or CH_3CN/BIH (6.7 mM of BIH) under illumination with λ > 370 nm. 171

Figure 49. The TON_{CO} values of **Re bpyPyr COF** (circles) and *fac*-[$Re(CO)_3$(bpy)Cl] (stars) under white light illumination with a) l > 370 nm and illumination at b) l > 420 nm with BIH as sacrificial donor. The highlight regions show the maximum TON for *fac*-[$Re(CO)_3$(bpy)Cl] and **Re bpyPyr COF** for their respective illumination condition. Experiments were performed in CO_2-saturated CH_3CN/BIH (6.7 mM of BIH). To ensure a rigorous comparison, experiments were conducted using 0.84 mmol of catalytic sites for both **Re bpyPyr COF** and *fac*-[$Re(CO)_3$(bpy)Cl] complex. 173

Figure 50. a) Cyclic voltammogram measured at a scan rate of 5.0 mV s^{-1} where I and II are the first and second reductions for **Re bpyPyr COF**. b) ATR-IR-SEC spectra of **Re bpyPyr COF** under an Ar atmosphere at the indicated potentials. c) A plot of the absorption measured at 2012 and 1838 cm^{-1} as a function of the applied potential. Overlaid on the data are fits to a modified Nernst equation. d) ATR-IR-SEC spectra measured under a CO_2 atmosphere at the indicated potentials. All potentials are reported *vs*. Fc^+/Fc (E_0 = 0.400 V *vs*. SHE) and all measurements were performed in a 0.1 M $TBAPF_6/CH_3CN$ electrolyte. 175

Figure 51. Proposed catalytic cycle for CO_2 reduction for **Re bpyPyr COF**. 179

Figure 52. Synthesis of **bpyDBC** COF and immobilization of $Re(CO)_5Cl$, yielding **Re bpyDBC** COF. 184

Figure 53. COF fragment reflecting the 2:1 ratio of bpy to DBC..... 186

Figure 54. (a) Experimental and Rietveld refined PXRD patterns of **bpyDBC** COF, (b) FTIR spectra of the two linkers $bpy(CHO)_2$ and DBCTA together with the spectrum of the **bpyDBC** COF. c) Experimental and Rietveld refined PXRD patterns of **Re bpyDBC** COF and (d) FTIR spectra of **bpyDBC**, **Re bpyDBC** and the molecular analog $Re(bpy)(CO)_3Cl$. 192

Figure 55. a) Structural variants of the two COFs and b) superposition of the four structural variants of the unit cell, illustrating how the threefold propeller contrast dominated by Re(I) is created. 193

Figure 56. a) STEM-HAADF image showing the highly ordered Re(I) sub-structure within the COF lattice. b) Magnified section of a) with the COF lattice. 194

Figure 57. TEM images of the **bpyDBC** COF (a) and **Re bpyDBC** COF (b). 195

Figure 58. a) Nitrogen sorption isotherms of **bpyDBC** and **Re bpyDBC** COF and b) pore size distributions of both COFs. 196

Figure 59. (a) UV-Vis absorption (continuous line) and PL emission (dotted line, λ_{exc} = 476 nm) of **bpyDBC** and **Re bpyDBC**. (b) Energy levels of the two COFs, and reduction potentials of the sacrificial donor BIH and the CO_2 to CO reduction. 197

Figure 60. CO production of the **Re bpyDBC** COF under illumination with (a) λ >370 nm and (b) λ >400 nm. Solid lines represent the linear fitting of the data to extract CO production rates. 199

Figure 61. PXRD pattern (a and b) and IR spectra (c) of the **Re bpyDBC** COF before and after 24 h of photocatalysis under illumination with λ > 370 nm and λ > 400 nm. 201

Figure 62. Schematic Diagram of CO_2 Electrolysis Driven by Renewable Electrical Energy. 206

Figure 63. Schematic representation of different types of electrochemical cells used for CO_2 reduction studies..... 207

Figure 64. Reduction pathway for *fac*-[Mn(bpy)$(CO)_3$Br] based on previous reports.[47, 373]..... 211

Figure 65. **PhenPy** COF fragment reflecting the 2:1 ratio of Phen to Py. 221

Figure 66. (a) Synthesis of **PhenPy** COF and immobilization of [Mn$(CO)_5$Br], yielding **Mn PhenPy** COF (schematic). (b) Experimental and indexed Pawley-refined PXRD pattern of **PhenPy** COF. Pawley refinement was conducted using the simulated structure model of **PhenPy**, based on the triclinic space group *P1.* (c) Unit cell of **PhenPy** COF. Alternating phenanthroline moieties in adjacent layers face towards different pores (inset). The cell parameters of the refined structure are provided in the Section S7. (d) SEM micrograph of the **PhenPy** COF powder, indicating a fibrillar morphology. (e) Nitrogen sorption measurements reveal high porosity with a BET surface area of 929 m^2g^{-1}. Inset: pore size distribution and cumulative pore volume of **PhenPy** 225

Figure 67. XPS spectra of **Mn PhenPy** COF (a-c) and **Mn PhenPy** COF applied to a gas diffusion electrode (d-f). 228

Figure 68. (a) PXRD patterns of the **PhenPy** and the **Mn PhenPy** COFs. (b) FTIR spectra of **PhenPy** and **Mn PhenPy** COF, as well as of the molecular analog *fac*-[Mn(**Phen**)$(CO)_3$Br]. (c) SEM micrographs of the **Mn PhenPy** COF. (d) CO_2 sorption measurements at 273 K (0 °C) indicating an enhanced affinity of **Mn PhenPy** COF for CO_2 (filled dots: adsorption, open dots: desorption). (e) Energy levels of the two COFs obtained from Tauc plot fitting of the optical absorption onsets and CV measurements (Figures S13, S14), and the CO_2 to CO reduction potential. (f) Cyclic Voltammetry of **Mn PhenPy** COF and *fac*-[Mn(**Phen**)$(CO)_3$Br] measured in a three-electrode setup in acetonitrile ($TBAPF_6$, 0.1M) under Ar at a scan speed of 10 mV s^{-1}. The colours are assigned as follows: **PhenPy** (green)**, Mn PhenPy** (pink), *fac*-[Mn(**Phen**)$(CO)_3$Br] (orange). 230

Figure 69. (a) Schematic representation of the catholyte-free MEA cell architecture employing a GDE with **Mn PhenPy** COF as active electrocatalyst. (b) Partial current densities for CO formation j_{CO} (chronoamperometry) and (c)

the respective TOF for CO, TOF_{CO}, of **Mn PhenPy** COF and *fac*-[Mn(bpy)$(CO)_3$Br] at different applied full-cell potentials (details in Table S1) measured using a catholyte-free MEA cell with 1 M KOH as anolyte and a *Sustainion*® anion-exchange-membrane. 234

Figure 70. (a) Faradaic efficiencies (left scales) and TOF (blue dots, right scales) values as a function of different applied potentials along with (b) long-term stability experiments conducted at applied full-cell potential of 2.8 V recorded for **Mn PhenPy** COF. 238

Figure 71. Schematic illustration of an a) Orthogonal, b) Assisted and c) Self-cascade Catalytic Reactions. 244

Figure 72. Schematic illustration of Cascade Reaction on a) Ag−Cu Nanozyme and b) PTF(Ni)/Cu for CO_2RR showing the *CO intermediate diffusing through the interface of the hybrid materials for the formation of C2+ products. Adapted from O'Mara[422] and Meng[423]. 246

Figure 73. Reaction of *cis*-[Ru(bpy)$_2$(CO)$_2$]$^{2+}$ (Ru−CO^{2+}) and *cis*-[Ru(bpy)$_2$(CO)(CHO)]$^+$ (Ru−CHO^+) with organohydride donors (BIHs). 255

Figure 74. a) Chemical structures of the **Re bpyPyr** and **Re-Ru bpyPyr** materials together with the post-synthetic immobilization strategy for incorporates the Ru(bpy)$_2$(CO)$_2$ moiety, b) FTIR spectra of **Re bpyPyr, Ru bpyPyr** and **Re Ru bpyPyr** 1:1 (Re/Ru), c) FTIR spectra of **Re Ru bpyPyr** prepared using different Re/Ru molar ratios of 2:1 and 1:1. The **Ru bpyPyr** structure contain only the Ru sites without any Re sites. 256

Figure 75. ^{1}H NMR spectra of the liquid phase collected during the light-induced (λ > 420 nm) reaction of **Re-Ru bpyPyr** (under Ar atmosphere), **Re bpyPyr** (under CO_2 atmosphere) and **Re-Ru bpyPyr** (under CO_2 atmosphere) in the presence of BIH (0.22 mmol) and LiOTf (0.22 mmol) in toluene. The highlighted peak is attributed to CH_3OH. 259

Figure 76. FTIR spectra of **Ru bpyPyr** recorded before and after photocatalytic irradiation under an Ar atmosphere. 261

Figure 77. a) Synthesis of **bpyCoPc** and immobilization of $Mn(CO)_5Br$, yielding **Mn bpyCoPc**, b) FTIR spectra of **Mn bpyCoPc**, **bpyCoPc** and their precursors, c) PXRD spectra of **Mn bpyCoPc**, **bpyCoPc**..... 263

Figure 78. a) Schematic representation of the H-type cell architecture employing a GDE with **Mn bpyCoPc** as active electrocatalyst. b) Cyclic Voltammetry (CV) of **Mn bpyCoPc** and **bpyCoPc** measured right before the bulk electrocatalysis in CO_2-saturated $KHPO_4$ (0.5 M) at a scan rate of 100 mV s^{-1}. c) Chronoamperometric responses during the bulk electrocatalysis of **Mn bpyCoPc** at 1.5 V *vs*. Ag/AgCl and d) Faradaic Efficiencies (FE) values as function of time at applied potential of 1.5 V *vs*. $Ag/AgCl/KCl_{(sat)}$. 265

Figure 79. (a) Schematic representation of the flow-cell architecture employing a GDE with **Mn bpyCoPc** as the electrocatalyst. (b) Chronoamperometric response during bulk electrolysis of **Mn bpyCoPc** at −2.0 V *vs.* $Ag/AgCl/KCl_{(sat)}$. (c) Faradaic efficiencies (FE) for CO, H_2, CH_3OH and HCOOH as a function of electrolysis time in the flow-cell configuration under a CO_2 flow rate of 30 mL min^{-1} using 0.5 M $KHCO_3$ as the electrolyte. 267

Figure 80. ^1H NMR spectra of the liquid phase collected after 30, 60, and 90 min of bulk electrolysis performed at an applied potential of −2.0 V *vs.* Ag/AgCl under a CO_2 atmosphere. The samples were prepared by mixing the electrocatalytic solution with D_2O and DMSO as the internal standard (δ = 2.78 ppm). 268

Figure 81. Infrared spectroelectrochemistry (IR-SEC) of **Mn bpyCoPc** in 0.1 M $TBAPF_6/CH_3CN$ electrolyte during the first and second reduction process under (a-b) Ar and (c-d) CO_2 atmospheres. The graphs on the left (a and c) corresponds to the first electron reduction process while the graphs on the right (b and d) are from the second electron reduction process. All potential are reported vs. Fc/Fc^+. 270

Figure 82. Proposed electrocatalytic catalytic pathway for **Mn bpyCoPc.** The Mn-COOH adduct (species d) can undergo reduction to produce either CO (green pathway) or HCOOH (red pathway). 273

LIST OF TABLES

Table 1. Standard reduction potentials (*vs.* SHE) for the multi-electron reduction of CO_2 in water at pH 7 (298 K, 1 atm, and 1 mol L^{-1} solute concentrations).[20] 38

Table 2. Photophysical properties in CH_3CN of the studied complexes (λ_{exc} = 375 nm). 72

Table 3. Photocatalytic performance of studied complexes in CH_3CN solution containing 0.03 mmol L^{-1} of complex..... 79

Table 4. Relevant examples of pristine inorganic semiconductors applied for the CO_2 photoreduction..... 97

Table 5. Relevant examples of inorganic semiconductors modified with metal nanoparticles, metal- and metal-free semiconductors applied for the CO_2 photoreduction..... 109

Table 6. Relevant examples of pristine COFs applied for CO_2 photoreduction..... 127

Table 7. Relevant examples of COFs- based hybrids applied for the CO_2 photoreduction..... 140

Table 8. COF-based hybrid Re(I) complexes applied in the photoreduction of CO_2 to CO. 200

Table 9. Comparison of the duration of the photocatalytic experiments for several COF-based CO_2 photocatalysts..... 202

Table 10. Comparison of performance of a selection of Mn-based CO_2 reduction electrocatalysts. 235

ABBREVIATIONS AND SYMBOLS

ATR	Attenuated Total Reflectance
ATR-IR-SEC	Attenuated Total Reflectance Infrared Spectroelectrochemistry
bbzp	2,6-Bis(2-benzimidazolyl)pyridine
BET	Brunauer–Emmett–Teller
BIH	1,3-Dimethyl-2-phenyl-2,3-dihydro-1H-benzimidazole
bpy	2,2′-Bipyridine
CB	Conduction Band
CO_2RR	Carbon Dioxide Reduction Reaction
COF	Covalent Organic Framework
CORR	Carbon Monoxide Reduction Reaction
CV	Cyclic Voltammetry
DBC	Dibenzochrysene
DFT	Density Functional Theory
EDX	Energy-Dispersive X-Ray Spectroscopy
FE	Faradaic Efficiency
Fc/Fc^+	Ferrocene/ferrocenium redox couple
FID	Flame ionization detector
FTIR	Fourier Transform Infrared Spectroscopy
GC-FID	Gas chromatography with flame ionization detection
GC-TCD	Gas chromatography with thermal conductivity detection
GDE	Gas-Diffusion Electrode
HAADF	High-angle annular dark-field
HER	Hydrogen Evolution Reaction

HOMO	Highest Occupied Molecular Orbital
ICP-OES	Inductively coupled plasma optical emission spectroscopy
IR-SEC	Infrared Spectroelectrochemistry
KIE	Kinetic Isotope Effect
LUMO	Lowest Unoccupied Molecular Orbital
MEA	Membrane Electrode Assembly
MLCT	Metal-to-Ligand Charge Transfer
MWCNT	Multi-walled carbon nanotubes
NMR	Nuclear magnetic resonance
NN	Diimine ligand
OCP	Open-circuit potential
OER	Oxygen Evolution Reaction
OTTLE	Optically Transparent Thin-Layer Electrochemical
pbiH	2-(2-Pyridyl)benzimidazole
phen	1,10-Phenanthroline
PL	Photoluminescence
Pyr	Pyrene
PXRD	Powder X-ray Diffraction
SEC	Spectroelectrochemistry
SEM	Scanning electron microscopy
STEM	Scanning Transmission Electron Microscopy
STEM-HAADF	High-Angle Annular Dark-Field Scanning Transmission Electron Microscopy
SWV	Square-wave voltammetry
TD-DFT	Time-Dependent Density Functional Theory

TGA	Thermogravimetric Analysis
TEM	Transmission Electron Microscopy
TEOA	Triethanolamine
TON	Turnover Number
TOF	Turnover Frequency
UV-vis	Ultraviolet–visible spectroscopy
VB	Valence Band
XPS	X-ray Photoelectron Spectroscopy
λ	Wavelength
ν	Frequence
ν**(CO)**	Carbonyl stretching frequency
ΔG^0	Standard Gibbs free energy change
ΔH^0	Standard enthalpy change
ΔS^0	Standard entropy change
E	Potential
E_{ox}	Oxidation Potential
E_{red}	Reduction Potential
$E_{1/2}$	Half-wave potential
E_{OCP}	Open-circuit potential
J	Current Density
***j*CO**	Partial Current Density for CO formation
τ	Excited-state lifetime
ϕ	Quantum yield

Table of Contents

1. Chapter 1 29

General Introduction 29

1.1. Global Energy And Climate Challenges 29

1.2. CO_2 Conversion Strategies 33

1.2.1. Photocatalytic CO_2 Reduction 33

1.2.2. Electrocatalytic CO_2 Reduction 36

1.3. CO_2 Reduction Challenges 37

1.4. Molecular Catalysts 39

1.5. Hybrid Catalysts 43

1.6. Covalent Organic Frameworks As Supporting Platforms For Hybrid Catalysts 45

1.7. Thesis Goals And Organization 48

2. Chapter 2 58

Mechanistic Insights Into CO_2-to-CO Photoreduction By Proton-Responsive Imidazole-Pyridine Re(I) Complexes 58

2.1. Introduction 58

2.2. Experimental Methods 61

2.3. Results And Discussion 66

2.4. Conclusions 91

3. Chapter 3 93

From Conventional Inorganic Semiconductors To Covalent Organic Frameworks: Advances And Opportunities In Heterogeneous Photocatalytic CO_2 Reduction 93

3.1. Introduction 93

3.2. Conclusions And Perspectives 147

4. Chapter 4 149

Unlocking CO_2 Photoreduction With Re(I) Single-Site Cof-Based Catalysts: Structure-Activity Relationships 149

4.1. Introduction 149

4.2. Experimental Section 151

4.3. Results And Discussion 157

4.4. Conclusions 180

5. Chapter 5 182

Designing Atomically Precise And Robust Cof Hybrids For Efficient Photocatalytic CO_2 Reduction 182

5.1. Introduction 182

5.2. Experimental Section 184

5.3. Results And Discussion 192

5.4. Conclusion 203

6. Chapter 6 205

Electrochemical CO_2 Conversion: Towards Scalability 205

6.1. From Photocatalytic To Electrocatalytic Systems 205

6.2. Earth-Abundant Catalyst As Promising Candidates For Replacing Noble-Metal Catalysts. 210

6.3. Mn(I) - Functionalized Covalent Organic Framework As Efficient Electrocatalyst For Co_2 Reduction In A Catholyte-Free Zero-Gap Electrolyzed 214

6.4. Experimental Section 215

6.5. Results And Discussion 224

6.6. Conclusion 239

7. Chapter 7 242

Towards Multi-Site Cascade Catalysts For Sequential CO_2 Reduction 242

7.1. Introduction 242
7.2. Experimental Section 248
7.3. Results And Discussion 253
7.3.1. Multi-Site Cascade Re-Rubpypyr Catalyst 253
7.3.2. Multi-Site Cascade Mn Bpycopc Catalyst 262
8. Chapter 8 275
Conclusions And Perspectives 275
8.1. General Conclusions 275
8.2. Perspectives 277
References 280
Appendix A 332
Appendix B 345
Appendix C 358
Appendix D 365

Chapter 1

General Introduction

1.1. Global energy and Climate Challenges

Meeting the growing global demand for energy while mitigating the environmental impacts associated with greenhouse gas (GHG) emissions represents one of the greatest technological challenges of the 21° century. Achieving sustainable development requires a progressive transition from a fossil fuel-based energy matrix to renewable and low-carbon energy technologies capable of ensuring both energy security and environmental preservation.[1, 2]

According to statistics published by the International Energy Agency (IEA), oil, natural gas, and coal derivatives collectively accounted for more than 80% of the global Total Energy Supply (TES) throughout the period from 1990 to 2023, reaching 80.7% in 2023 (**Figure 1**).[3] This persistent dependence highlights the enormous challenge associated with replacing conventional energy sources on a global scale. [4]

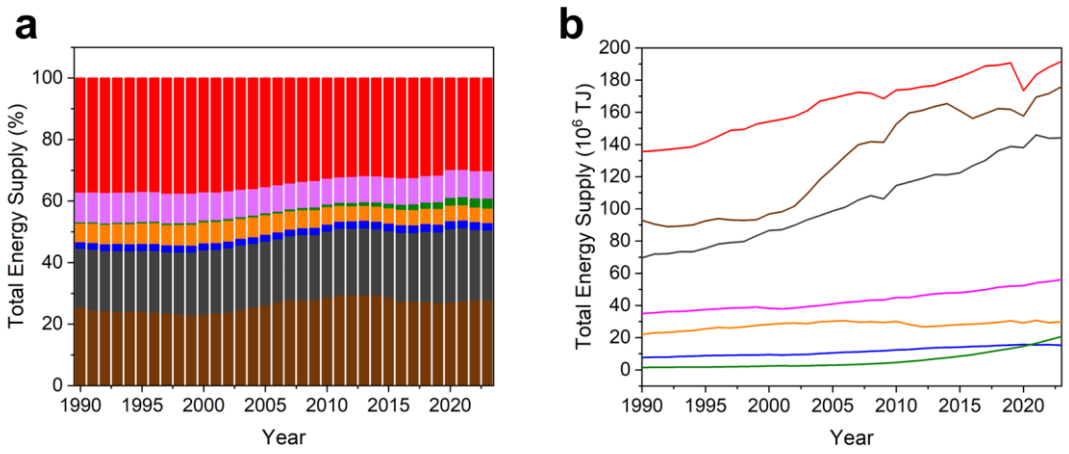


Figure 1. Percentual (a) and raw amount (b) of the global Total Energy Supply (TES) and by energy source between 1990 and 2023, according to the International Energy Agency (IEA) Red: Oil and oil products; Pink: Biofuels and waste; Brown: Coal and coal products; Blue: Hydropower; Grey: Natural gas; Orange: Nuclear; Green: Solar, wind, and other renewables.[3]

Although renewable energy sources have experienced remarkable growth over the last three decades, their expansion has largely accompanied, rather than replaced, fossil fuel consumption. Consequently, the relative contribution (**Figure 1a**) of fossil fuels to the global energy matrix has remained nearly constant, while the absolute consumption (**Figure 1b**) of fossil fuels-derived energy has continued to increase. This observation evidences that the current energy transition is progressing at a slower pace than what is required to substantially reduce global carbon emissions.[5]

The extensive use of fossil fuels is directly associated with anthropogenic Greenhouse Gas (GHG) emissions, with carbon dioxide (CO_2) accounting for approximately 75% of total anthropogenic CO_2 emissions through the combustion of coal, oil, and natural gas.[6] The latest Climate Change 2023 Synthesis Report published by the Intergovernmental Panel on Climate Change (IPCC) identifies CO_2 as the largest contributor to the global warming crisis.[7] According to the

report, the global average surface temperature increased by approximately 1.1 °C during the period 2011-2020 relative to the pre-industrial baseline (1850-1900), with the best estimate indicating that global warming will reach 1.5 °C in the near future under the currently considered emission scenarios (**Figure 2a**). Limiting global warming to 1.5 °C has become a central international objective because, once exceeding this threshold is exceeded, a significantly increase the in the frequency and severity of extreme weather events, biodiversity loss, and socioeconomic impacts are expected.

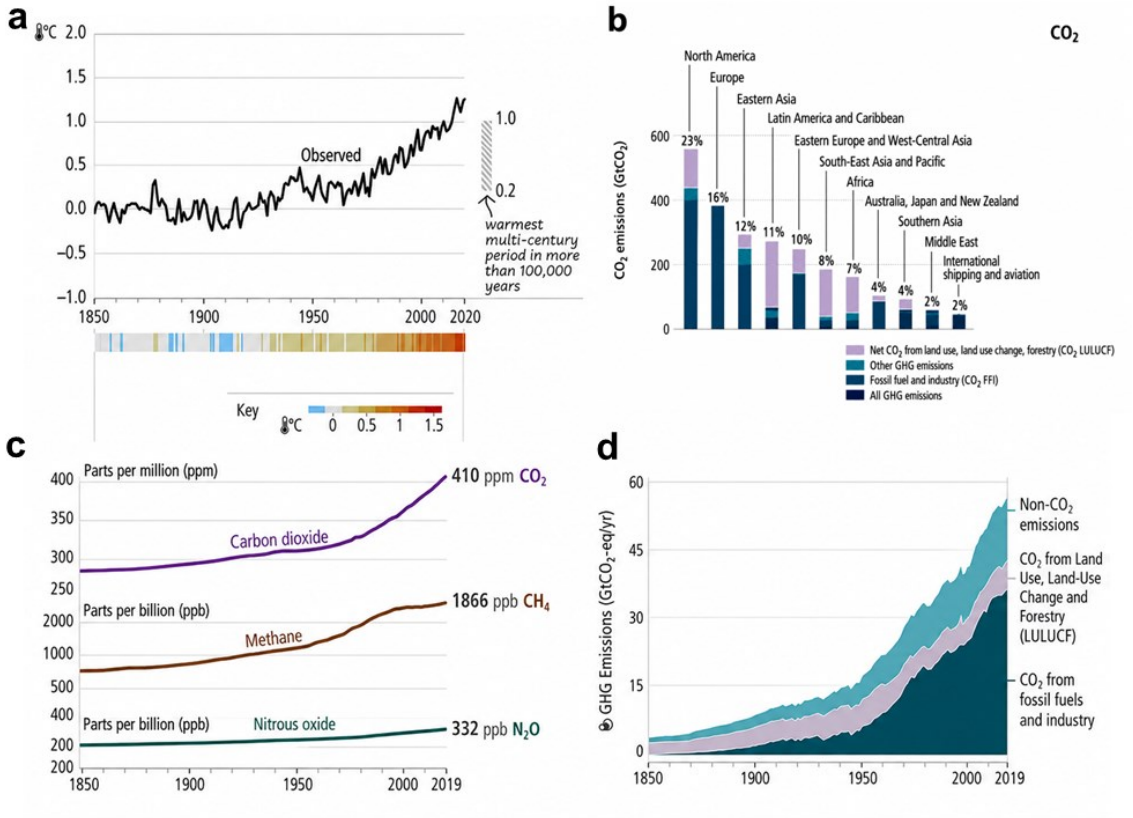


Figure 2. (a) The global surface temperature since 1850-1900. (b) Historical cumulative net anthropogenic CO_2 emissions per region from 1850 to 2019 in $GtCO_2$.(c) Atmospheric concentrations of several Greenhouse Gas (GHG) including the three major well-mixed GHGs CO_2, CH_4 and N_2O. (d) Global net anthropogenic GHG emissions include CO_2 from fossil fuel combustion and industrial processes (CO_2-FFI) (dark green); net CO_2 from land use, land-use change and forestry (CO_2-LULUCF) (green); CH_4; N_2O; and fluorinated gases

(HFCs, PFCs, SF_6, NF_3) (light blue). Adapted from Climate Change 2023 Synthesis Report.[7]

Together the data presented in **Figure 2b-d** illustrate the cumulative anthropogenic CO_2 emissions by geographical region, historical evolution of the major greenhouse gases (CO_2, CH_4, and N_2O) and main sources of CO_2 emission between 1850 and 2019. These data show that CO_2 is dominantly emitted from more historically developed regions and it is also the dominant GHG while its main emission source is from fossil-fuel consumption. It is important to recognize that the historical increase in CO_2 emissions has been closely associated with economic and industrial development. In this context, strategies aimed at capturing and recycling anthropogenic CO_2 into value-added chemicals and fuels offer an attractive alternative to complement emission reduction efforts while supporting the transition toward a more sustainable carbon economy.

These global challenges have stimulated intensive research toward carbon-neutral energy technologies based on renewable resources.[8] The large-scale implementation of solar and wind energy, carbon capture and utilization (CCU), and carbon capture and storage (CCS) are among the principal strategies currently being pursued to reduce anthropogenic CO_2 emissions. These efforts are closely aligned with the United Nations Sustainable Development Goals (SDGs), particularly Goals 7 (Affordable and Clean Energy), 11 (Sustainable Cities and Communities), and 13 (Climate Action).

1.2. CO_2 conversion strategies

CO_2 can be converted into value-added chemicals through several catalytic routes, including thermocatalysis, plasma-assisted catalysis, biological conversion, photocatalysis, electrocatalysis and photoelectrocatalysis.[9-13] Conventional thermocatalytic routes generally rely on high temperatures, elevated pressures, and H_2-rich atmospheres to activate the thermodynamically stable CO_2 molecule. [14] In contrast, photo- and electrocatalytic processes operate under considerably milder conditions while allowing direct coupling with renewable energy sources, making them promising alternatives for sustainable CO_2 utilization. Consequently, these two strategies constitute the primary focus of this thesis.

1.2.1. Photocatalytic CO_2 reduction

Inspired by natural photosynthesis, in which photosynthetic organisms convert solar energy, water, and CO_2 into chemical energy, photocatalytic CO_2 reduction has emerged as one of the most promising strategies for reducing the carbon footprint of conventional industrial processes. Artificial photosynthetic systems aim to convert CO_2 into energy-rich compounds (solar fuels) by using sunlight as the energy source and organic electron donors as reducing agents, thereby mimicking the natural photosynthetic processes occurring in plants and algae.[15-17]

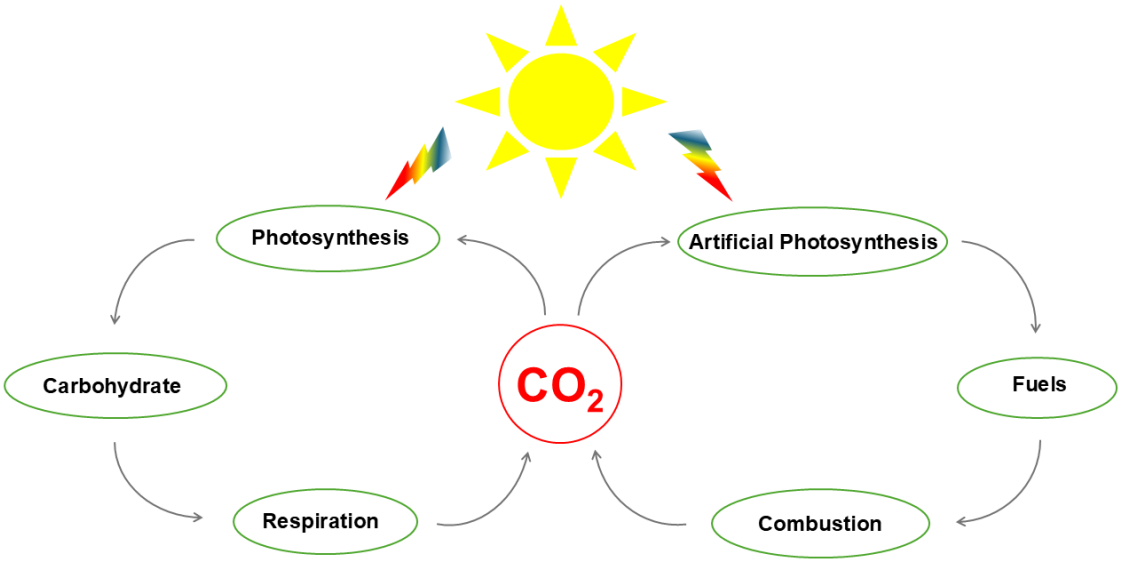


Figure 3. Natural (left) and Artificial Photosynthetic (right) pathways.

Figure 3 illustrates an ideal sustainable carbon cycle in which the excess CO_2 produced by the combustion of fossil fuels is captured and converted back into energy-rich fuels through an artificial system. This approach complements the natural carbon cycle by recycling anthropogenic CO_2, thereby helping to maintain atmospheric CO_2 concentrations at a more stable level.

From a mechanistic perspective, photocatalytic CO_2 reduction consists of a series of concerted photochemical reactions involving three fundamental components: a photosensitizer or light harvester (PS), an electron donor (D), and a catalyst (Cat). Alternatively, the light harvester and the catalytic center can be a single species (PCat). **Figure 4** schematically illustrates the role of these components during the photocatalytic CO_2 reduction cycle.

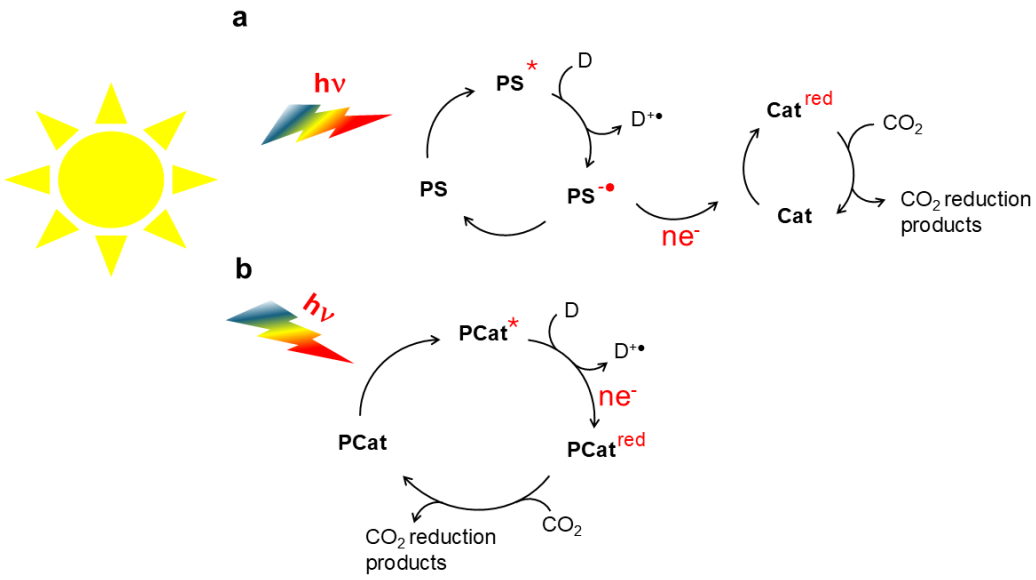


Figure 4. Schematic representation of the main components of a photocatalytic CO_2 reduction system showing the roles of the photosensitizer/light harvester (PS), electron donor (D), catalyst (Cat) and photocatalyst (PCat).

Figure 4a illustrates a conventional photocatalytic system in which the photosensitizer initially absorbs incident solar radiation and is promoted to an excited state. In the presence of a suitable sacrificial electron donor, typically an amine.[18] The excited photosensitizer is reductively quenched to generate a strongly reducing species capable of transferring one or more electrons (ne^-) to the catalyst, depending on the nature of the electron donor and the photocatalytic system.[19] The reduced catalyst (Cat^{red}) subsequently activates and reduces CO_2 to produce the desired products.

Alternatively, certain catalysts are capable of simultaneously acting as both the light-harvesting unit and the catalytic center (**Figure 4b**).[20-22] In these systems, the photocatalysts (PCat), light absorption leads to multiple reductive quenching steps, leading to the formation of a catalytic center able to transfer electrons to CO_2, promoting its conversion into different reduction products.

It is important to emphasize that the mechanisms shown in **Figure 4** represent only a simplified overview of the fundamental principles governing photocatalytic CO_2 reduction. The elementary reaction steps involved in CO_2 activation, electron accumulation, proton transfer, and product formation vary considerably depending on the catalyst and the reaction conditions. These aspects, together with the crucial role of proton sources in determining catalytic activity and selectivity, will be discussed in greater detail in Chapter 2.

1.2.2. Electrocatalytic CO2 reduction

In the electrocatalytic CO_2 reduction, electrical energy (ideally from a renewable source) is supplied by an external power source and electrons are transferred from the cathode to the catalyst (**Figure 5**), which in turn drives the CO_2 reduction. [23] The overall cycle involves also an oxidation reaction on the anode (typically the oxygen evolution reaction, OER).

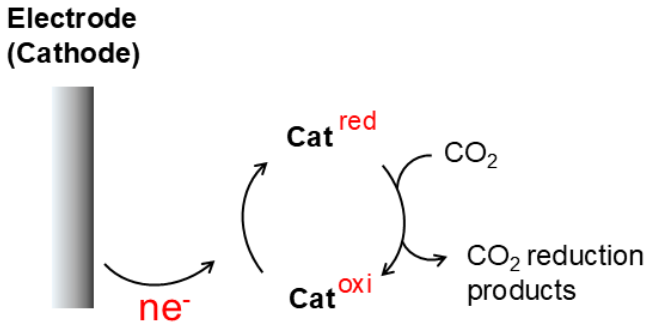


Figure 5. Schematic representation of an electrochemical CO_2 reduction system. Adapted from Kuramochi.[20]

Compared with photocatalytic systems, electrocatalytic CO_2 reduction offers several practical advantages. Electrons transfer rates are generally faster and can be controlled by the applied potential to the electrode as well as the

oxidation states of the catalysts on the electrode surface.[20, 24] The reaction rate and product selectivity can be directly controlled through the applied potential or current density, allowing precise investigation of catalytic mechanisms and optimization of operating conditions.[25] Furthermore, electrochemical setups can be coupled with other spectroscopic techniques (spectroelectrochemistry, SEC) allowing species of interest to be characterized in situ during the electrolysis of small amounts of materials. This approach has been successfully shown combined with ultraviolet-visible (UV-vis) absorption,[26] nuclear magnetic resonance (NMR),[27] fluorescence,[28] electron paramagnetic/spin resonance (EPR/ESR),[29] and infrared (IR) spectroscopy.[30] Detailed explanation of spectroelectrochemical studies on homogeneous and heterogeneous systems will be discussed in Chapters 2 and 4, respectively.

From an application perspective, electrochemical cells or electrolyzers can be readily integrated with multiple power sources, facilitating continuous operation independently of sunlight availability. Furthermore, recent advances in membrane electrode assemblies (MEAs),[31] and gas-diffusion electrodes (GDEs)[32] have further improved CO_2 utilization efficiency and current densities, bringing electrocatalytic CO_2 conversion closer to industrial implementation.

1.3. CO_2 Reduction challenges

The possible CO_2 reduction reactions are summarized in **Table 1** together with their corresponding standard reduction potentials in water at pH 7 (298 K, 1 atm, and 1 mol L^{-1} solute concentrations). The selective formation of a particular product depends on several factors, including the electronic properties of the

catalyst, reaction conditions, and the nature and concentration of the proton source.[20, 33]

Table 1. Standard reduction potentials (*vs.* SHE) for the multi-electron reduction of CO_2 in water at pH 7 (298 K, 1 atm, and 1 mol L^{-1} solute concentrations).[20]

$CO_{2(g)} + 2H^+ + 2e^- \rightarrow HCOOH_{(aq)}$	-0.61 V	(1)
$CO_{2(g)} + 2H^+ + 2e^- \rightarrow CO_{(g)} + H_2O_{(l)}$	-0.52 V	(2)
$CO_{2(g)} + 4H^+ + 4e^- \rightarrow HCHO_{(aq)} + H_2O_{(l)}$	-0.48 V	(3)
$CO_{2(g)} + 6H^+ + 6e^- \rightarrow CH_3OH_{(aq)} + H_2O_{(l)}$	-0.38 V	(4)
$CO_{2(g)} + 8H^+ + 8e^- \rightarrow CH_{4(g)} + 2H_2O_{(l)}$	-0.24 V	(5)

Because these reactions proceed through proton-coupled electron transfer (PCET) steps, the availability and nature of the proton source strongly influence both catalytic activity and product selectivity.[35-37] Moreover, proton reduction to molecular hydrogen (H_2) frequently competes with CO_2 reduction, particularly in catalytic systems designed to produce CO or formic acid. This competition arises because the two-electron reduction of protons to H_2 ($E° = -0.41$ V *vs.* SHE at pH 7) occurs at potentials comparable to those required for the two-electron reduction of CO_2 (Equations 1-2). Consequently, the development of catalysts capable of preferentially interact with and activate CO_2 while suppressing the competing hydrogen evolution reaction remains one of the major challenges in the field.[38]

1.4. Molecular catalysts

Homogeneous catalysts, such as metalloporphyrins and metal complexes, are particularly attractive due to their high selectivity towards different CO_2 reduction products. [39] Metal complexes, such as Re(I), Mn(I), and Ru(II), are widely studied for CO_2 reduction due to their multiple accessible redox states.[20] This enables multielectron reduction processes, enhancing catalytic efficiency. The flexibility in ligand design allows for fine-tuning of catalytic performance and offers mechanistic insights into the factors influencing catalytic activity. The **Figure 6** shows some common metal complexes with activity for CO_2 reduction. Most of the metal complexes yield CO and/or HCOOH as the two-electron reduction products of CO_2. Furthermore, most of these metal complexes have high activation energies for the proton reduction, which results in a higher selectivity for CO_2 reduction, even under aqueous conditions.[20]

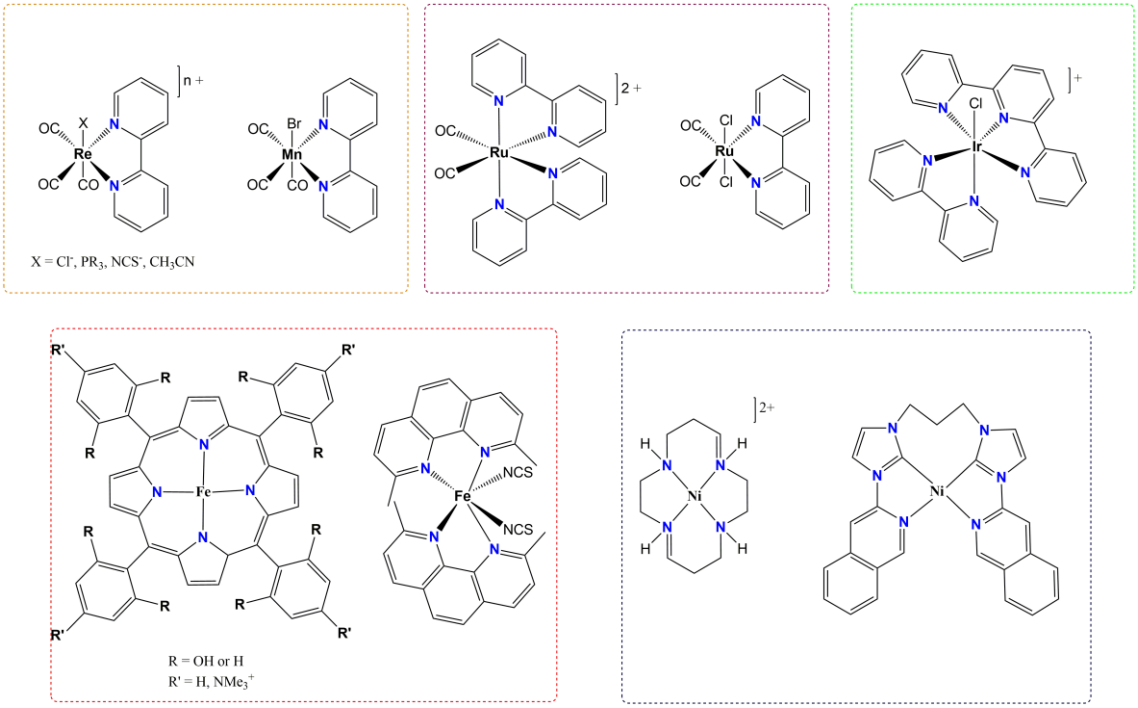


Figure 6. Representative metal complexes structures of some CO_2 catalysts.[20]

A class of molecular catalysts that has attracted considerable attention for photocatalytic and electrocatalytic CO_2 reduction is the family of fac-$Re(CO)_3(NN)X$ complexes, where NN is typically a diimine ligand such as 2,2'-bipyridine and X is a halide ligand (**Figure 6**).[40-44] These complexes combine several desirable characteristics for CO_2 reduction, including strong visible-light absorption depending on the NN ligand, accessible metal- and ligand-centered redox processes, high selectivity toward CO formation, and the possibility of systematically tuning their electronic properties through ligand modification. Consequently, they have become benchmark systems for mechanistic investigations and catalyst development in molecular CO_2 reduction.

The catalytic activity of these complexes is closely related to the synergistic participation of both the metal center and the coordinated diimine ligand. Upon reduction, the lowest unoccupied molecular orbital (LUMO), largely localized on the diimine ligand π^* orbitals, is populated, generating a reduced species with enhanced nucleophilicity and reactivity toward CO_2.[43-45] The ability to store electrons in the ligand framework facilitates the multielectron transformations required for CO_2 activation and reduction under mild conditions.

The first report of a *fac*-$Re(CO)_3(NN)X$ complex as a catalyst for CO_2 reduction was published by Lehn and co-workers in 1984, who demonstrated highly selective conversion of CO_2 to CO.[40] Since then, this family of complexes has been extensively investigated with the aim of understanding the fundamental steps governing catalytic activity, selectivity, and deactivation pathways.[42]

One of the earliest mechanistic questions concerned the nature of the vacant coordination site required for CO_2 binding. In 1986, Lehn and co-workers proposed that catalytic activation involved dissociation of one carbonyl ligand, generating an open coordination site for CO_2 binding and subsequent reduction.[41] Shortly thereafter, Meyer and co-workers proposed an alternative mechanism in which reduction of the complex promotes dissociation of the halide ligand rather than carbonyl loss, producing a five-coordinate intermediate capable of binding and activating CO_2.

Subsequent advances in spectroelectrochemical techniques provided important insights into these competing proposals. In particular, FTIR spectroelectrochemical studies performed by Andrews and co-workers in 1992 revealed spectral signatures consistent with halide labilization following formation of the one-electron reduced species (OERS).[46] **Figure 7** presents the currently accepted reduction pathway for the *fac*-$Re(CO)_3(bpy)Cl$ complex and its derivatives, showing the major reduced intermediates that have been characterized to date.

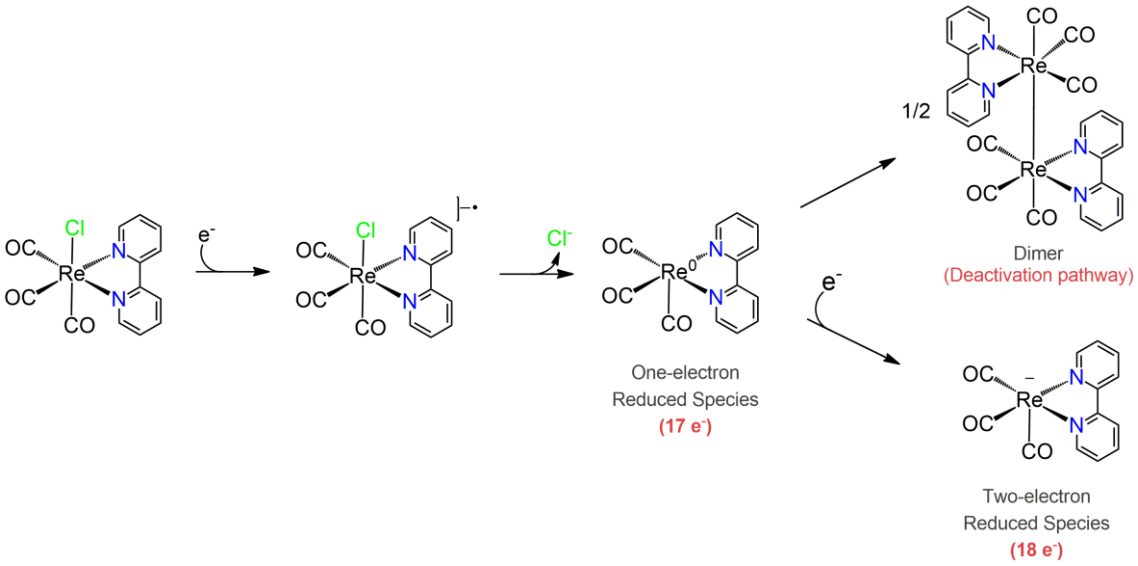


Figure 7. Most accepted reduction pathway for the *fac*-$Re(CO)_3(bpy)Cl$ catalyst.

These observations supported the formation of a five-coordinate intermediate capable of binding CO_2 and undergoing subsequent proton-coupled electron transfer steps to produce CO and H_2O. However, two distinct five-coordinate reduced species have been proposed to form during this catalytic pathway, the one-electron reduced species (OERS) and the two-electron reduced species, which may serve as the active intermediates for CO_2 reduction. Among these, the latter (an 18-electron species) is generally considered to be more stable following the fundaments of the organometallic chemistry. On the other hand, two generated OERS typically reacts to form metal-metal bonded dimers, thereby removing active species from the catalytic cycle.[47, 48] Such deactivation pathways not only decrease catalytic performance but also complicate the long-term operation of homogeneous photocatalytic systems.

Despite decades of research, several aspects of the catalytic cycle remain under active debate. The nature of the catalytically active species, the role of proton donors, the participation of dimeric intermediates, and the influence of

ligand electronic structure on charge accumulation and CO_2 activation continue to be investigated. [13, 23, 24] Recent studies employing time-resolved spectroscopy, spectroelectrochemistry, computational methods, and operando characterization techniques have revealed that subtle changes in ligand structure can significantly alter the reaction pathway and catalytic performance.[49, 50] Consequently, mechanistic investigations remain essential for establishing structure-activity relationships and guiding the rational design of more efficient molecular CO_2 reduction catalysts.

Molecular catalysts offer several advantages for CO_2 reduction, including their solubility in a wide range of solvents, the possibility of fine-tuning their electronic and steric properties through ligand design, and the ability to characterize and isolate catalytic intermediates using conventional spectroscopic and electrochemical techniques.[20] These characteristics have made molecular catalysts invaluable model systems for mechanistic investigations and the establishment of structure-activity relationships.

Despite these advantages, the practical application of homogeneous catalysts is often limited by their relatively low stability under catalytic conditions. [15, 19, 20] Catalyst deactivation may occur through a variety of pathways, including ligand dissociation, radical side reactions, and the above mentioned formation of inactive dimeric species.

1.5. Hybrid catalysts

Heterogeneous photocatalysts, including metal nanoparticles, inorganic semiconductors, and two-dimensional materials, generally exhibit superior structural stability and facilitate catalyst recovery and reuse.[51, 52] These materials

have therefore been extensively investigated for photocatalytic CO_2 reduction. However, heterogeneous catalysts often suffer from lower selectivity toward a single reduction product due to the presence of multiple surface-active sites, which can promote competing reaction pathways.[53] Moreover, the characterization of catalytic intermediates is considerably more challenging than in molecular systems because the active sites are frequently poorly defined and inaccessible to many conventional spectroscopic techniques. Consequently, establishing detailed mechanistic pathways and rationally correlating catalyst structure with activity remains difficult in many heterogeneous systems.

The complementary advantages and limitations of molecular and heterogeneous catalysts have motivated the development of hybrid photocatalysts, which seek to combine the molecular-level tunability and selectivity of homogeneous catalysts with the robustness and recyclability of solid-state materials.[54-58] In these systems, molecular catalysts are immobilized onto semiconductor surfaces or porous supports, allowing the catalytic center to retain its well-defined structure while benefiting from enhanced charge separation, improved catalyst stability, and suppression of deactivation pathways such as dimerization.

Among the pioneering examples of this approach, the Reisner group reported a hybrid catalyst consisting of Re(I) tricarbonyl complexes immobilized on TiO_2 particles.[59] Transient absorption spectroscopy revealed that the enhanced photocatalytic activity of the hybrid material was associated with an increased lifetime of the reduced Re catalytic intermediate. Furthermore, surface immobilization reduced the probability of bimolecular deactivation processes, evidencing one of the key advantages of catalyst heterogenization.

The development of hybrid photocatalysts has also been an important research direction within our group. For example, Faustino and co-workers reported a hybrid system based on the immobilization of a Re(I) catalyst onto hexaniobate nanoscrolls.[60] The slow back-electron transfer and the strong reducing power of the semiconductor conduction band significantly enhanced photocatalytic performance of the Re(I) complex. Similarly, Silva and co-workers developed a photocatalyst based on the immobilization of a Re(I) complex onto a CuO/Nb_2O_5 heterostructure.[61] In this system, efficient electron injection and charge separation were achieved through the semiconductor interface, while CuO clusters expanded visible-light absorption and promoted the reduction of catalytic intermediates, resulting in improved CO production and reduced side reactions.

1.6. Covalent Organic Frameworks as supporting platforms for hybrid catalysts

More recently, Covalent Organic Frameworks (COFs) have emerged as particularly attractive platforms for the construction of hybrid photocatalysts (**Figure 8**).[62] Since their first report by Yaghi and co-workers, COFs have attracted considerable attention owing to their high crystallinity, permanent porosity, low density, and exceptional structural tunability.[63] These materials are constructed from organic building blocks linked through strong covalent bonds into two- or three-dimensional periodic frameworks. Through the rational selection of molecular building blocks, the pore architecture, electronic

properties, and chemical functionality of COFs can be precisely controlled, making them highly attractive for photocatalytic applications.

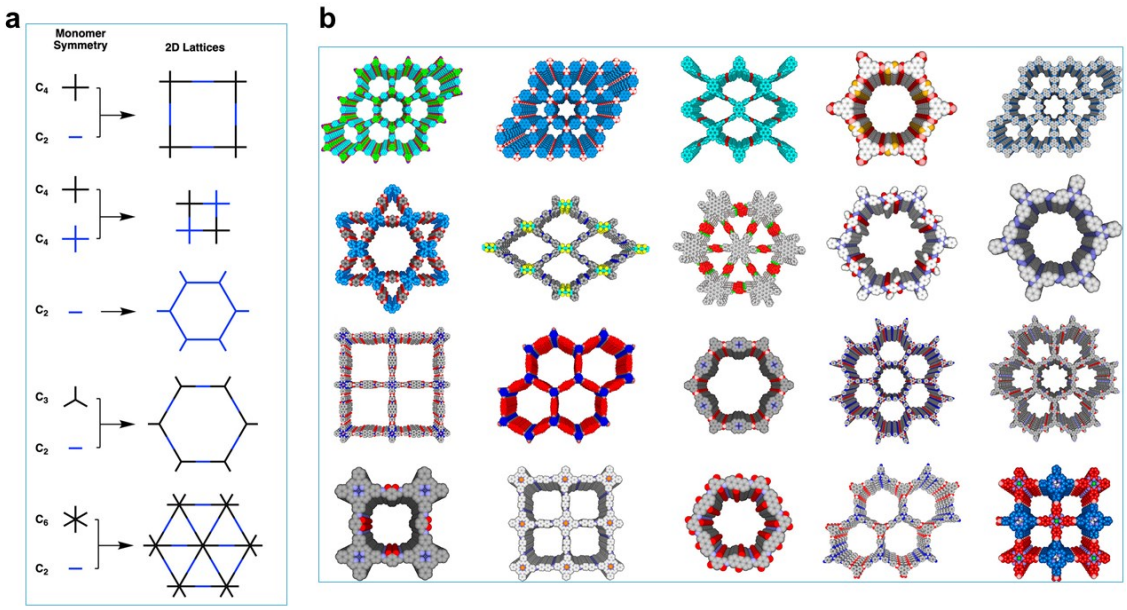


Figure 8. Examples of monomer symmetry combination for producing different 2D Lattices (b) and some published lattices and morphologies of COFs (b).[64]

COFs can actively participate in photocatalysis by harvesting light, transporting charges, and concentrating reactants within their porous structure. In addition, their highly ordered architecture enables the incorporation of catalytic sites in a site-isolated manner, minimizing intermolecular interactions that often lead to catalyst deactivation in homogeneous systems (**Figure 9**), serving as a supporting material for making stable hybrid photocatalysts.

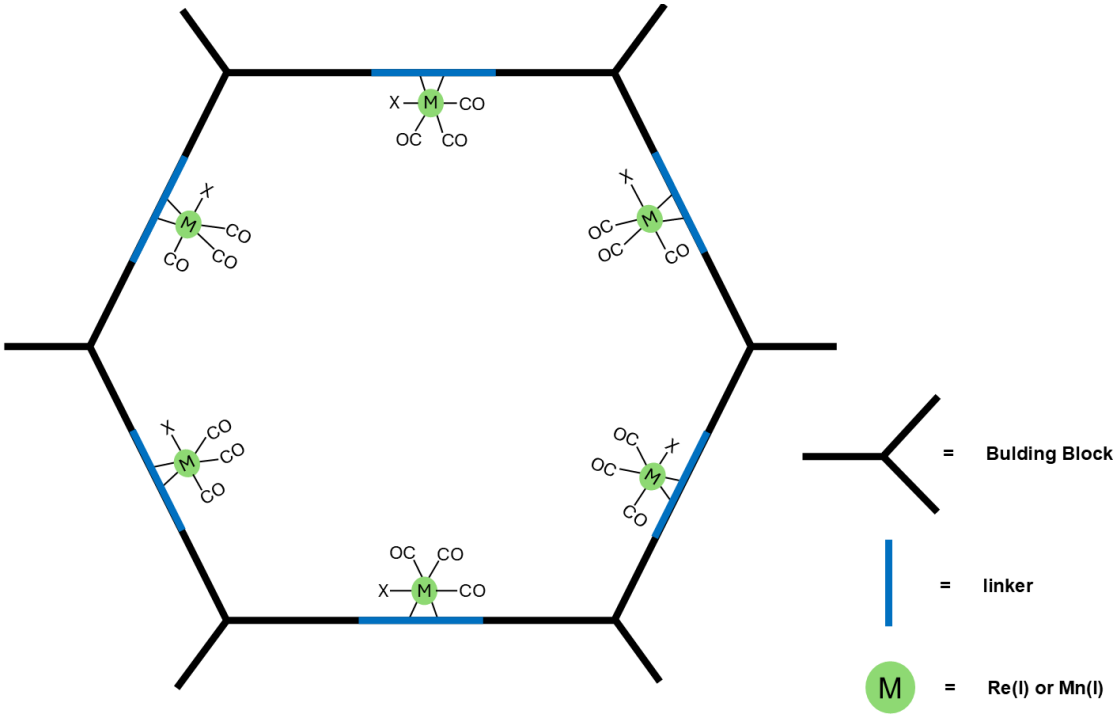


Figure 9. Covalent Organic Frameworks as stable platforms for making hybrid COFs CO_2 photocatalysts.

These characteristics position COFs as an ideal platform for bridging the gap between molecular and heterogeneous photocatalysis.[65, 66 67] A landmark example was reported by Cooper and co-workers, who demonstrated the incorporation of Re(I) tricarbonyl catalytic centers into a bipyridine-containing COF.[68] In this system, the bipyridine units embedded within the framework acted as coordination sites for the Re(I) catalyst, yielding a material that combined the selectivity of molecular catalysts with the stability and recyclability of heterogeneous support. The resulting hybrid photocatalyst exhibited efficient and selective CO_2-to-CO conversion while maintaining enhanced stability under photocatalytic conditions.

Although significant progress has been achieved in recent years, the field of COF-based photocatalysts remains relatively young. Important challenges

remain, including the long-term structural stability of COFs under photocatalytic operating conditions, the optimization of charge transport within the framework, the accessibility of catalytic sites, and the scalability of linker synthesis and material production. Addressing these challenges is essential for the rational design of next-generation hybrid photocatalysts capable of efficient and durable solar fuel production.[62]

1.7. Thesis goals and organization

The central objective of this thesis is to advance the understanding and rational design of catalytic systems for the selective conversion of CO_2 into solar fuels, with particular emphasis on molecular catalysts and their subsequent integration into Covalent Organic Frameworks (COFs) to develop highly selective and stable hybrid catalytic platforms. To achieve this goal, the work combines mechanistic investigations, critical analysis of literature, and the development of hybrid catalytic materials, providing fundamental insights into the factors governing catalytic activity, selectivity, and stability. Furthermore, the thesis explores the implementation of these catalysts in scalable electrocatalytic devices and, in its final part, presents a proof-of-concept strategy for integrating multiple catalytic sites within a single organic framework structure to promote cascade CO_2-to-CO-to-CH_3OH conversion.

Following this introductory chapter, the thesis is organized into three main parts, which follow a progressive scientific strategy in which the limitations identified in one stage motivate the development of the next. The work therefore progresses from understanding the limitations of molecular catalysts, to their

immobilization within COFs, subsequent framework engineering, implementation in scalable electrochemical devices, and finally the integration of complementary catalytic functions within a single porous architecture.

Part I, Photocatalytic Molecular and Hybrid Catalysts, focuses on the fundamental aspects governing photocatalytic CO_2 reduction using Re(I)-based molecular and COF-supported catalysts. Chapter 2 presents the article entitled "Mechanistic Insights into CO_2-to-CO Photoreduction by Proton-Responsive Imidazole-Pyridine Re(I) Complexes". This work investigates the photophysics, electrochemistry, and photochemical properties of two imidazole-pyridine based complexes, *fac*- [$Re(CO)_3$(pbiH)Cl], (Re-pbiH), and fac-[$Re(CO)_3$(bbzp)Cl] (Re-bbzp), where pbiH= 2-(2-pyridy)benzimidazole, bbzp = 2,6-bis(2-benzimidazolyl)pyridine. Their application as photocatalysts for CO_2-to-CO reduction upon light irradiation (λ > 370 nm) in CO_2-saturated CH_3CN was then investigated and rationalized. The superior activity of Re-bbzp was justified using IR spectroelectrochemistry (IR-SEC) together with *in-situ* FTIR and UV-vis spectroscopy under photocatalytic conditions, along with kinetic isotopic effect studies and complementary DFT and TD-DFT computational studies. Overall, these results provide new insights into the role of ligand-based proton-responsive sites in Re(I) tricarbonyl complexes and their impact on CO_2 reduction photocatalysis. Importantly, despite the increased steric bulk and enhanced proton-relay character introduced by the bbzp ligand, these molecular systems remain subject to deactivation pathways associated with the formation of Re-Re species during catalysis. Thus, the molecular study identified a key limitation that motivated the subsequent immobilization of Re(I) catalytic sites within a porous framework. In this section the synthesis and structural characterization of the

Re(I) complexes were developed, as well as photophysical studies, electrochemical measurements, photocatalytic experiments, spectroelectrochemical and in-situ spectroscopic investigations and computational studies.

Chapter 3 comprises the review article "From Conventional Inorganic Semiconductors to Covalent Organic Frameworks: Advances and Opportunities in Heterogeneous Photocatalytic CO_2 Reduction". This chapter critically discusses the evolution of heterogeneous photocatalytic systems for CO_2 reduction, highlighting the advantages and limitations of conventional semiconductor materials while introducing Covalent Organic Frameworks as highly modular platforms capable of incorporating atomically precise catalytic sites for solar fuel production. The review therefore provides the broader conceptual framework for the transition from molecular catalysts to structurally defined heterogeneous systems, highlighting COFs as platforms capable of addressing some of the limitations associated with homogeneous molecular photocatalysts while retaining molecular-level control over catalytic sites. In this section we conducted a literature survey, organization and critical analysis of the literature, prepared the figures and tables, and drafted revised the final manuscript.

Chapter 4 presents then the work entitled “Unlocking CO_2 Photoreduction with Re(I) Single-Site COF-based Catalysts: Structure-Activity Relationships”. In this chapter, we developed an imine-linked bipyridine-pyrene COF (bpyPyr COF) post-synthetically functionalized with $[Re(CO)_3Cl]$ units to afford a hybrid material containing well-defined molecular CO_2 reduction sites. The **Re bpyPyr COF** promotes the photo-reduction of CO_2 to CO and a systematic variation of the

[$Re(CO)_3Cl$] loading revealed the structural changes in the 2D COF scaffold. Compared with the molecular analogue *fac*-[$Re(CO)_3(bpy)Cl$], the COF-based catalyst displays improved operational stability under both UV and visible irradiation and FTIR spectroelectrochemical experiments confirmed that the molecular reduction pathway is largely retained upon immobilization. These results highlight the potential of COF scaffolds to spatially organize molecular catalytic centers, enabling high catalyst loading, and enhanced stability for photocatalytic CO_2 reduction. Thus, the first hybrid system demonstrated that immobilization of molecular Re(I) sites within a COF can mitigate the limitations associated with molecular catalyst deactivation while preserving the fundamental molecular catalytic pathway. However, this system also revealed a new question: how does the structural organization of the framework control the accessibility, distribution, and stability of the immobilized catalytic sites. In this section the synthesis and characterization of the bpyPyr COF and Re-functionalized materials were developed as well as photocatalytic experiments, spectroscopic and spectroelectrochemical investigations, structural and catalytic data analysis, and the preparation of the manuscript.

Building upon these concepts, Chapter 5 presents the article "Designing Atomically Precise and Robust COF Hybrids for Efficient Photocatalytic CO_2 Reduction". This chapter addresses the structural limitations identified in the bpyPyr system through the development of a more rigid and highly porous dibenzochrysene-based COF. In this chapter a new dibenzochrysene-based Covalent Organic Framework was developed to accept Re(I) centers, while maintaining high crystallinity through the use of more rigid building blocks and providing a different pore environment now for keeping its high crystallinity by

using more rigid building blocks. This COF leads to long-term stability under illumination, whereas the efficient light-harvesting capability and the strong electronic interactions between the COF and the Re(I) centers lead to CO evolution rates of up to 1.16 mmol g^{-1} h^{-1}, which ranks amongst the highest CO rates reported in the literature for similar systems without the use of an additional photosensitizer. The modified framework therefore demonstrates how rational control over pore structure, rigidity, and electronic interactions can substantially enhance photocatalytic performance. Moreover, the highly planar and ordered framework enabled, to the best of our knowledge, the first direct STEM-HAADF visualization of the ordered distribution of Re(I) catalytic sites within a COF structure, providing structural evidence connecting the molecular catalytic centers with their organization within the porous framework. In this section we conducted the photocatalytic experiments, spectroscopy data interpretation, analysis of structural and catalytic results. We also contributed to the interpretation of the relationship between COF structure, Re(I) site distribution, and photocatalytic performance, as well as to the preparation and revision of the manuscript.

Part II, electrochemical CO_2 conversion: towards scalability, extends these concepts toward scalable CO_2 conversion technologies driven by renewable electricity. While the photocatalytic studies in Part I demonstrated that framework engineering can improve the stability, accessibility, and activity of molecularly defined catalytic sites, the next challenge was to translate these principles into electrochemical systems with higher reaction rates and device-level scalability. After a brief introduction discussing the evolution of electrochemical reactor architectures and the scalability of CO_2 electroreduction, Chapter 6 presents the

work entitled "Mn(I)-Functionalized Covalent Organic Framework as an Efficient Electrocatalyst for CO_2 Reduction in a Catholyte-Free Zero-Gap Electrolyzer". The reported Mn phenPy COF catalyst achieves an outstanding turnover frequency of 617 h^{-1} (quantified per total concentration of catalytic sites) and a CO evolution of 222 μmol cm^{-2} (at a full-cell potential of 2.8 V) with a partial CO current density of 23 mA cm^{-2} at 2.8 V within 30 min. Moreover, the COF structure provides a defined environment for the Mn(I) catalytic sites and actively suppresses Mn^0–Mn^0 dimer formation and supports stable operation at high potentials with a partial current density of 23 mA cm^{-2}. The synergy between the crystalline nature of the COF and the MEA cell architecture, facilitating direct interactions between the modified electrode and the CO_2 gas, enhances both the catalytic activity and stability. Importantly, this work represents the first demonstration, to the best of our knowledge, of a Mn(I)-functionalized COF operating in a catholyte-free zero-gap electrolyzer, establishing the compatibility of molecularly defined COF catalysts with device architectures designed for scalable CO_2 electroreduction. The resulting TOF of 617 h^{-1} also compares favorably with previously reported COF-based electrocatalysts. In this section we conducted the preparation of the electrocatalytic materials and electrodes, electrochemical characterization, catalytic testing, product analysis, and interpretation of the electrochemical results. We were also involved in the analysis of the structure-performance relationship and in the preparation and revision of the manuscript.

Part III, towards multi-site cascade catalysts for sequential CO_2 reduction, explores a new catalyst design strategy based on the integration of complementary molecular catalytic centers within a single porous organic

framework. The previous parts established that molecular catalyst design and framework engineering can control individual catalytic functions, while scalable reactor architectures can translate these materials into practical electrochemical configurations. The remaining challenge addressed in Part III is therefore functional integration: rather than using the framework solely to isolate and stabilize a single catalytic site, can multiple complementary catalytic functions be organized within the same porous architecture to enable sequential transformations?

Chapter 7 first presents the **Re-Ru bpyPyr** system as a multi-site cascade catalyst for photocatalytic CO_2-to-CH_3OH conversion. Building upon the Re(I)-COF systems developed in Part I, this chapter integrates Lehn-type Re(I) tricarbonyl catalytic sites (*fac*-$Re(CO)_3(bpy)Cl$), responsible for selective CO_2-to-CO conversion, with Tanaka-type Ru carbonyl catalytic centers (*cis*-$[Ru(bpy)_2(CO)_2]^{2+}$) known to promote CO hydrogenation toward methanol(CH_3OH). The resulting dual-site COF provides a proof-of-concept molecularly defined cascade catalyst in which CO generated at Re(I) sites is subsequently transformed by neighboring Ru centers under photocatalytic conditions. Photocatalytic studies under visible light irradiation and spectroscopic characterization provide preliminary evidence for CH_3OH formation and establish a new framework for designing porous catalysts that integrate sequential CO_2 reduction reactions within a single organic structure. This represents, to the best of our knowledge, the first proposal within this thesis of a COF-based multi-site cascade catalyst designed to integrate sequential CO_2-to-CO and CO-to-CH_3OH catalytic functions within a single porous architecture. In this section we conducted the synthesis and characterization of the Re–Ru bpyPyr materials,

photocatalytic experiments, spectroscopic characterization, product analysis, and interpretation of the catalytic results as well as the development of the multi-site cascade catalyst concept.

Finally, the second proposed system, **Mn bpyCoPc**, is a multi-site cascade catalyst for electrocatalytic CO_2-to-CH_3OH conversion. This section investigates a porous catalyst containing Mn(I) carbonyl and cobalt phthalocyanine (CoPc) catalytic centers designed to promote sequential CO_2-to-CO-to-CH_3OH conversion. The catalyst was first evaluated in a conventional H-type electrochemical cell, where CH_3OH formation was detected in the liquid phase, providing preliminary evidence for cooperative catalytic behavior and subsequently employed in a flow-cell reactor, which evidenced the compatibility of the multi-site cascade catalyst architecture with scalable electrochemical reactor configurations, reaching a FE for CH_3OH of 14.7%. Furthermore, mechanistic investigations using ATR-IR spectroelectrochemistry revealed the sequential formation of reduced Mn intermediates involved in CO_2 activation. Together with the Re-Ru bpyPyr system, this work extends the multi-site concept from photocatalytic to electrocatalytic CO_2 conversion and provides a proof-of-concept for integrating complementary molecular catalytic functions within a porous framework under electrochemical conditions. In this section we conducted the preparation and characterization of the Mn-bpyCoPc catalyst, electrochemical experiments in H-type and flow-cell configurations, product analysis, spectroelectrochemical investigations, data analysis, and interpretation of the catalytic and mechanistic results.

Together, the studies presented in Part III extend the concept of COF-based hybrid catalysts beyond catalyst immobilization toward the construction of

cooperative catalytic architectures. By exhibiting the feasibility of integrating multiple complementary catalytic functions within a single porous framework, this part establishes a foundation for the development of multi-site cascade catalysts for the selective production of liquid fuels from CO_2.

Part I

Chapter 2

Mechanistic Insights into CO_2-to-CO Photoreduction by Proton-Responsive Imidazole-Pyridine Re(I) Complexes

2.1. Introduction

Since the first report by Lehn *et. al*. employing the parental complex *fac*-[$Re(CO)_3$(bpy)Cl], bpy = 2,2'-bipyridine, subsequent studies have investigated the reaction mechanisms and the role of the polypyridyl ligand on the catalytic processes.[20, 22, 40, 44, 49, 61, 69-71] The irradiation of such complexes typically gives rise to metal-to-ligand charge transfer (MLCT) excited states characterized by relatively long lifetimes and suitable energetics for CO_2 to CO conversion.[72, 73]

As showed in **Figure 4**, in a photo-induced CO_2 reduction a sacrificial donor is usually necessary. Triethanolamine (TEOA) has typically been employed, but Ishitani et. al., have shown that the use of benzomidazole derivatives, such as 1,3-dimethyl-2-phenyl-2,3-dihydro-*1H*-benzo[d]imidazole (BIH), can lead to better photocatalytic performance.[74] As shown in **Figure 10**, BIH is capable of donating two electrons and one proton, which also has a stronger reducing power compared to triethanolamine (TEOA) and triethylamine (TEA) as discussed in previous works.[20, 74-77]

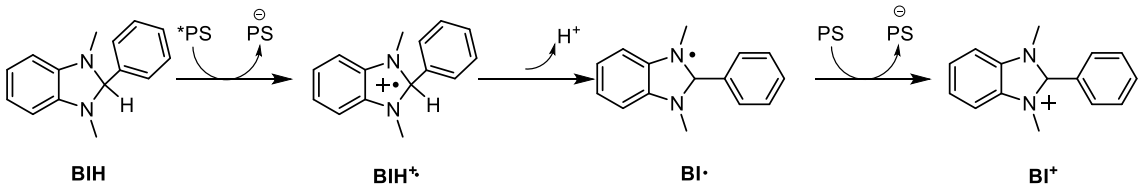


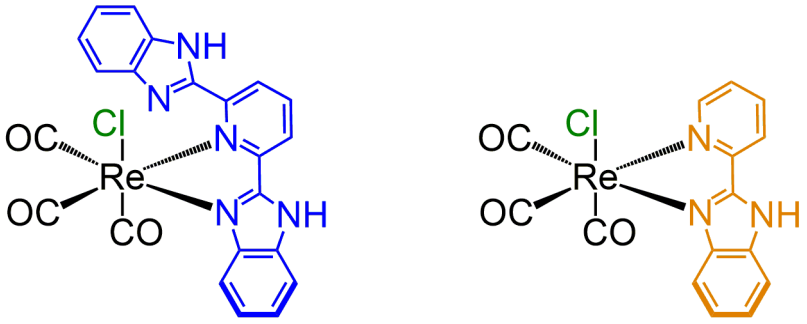
Figure 10. Oxidation process of the sacrificial donor BIH in the photochemical CO_2 reduction. PS stands for photosensitiser.

Additionally, the presence of a Brønsted acid in the reaction medium or in the catalysts's secondary coordination sphere is also beneficial for photocatalysis.[78] In the accepted catalytic cycle, CO_2 coordination to the reduced catalyst is followed by proton transfer to yields a Re-CO_2H intermediate that is further reduced and protonated to yield CO and H_2O.[79, 80] The presence of a proton relay close to the metal center may stabilize an intermediate and improve reaction rates as observed for other homogeneous catalysts.[81-85]

Re(I)-based imidazole-pyridyl complexes combine excited state redox chemistry with a proton relay close to the metal center. Such intriguing properties have been previously exploited. For example, Qiu *et. al*. reported a series of Re(I) complexes with an imidazole-pyridine framework in which a π-extended pyrene was covalently bonded to the N-atom of the imidazole ring. The complexes exhibited extended triplet excited state lifetimes and high photoactivity for CO_2 reduction.[72] Siewert and coworkers reported a series of bi-nuclear Re(I) complexes with imidazole-pyridyl ligands[86, 87] as well as pyrazole-pyridyl ligands[88] in which the role of the proton responsive groups were explored for electrochemical CO_2 reduction. Furthermore, Warren and coworkers reported imidazole-based Re(I) complexes in which alkalization of the imidazole proton resulted in loss of catalytic activity towards CO_2 reduction, evidencing the role of ligand-centered proton acceptor sites on CO_2 activation.[89] Moreover, Sinha *et. al.*

reported CO_2 reduction by *fac*-[$Re(CO)_3$(bbzp)Cl], bbzp = 2,6-bis(2-benzimidazolyl)pyridine in aqueous media.[90, 91] The role of the pendant non-chelating benzimidazolyl group was compared with a Re(I) complex bearing a substituted terpyridine ligand. All of these reports emphasize the importance of the imidazole group(s) in enhancing stability and reactivity, however to our knowledge, prior work has not explored the photophysical and photochemical properties of the catalysts or their catalytic mechanism during CO_2 reduction cycle.

In this work, the photophysical properties of two Re(I) tricarbonyl complexes, *fac*-[$Re(CO)_3$(pbiH)Cl] (Re-pbiH) and *fac*-[$Re(CO)_3$(bbzp)Cl] (Re-bbzp), pbiH = 2,6-bis(2-benzimidazolyl)pyridine, **Figure 11**, are reported. The role of the additional benzimidazolyl group of the bbzp ligand is described along with their performance as photocatalyst in the CO_2 reduction reaction (CO_2RR). The results bring new insights into the role of the pendant N-imidazolyl atom as proton relay for CO_2 reduction to CO.



Re-bbzp **Re-pbiH**

Figure 11. Chemical structures and abbreviations of the Re(I) catalysts.

2.2. Experimental Methods

Materials. All solvents were HPLC grade. For electrochemical measurements, CH_3CN was dried prior to use (water content <0.001%). The $Re(CO)_5Cl$, 2-(2-pyridy)benzimidazole (pbiH), 2,6-bis(2-benzimidazolyl)pyridine (bbzp) and tetrabutylammonium hexafluorophosphate ($TBAPF_6$) were purchased from Sigma-Aldrich and used as received.

Synthesis of Re-pbiH and Re-bbzp complexes. The Re(I) complexes with general formula *fac*-$Re(CO)_3(NN)Cl$, was carried following the procedure reported for other Re(I) complexes.[92-95] $[Re(CO)_5Cl]$ (0.27 mmol)[95] and the pbiH or bbzp ligand (0.33 mmol) were refluxed in toluene for 3 hours. The mixture was hot-filtered, washed with ethyl ether and the solid was dried under vacuum. For **Re-pbiH**: Yield: 94%. ^1H NMR ($(CD_3)_2SO$) 400 MHz, δ/ppm): 9.08 (d, J = 5.4 Hz, 1H), 8.54 (d, J = 7.9 Hz, 1H), 8.42 (t, J = 7.8 Hz, 1H), 7.88-7.75 (m, 3H), 7.62-7.53 (m, 2H). (–)–HRESIMS *m/z* 499.9803 $[M–H]^–$ (calculated for $C_{15}H_8ClN_3O_3Re^-$, 499.9817 (Δ 2.80 ppm)). Anal. Calcd. for $C_{15}H_9ClN_3O_3Re$ C, 35.97%; H, 1.81%; N, 7.08%. Found: C, 36.10%; H, 1.73%; N, 7.13%. For **Re-bbzp**: Yield: 80.8%. ^1H NMR ($(CD_3)_2SO$) 400 MHz, δ/ppm): 8.69 (d, J = 7.9 Hz, 1H), 8.57 (t, J = 7.9 Hz, 1H), 8.10 (d, J = 7.7 Hz, 1H), 7.93-7.85 (m, 2H), 7.82 – 7.53 (m, 4H), 7.32 (d, J = 5.8 Hz, 2H. (–)–HRESIMS *m/z* 616.0172 $[M–H]^–$ (calculated for $C_{22}H_{12}ClN_5O_3Re^-$, 616.0191 (Δ –3.08 ppm)). Anal. Calcd. for $C_{22}H_{13}ClN_5O_3Re$ C, 42.82%; H, 2.12%; N, 11.35%. Found: C, 42.63%; H, 2.38%; N, 11.72%.

Synthesis of BIH and BID. The (1,3-dimethyl-2-phenyl-2,3dihydro-1H-benzo[d]imidazole) and its deuterated structure were prepared as previously

reported. [18, 49] First, 2-phenyl-1,3-dimethylbenzimidazolium iodide was obtained from a two-step methylation reaction of 2-phenylbenzimidazole. The solid was reduced in the presence of $NaBH_4$ or $NaBD_4$ to yield BIH or BID, respectively. **BIH**: ^{1}H NMR (400 MHz, DMSO-d^6, δ): 7.55 (dd, J = 6.4, 1.9 Hz, 2H), 7.45 (dd, J = 5, 19 Hz, 3H), 6.62 (dd, J = 5.4, 3.3 Hz, 2H), 6.45 (dd, J = 5.4, 3.2 Hz, 2H), 4.87 (s, 1H), 2.48 (s, 6H). **BID**: ^{1}H NMR ^{1}H NMR (400 MHz, DMSO-d^6, δ): 7.55 (dd, J = 6.4, 1.9 Hz, 2H), 7.45 (dd, J = 5, 19 Hz, 3H), 6.62 (dd, J = 5.4, 3.3 Hz, 2H), 6.45 (dd, J = 5.4, 3.2 Hz, 2H), 2.48 (s, 6H).

Structural Characterization. Attenuated total reflectance Fourier-transformed infrared (ATR-FTIR) spectra were recorded in a Perkin Elmer Frontier spectrometer equipped with a diamond crystal plate, using 16 scans at a resolution of 2 cm^{-1}. ^{1}H NMR spectra were recorded in a Bruker Ascend 400 MHz spectrometer using the residual solvent signal as internal standard. High-resolution mass spectra (HRESIMS) with electrospray ionization were measured on an Agilent QTOF (6520B model) spectrometer, operating in the negative mode. Elemental analysis was carried out in a Perkin Elmer 2400 CHNS analyzer.

Photophysical Characterization. Electronic absorption spectra were recorded in a Thermo Evolution 201 spectrophotometer. Room temperature emission measurements were performed in argon degassed CH_3CN solutions in a 1.000 cm quartz cuvette using a Horiba Fluorolog 3 fluorimeter equipped with a standard tungsten-halogen lamp. Emission quantum yields were determined taking *fac*-[Re(CO)$_3$(bpy)Cl], as standard (ϕ_{em} = 0.006 in CH_3CN at 298 K).[96] For emission measurements at 77 K the samples were dissolved in degassed 5:4 (v/v) butyronitrile. Nanosecond time-resolved photoluminescence decays were

collected using a Photon Technology International (PTI) GL-301 nitrogen dye laser with a 380 nm excitation. The PL signal was collected using a ScienceTech Model 9010 monochromator and signal enhanced by a Hamamatsu R928 photomultiplier tube and digitalized using a LeCroy Waverunner 4024HD oscilloscope. The singlet oxygen quantum yield (Φ_Δ) was determined by monitoring the singlet oxygen phosphorescence emission spectrum in a custom-designed system equipped with a cooled InGaAs detector (DSS-IGA 020L - Horiba) coupled to a spectrometer (iHR320 - Horiba). The third harmonic (λ_{exc} = 355 nm) from a Nd:YAG Brilliant Quantel System (Q-switched, 10 Hz repetition rate, ~7 ns FWHM) was used as excitation source. The Φ_Δ values were calculated relative to the *fac*-[$Re(CO)_3(bpy)Cl$, (Φ_Δ = 0.28) standard,[93] using the **Equation 7**. I and I_0 represent the integrals of the intensities of the singlet oxygen emission spectra for the studied samples and the standard, respectively. A and A_0 denote the respective absorbances of the sample and the standard solutions at the excitation wavelength (355 nm). The absorbance values of the samples at the excitation wavelength were adjusted to approximately 0.2. All experiments were conducted at room temperature (25 ± 1°C) and under O_2-saturated conditions.

$$\Phi_\Delta = \left(\frac{I}{I_0}\right)\left(\frac{1-10^{-A_0}}{1-10^{-A}}\right)\Phi_{\Delta_0} \qquad \textbf{(7)}$$

Electrochemical Measurements. Electrochemical measurements were obtained in a μAutolab PGSTAT204 potentiostat/galvanostat (Autolab) using a glassy carbon as working electrode, a platinum wire as counter electrode, and a silver wire as pseud-reference electrode. All measurements were carried out in Ar or CO_2 saturated anhydrous CH_3CN with tetrabutylammonium hexafluorophosphate (0.1 mol L^{-1}) as a supporting electrolyte. Potentials are reported *vs.* Fc^+/Fc (E^0 = 0.400 V *vs*. SHE). Cyclic voltammetry measurements

were carried out with a scan rate of 100 mV s^{-1}. Square Wave Voltammetry (SWV) measurements were performed on Re-bbzp and *fac*-$Re(CO)_3(bpy)Cl$ complexes over a frequency range of 50-400 Hz to determine the number of electrons involved in each reduction process. The Lovric method (**Equation 8**) was employed for these calculations, where the αn value was obtained from the linear plot of peak potential (Ep) *versus* log(*f*). The α value was fixed at 1.0, based on the well-characterized *fac*-[$Re(CO)_3(bpy)Cl$], bpy = 2,2'-bipyridine, complex, for which the number of electrons involved in each process is well established in the literature.

$$\frac{\Delta E}{\Delta log\, f} = \frac{-2.3RT}{\alpha nF} \quad \textbf{(8)}$$

Computational Methods. Density Functional Theory (DFT) calculations were performed with the Gaussian 09W software using the m06 functional and jorge-TZP-DKH basis to geometry optimization. The oscillator strength for the main electronic transitions were obtained by the time-dependent Density Functional Theory (TD-DFT) using m06 functional and jorge-TZP-DKH basis for Re-bbzp and def2-TZVP for Re-pbiH. All calculations were performed using an IEFPCM continuum solvation model and considering a solvent with inherent properties of CH_3CN.[97]

For the isodesmic reaction, $BIH^{\bullet+}$ + *fac*-[$Re^0(CO)_3(bbzp)$] ⇌ $BI^{\bullet}$ + *fac*-[$Re^0(CO)_3(bbzpH^+)$], the DFT-computed free energies for each species were calculated considering acetonitrile as solvent (see computed stationary points in supporting information). Based on **Equations 9-11** and the previously reported pK_a for $BIH^{\bullet+}$ of 14.4, the values for $DG_{(reaction)}$, $DG_{(fac\text{-}[Re0(CO)3(bbzpH+)])}$ and pK_a for *fac*-[$Re^0(CO)_3(bbzpH^+)$] were calculated to be 6.93 kcal mol^{-1}, 25.13 kcal mol^{-1} and 19.9, respectivelly.

$$\Delta G_{(reaction)} = (G_{(fac-[\mathrm{Re0(CO)3(bbzpH+)}])} + G_{(\mathrm{BI}\bullet)}) - (G_{(fac-[\mathrm{Re0(CO)3(bbzp)}])} + G_{(\mathrm{BIH}\bullet^{+})})$$ (**9**)

$$\Delta G_{(reaction)} = \Delta G_{(fac-[\mathrm{Re0(CO)3(bbzpH+)}])} - \Delta G_{(\mathrm{BIH}\bullet^{+})}$$ (**10**)

$$\Delta G = 1.264\, pK_a$$ (**11**)

Photocatalytic Studies. CO_2 photoreduction experiments were carried out in a closed double-jacket glass reactor with a total volume of 16 mL. The reactor was loaded with 10 mL of a 0.03 mmol L^{-1} acetonitrile solution of the catalyst and an excess of 6.7 mmol L^{-1} mg of BIH. The mixture was then purged with CO_2 until saturation and exposed to a 300 W Xe lamp equipped with a water filter and a 370 nm long pass filter with an irradiance of 100 mW cm^{-2}. The reactor was kept at 25°C with a thermally controlled water circulator. At given time intervals, 100 µL of the headspace atmosphere was sampled using a gastight syringe and analyzed by gas chromatography (Shimadzu GC2014 equipped with a flame ionization detector (FID) and a methanizer) to quantify CO formation. A 500 mL aliquot was analyzed for H_2 with a PerkinElmer Clarus 580 – GC equipped with a thermal conductivity detector. Photocatalytic experiments were also performed in a custom reactor illuminated with a Newport Oriel 1 kW Solar Simulator (model 91191-1000; 900 W Xe lamp and LP370 long pass filter) connected in-line to the sample loop of a gas chromatograph (Agilent GC 8890). Gaseous products were separated with a carbonPLOT column and a molecular sieve column in series. The carbonPLOT column decelerated the elution of CO_2 relative to the other lighter gases (O_2, N_2, H_2, and CO), while the molecular sieves separated each gas with specific retention times. A thermal conductivity detector (TCD) was used to detect O_2, N_2, and H_2. A methanizer, equipped with a nickel

hydrogenation catalyst, was paired with a flame ionization detector (FID) to detect CO_2 and CO. Argon (Ar) was used as the carrier gas.

FTIR Spectroelectrochemical (IR-SEC) experiments. IR spectroelectrochemical studies were performed using an optically transparent thin-layer electrochemical (OTTLE) cell with a calcium fluoride (CaF_2) window. All spectroelectrochemical experiments were conducted in 0.1 M TBAH/acetonitrile solutions under an Ar/CO_2 atmosphere. Blank acetonitrile solutions with 0.1 M TBAH were used as background. A PerkinElmer Frontier spectrometer was used to monitor thin-layer bulk electrolysis coupled with a μAutolab PGSTAT204 potentiostat/galvanostat (Autolab). A platinum grid working electrode, platinum wire counter electrode, and silver wire pseudo-reference electrode was employed for the chronoamperometric studies.

In-situ FTIR experiments. The in-situ FTIR experiment was performed using an optically transparent thin-layer electrochemical (OTTLE) cell with a sodium chloride (NaCl) window. All in-situ experiments were performed in solutions containing 0.03 mmol L^{-1} of photocatalyst and an excess of 6.7 mmol L^{-1} of BIH in acetonitrile under Ar/CO_2 atmosphere. The Perkin Elmer Frontier spectrometer was employed to monitor the formed intermediates as a function of time (I_{irr}> 370 nm; P_{irr} = 100 mW cm^{-2}).

2.3. Results and Discussion

Structural characterization

The synthesis of both complexes was successfully achieved as confirmed by ^{1}H NMR (**Figure 12**), elementary analysis and mass spectrometry (**Figure A1**

and **A2)**.[90, 91] The ^{1}H NMR spectra of both complexes are characterized by peaks in the aromatic region, which are downfield from those observed for the free ligands due to coordination to the Re(I) center. The peak positions and their corresponding coupling constants agree well with those previously reported for these complexes.[90, 91] Additionally, between 13 and 15 ppm, broad singlet peaks observed for both species are attributed to the hydrogen atom bonded to the N-atom in the imidazole ring coordinated to the Re(I) center. For the Re-bbzp complex, one additional singlet is observed at 13.3 ppm, corresponding to the pendant imidazole ring. The broad shape of these peaks provides evidence of their acidic character [98]. As expected, the interaction of the imidazole ring with the Re(I) center leads to an increase in the Brønsted acid character of the neighbor NH group, which becomes more downshielded.

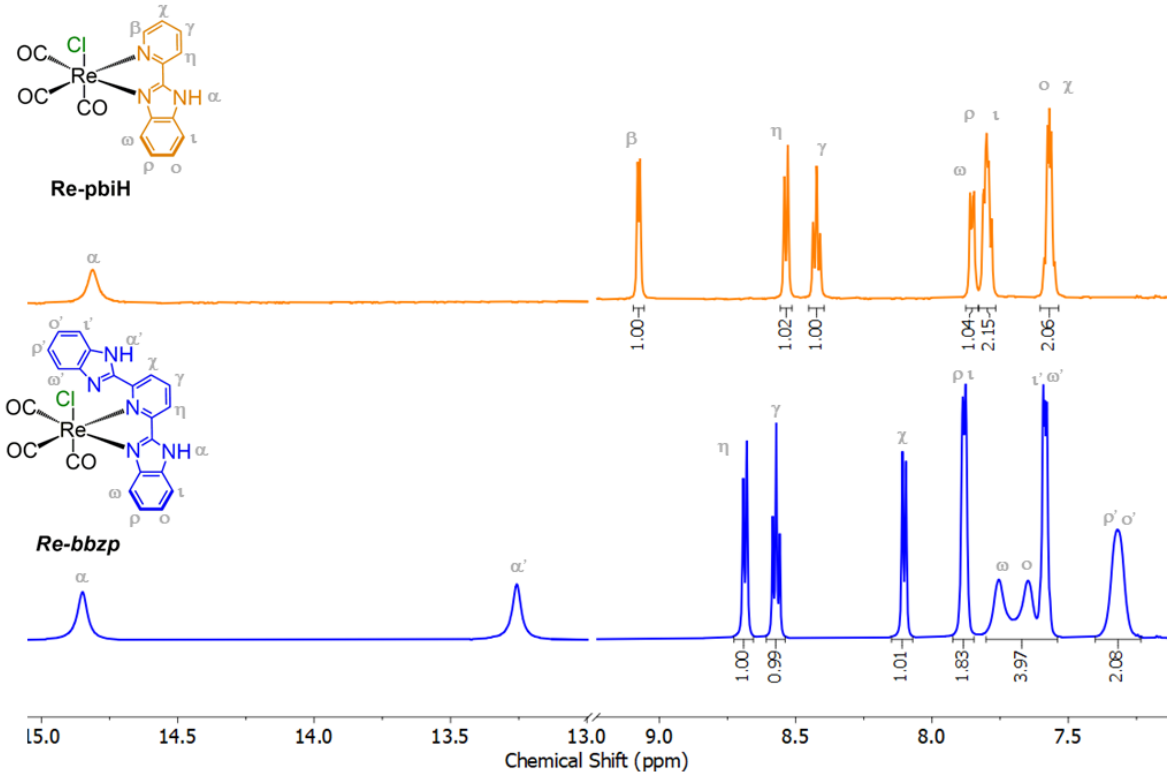


Figure 12. The ^{1}H-NMR spectra of Re-pbiH (orange) and Re-bbzp (blue) in DMSO-d^{6}.

Photophysical properties

The electronic absorption spectra of both complexes were measured in CH_3CN at 298 K, **Figure 13a.** For both complexes, highly intense absorption bands ($\varepsilon > 10^4$ L mol^{-1} cm^{-1}) between 240 and 360 nm are observed and attributed to allowed intraligand ($IL_{\pi\rightarrow\pi^*}$) transitions. At lower energies (λ >360 nm), an absorption tail is observed, corresponding to a metal-to-ligand charge transfer (MLCT) transition.[45, 93, 94, 99] For the Re–pbiH complex, the MLCT band is clearly observed, with a maximum at 375 nm (ε = 4.2 x 10^3 L mol^{-1} cm^{-1}). In contrast, for Re–bbzp, the MLCT and IL bands overlap in energy due to the extended π-conjugation of the bbzp ligand.

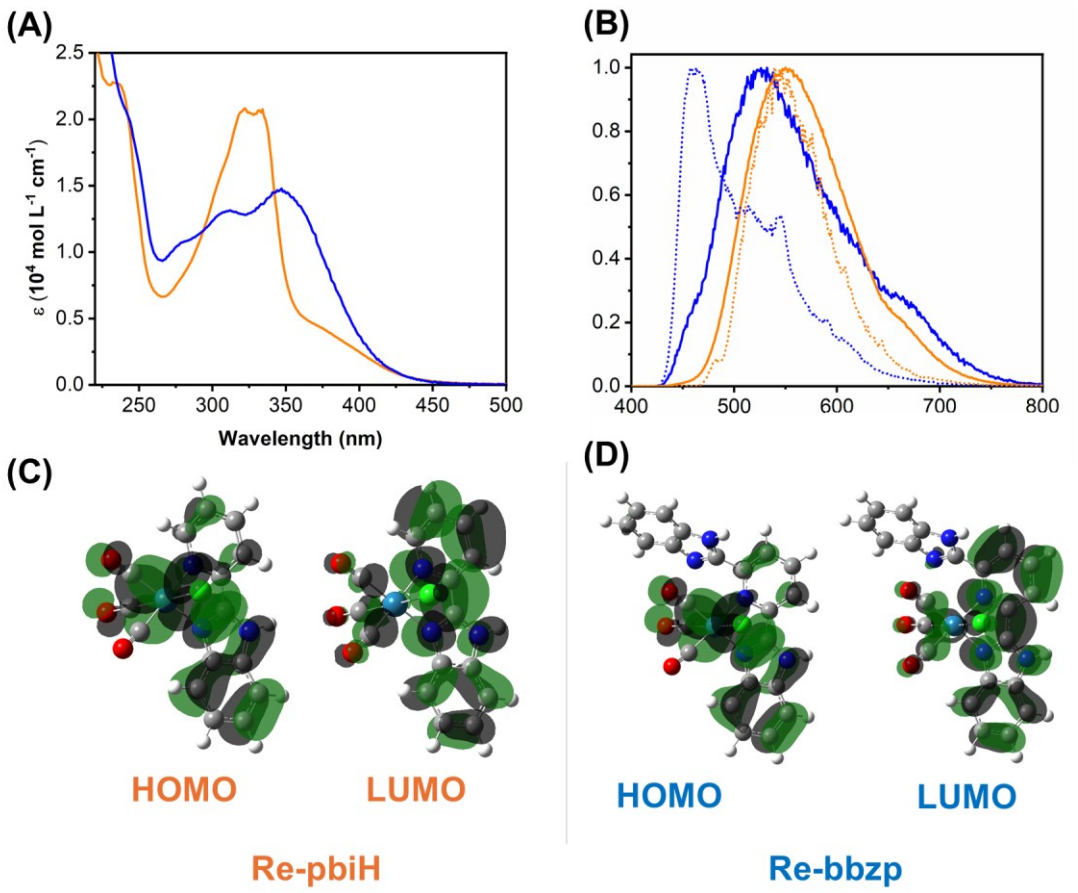


Figure 13. Absorption spectra (a) of the Re-pbiH (orange) and Re- bbzp (blue) in CH_3CN at 298 K as well as these emission spectrum (b) in CH_3CN at 298 K (solid lines) and butyronitrile at 77 K (dashed lines); λ_{exc} = 375 nm. Surface contours of the HOMO and LUMO orbitals for the Re-pbiH (c) and Re-bbzp (d) complexes.

To gain a more detailed understanding of the lowest-lying excited states of these complexes, TD-DFT calculations were performed using CH_3CN as solvent (dielectric constant = 37.5). The first 30 calculated transitions were compared with the corresponding experimental data (**Figures A3** and **A4**). The calculated spectra show good agreement with the experimental results. The main electronic transitions with their respective oscillator strengths are summarized in **Tables A1** and **A2**. The calculations indicate that the lowest absorption bands for both complexes originate mainly from the HOMO-LUMO transitions, which the contours are displayed in **Figure 13c** and **Figure 13d**. For both complexes, the

HOMO is primarily centered on the d orbitals of the Re(I) center, with some contribution from the π orbitals of the imidazole ligands. The LUMO is mainly localized on the π^* orbitals of the pbiH and bbzp ligands, confirming their mixed MLCT/IL character.

Steady-state emission measurements were performed to investigate the excited-state properties of the complexes in CH_3CN at 298 K and in glassy butyronitrile at 77 K (**Figure 13b**). The emission spectra at room temperature displayed large Stokes shifts, typical of triplet-emitting states. The emission bands for both complexes are broad and unstructured, as expected for ^{3}MLCT emitters, and resemble those of other Re(I) tricarbonyl polypyridyl complexes.[93, 94, 99, 100] In glassy medium at 77 K, both emission bands undergo a blue shift, which is more pronounced for Re–bbzp than for Re–pbiH, consistent with restricted outer-sphere reorganization that strongly influences ^{3}MLCT emitters.[96, 101]

Time-resolved emission measurements at 298 K and in CH_3CN (**Figure 14**) reveal a relatively short (τ < 7 ns) mono-exponential decay for Re–bbzp, while for Re–pbiH a double-exponential decay is observed with longer lifetimes (τ_1 = 42 ns, 54% and τ_2 = 466 ns, 46%).

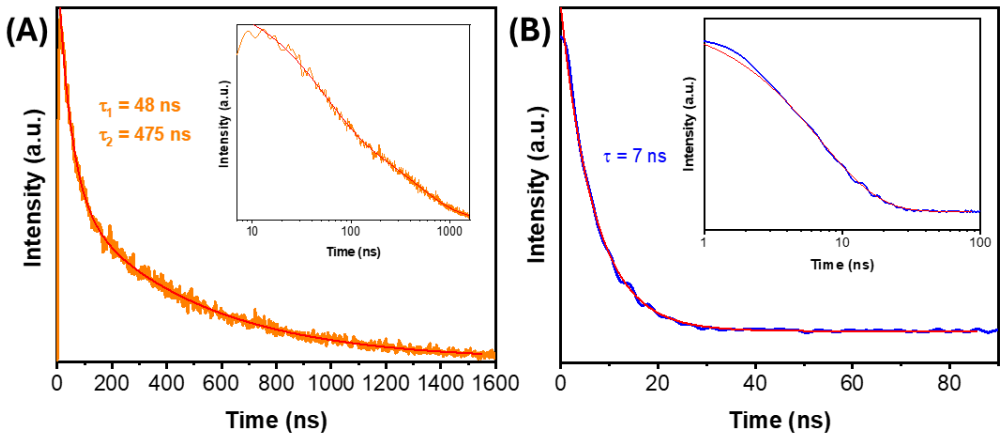


Figure 14. Emission lifetimes measurements for Re-pbiH (a) and Re-bbzp (b) in in CH_3CN at 298 K. *Inset:* log(t) vs I plot of the decays.

The shorter 7 ns lifetime for Re-bbzp agrees well with the smaller emission quantum yield observed for this complex when compared with Re-pbiH, **Table 2**.

Furthermore, the photophysical data are also compared with the well-known *fac*-[$Re(CO)_3$(bpy)Cl] (Re-bpy) complex. The decrease in t and Φ_{em} indicate that the additional pendant benzimidazolyl group in the bbzp ligand promotes non-radiative decay. Further evidence for that is also found in O_2-saturated medium, in which the singlet oxygen formation yield (Φ_Δ) by Re-pbiH is 6-fold higher than that for Re-bbzp.

Table 2. Photophysical properties in CH_3CN of the studied complexes (λ_{exc} = 375 nm).

Complexes	λ_{max}^{abs} (nm)	f_{em}	f_D	t (ns)[a]	k_r (x 10^4 s^{-1})	k_{nr} (x10^6 s^{-1})	λ_{max}^{em} (298 K)
Re-pbiH	320, 375	0.0141	0.30	42 (54%) 466 (46%)	33.6[b]	23.4[b]	550 nm
Re-bbzp	300, 360	0.0007	0.05	~7.0	10.0	142.7	520 nm
Re-bpy	370	0.0058		29.7	66.7	110	590 nm

[a]Photoluminescence lifetimes probed at the emission maxima. [b]Calculated considering the faster decay

The photophysics of Re-pbiH however seem to be more complex as two distinct excited state relaxation mechanisms were present and the excited state was less sensitive to solvent or temperature.When an excess of acid was added to prevent deprotonation of the Re-pbiH complex, a monoexponential decay was observed along with a red shifted emission spectrum, (**Figure 15a-b and d**). Moreover, the bi-exponential decay (τ_1 = 42 ns and τ_2 = 466 ns) that was evident when the excited state was probed at the emission maximum was mono-exponential (τ_1 = 49 ns) when the excited state was instead probed at longer wavelengths (**Figure 15c**).

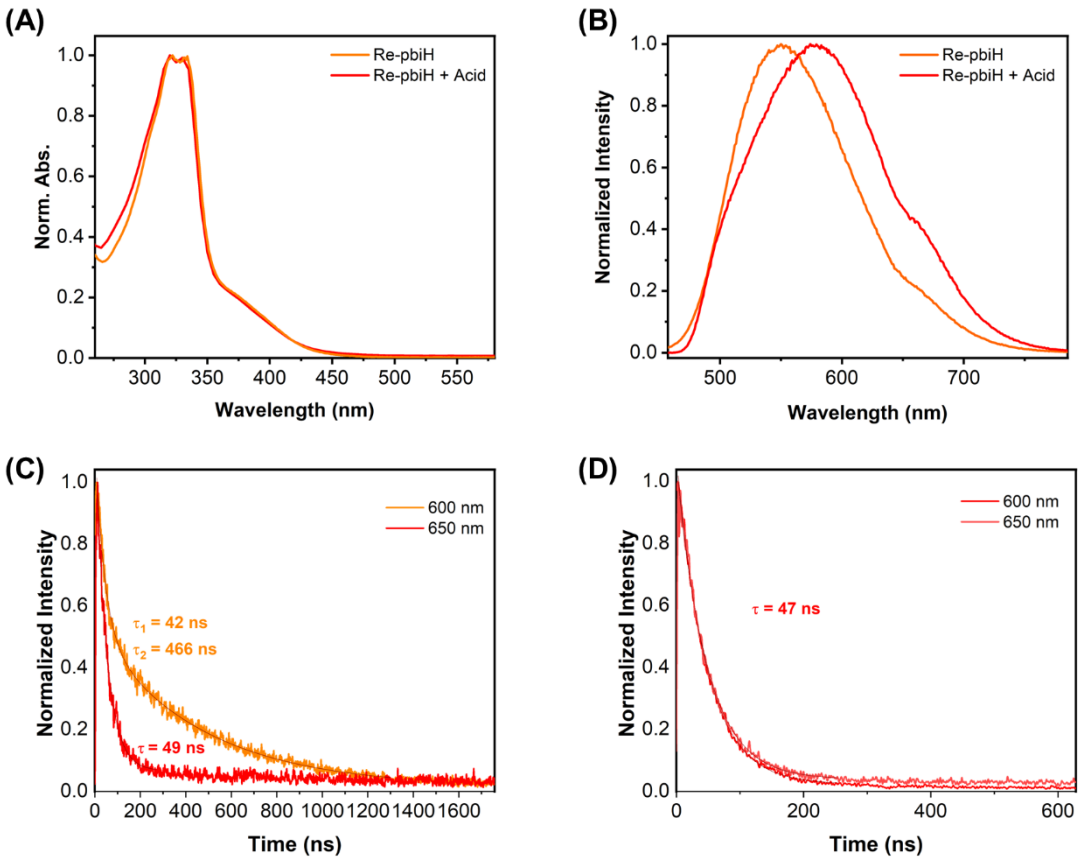


Figure 15. Absorption spectra (A) and emission spectra (B) of pure Re-pbiH in CH_3CN and after addition of $HClO_4$ (acid). Emission decay (C) for Re-pbiH monitored at different wavelengths (C) and emission decay for Re-pbiH in CH_3CN and after addition of $HClO_4$ (acid) (D).

The excited state lifetime with the added acid (τ = 47 ns) was very similar to the fast decay observed for Re-pbiH in CH_3CN (τ = 42 ns). Hence this data provides clear evidence for the existence of an acid-base equilibrium in acetonitrile where both the protonated form and the conjugate base are emissive. Therefore, the double-exponential decay observed for the Re-pbiH in CH_3CN is tentatively assigned to emission from both the protonated and the deprotonated species.

Electrochemical properties

The investigated complexes were characterized in acetonitrile solution with 0.1 M $TBAPF_6$ as the supporting electrolyte, **Figure 16**. At cathodic potentials, Re-pbiH exhibited two close reduction peaks, E_p = –2.4 V and E_p = –2.5 V *vs*. Fc^+/Fc, similar to those observed for Re-bbzp at slightly more negative potentials E_p = –2.5 V and –2.7 V *vs*. Fc^+/Fc. These observations align with previous literature reports,[102-105] which have shown that tricarbonyl rhenium complexes typically undergo two sequential reduction processes.

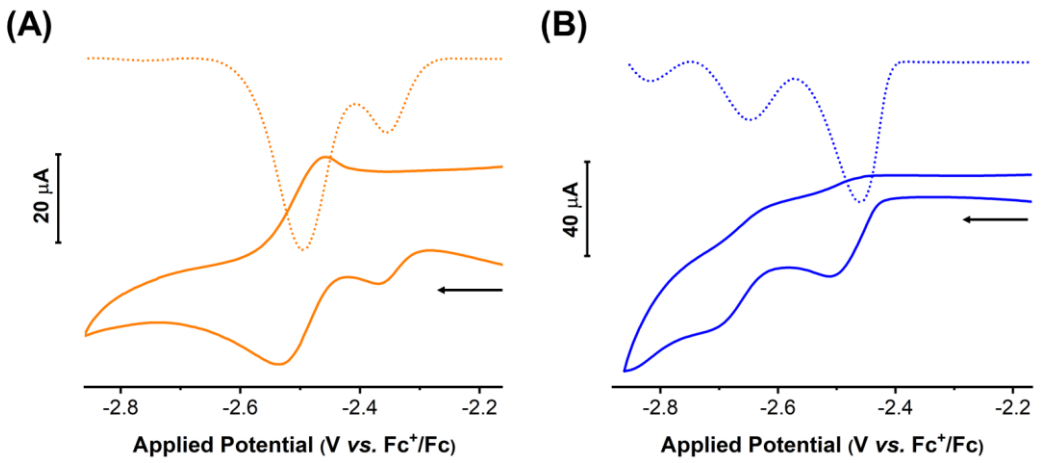


Figure 16. Cyclic voltammograms recorded, with a scan rate of 100 mV s^{-1} (solid line), and Square Wave Voltammograms measured at a frequency of 50 Hz (dashed line) for Re-pbiH (A) and Re-bbzp (B) complexes in argon-saturated 0.1 M $TBAPF_6/CH_3CN$. The arrow indicates the scan directions.

Square Wave Voltammetry (SWV) was used to elucidate the number of electrons involved in each reduction peak (**Figure 17)**. According to Lovric's study, the number of electrons involved in an irreversible process can be calculated by the linear relationship between the peak potential (E_p) versus log *f (f = applied frequency).*[106, 107] The angular coefficient ($\frac{\Delta E}{\Delta \log f}$) corresponds to the

Equation 8, which was used to estimate the n value (where α = transfer coefficient and n = number of electrons). Assuming α = 1.0, an n value was obtained for each process, showing that the first reduction peak to involve n = 2, while n = 1 for the second reduction, **Figure 17.**

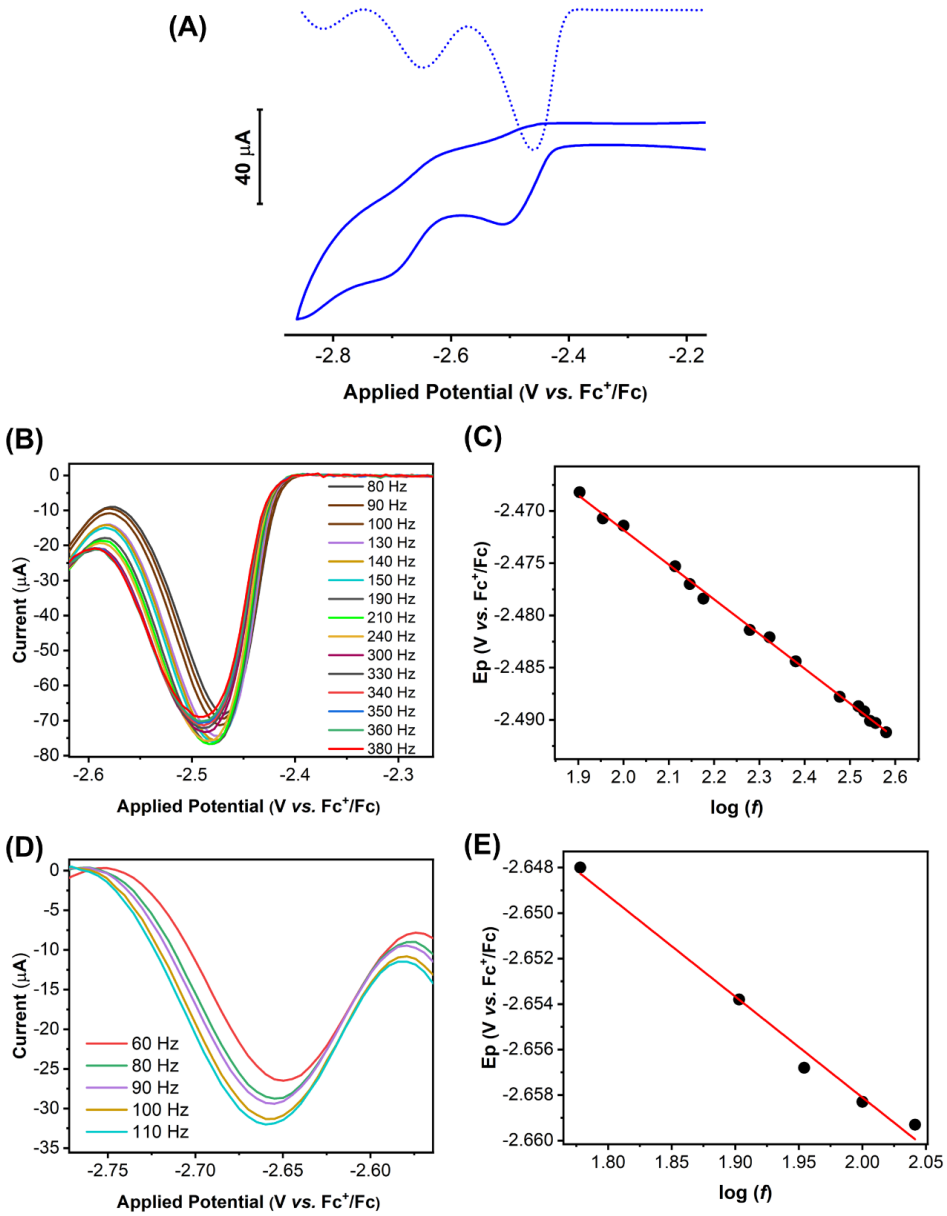


Figure 17. (a) Cyclic Voltammogram at 100 mV s^{-1} of scan rate (solid line) and Square Wave Voltammetry at 50 Hz of frequency (dashed line) for Re-bbzp complex. (b) and (c) are showing the SWV as a function of applied frequency (*f*) variation as well as its linear dependence along to the applied frequency for the first reduction process (n = 2.0), respectively. (d) and (e) are showing the SWV

as a function of applied frequency (*f*) variation as well as its linear dependence along to the applied frequency for the second reduction process (n = 1), respectively.

This behavior agrees well with the literature, where the first peak is attributed to ligand-based reduction with chloride labilization, resulting in n = 2 in the Lovric's equation due to the involvement of one electron and anionic charge labilization.[45] The second reduction peak has previously been assigned to a metal reduction, with only one electron participating (n = 1).[108-110] To validate the Lovric approach, the same experiment and analysis was performed on the well-known *fac*-[$Re(CO)_3$(bpy)Cl] (**Figure 18**), which revealed that n = 2 and n = 1 for the first and second reduction, respectively.

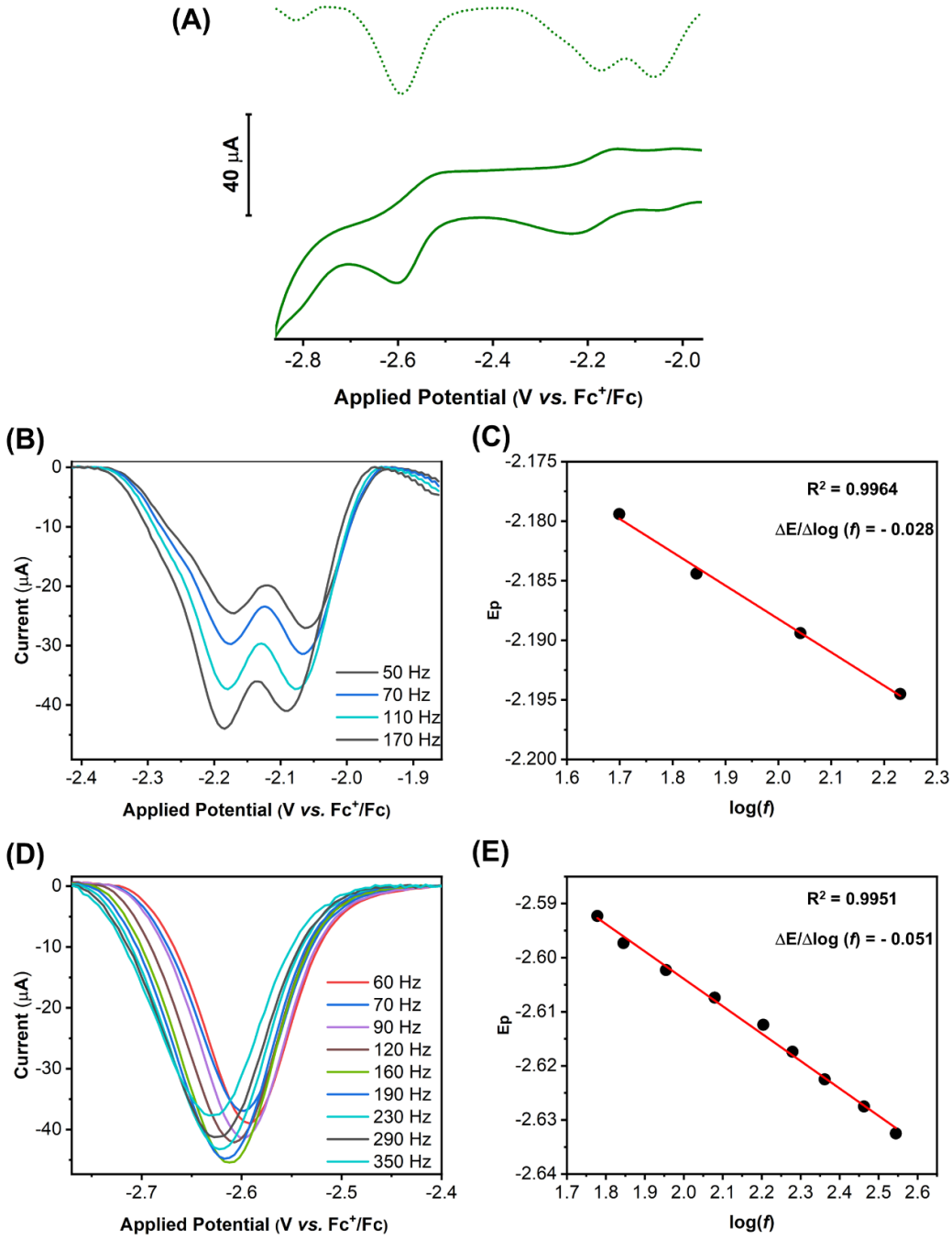


Figure 18. (a) Cyclic Voltammogram at 100 mV s^{-1} of scan rate (solid line) and Square Wave Voltammetry at 50 Hz of frequency (dashed line) for *fac*-$Re(CO)_3(bpy)Cl$ complex. (b) and (c) are showing the SWV as a function of applied frequency (*f*) variation as well as its linear dependence along to the applied frequency for the first reduction process (n = 2.0), respectively. (d) and (e) are showing the SWV as a function of applied frequency (*f*) variation as well as its linear dependence along to the applied frequency for the second reduction process (n = 1.0), respectively.

Photodriven CO_2 Reduction

Photoreduction of carbon dioxide was evaluated by employing a Xe lamp with a 370 nm long pass filter as a white light excitation source. With l_{exc} > 370 nm, only the photocatalyst absorbs light and not the electron donor (see Re-bbzp, Re-pbiH and BIH overlapped absorption spectrum in **Figure A4**). Solutions containing 0.03 mmol L^{-1} of photocatalyst and an excess of 6.7 mmol L^{-1} of BIH as a donor in acetonitrile were irradiated under a CO_2 atmosphere. The gaseous products were monitored by Gas Chromatography with samples being collected from the headspace every 30 min interval for 300 min.

In the present conditions, CO was identified as the sole CO_2 reduction product. Control experiments carried out under an argon atmosphere or in the absence of the photocatalysts or in the dark did not yield any CO. In **Figure 19**, the CO evolution as a function of the irradiation time for both complexes is shown.

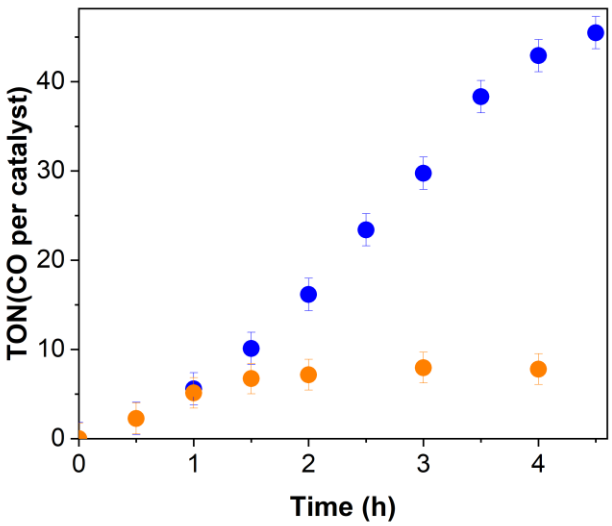


Figure 19. The *turnover number* (TON) for CO formation photocatalyzed by Re-pbiH (orange) and Re-bbzp (blue) complexes. Experiments were performed in

CO_2-saturated 10 mL CH_3CN solutions containing 6.7 mmol L^{-1} of BIH and 0.03 mmol L^{-1} of photocatalysts (λ > 370 nm).

The Re-bbzp complex exhibited significantly better performance, reaching a *turnover number* (TON) of 45 ± 2 after 4.5 hours of irradiation, while Re-pbiH exhibits a maximum TON of 8 ± 1 in the same reaction conditions. Long-term (20h) CO evolution experiments for Re-bbzp confirm that the plateau is achieved around 4.5 h of photocatalysis, **Figure A5**.

On the other hand, when BIH was used as a donor in the presence of triethanolamine (CH_3CN/TEOA 5:1 v/v), a decrease in the Re-pbiH catalysis was observed for CO_2 reduction with H_2 being formed instead. For the more optimal photocatalyst, Re-bbzp, a complete loss of CO_2 reduction was observed under this condition over the three hour time interval of the experiment (**Table 3**).

Table 3. Photocatalytic performance of studied complexes in CH_3CN solution containing 0.03 mmol L^{-1} of complex.

Complex	Donor agent	Irradiation time	TONco	TON_{H2}	CO Selectivity
$Re(CO)_3(pbiH)Cl$	BIH/TEOA[a]	3 h	4	1	75 %
$Re(CO)_3(pbiH)Cl$	BIH[b]	3 h	8	0	100 %
$Re(CO)_3(bbpz)Cl$	BIH/TEOA[a]	3 h	0	0	-
$Re(CO)_3(bbpz)Cl$	BIH[b]	3 h	30	0	100 %

[a] CH_3CN/TEOA 5:1 v/v. [b] 6.7 mmol L^{-1} of BIH.

Furthermore, photocatalytic experiments carried out with different concentrations of added water (0.001, 0.002 and 0.020%) for Re-bbzp complex revealed enhanced catalyst deactivation as the water concentration increased (**Figure 20a**).

We hypothesize that protonation of an N-H site on the additional benzimidazolyl moiety on the bbzp ligand is a key step to promote the CO_2 reduction as its proximity to the metal center favors the stabilization of key reaction intermediates. The addition of a second proton acceptor (water or TEOA) introduces a competing pathway for the N-H protonation, thereby inhibiting CO_2 photocatalytic activity.

Ligand-assisted proton transfer

To investigate this possibility, an isodesmic reaction was considered between the oxidized form of BIH ($BIH^{\bullet+}$) and the first reduced Re-bbzp species formed following chloride labilization (see next section). Isodesmic reactions enable accurate theoretical pK_a determinations by comparing a target acid to a reference acid with a known pK_a.[111] Here, the reported pK_a value of $BIH^{\bullet+}$ (14.4 in acetonitrile) was employed as the reference.[18] The calculated pK_a of 19.9 for the first reduced and protonated intermediate supports the feasibility of protonation at a third amine site during the catalytic pathway as shown in **Figure 20c**, and is also compatible to the effective acidity of CO_2-derived species in acetonitrile medium (pKa ≈ 23-25).[112, 113]

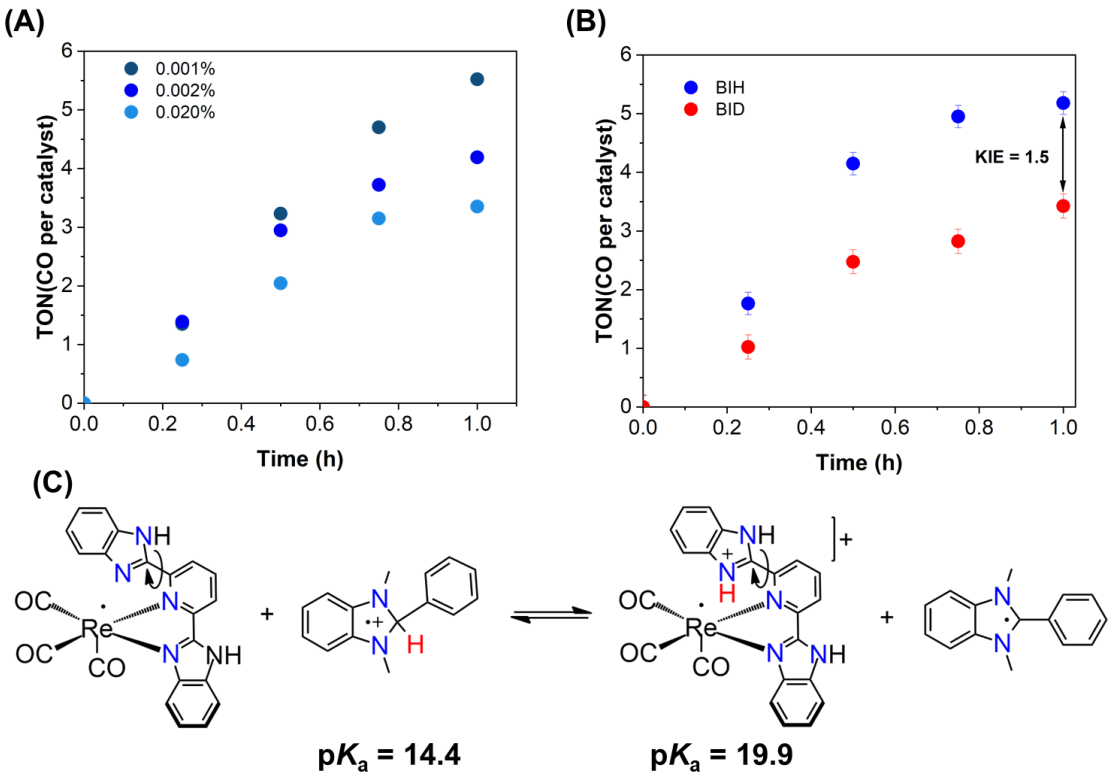


Figure 20. (a) *Turnover number* (TON) for CO formation mediated by Re-bbzp in CO_2-saturated CH_3CN containing BIH (6.7 mmol L^{-1}) and Re-bbzp (0.03 mmol L^{-1}) and the indicated H_2O concentrations (λ_{exc} > 370 nm). (b) *Turnover number* (TON) for CO formation using BIH and BID from which a kinetic isotope effect was extracted, KIE = 1.5. (c) Isodesmic reaction employed to estimate the pK_a of the protonated reduced Re-bbzp intermediate, using $BIH^{\bullet+}$ as the reference acid.

Such an interaction is expected to facilitate CO_2 activation during the reduction process and aligns well with the conclusion by Mukherjee and Siewert that proton relays near the axial positions have beneficial effects on the catalytic activity of Re(I) complexes.[48]

To experimentally probe proton transfer from the coordinated bbzp ligand to the CO_2 adduct, photocatalytic experiments were conducted using BID as the electron donor (**Figure 20b**), in which the labile proton of BIH is replaced by deuterium (see **Figure A6** for ^1H NMR characterization). Photocatalysis performed with BID exhibits a kinetic isotope effect (KIE) of 1.5 in relation to that

with BIH, indicating that proton transfer from BIH to the reduced Re-bbzp species is involved in the rate-determining steps of the catalytic cycle.

Density functional theory (DFT) geometry optimizations further reveal that this protonated N-H site is oriented toward the CO_2 molecule coordinated to the metal center, enabling the formation of a stabilizing hydrogen bond between the ligand and the CO_2 adduct (**Figure 21**).

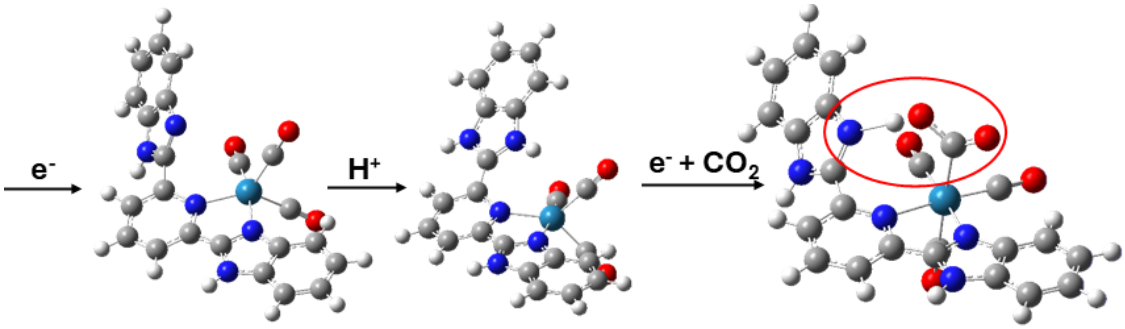


Figure 21. DFT-optimized geometry of the two-electron- and one-proton-reduced Re-bbzp species featuring a CO_2 adduct intermediate.

The proposed ligand-assisted proton transfer mechanism provides a simple explanation for the superior photocatalytic activity of Re-bbzp relative to Re-pbiH for CO_2 reduction. The Re-bbzp achieves optimal photocatalytic performance without the presence of Brønsted bases, which would otherwise compete with ligand protonation and disrupt the ligand-assisted proton relay essential for efficient CO_2 reduction. To gain further mechanistic insights into the CO_2 reduction activity of Re-bbzp complex, spectroelectrochemical FTIR (IR-SEC) and *in-situ* FTIR experiments were performed under both Ar and CO_2 atmospheres.

Catalytic pathway analysis of Re-bbzp complex

During IR-SEC measurements, the characteristic CO stretching modes (A_1 and E, molecular symmetry C_{3v})[114] of Re-bbzp were monitored during potential steps that initiated the first or second reductions (**Figure A7**). The observed spectral data closely resemble those reported for *fac*-[$Re(CO)_3$(bpy)Cl] derivatives.[108, 115-118] **Figure 22a** and **7b** highlight the evolution of the νCO region during the reduction of Re-bbzp under Ar and CO_2 atmospheres, respectively as well as the proposed electrochemical reduction pathway (**Figure 22c**).

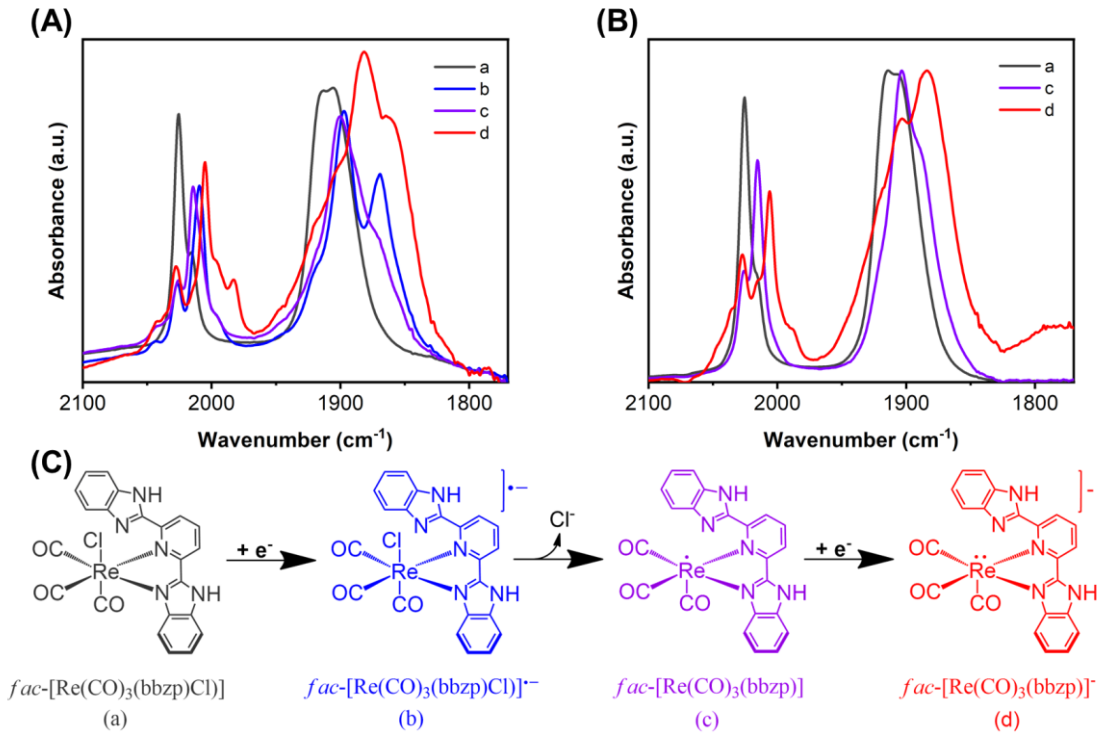


Figure 22. Infrared spectroelectrochemistry (IR-SEC) of Re-bbzp in 0.1 M $TBAPF_6/CH_3CN$ electrolyte for the first (E_p = –2.5 V *vs*. Fc^+/Fc) and second (E_p = –2.7 V vs. Fc^+/Fc) electron reduction process under Ar (A) and CO_2 (B) atmosphere. (C) Proposed reduction pathway for Re-bbzp complex (a) to species (b), (c) and (d) color-coded to the spectral assignments in (A) and (B).

Upon the first reduction, the complex *fac*-[$Re(CO)_3$(bbzp)Cl] **(a)** gives rise to new νCO bands at 2009, 1897, and 1869 cm^{-1}, that are assigned to the reduced

intermediate *fac*-[Re(CO)$_3$(bbzp)Cl]$^{-\bullet}$ **(b)**. In this species, the added electron is primarily localized on the π^* orbitals of the diimine ligand, increasing the electron density at the Re(I) center and weakening the CO bonds, resulting in a νCO shift to lower frequencies. [118-121] After approximately 60 s at the same applied potential, species **(b)** gradually convert into species **(c)**, *fac*-[Re(CO)$_3$(bbzp)], characterized by new bands at 2014 and 1900 cm^{-1} (**Figure 23**).

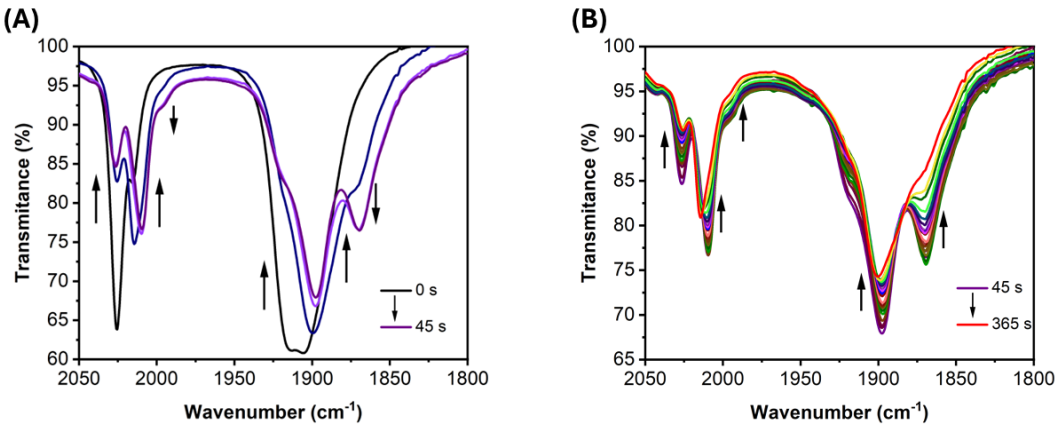


Figure 23.IR-SEC of Re-bbzp in acetonitrile with Bu$_4$NPF$_6$ electrolyte for the first electron reduction process under Ar atmosphere (Δt = 15s).

This transformation is attributed to chloride labilization, yielding a pentacoordinated, one-electron-reduced species. The corresponding νCO shift to higher frequencies reflects a decrease in electron density at the metal center following chloride dissociation.[49, 109, 122] This pathway is further supported by Lovric's analysis, which indicates n = 2 for the first reduction process, consistent with the involvement of two charged species. Notably, species **(c)** remains stable over extended times at this potential.

A potential step beyond the second reduction potential led to the appearance of additional νCO bands centered at 2005, 1983, 1882, and 1867 cm^{-1}, assigned to the two-electron-reduced species *fac*-[Re(CO)$_3$(bbzp)]$^-$ **(d)**.

The second reduction increases electron density on the Re center, leading to a νCO shift to lower frequencies.[123]

Comparative IR-SEC experiments performed under a CO_2 atmosphere revealed a similar reaction chemistry. Eventual differences in the peak shapes when compared to those under Ar atmosphere are attributed to changes in the relative concentration of the species as the different potentials are applied and, therefore were not considered in the analysis. Different from what is observed under argon, in the presence of CO_2 the intermediate *fac*-$[Re(CO)_3(bbzp)Cl]^{-\bullet}$ **(b)** was not observed (**Figure 24).** This suggests that the presence of CO_2 accelerates chloride labilization, likely because it is a better p* acceptor ligand than Cl^-, favoring rapid formation of species **(c)**, which is subsequently reduced to species **(d)**.

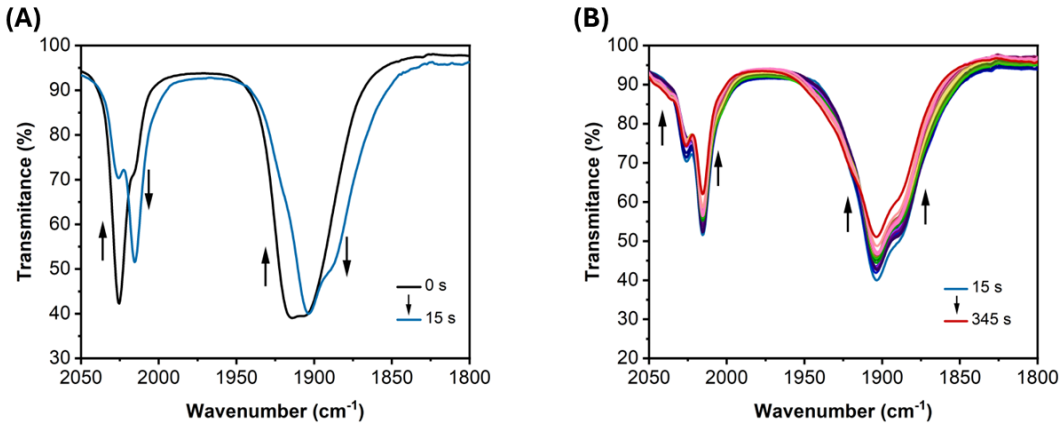


Figure 24. IR-SEC of Re-bbzp in acetonitrile with Bu_4NPF_6 electrolyte for the first electron reduction process under CO_2 atmosphere (a) t < 15 s (b) t > 15 s. (Dt = 15s).

In-situ FTIR experiments, **Figure 25,** conducted during photocatalytic CO_2 reduction reveal spectral changes closely matching those observed by IR-SEC, confirming the formation of analogous intermediates under photochemical conditions (see direct comparison in **Figure A8**).

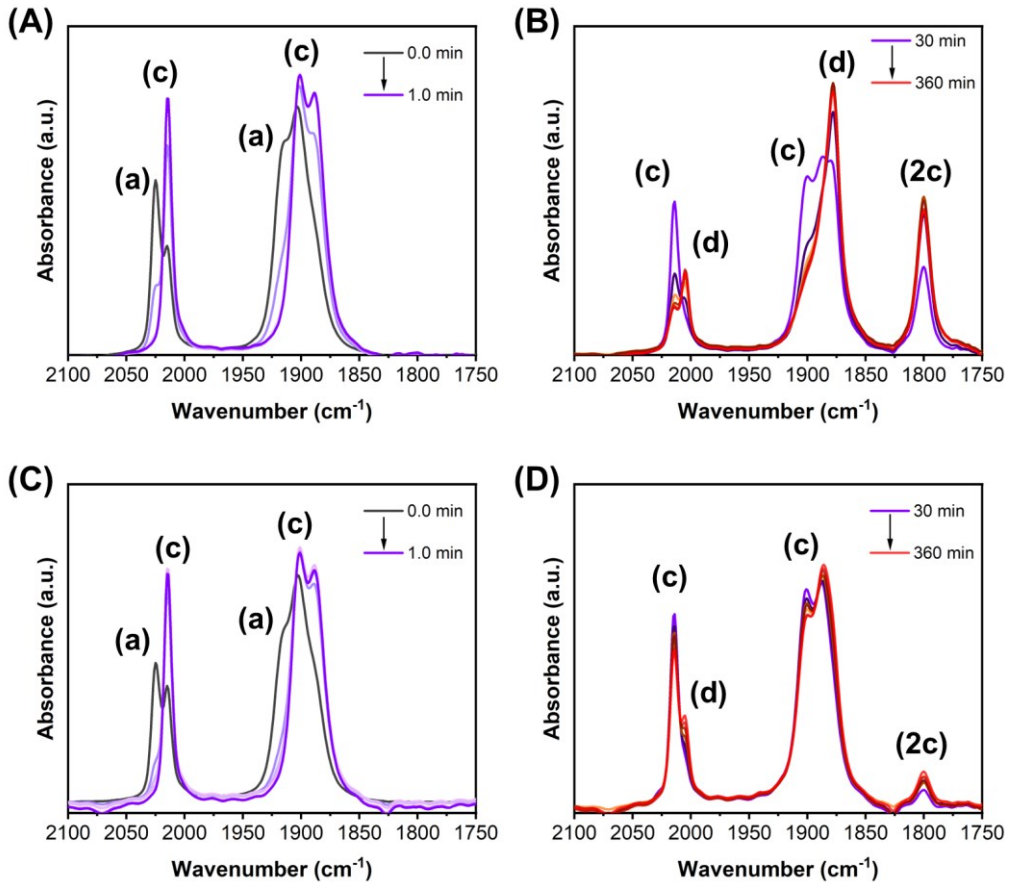


Figure 25. *In-situ*-FTIR- spectra measured over the indicated photolysis time for Re-bbzp in Ar-saturated (a and b) and CO_2-saturated (c and d) CH_3CN solutions containing excess BIH.

Under argon atmosphere, (**Figure 25a-b**), *fac*-[$Re(CO)_3$(bbzp)] **(c)** forms rapidly (<1 min) without detectable accumulation of species *fac*-[$Re(CO)_3$(bbzp)$Cl]^{-\bullet}$ **(b)**. Prolonged irradiation leads to gradual formation of the two-electron-reduced *fac*-[$Re(CO)_3$(bbzp)]$^-$ **(d)**. Concurrently, an additional band at 1800 cm^{-1} appears, attributed to a μ-CO-bridged dimeric species [$Re(CO)_3$(bbzp)]$_2$ (**2c**).

The formation of dimeric species during photocatalytic CO_2 reduction by *fac*-[$Re(CO)_3$(NN)Cl]-type complexes (where NN = 2,2'-bipyridine derivatives) is a well-established and extensively documented deactivation pathway. Kubiak

and Fujita independently isolated and spectroscopically characterized Re–Re bonded dimers $[Re(CO)_3(NN)]_2$, which display exclusively terminal CO stretching modes in the ~1840–2000 cm^{-1} region and a characteristic absorption near 700 nm.[49, 124, 125] In contrast, the *in situ* FTIR spectra of Re-bbzp show an additional band at 1800 cm^{-1} without the presence of a new visible absorption band (**Figure A9**). This spectral signature is assigned to a μ-CO-bridged dimeric species rather than a metal–metal bonded Re–Re dimer. Bridging CO ligands are well known to exhibit IR absorptions in the 1700–1850 cm^{-1} range, as reported for μ-CO-bridged cobalt and chromium carbonyl complexes.[126-128] Hence, the pendant benzimidazolyl group in the bbzp ligand appears to provide steric hindrance for Re-Re bond formation.

Under a CO_2 atmosphere, the same intermediates were observed, but with markedly different kinetics. Species *fac*-$[Re(CO)_3(bbzp)]$ **(c)** persisted for significantly longer times, while formation of species *fac*-$[Re(CO)_3(bbzp)]^-$ **(d)** was suppressed relative to those measured under an argon atmosphere, supporting a catalytic mechanism in which the two-electron-reduced, *fac*-$[Re(CO)_3(bbzp)]^-$ is the active species for CO_2 reduction. Moreover, the μ-CO-bridged dimer band at 1800 cm^{-1} was substantially less intense, indicating that CO_2 inhibits dimer formation and stabilizes catalytically relevant intermediates.

Figure 26 displays the kinetic evolution of the monitored species by tracking fixed wavenumbers at 2025, 2015, 2005, and 1800 cm^{-1}, corresponding to species (a), (c), (d), and (2c), respectively.

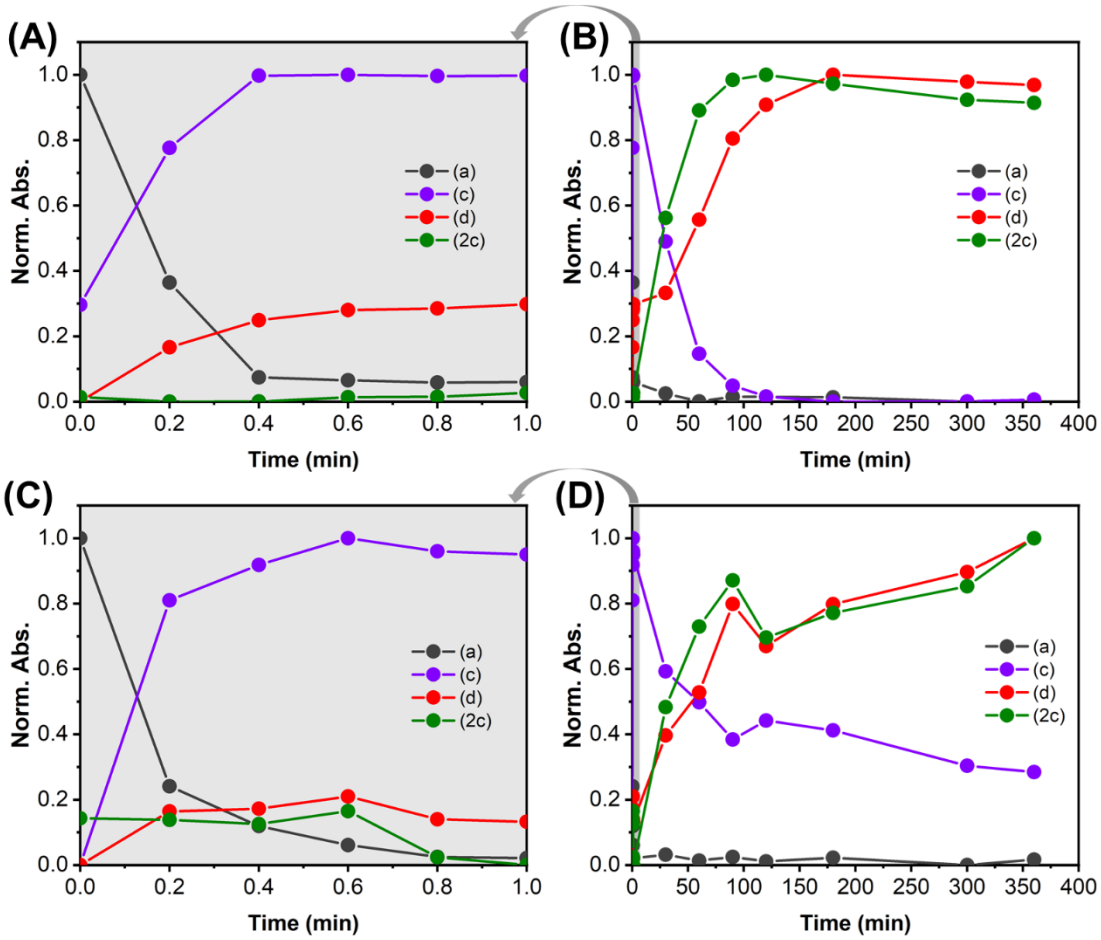


Figure 26. kinetic monitoring for each species based their corresponding peaks (2025 (a), 2015 (c), 2005 (d) and 1800 cm^{-1} for (2c)) under Ar (A and B) and CO_2 (B and C) atmosphere.

Within the first minute of irradiation, the complex *fac*-$[Re(CO)_3(bbzp)Cl]$ **(a)** is fully consumed and converted predominantly into *fac*-$[Re(CO)_3(bbzp)]$ **(c)**, with partial formation of the two-electron-reduced species *fac*-$[Re(CO)_3(bbzp)]^-$ **(d)**. Upon prolonged irradiation *fac*-$[Re(CO)_3(bbzp)]$ **(c)** is progressively consumed, accompanied by the growth of the μ-CO-bridged dimeric species $[Re(CO)_3(bbzp)]_2$ **(2c)** and continued formation of *fac*-$[Re(CO)_3(bbzp)]^-$ **(d)**. Notably, the formation rate of *fac*-$[Re(CO)_3(bbzp)]^-$ **(d)** decreases as the concentration of $[Re(CO)_3(bbzp)]_2$ **(2c)** increases, indicating that dimerization

occurs in parallel with the two-electron reduction of *fac*-[Re(CO)$_3$(bbzp)] **(c)**. Under a CO_2 atmosphere, distinct kinetics were observed. In this case, *fac*-[Re(CO)$_3$(bbzp)] **(c)** was not fully consumed, while the formation of *fac*-[Re(CO)$_3$(bbzp)]$^-$ **(d)** and [Re(CO)$_3$(bbzp)]$_2$ **(2c)** occurred as competing processes. Since no subsequent decrease in the concentration of [Re(CO)$_3$(bbzp)]$_2$ **(2c)** was observed, this pathway was identified as a photocatalytically inactive deactivation route, arising from the coupling of two equivalents of *fac*-[Re(CO)$_3$(bbzp)] **(c)**. Moreover, we propose that after CO formation and release of H_2O, the resulting Re species is rapidly reduced by BIH, regenerating *fac*-[Re(CO)$_3$(bbzp)] **(c)**. This regeneration process is supported by the persistent presence of species **(c)** throughout the experiments conducted under CO_2 atmosphere.

Finally, based on these findings, a photocatalytic cycle for Re-bbzp using BIH as electron donor is proposed (**Figure 27**), incorporating intermediates identified by both IR-SEC and *in-situ* FTIR. Protonation of the Re-bbzp framework by BIH$^{\bullet+}$ was supported by the observed kinetic isotope effect (KIE = 1.5) when BID is used as electron donor as discussed previously. We assign the active species for reaction with CO_2 to the two-electron reduced species that was observed under an argon atmosphere yet was absent under a CO_2 atmosphere. The formation of the μ-CO-bridged dimeric species contributes to the photocatalytic deactivation and it occurs as a side reaction from the one-electron reduced species as demonstrated by the *in-situ* FTIR experiments.

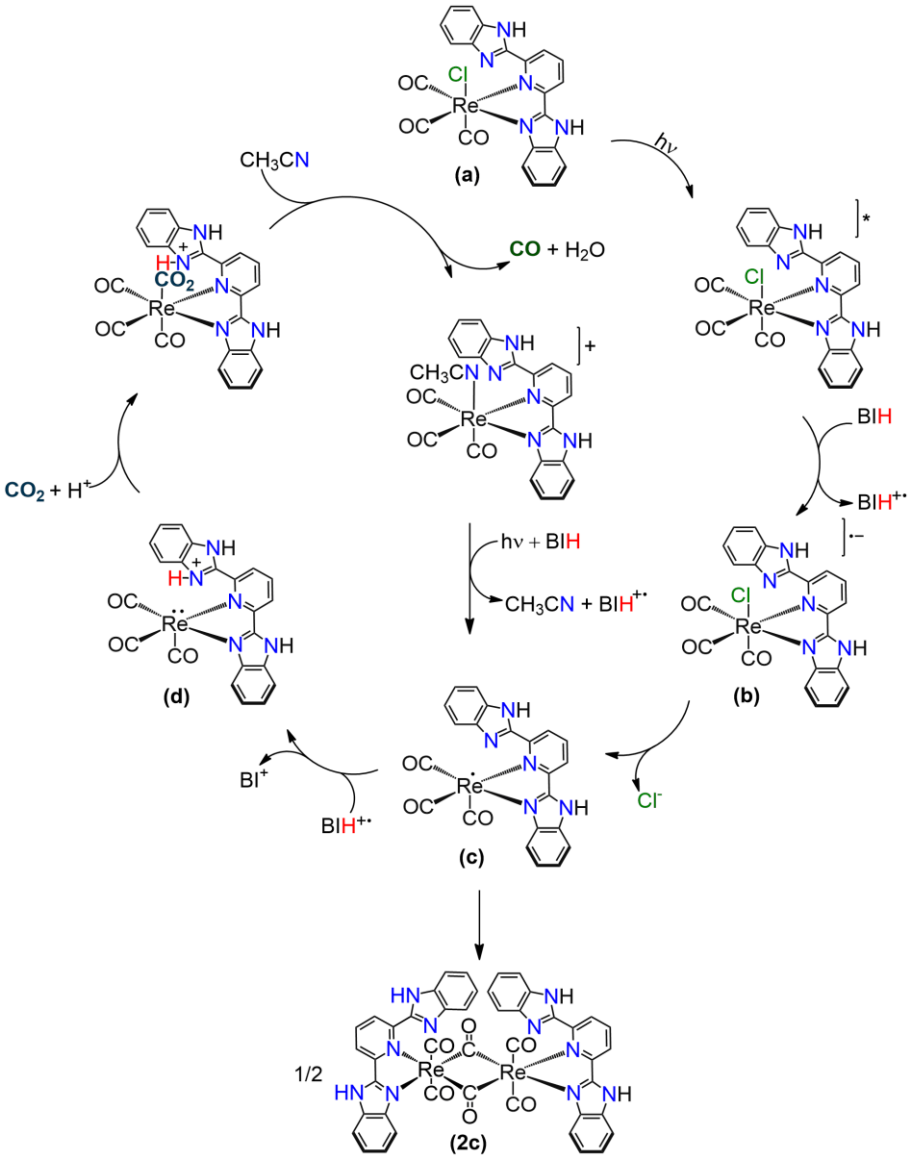


Figure 27. Proposed photocatalytic cycle for Re-bbzp using BIH as electron donor in acetonitrile.

2.4. Conclusions

In this study, the photocatalytic CO_2-to-CO reduction behavior of two Re(I) tricarbonyl complexes bearing imidazole–pyridine ligands, *fac*-[$Re(CO)_3$(pbiH)Cl] and *fac*-[$Re(CO)_3$(bbzp)Cl], was investigated with the aim of elucidating the role of ligand structure on catalytic activity and mechanism. While both complexes display comparable photophysical and electrochemical properties, the incorporation of an additional benzimidazole unit in Re-bbzp led to a pronounced enhancement in photocatalytic performance relative to Re-pbiH. A combination of IR spectroelectrochemistry and *in situ* FTIR spectroscopy under photocatalytic conditions enabled direct identification of key intermediates involved in the catalytic cycle. These studies reveal that chloride labilization occurs rapidly upon reduction, generating a pentacoordinate one-electron-reduced Re species that can undergo further reduction to form the two-electron-reduced intermediate (active species towards the CO_2 reaction). In parallel, dimerization pathways were observed, which act as deactivation channels during photocatalysis. Importantly, the *in situ* FTIR data indicate that dimer formation proceeds predominantly through μ-CO-bridged species rather than the well-known Re–Re metal–metal bonded dimers reported for related Re(I) tricarbonyl complexes.

The superior activity of Re-bbzp was rationalized by its ability to function as a ligand-based proton-responsive system. Kinetic isotope effect measurements using a deuterated BIH donor support the involvement of proton transfer steps during the catalytic cycle, consistent with a mechanism in which protonation of the pendant benzimidazole unit facilitates CO_2 activation. The sensitivity of catalytic performance to the presence of external Brønsted bases

further underscores the critical role of ligand protonation dynamics in governing reactivity. Overall, these results demonstrate that the integration of proton-responsive functionalities into imidazole-pyridine ligands serve as an effective strategy to promote productive catalytic pathways. This mechanistic insight provides a foundation for the rational design of next-generation Re(I) photocatalysts and related molecular systems for CO_2 reduction.

.

Chapter 3

From conventional inorganic semiconductors to covalent organic frameworks: Advances and opportunities in heterogeneous photocatalytic CO_2 reduction

3.1. Introduction

The enhancement of renewable sources in the global energy matrix is a key step towards a sustainable growth of human society, as so far, the world's primary energy demand is still supplied predominantly by fossil fuels. This scenario brings growing concerns on the intensification of the greenhouse effect due to the increase of atmospheric CO_2 concentration and drives the search for innovative green energy solutions. Such solutions include the large-scale utilization of solar and wind energies as well as the capture and conversion of CO_2. These targets are part of the UN sustainable goals 7, 11, and 12, and hence, are at the core of intensive research in chemistry, physics, and engineering.

From the material science point of view, intensive research efforts have been devoted to the development of catalytic materials to conduct CO_2 reduction with high selectivity, long-term stability, and at low overpotentials. Both electro- and photo-catalysts have been proposed based on metallic particles, inorganic semiconductors, 2D- materials, and metal complexes.[129-132] Among the investigated electro- and photocatalysts for CO_2 reduction, heterogeneous

materials typically exhibit long-term stability but low selectivity, while homogeneous molecular catalysts such as metalloporphyrins and metal complexes exhibit high selectivity but relatively low turnover numbers (TON). Immobilization of a molecular or metallic catalyst on solid supports has been found to hinder the detrimental side reactions of homogeneous catalysts such as dimerization and other radical reactions.[133, 134] Metal oxides,[135-138] carbon nanostructures,[139, 140] and polymeric[141] materials such as C_3N_4 were shown to serve as suitable substrates for the immobilization of molecular photo(electro)catalysts.

More recently, the rise of covalent organic frameworks (COFs) has opened a novel route towards improving the current performance of hybrid catalysts.[142] COFs are molecular frameworks, built by rigid organic building blocks that are connected *via* strong yet slightly reversible covalent bonds. By a rational selection of the building block's symmetry, three-dimensional or two-dimensional frameworks featuring long-range order and porosity are formed. In addition to their modular structure, COFs are tailor-made materials with a view on their chemical and physical properties. Particularly, COFs can be designed to absorb large portions of solar light and to offer well-defined binding sites for CO_2 molecular catalysts. As a result, COFs provide a variety of options to control and to optimize the catalytic activity through the purpose-directed adjustment of the structural, morphological, and optoelectronic properties.

In this review, we focus our attention on the application of conventional inorganic semiconductors, such as metal oxides in photoinduced CO_2 reduction, and compare them to the relatively new class of semiconductors based on covalent organic frameworks. The discussion is focused on the photoinduced

processes, *i.e.* those involving direct light-absorption, charge carrier generation and separation followed by the electron transfer to adsorbed CO_2 molecules. The manuscript is composed of two main sections: the first section provides a brief historical synopsis on the application of inorganic semiconductors for the photocatalytic CO_2 reduction reaction (CO_2RR) followed by strategies to improve the corresponding efficiency and selectivity. In the second section, the focus lies on the application of COFs as photocatalysts for the CO_2RR. Herein, the correlations between structure, stability, and photocatalytic activity are discussed.

The main goal of this review is to highlight recent advances regarding the material design and to demonstrate the impact of structural and electronic properties on the photocatalytic CO_2 reduction efficiency. Furthermore, organic-inorganic hybrid designs aiming to improve charge carrier separation and catalysis are also discussed. The review closes with current challenges in purpose-directed material engineering, long-term photocatalytic performance of the catalysts, and upscaling. Hence, we hope that this review will contribute to the further advances in the artificial photosynthetic systems aimed at selective and efficient CO_2 reduction.

Development of inorganic semiconducting photocatalysts for CO_2 reduction

To date, several approaches for converting CO_2 into fuels have been proposed. Among those based on renewable energy sources, the photochemical route that mimics the natural photosynthesis has been extensively pursued as it employs the most naturally accessible source of energy (sunlight) and electrons (water) to carry out the desired CO_2 conversion. Both molecular species and

crystalline semiconductors have been proposed as photocatalysts for CO_2 reduction, each of them with advantages and disadvantages in terms of production feasibility, stability (turnover number), reactivity (turnover frequency), and selectivity towards the multiple reduction products.[129]

In 1978, Halmann *et al*. published a pioneering work on the formation of liquid fuels through CO_2 photoelectrochemical reduction over a *p*-GaP photocathode. The authors demonstrated that further developments of semiconducting solids for the photoelectrochemical CO_2 reduction may provide an alternative approach to the production of organic raw materials and fuels.[136] Subsequently, in 1979, Inoue *et. al* reported the selective photoreduction of CO_2 over different semiconductor powders (TiO_2, ZnO, CdS, GaP, SiC, and WO_3) suspended in aqueous solutions and established a relationship between the reactivity and the semiconductor conduction band energy.[137] The proposed mechanism involves water oxidation by holes located in the valence band of the photoexcited semiconductor followed by proton releasing which are consumed in the CO_2 reduction reaction by the photogenerated electrons in the conduction band. **Figure 28** illustrates the operating principle of photocatalytic conversion of CO_2 by a semiconductor including different products that can be obtained.[138]

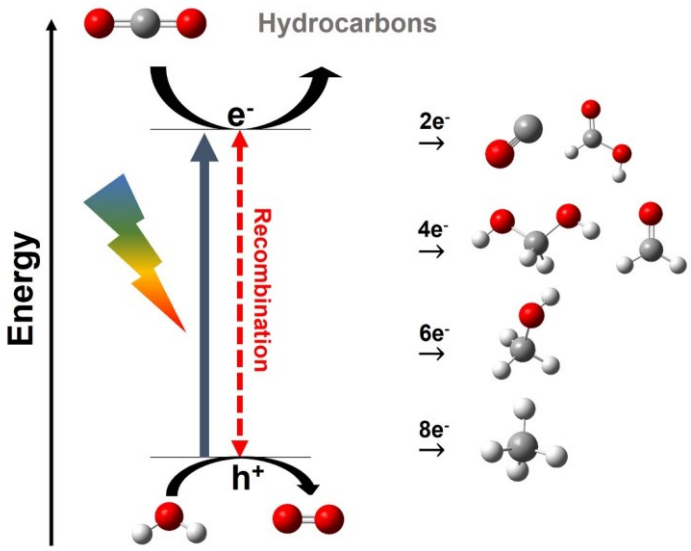


Figure 28. Schematic illustration of the operating principle of the photocatalytic CO_2 conversion (red balls: O, grey balls: C, white balls: H).

Pristine inorganic semiconductors

The aforementioned seminal works have encouraged the investigation of CO_2 photoreduction over different semiconductors. The application of inorganic semiconductors as a photocatalyst for the CO_2 conversion offers several advantages such as low cost, facile preparation, high chemical stability, and in some cases activation under visible light.[139-141] Selected examples of CO_2 photoreduction over pristine metal oxides are summarized in **Table 4**.

Table 4. Relevant examples of pristine inorganic semiconductors applied for the CO_2 photoreduction

Semiconductor	Surface area	Conversion rate (μmol g^{-1} h^{-1})	Main product	Sacrificial agent/ solvent	Light source	Ref.

	(m^2 g^{-1})		**(selectivity)**			
ZnO	1.3 to 82.1	8.68 to 407	CO	H_2O	125 W (Hg)	[143]
$BiVO_4$		2.27 to 3.97	CO	H_2O/$NaHCO_3$	400 W (Hg)	[144]
ZnO	16.26 to 31.45	1.63 to 3.81	CO	H_2O*	300 W (Xe)	[145]
BiOCl	-	1.01	CO	H_2O	500 W (Xe)	[146]
ZnO	9.50 to 17.96	0.62 to 0.95	CO	Na_2SO_3/NaOH	300 W (Xe)	[147]
ZnO	-	0.36 to 0.76	CO	Na_2SO_3	300 W (Xe)	[148]
TiO_2	46.50 to 145.60	~ 0.25 to 0.58	CO	H_2O*	150 W (oriel®)	[149]
α-Fe_2O_3	17.00 to 59.00	~ 0.11 to 0.28	CO	NaOH	8 W (Hg)	[150]

ZnO	-	1.32 to 28.4	CH_3OH	$NaHCO_3$	150 W (Hg)	[151]
$BiVO_4$	-	14.58	CH_3OH	NaOH	300 W (Xe) LP-420 nm	[152]
TiO_2	-	43.2 to 67.9	CH_4	H_2O*	50 W (LED) LP-650 nm	[153]
CuO	-	1.0 to 56.3	CH_4	H_2O	150 $mWcm^{-2}$	[154]
Cu_2O	50.00	19.2	CH_4	H_2O*	Hg – UV + visible	[155]
CuO	1.00 to 118.00	0.19 to 16.7	CH_4	H_2O	11 W	[156]
KNb_3O_8 and HNb_3O_8	2.70 to 39.40	0.11 to 3.6	CH_4	H_2O	350 W (Xe)	[157]

Bi_2WO_6	0.73 and 42.87	0.33 and 2.6	CH_4	H_2O	300 W (Xe) LP-400 nm	[158]
WO_3	8.50 to 65.00	0.0042 to 2.12	CH_4	H_2O*	300 W (Xe) LP-420 nm	[159]
TiO_2	38.89 to 98.12	0.91 to 2.1	CH_4	H_2O	300 W (Xe) LP-420 nm	[160]
WO_3	-	1.16	CH_4	H_2O*	300 W (Xe) LP-420 nm	[161]
Bi_2WO_6	0,60 and 5.63	0.045 and 1.10	CH_4	H_2O*	300 W (Xe) LP-420 nm	[162]
Bi_2WO_6	-	0.19 to 0.77	CH_4	H_2O	500 W (Xe)	[163]

					LP and SP 400 nm	
TiO_2	92.00 to 244.00	0.41	CH_4	H_2O*	300 W (Xe)	[164]
WO_3	0.74 to 7.10	0 to 0.34	CH_4	$AgNO_3$	300 W (Xe) LP-400 nm	[165]
$BiVO_4$	-	5.5 to 108	C_2H_5OH	H_2O	350 W (Xe) LP-400 nm	[166]
WO_3	-	9.4	CH_3COOH	H_2O	300 W (Xe)	[167]
Nb_2O_5	11.00 to 20.00	~0.005 to 0.8	CH_3COOH	H_2O	5 W	[168]

* = water vapour.

Morphology and crystal structure

Given the well-known photoreactivity of TiO_2 for oxidative reactions (such as organic pollutant degradation and water oxidation)[142], the effect of its crystalline structure, engineered defects, and morphology on CO_2 conversion was investigated.[139-141] Liu *et al.* compared the photocatalytic activity for CO_2 reduction over three TiO_2 nanocrystalline polymorphs (anatase, rutile, and brookite) that were engineered *via* helium pretreatment exhibiting defect-free and oxygen-deficient surfaces. The authors observed the formation of CO and CH_4 as the major and minor products for all TiO_2 polymorphs, respectively. The CO_2 photoreduction to CO and CH_4 was remarkably enhanced over the defective anatase and brookite TiO_2 (up to 10-fold enhancement) as compared to the defect-free surfaces, reaching a formation rate of ~3.0 μmol $g^{-1}h^{-1}$. Herein, the brookite phase exhibited the optimal density of oxygen vacancies for the efficient CO_2 photocatalysis. The role of surface defects on the photoactivity and selectivity was rationalized by means of *in-situ* diffuse reflectance infrared Fourier transform spectroscopy (DRIFTS) measurements.[149] Liu *et al.* have shown a polymorph-dependent reactivity of $BiVO_4$ towards CO_2 reduction. The monoclinic phase of $BiVO_4$ performed better than the tetragonal phase due to the greater absorption in the visible wavelength range.[166]

Further studies on the relationship between the oxide morphology and the CO_2 photoreduction activity and selectivity were carried out by different research groups.[143, 145, 150, 157, 158, 161] For example, Huang *et al.* prepared TiO_2 particles *via* a hydrothermal method under strict control of the temperature and reaction time to promote the formation of nanotubes and nanorods. The authors showed that

CO_2 conversion to CH_4 over TiO_2 nanotubes and nanorods are respectively 2.13 and 1.41 times more efficient than over TiO_2 nanoparticles featuring random shape. This enhanced performance was attributed to the larger specific surface area, the higher concentration of oxygen vacancies, and crystalline defects. Such properties were found to contribute to a better interaction with CO_2.[160]

For ZnO particles prepared *via* a solvothermal method to yield microspheres (S-1), microflowers (S-2), and nanorods (S-3), Liu *et al.* also observed a morphological dependence of the CO_2 conversion. Herein, ZnO nanorods exhibited a superior performance as shown in **Figure 29** caused by its larger surface area (2 times larger than the other materials) and by the synergistic effect of the exposed facets ratio.[145] In addition, a more negative conduction band position of the nanorods provided a higher driving force for the CO_2 reduction. Xie *et al.* performed a similar investigation on WO_3 morphologies, showing that the quasi-cubic-like WO_3 was inactive for CO_2 photoreduction, while the rectangular sheet-like WO_3 exhibited significant activity. The authors attributed the activity of this material to its higher specific surface area and to the more suitable conduction band position.[165]

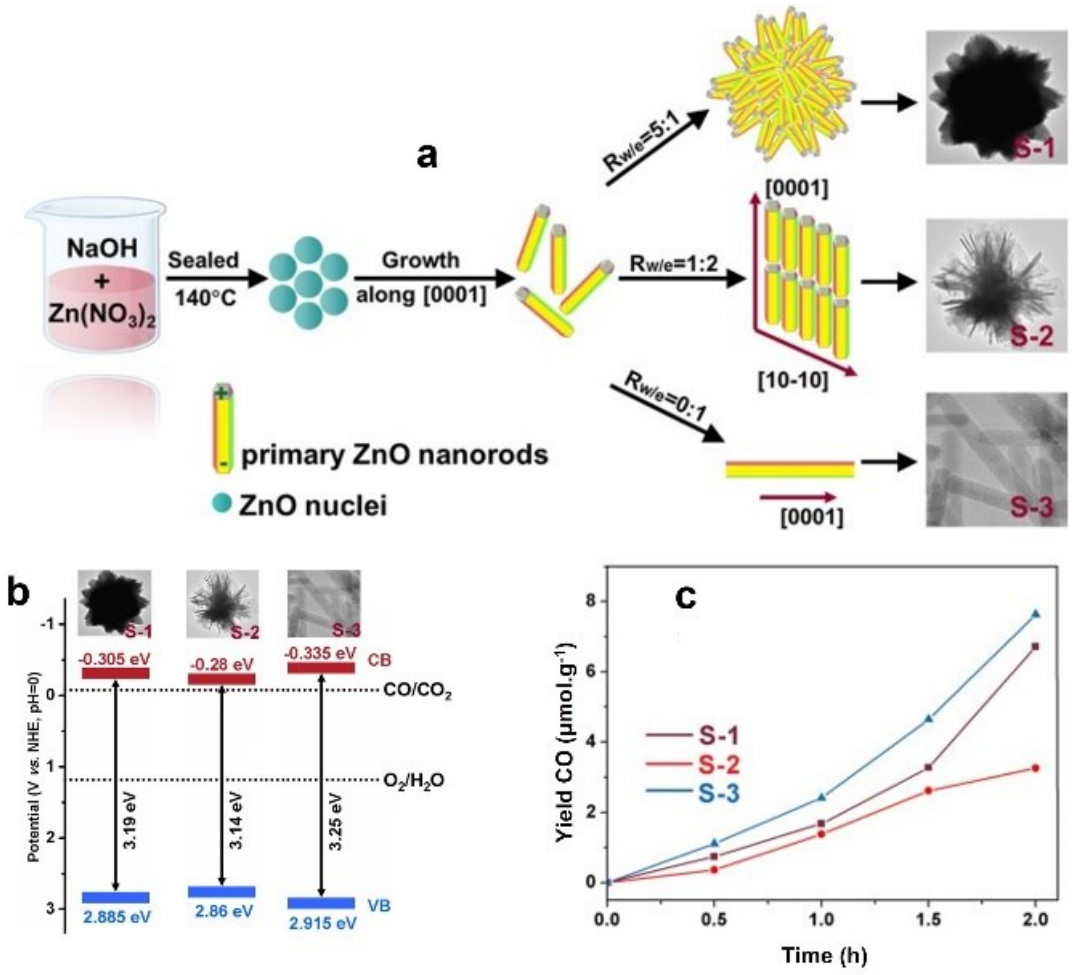


Figure 29. (a) Preparation of different ZnO nanostructures and (b) the determined conduction band (CB) and valence band (VB) potentials of ZnO microspheres (S-1), microflowers (S-2), and nanorods (S-3) *vs*. NHE (pH = 0) and (c) their respective photocatalytic activity towards CO evolution. Adapted with permission.[145] Copyright 2016, Springer Nature.

Cu-based semiconductors have been widely employed as photocatalysts for CO_2 reduction due to their abundance, low toxicity, extended light absorption, low recombination rate of the photogenerated electron-hole pairs and suitable electronic positions of the valence and conduction bands.[154-156, 169] For example, Nogueira *et al.* have shown that different synthesis routes of CuO affect the CO_2 photoreduction efficiency. CuO nanoparticles obtained by a solvothermal method showed the highest CH_4 production rate compared to the CuO obtained by other

methods, **Figure 30a**. The authors concluded that the CuO produced by the solvothermal method exhibits greater specific surface area and unique morphology that supports superficial activation of both CO_2 and H_2O, **Figure 30b**.[156]

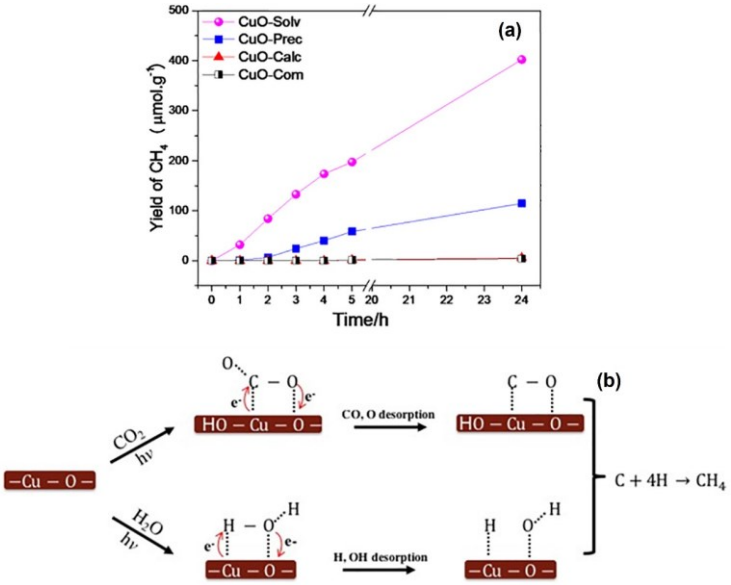


Figure 30. (a) CH_4 evolution kinetics from CO_2 photoreduction over CuO prepared *via* solvothermal synthesis (CuO-Solv), co-precipitation (CuO-Prec), calcination method (CuO-Calc), and commercially acquired (CuO-Com). (b) Simplified scheme of the CO_2 photoreduction process on the CuO surface. Adapted with permission.[156] Copyright 2020, Elsevier.

In further studies Ávila-López *et al.* explored the photocatalytic activity of CuO in different configurations, namely as powder, thin film, and coatings on glass fiber mesh. While CH_4 formation was observed for all configurations, CuO coated on glass fiber mesh performed the best due to its high specific surface area and high concentration of surface defects.[154] It has been suggested that the CO_2 reduction performance strongly depends on its interaction with the catalyst surface, which can be tuned by surface groups and the reaction conditions.

Surface integrity

The nature and adsorption capacity of the photocatalyst surface allow to control the product selectivity of CO_2 reduction *via* specific superficial interactions.[149, 152, 162, 170] Since CO_2 behaves like a Lewis acid, alkali metal oxides can improve the CO_2 adsorption and, consequently, increase the reactivity. Yu *et al.* demonstrated that TiO_2 with a high density of -OH surface groups exhibited the highest CH_4 formation rate (~5.42 μmol g^{-1} h^{-1}) under UV illumination. As the calcination temperature and the time of the synthesis were increased, the photoactivity of TiO_2 declined due to the removal of -OH surface groups.[170] Similarly, Li *et al*. showed for ZnO particles that the vacancy defects (controlled by different annealing treatments) influence the performance of the CO_2 reduction. Herein, the vacancy defects favor the interaction between ZnO and CO_2 and promote better charge carrier separation.[147] The pivotal role of oxygen vacancies on CO_2 reduction by metal oxides was also reported in other works.[144, 146, 148, 151, 159, 163, 167]

Niobium-based materials exhibit high chemical stability and excellent electronic properties. Despite their remarkable features, they have only been applied recently for the CO_2RR.[171, 172] Silva *et al.* showed that the acidity of the Nb_2O_5 surface can be tuned to selectively induce the formation of various CO_2 reduction products (CO, HCOOH, CH_4, CH_3COOH). The authors could control of the surface acidity by annealing the sample at different temperatures. The proposed reaction mechanism, Figure 4, involves the formation of different intermediates as a function of the surface protonation.[168]

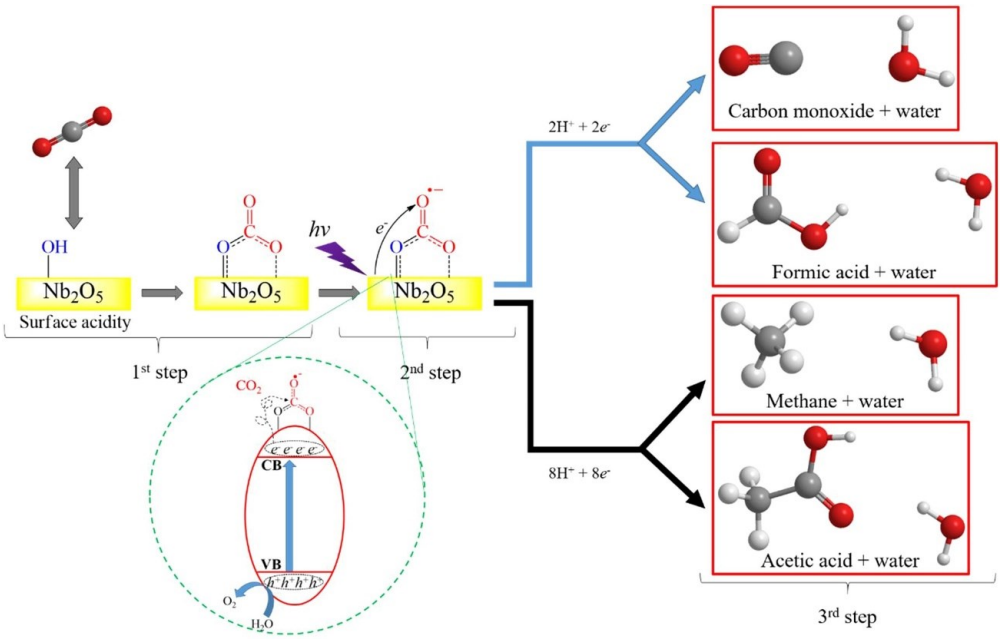


Figure 31. Proposed pathways for CO_2 photoreduction over the acidic surface of Nb_2O_5. Reproduced with permission.[168] Copyright 2019, Elsevier.

In further studies Li *et al*. reported the application of differently synthesized Nb-based materials for CO_2RR. Materials obtained through the hydrothermal method were more active than materials prepared through the traditional solid-state methodology. Herein, HNb_3O_8 performed better than KNb_3O_8, which was attributed to the protonic acidity of the former promoting the photocatalytic reduction of CO_2 to CH_4.[157] Moreover, all Nb-based materials demonstrated higher photocatalytic activity in comparison to the benchmark photocatalyst, TiO_2 P25, producing CH_4 as the main product.

Many research efforts have been devoted to control the morphology and crystallinity of the pristine semiconductors as well as their surface integrity in order to improve the CO_2 conversion efficiency *via* creating suitable conditions for CO_2 adsorption and activation. However, such strategies do have their intrinsic limits.[157, 165, 166, 173] So far, the highest rates for CO_2 photoreduction conducted on pristine inorganic semiconductors did not exceed the range of 10

μmol h^{-1} g_{cat}^{-1} (Table 1). Some efforts have been focused on the process engineering to improve the efficiency. For example, Galli *et al.* proposed an innovative photoreactor operating under high pressure (7 bar) and 80 ºC for the photoreduction of CO_2 to formic acid over TiO_2 P25. The unconventional conditions allowed increasing the CO_2 solubility in the liquid phase, thus improving the overall performance compared to prior works.[174]

Modified inorganic semiconductors

The poor performance of the pristine semiconducting photocatalysts is generally attributed to their fast charge carrier recombination, poor visible light harvesting, and the sluggish surface redox reactions resulting from their low catalytic activity, as well as the low electronic conductivity leading to slow electron transfer rates. Additionally, as water serves as hole scavenger, the competing H_2 evolution reaction reduces the CO_2 reduction efficiency. Hence, an efficient CO_2-photocatalyst should be highly active for CO_2 reduction and exhibit a negligible activity for H_2 evolution. Most of the pristine inorganic semiconductors are not able to fulfil this crucial requirement.[129, 175]

Different approaches have been proposed to improve the semiconductor features such as doping, decoration with metal nanoparticles or creation of heterojunctions with metal oxides or metal-free semiconductors. These strategies can enhance the charge carrier separation efficiency, the visible light harvesting and the CO_2 activation through specific adsorption sites. Additionally, such modifications have the potential to control the CO_2 reduction selectivity.[176-180] Relevant examples of photocatalyst modification for CO_2 reduction are summarized in Table 2. Note that the conversion rates are on average about one

order of magnitude higher than those observed for the pristine materials (**Table 4**).

Table 5. Relevant examples of inorganic semiconductors modified with metal nanoparticles, metal- and metal-free semiconductors applied for the CO_2 photoreduction.

Composites	**Surface area (m^2 g^{-1})**	**Conversion rate (μmol g^{-1} h^{-1})**	**Main product**	**Sacrificial agent/ solvent**	**Light source**	**Ref.**
Pt/ In_2O_3 and Pt/C-In_2O_3		133.5 and 633	CO	H_2O	300 W (Xe)	[177]
Co/CdS	-	392	CO	Na_2CO_3	300 W (Xe) LP-420 nm	[181]
MoS/TiO_2	-	267	CO	H_2O	300 W (Xe) LP-400 nm	[182]
g-C_3N_4/N-Nb_2O_5	63.1283 to 238.8736	253.34	CO	$NaHCO_3$	300W (Xe)	[183]
Ru-mC_3N_4	-	66.7 to 250	CO	DMF/H_2O	34 W	[184]

CdS/BCN	~250	250	CO	ACN/TEOA /$CoCl_2$	300 W (Xe) LP-420 nm	[185]
Ag/Zn-Ga_2O_3		117	CO	$NaHCO_3$	400 W (Hg)	[180]
CeO_2-TiO_2	182.4	72	CO	H_2O	300 W (Xe)	[186]
BCN/In_2O_3	4.6 to 61.7	7.94	CO	H_2O	300W (Xe) LP-400 nm	[187]
NiO-gC_3N_4	13.94 to 70.09	~0.80 to 2.75	CO	TEOA/ H_2O	300W (Xe)	[188]
RGO@CuZnO@Fe_3O_4	-	2656	CH_3OH	DMF/H_2O	20 W white cold LED LP-400 nm	[189]
CuO/$NaTaO_3$	-	1302	CH_3OH	C_3H_8O	250 W (Hg)	[190]
Cu/TiO_2	28	118.5	CH_3OH	NaOH	8 W (Hg)	[179]

					254 nm	
RGO-ZnO	23.69	68.8 to 87.7	CH_3OH	NaOH	300 W (Xe)	[191]
Ru-TiO_2	26.96	78.16	CH_3OH	DMF/H_2O	20 W LED	[192]
RGO-ZnO	-	45.75	CH_3OH	$NaHCO_3$	500 W (Xe)	[193]
Cu_2O/TiO_2	48 to 120	12-70	CH_3OH	H_2O	300 W (Xe)	[194]
In/TiO_2	42.98 to 123.00	31 to 244	CH_4	H_2O*	500 W (Hg)	[195]
Pt-Au-Cu-Pd-Ru/$NaTaO_3$	-	2.16 to 139.1	CH_4	H_2O/H_2	300 W (Xe)	[196]
CuO/BiOCl		94.9 to 114.1	CH_4	H_2O	300 W (Xe)	[197]
Ni/In_2O_3	55.05 to111.80	21.3 to 66.2	CH_4	H_2O	300 W (Xe) LP-420 nm	[198]

ZnO/ZnTe morphologies	5.60 and 18.20	38.8 and 44.6	CH_4	H_2O	300 W (Xe) LP-420 nm	[178]
CoS/gC_3N_4	5.72 to 94.04	40.58	CH_4	H_2O	300W (Xe)	[199]
TiO_2@g-C_3N_4	63.112 to 95.965	32.49	CH_4	H_2O*	300W (Xe) λ:420-700nm	[200]
gC_3N_4/ZnO	-	19.8	CH_4	$NaHCO_3$ /H_2O*	300 W (Xe) LP-420 nm	[201]
gC_3N_4-$W_{19}O_{49}$	-	1.38	CH_4	H_2O*	300W (Xe)	[202]
$Au/Pt/TiO_2$	-	0.57	CH_4	H_2O	500 W (Xe)	[203]
CuO/TiO_2	~790 to 1600	~790 to 1600	$C_2H_4O_2$	CH_3OH	250 W (Hg)	[204]

H_2O* = Water vapour.

RGO = Reduced graphene oxide.

BCN = boron carbon nitride.

ACN = acetonitrile.

DMF = N,N-Dimethylmethanamide.

TEOA = triethanolamine.

Semiconductor/metal composites

For the decoration of inorganic photocatalysts with metallic particles typically Au, Pt, Cu and Ag particles are applied, mainly because of their selectivity for the formation of specific CO_2 reduction products. Several examples of metal-loaded TiO_2 and other semiconductors are reported in the literature with conversion rates higher than those for the respective pristine materials and with variable product selectivity depending on the reaction medium and the metal co-catalyst.[190, 194-196, 198, 203] Zhang *et al.* have showed that TiO_2 nanofibers decorated with Au and/or Pt nanoparticles perform remarkably better compared to pristine TiO_2. The bare oxide converted CO_2 to CH_4 with a rate of 6 μmol g^{-1} h^{-1}, while the modified TiO_2 exhibited production rates of up to 114 μmol g^{-1} h^{-1}. The authors attributed the improved performance to the synergistic effect of the electron-sink function of Pt nanoparticles and to the Au surface plasmon resonance that improved charge carrier separation and the visible light harvesting, respectively.[203] Tahir and Amin have shown an 8-fold increase of the photoinduced CH_4 generation for In-TiO_2 systems in comparison to bare TiO_2, **Figure 32**. The In clusters act as electron acceptor, enhancing the charge carrier efficiency and also as CO_2 reduction site.[195] Similarly, Wan *et al.* reported an In_2O_3/Ni system for CH_4 production from CO_2. Ni decoration increases the visible light absorption and the CO_2 adsorption capability due to the introduction of the active sites.[198] This effect was reported by several authors for different systems

and underscores the crucial role of the co-catalysts on improving the photocatalytic activity.[180, 190, 195, 196, 198, 203]

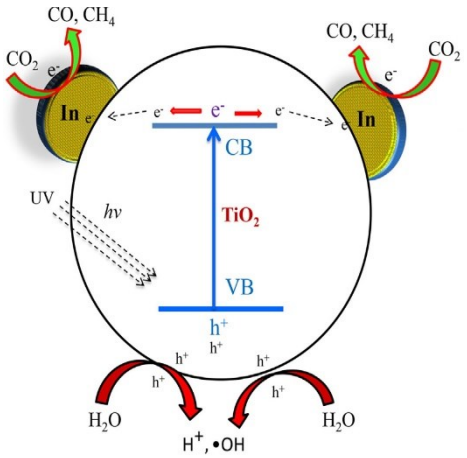


Figure 32. Photocatalytic reduction of CO_2 with H_2O as a hole scavenger over In-doped TiO_2 photocatalyst. Adapted with permission.[195] Copyright 2015, Elsevier.

Heterojunction composites

The combination of two different semiconductors with different band gaps and energy band levels (conduction and valence band) has been shown to enhance the light harvesting and charge carrier separation efficiencies, boosting CO_2 photoreduction.[182, 186,11, 192, 194, 197, 205-207] Jia *et al.* found that a MoS_2/TiO_2 heterojunction exhibits excellent photocatalytic performance under visible light illumination. Such improvement has been attributed to the higher separation efficiency of the photogenerated charge carriers as illustrated in **Figure 33**, along with a strong response to visible light.[182]

Qin *et al*. investigated the CO_2 reduction to methyl formate over a CuO/-TiO_2 composite and observed high photocatalytic activity with a rate of 1600 μmol g^{-1} h^{-1} due to the efficient charge carrier mobility following photoexcitation.[204]

Ehsan and He synthesized a ZnO/ZnTe heterostructure *via* an *in situ* hydrothermal method and applied the newly formed material for CO_2 photoconversion to CH_4 under visible light illumination. The influence of the ZnO morphology in the heterostructure was studied, revealing that ZnO nanosheets exhibit a higher activity than ZnO nanorods. The former has a larger specific surface area and, hence, larger heterojunction interface.[178] In general, the formation of the heterostructures promotes charge carrier transfer processes, prevent charge recombination and thus leads to improved photocatalytic activities.[11, 182, 186, 192, 194, 197, 205-207]

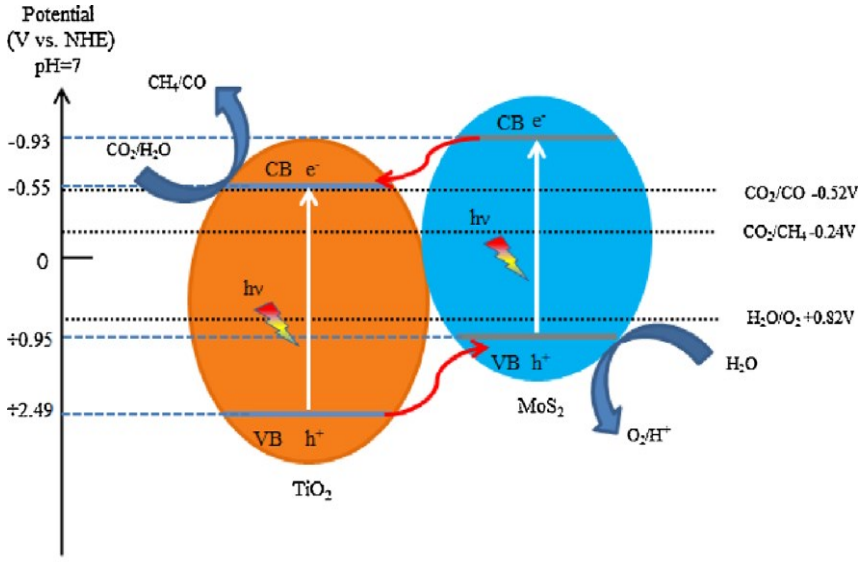


Figure 33. Schematic representation of the energy band positions in MoS_2/TiO_2 heterojunction composites and corresponding photoinduced charge carrier processes. Adapted with permission.[182] Copyright 2019, Elsevier.

Metal-free semiconductors (*e.g.*, graphene and g-C_3N_4) have recently gained attention in the community due to their remarkable properties such as visible light activity, earth abundance, cost-effectiveness, good electrical conductivity, and non-toxicity.[176] These organic semiconductors are very well suited for the combination with metal oxides to yield photocatalytic active

heterostructures.[184, 185, 189, 191, 193, 201, 208] For example, Li *et al.* showed that a heterojunction formed between ZnO and reduced graphene oxide (RGO) improves the CO_2 conversion to ethanol by 75%. The enhanced performance was attributed to the enlarged light absorption of ZnO in the presence of RGO. Additionally, the size of ZnO nanoparticles and their crystallinity were influenced by the RGO content.[193]

Sharma *et al.* developed a synthetic method to introduce single-site ruthenium atoms into the mesoporous C_3N_4 network. This modification improved the methanol production under visible light at ambient conditions. The authors showed that the interface of the hybrid material acts as a bridge, increasing the charge carrier density on Ru, thus reducing the barrier for the electron transfer and enhancing the photocatalytic activity.[184] More details on the formation of heterojunctions using different semiconductors as well as modification by metal nanoparticles can be found in previous reviews.[11, 129, 175, 176, 205, 209-211]

Parallel to the exploration of metal-free semiconductors for CO_2 conversion and other photocatalytic applications, an emerging new class of ordered structures, namely the covalent organic frameworks has opened new perspectives for the field. While metal oxide and chalcogenide semiconductors exhibit some intrinsic limits in terms of synthetic flexibility, COFs can be designed using a myriad of chemical structures to obtain ordered materials with improved visible light absorption, high specific surface area, and well-defined porosity. Their application in CO_2 photoreduction is relatively new, and promising results have already been reported by different research groups. Hence, in the next section, an overview of the recent advances in the application of these materials for the CO_2 photoreduction is provided. Emphasis will be given on the correlations

between their photoreactivity and the corresponding chemical structure. The main differences observed between the photochemical behavior of COFs and metal oxide semiconductors are discussed as well.

Covalent Organic Frameworks as alternative CO_2 reduction photocatalysts: Properties, preparation strategies, and challenges

Covalent Organic Frameworks have attracted significant interest since 2005 following the first reports on their crystalline porous nature, their high chemical stability, and their virtually unlimited structural tunability.[63] Comprised of earth-abundant and light-weight elements (C, B, N, O, etc.), COFs are promising candidates for a large variety of applications, such as gas storage,[212-214] molecular separation,[215, 216] energy storage,[217-220] catalysis,[131, 134, 221] and optoelectronics.[222-224] COFs are constructed *via* covalent connections of organic building units (often denoted as linkers) yielding crystalline networks as two- or three- dimensional compounds, depending on the connectivity mode. The slightly reversible nature of the covalent coupling reactions permits the formation of crystalline structures rather than an amorphous polymer, as it allows for error correction and rearrangement of the network by cleaving and reforming connections within the lattice. Planar or nearly planar aromatic molecules promotes the formation of layered materials with 2D molecular sheets. Building units with a 3D spatial character allows for polymerization propagation in all directions, resulting in the formation of 3D networks, which, in some cases, exhibit an interpenetrated structure. 2D and 3D COF networks exhibit well-defined pore openings and dimensions.

The first reported COFs were formed *via* the co-condensation of boronic acids with catechols to form five-membered boronate ester rings as linkages and *via* self-condensation of boronic esters to boroxines.[63] As these linkage types are highly sensitive towards hydrolysis, imine linkages formed by the condensation between aldehydes and primary amines were introduced. Ever since, a growing number of novel linkage types have yielded COFs with improved chemical stability and versatile optoelectronic properties.[223-228] However, it should be noted that several coupling reactions possess a rather limited reversibility, (*e.g.* the formation of sp^2 C-bonds through the Knoevenagel condensation) impeding the formation of highly crystalline structures.[229]

By the rational combination of organic building units and covalent linkage motifs, structural and optoelectronic properties of COFs can be precisely tuned. This remarkably straight-forward “design-follows-function” approach has recently triggered intensive research on COFs as alternative platforms for photocatalysis.[132, 133, 182, 208] The highly ordered organic polymers feature the following advantages: (a) π-stacking interactions between 2D COF sheets facilitate the charge carrier transport along and between COF planes; (b) chromophore building blocks and π delocalization in an extended conjugated structure promote efficient light harvesting; (c) high crystallinity and a high degree of structural order can prevent the recombination of charge carriers; (d) open porous structures and high surface areas enable rapid mass transport and diffusion of molecules as well as access to a high density of catalytically active sites; (e) the aforementioned flexibility in designing COF structures allows for the incorporation of building blocks, comprising heteroatoms (N,S, O etc.), defined binding sites for Lewis acids (typically metal ions) or specific side groups; and (f)

the molecular nature of COFs allows one to conduct fundamental studies on charge carrier kinetics and catalysis, guiding the development of clear atomistic structure-property relationships.

Based on these unique features, COFs have already been tested for the electrocatalytic and photocatalytic CO_2 reduction reaction.[230] The first reported COF-based electrocatalyst for CO_2 reduction was an imine-linked COF comprising a Co(II) porphyrine as catalytic unit,[231] while a Covalent Triazine Framework (CTF) synthesized *via* the condensation polymerization between cyanuric chloride and perylene diimide exhibited photocatalytic activity for the artificial photosynthesis of formic acid from CO_2 in a photocatalyst-enzyme coupled system.[232]

While many excellent review articles are devoted to the application of covalent organic frameworks as photocatalysts, often with a focus on the relationship between structure and catalytic activity of these materials,[130-132,133, 134, 233] only few reports are solely and thoroughly discussing the application of COF-based systems in the photocatalytic CO_2 reduction.[208, 230, 234] Hence, in the second part of this review, we provide an in-depth analysis of the structural parameters affecting the photocatalytic performance of pristine COFs as a CO_2 photocatalyst, followed by a discussion on different methodologies to form COF-hybrid systems comprising metal-based catalysts for enhanced performance.

Pristine covalent organic frameworks

Several pristine COFs have been reported in the literature as photocatalysts for the CO_2RR. Herein, the crystalline and porous framework itself is able to catalyze the reaction, being in some cases supported by

photosensitizers (e.g. $Ru(bpy)_3Cl_2$) and sacrificial electron donors such as triethanolamine (TEOA), triethylamine (TEA) or ascorbic acid (AA). The application of these purely organic systems is pointing towards a more sustainable and green direction of CO_2 utilization compared to modified metalated COF-based catalysts, as there are no secondary environmental effects and no short-term inactivation or loss of the catalytic metal center.[132, 233, 235]

Building units

The rational selection of the building units allows for the precise control over the electronic band structure of COFs and thus their light harvesting efficiency and the thermodynamic driving force for CO_2 reduction. By the incorporation of electron-donor and acceptor heterojunctions, enhanced charge carrier generation, separation and transport can be achieved.[236-240] The combination of light-harvesting chromophores as building blocks such as porphyrins, pyrene or imidazole together with extended structural conjugation enables excellent light absorption of COFs with intrinsic band gaps ranging from about 1.3 eV to 2.9 eV.[241] Often, the band gap of the conjugated structure is similar to the smallest HOMO-LUMO gap of the constituting molecules, confirming the concept of reticular chemistry. However, increasing conjugation within the frameworks leads to a reduction of the COF band gap compared to that of the linkers.[242, 243]

In order to catalyze the CO_2 reduction, the conduction band potential of a COF-based photocatalyst has to be more negative than the reduction potential of CO_2 to the desired product. Introducing heteroatoms (N, S, O) into the COF building units has a significant influence on their electronic donor and acceptor

strength and thus on the electronic band structure of the COF. Hence, regulating the HOMO and LUMO energetic levels of the building units has a direct impact on the thermodynamic driving force for the catalytic reaction.[244] In addition, through the combination of electron-rich (high donor strength, e.g. anthracene, carbazole) and electron-deficient (high acceptor strength, e.g. benzothiadiazole, tetrazine) building units, donor-acceptor heterojunctions within the COF structure can be created. Jakowetz *et al*. applied elaborated transient absorption techniques to reveal that Donnor-Acceptor (D-A) moieties in COFs enable a significant delocalization of excitons across the lattice, thus creating long lived charge carriers with lifetimes of up to tens or hundreds of microseconds.[245]

Several groups have employed the aforementioned strategies to improve the optoelectronic properties of COF-based photocatalysts. Lei and collaborators constructed a carbazole-triazine based donor-acceptor COF, with the carbazole moiety possessing excellent hole-transporting capabilities and the triazine moiety offering high electron drift mobility. The D-A heterojunction within the COF allowed for an efficient HOMO-LUMO separation facilitating the separation of photogenerated electron-hole pairs and promoting intramolecular charge transfer, **Figure 34**.[238] The so-called CT-COF converted CO_2 to CO at a rate of 102.7 μmol g^{-1} h^{-1} and a selectivity of 98% without any additional sacrificial agent, using solely water. As the nitrogen atoms in the triazine ring contribute to both HOMO and LUMO, they are assigned to be the catalytically active centers. Additionally, the heteroatoms stabilize the negative charges effectively, thus prolonging the lifetime of photogenerated electrons. In 2018, Fu *et al.* reported two azine-based COF photocatalysts able to reduce CO_2 in aqueous medium without any photosensitizer or organic sacrificial donor. Both COFs exhibited

improved photocatalytic activity in comparison with the well-known g-C_3N_4 under similar experimental conditions, producing up to 13.7 μmol g^{-1} h^{-1} of CH_3OH.[246]

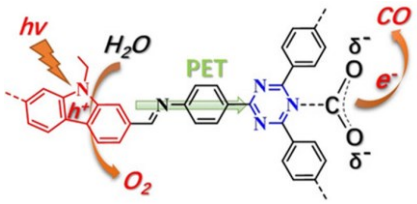


Figure 34. Proposed photoinduced electron transfer from the carbazole to the triazine moiety and the reaction pathway in the photoreduction of CO_2 (PET = Photoinduced Electron Transfer). Reproduced with permission.[238] Copyright 2020, John Wiley and Sons.

An interesting study by Peng *et al.* aimed to rationalize the photocatalytic performance of pristine COFs towards CO_2 reduction as a function of different functional groups in the same host framework. The authors prepared ketoenamine-based COFs TpBD-X, in which X = -H_2, -$(CH_3)_2$, -$(OCH_3)_2$ and –$(NO_2)_2$. The different COFs exhibit similar structural parameters and porosities. However, the electron-donating groups such as - $(OCH_3)_2$ and - $(CH_3)_2$ affect the light absorption and enhance the photogenerated charge carrier separation efficiency. Together with an increase of the conduction band energy (- 1.04 V vs NHE for TpBD-$(OCH_3)_2$ against - 0.81 V for TpBD-H_2), the authors concluded that the implementation of electron-donating groups favors CO_2 reduction.[242] The effect of other functional groups on the performance of COF-based photocatalysts has been also reported elsewhere.[247-249]

Linkage motifs

A compelling approach towards tuning and controlling the electronic interactions and optoelectronic properties within the COF is to vary the linkage

motif which connects the monomers. These linkage motifs differ significantly in chemical stability, conjugation, and flexibility. The first linkage motif employed in a COF was the B-O bond, involving boronate esters and boroxine rings.[63] This linkage motif is moderately stable, yet prone to hydrolysis in acidic and basic conditions, exhibiting limited electronic coupling within the layer as it does not result in conjugated building blocks.[250] Considering charge transport in COFs with limited intralayer conjugation, charge carriers are expected to travel mainly along the stacking direction imposing limits on the charge carrier distribution required for efficient photocatalysis. Yet, the interlayer carrier mobility is generally limited, likely due to a lack of driving force for charge separation between the layers. The imine bond formation *via* the condensation of aldehyde and amine has been established to form highly crystalline COFs with higher chemical stability as well as a conjugation throughout the framework across the linkages.[251, 252]

The conjugation has a direct impact on absorption and optoelectronic properties, offering additional transport paths for charge carriers in the lateral direction. Although imine bonds are still sensitive towards hydrolysis, further stability can be built into COFs by employing a keto-enol tautomerism[253] or post-modifications of the imine bonds.[226, 227, 254] A long-standing goal of the COF research community was reached in 2016 by the first report of a fully sp^2 carbon-conjugated COF, employing the Knoevenagel or aldol condensation as C-C coupling reaction.[223] These sp^2-C COFs with extraordinary chemical stability and extended π-conjugated framework usually yield a narrower band gap material with an improved light-harvesting capability. For example, Xiang *et al.* and Fu *et al.* synthesized sp^2-C COF for CO_2RR with high conjugation and crystallinity, which facilitated the long-range delocalization of electrons and improved the

electron delivery to the catalytically active sites. Both COFs showed conversion rates of over 1000 μmol g^{-1} h^{-1} and selectivity towards CO of over 80%.[68, 255]

Interlayer interactions

The rational choice of building blocks does not only dictate the intrinsic optoelectronic properties but also the structuring ability, as the geometry of these monomers defines different lattices and pore structures. **Figure 35a** shows that in a 2D arrangement the units are stacked through π-π interactions, with a spatial separation between the layers of usually about 3 to 5 Å. The layered structure is an ideal pre-requisite for photo- and electrocatalysts as the columnar π-arrays enhance the light absorption and on the other hand form one-dimensional open channels with predesigned pathways to facilitate both charge carrier and mass transport.[232, 256, 257] Er *et al.* conducted DFT calculations to analyse the electronic properties of a triphenylene donor – benzothiadiazole acceptor COF.[258] The authors studied the dependence of the band structure and carrier effective masses on the number of layers. The study revealed that the experimentally observed high conductivity in layered D-A COFs is a result of enhanced intralayer charge transfer promoted by strong interlayer interactions. The effective mass of charge carriers decreased along the vertical direction as the π- stacking is enhanced.

The very first study of COFs as electrocatalysts for the CO_2RR showed that porphyrin columns integrated into the framework facilitate electron transport from the electrode to the catalytic site.[231] The Co(II) decorated COF-367-Co exhibited a 4.9-fold increased turnover number for the CO_2-to-CO reduction than its monomeric counterpart Co(II) porphyrin, indicating that the π-π stacking of the

COF plays an integral role in the charge carrier separation and transport. However, separated 2D COF nanosheets have also shown significant CO_2 conversion into CO (see next section for details), indicating that intralayer bonding within COFs also contributes to efficient photocatalysis.[259]

Extending the networks into three-dimensional arrangements results in 3D COFs (**Figure 35**). Only very few 3D COF-based photocatalysts have been reported in the literature, as the interpenetrated structure of 3D COFs often impedes the direct use of the backbones as catalytic centers, while the small pore size, usually in the micropore range, limits the scope of catalysts that can be integrated into the pore walls.[132, 260, 261]

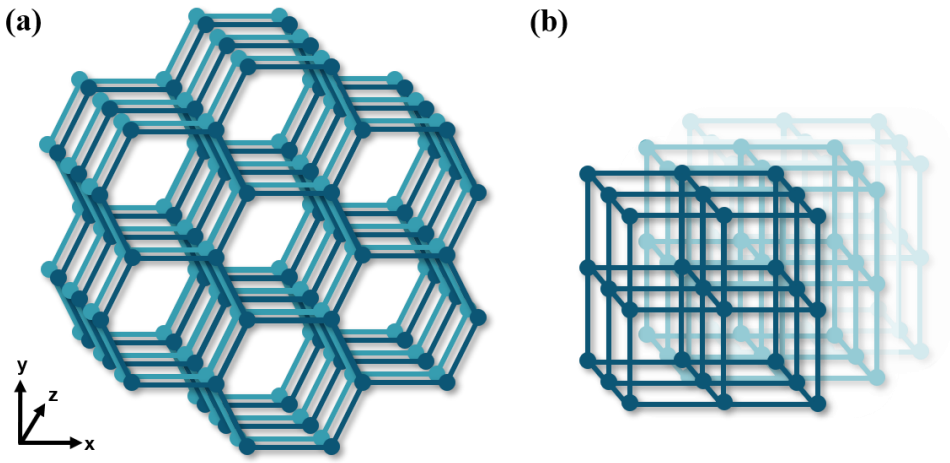


Figure 35. Schematic representation of 2D and 3D COF networks. (a) 2D COFs consist of 2D sheets in the x-y-plane, stacked through π-π interactions in the z-direction. (b) In 3D COFs, the covalent bonds extend in all three spatial directions, often with *n*-fold intercalation.

Crystallinity and porosity

High crystallinity and surface area are imperative for COF-based photocatalysts since such properties enhance the adsorption and diffusion of CO_2 and the as formed inherent channels make promising hosts for guest molecules.

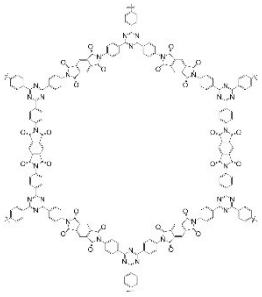
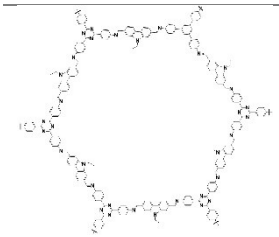
The highly porous nature of COFs also enables high throughput mass transfer and access to a high density of active sites. Several studies have demonstrated that a lack of periodically ordered COF structures leads to a significantly lower CO_2 conversion rate as it directly translates to a lower degree of accessibility of active sites and longer transportation distances of photogenerated charge carriers.[238, 262, 263] The importance of the COF morphology was highlighted by Liu *et al.* who described ultrathin two-dimensional imine-based COFs with Co^{2+} centers. The 2D COF nanosheets were able to promote CO evolution from aqueous CO_2 solution at a rate as high as 10162 μmol g^{-1} h^{-1} and 78% selectivity, while the same photocatalyst as bulk material yielded only 124 μmol g^{-1} h^{-1} of CO under the same experimental conditions.[259] The superior performance of the 2D-COF photocatalyst was attributed for the better CO_2 adsorption capacity, almost twice higher than that for the bulk material, as well as to the improved electron transfer properties since the active Co^{2+} sites are not buried in contrast to the bulk photocatalyst.

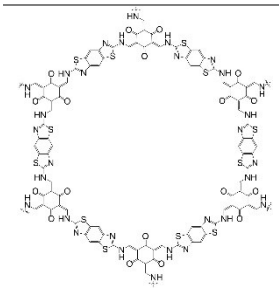
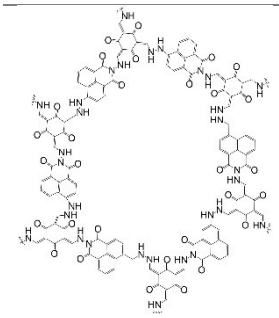
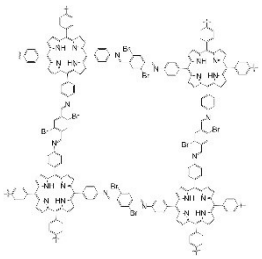
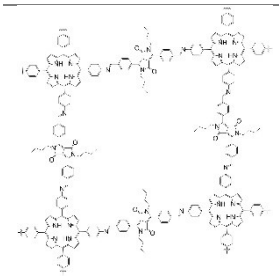
High porosity and large surface areas are favorable for capturing CO_2 and for stabilizing active sites for the photocatalytic CO_2 reduction.[237, 264] Due to dipole-quadrupole interactions, nitrogen heteroatoms in the COF structure have a high affinity towards CO_2 molecules, thus enhancing the gas uptake as well as promoting the selectivity.[265] This aspect is a forefront advantage of COFs in comparison to inorganic semiconductors. Hence, N-rich building blocks (triazine, pyridine, azine) are often employed in COF-based catalysts as well as imine bonds as a linkage motif.[246, 262, 266-268]

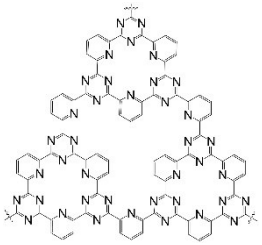
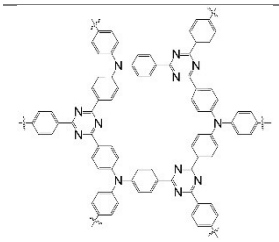
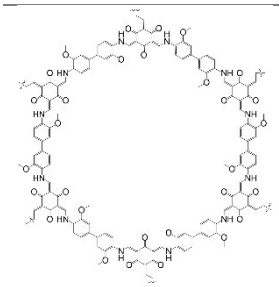
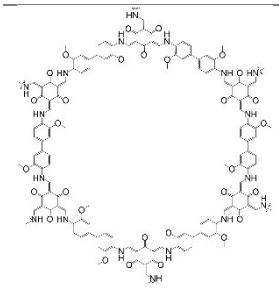
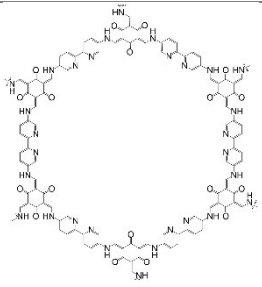
The **Table 6** provides an overview of the relevant pristine COF-based photocatalysts for CO_2 reduction. It should be noted that most COFs exhibit

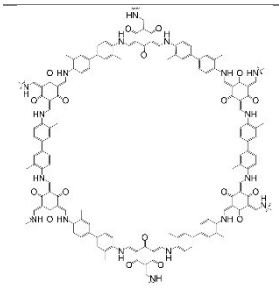
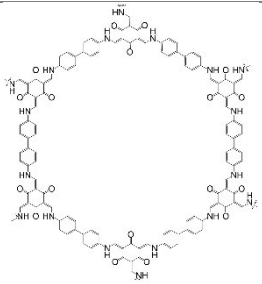
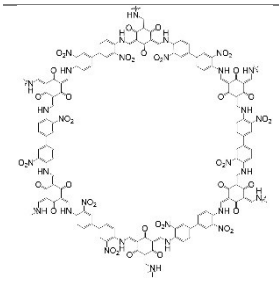
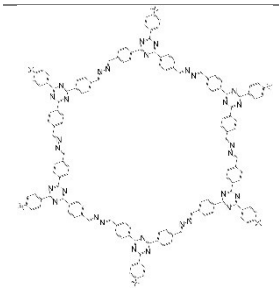
surface areas higher than 500 $m^2 g^{-1}$, values not easily reached for traditional metal oxide semiconductors. Most COFs that have been tested for CO_2RR, are able to perform a two-electron reduction to CO_2, yielding CO or HCOOH. Yet some groups report CO_2 reduction by four, six or eight electrons yielding formaldehyde, methanol or methane, respectively.

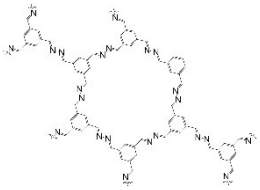
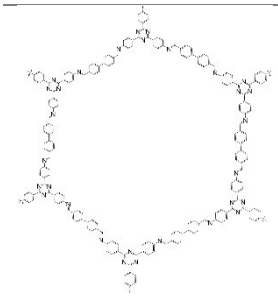
Table 6. Relevant examples of pristine COFs applied for CO_2 photoreduction.

COF	Surface area ($m^2 g^{-1}$)	Conversion rate (μmol $g^{-1} h^{-1}$)	Main product (selectivity)	Sacrificial agent/ solvent	Light source	Ref.
 **PI-COF-TT**	825	483	CO (93%)	TEOA / CH_3CN - H_2O	780 mW cm^{-2} (Xe) 200 to 800 nm	[265]
 **CT-COF**	521	102.7	CO (98%)	H_2O	300 W (Xe) > 420 nm	[238]

 **TpBb-COF**	913	89.9	CO (99%)	H_2O [a]	40 W (LED) >420 nm	247
 **NAHN-Tp**	138	88.6	CO (98%)	TEOA / CH_3CN [b]	300 W (Xe) >420 nm	269
 **TAPBB-COF**	843	26.4	CO (96%)	H_2O	20 mW.cm^{-2} (Xe) 200 to 1000 nm	270
 **PD-COF-23**	181	20.9	CO (99%)	TEOA / CH_3CN - H_2O	300 W (Xe) -	236

 **CTF-py**	1122	13.4	CO (-)	TEOA[c] / CH_3CN	300 W (Xe) 200 to 1100 nm	[268]
 **DA-CTF**	715	4.65	CO (-)	TEOA / CH_3CN [b]	- (Xe) > 420 nm	[271]
 **TFP-DM COF**	421	19.2	HCHO (-)	H_2O	20 $W.cm^{-2}$ (LED) -	[272]
 **TpBD-$(OCH_3)_2$**	388	108.3	HCOOH (-)	TEOA / CH_3CN	300 W (Xe) 420 to 800 nm	[273]
	819	102	HCOOH (-)	TEOA / CH_3CN	300 W (Xe)	[274]

TpBpy					420 to 800 nm	
 **TpBD-$(CH_3)_2$**	406	86.3	HCOOH (-)	TEOA / CH_3CN	300 W (Xe) 420 to 800 nm	[273]
 **TpBD-H_2**	535	45.7	HCOOH (-)	TEOA / CH_3CN	300 W (Xe) 420 to 800 nm	[273]
 **TpBD-$(NO_2)_2$**	259	22.2	HCOOH (-)	TEOA / CH_3CN	300 W (Xe) 420 to 800 nm	[273]
 **N_3-COF**	1412	0.57	CH_3OH (-)	H_2O	500 W (Xe) 420 to 800 nm	[246]

 **ACOF-1**	1053	0.36	CH_3OH (-)	H_2O	500 W (Xe) 420 to 800 nm	[246]
 **Imine-CTF**	602	7.10	CH_4 (-)	TEOA / H_2O	300 W (Xe) >420 nm	[262]

[a]Gas-solid system; [b]co-catalyst; [c]TEOA: triethanolamine.

The application of pristine COF photocatalysts benefits from the high visible light-harvesting efficiency and high CO_2 adsorption capacity. However, COF as a single photocatalyst suffers from sluggish charge carrier separation and transfer to the adsorbed CO_2, thus, the purpose-directed design of COF-based hybrids embedding redox active molecules or nanoparticles is an attractive strategy to promote the photocatalytic efficiency. COFs with their high crystallinity and porosity are ideal templates for the incorporation of catalytically-active centers. Unlike other materials, these centers can be introduced into the framework with atomistic precision, allowing for a rigorous structural control of the heterogeneous catalysts.[230, 275] This unique feature not only enables the synthesis of novel, more powerful hybrid systems, but also opens up new pathways for a deeper understanding of the underlying photocatalytic mechanism. Hence, the combination of COFs with metal-based co-catalysts such

as nanoparticles, complexes or metal oxides is being increasingly adopted to improve the performance of the COF-based photocatalysts. The synergistic effects of COFs combined with metal co-catalysts are discussed in the following section.

COF-based hybrids

The previous section illustrated that pristine COFs with building units containing heteroatoms such as N, S, O can indeed serve as photocatalytic materials themselves. However, the fabrication of multicomponent COF-based hybrid systems is gaining scientific significance due to the synergistic effects between the different classes of materials.[275] The combination of COFs exhibiting high surface area, hierarchical porosity, high chemical stability and enhanced light-harvesting abilities with inorganic co-catalysts yields photocatalytic active hybrids with superior features relevant for applications in photo(electro)catalysis.[230, 275] As the detailed description of the synthetic procedures for COF-based organic-inorganic hybrid systems for the photocatalytic CO_2RR was reviewed by Lu *et al.*, in the following sections we will focus on the features and performance of the corresponding hybrids.[230]

COF/Single metal sites hybrids

Metallic co-catalysts can be integrated into the COF structure using various approaches. A rather subtle path is the use of porphyrin-units as anchors for metal ions. Several studies have demonstrated that COFs containing metalated porphyrins have a much stronger photocurrent response than COFs with metal-free porphyrin rings, indicating a more efficient separation of

photogenerated electron-hole pairs.[67, 236, 276, 277] Porphyrins are also promising alternatives to other complexing building units such as bipyridine or phenanthroline, owing to their strong chelating coordination ability towards metal ions. Implemented in COF photocatalysts, porphyrins can stabilize the active metal centers more efficiently, avoiding metal leaching during CO_2 reduction and subsequent loss of activity.[278] Lu and co-workers reported a Zn-decorated porphyrin COF for the photocatalytic reduction of CO_2 to CO and simultaneous H_2O oxidation to O_2. A conversion rate of 12.33 μmol g^{-1} h^{-1} was reached with a product selectivity of 100%.[67] Further examples are listed in Table 4.

Not only single metal ions but also molecular catalysts can be integrated into the COF structure *via* a coordination approach using functional groups such as bipyridine, anthraquinone, sulfone and others.[249, 279] Key examples of molecular catalysts involve Re(I) and Mn(II) tricarbonyl units, as well as Ni(II), Co(II), Fe(II) and Ru(II) complexes.[265, 268, 279-281] Often, these molecular catalysts undergo detrimental side reactions in solution such as dimerization, triplet-triplet annihilation or other radical deactivation pathways, undermining their catalytic activity over the long term.[282, 283] To overcome such problems, “heterogenization” or hybridization of the molecular catalysts onto suitable solid-state matrices has been proposed, significantly improving their stability and in some cases enhancing their activity as well. Studies suggest that the introduction of metal complexes enhances the intramolecular charge transfer between the COF skeleton and the metal center and inhibits charge carrier recombination.[255, 268, 281] Hence, the incorporation into COFs not only enhances the photocatalytic performance of the molecular catalysts but also prolongs their activity, combining

two necessary aspects for the design of efficient photocatalysts for CO_2 reduction.

Yang *et al.* employed transient absorption spectroscopy and XPS to show the influence of Re(I) on the intramolecular charge transfer (ICT) in a COF photocatalyst.[66] Upon visible light excitation, an ICT state is formed with electrons being transferred from the COF moiety to the Re(I) center. The as-generated ICT state has a much longer lifetime in relation to the MLCT state of the pristine metal complex (171 ps *vs* 200 fs, respectively), allowing for more efficient quenching by the sacrificial donor TEOA to form a $TEOA^+$-$(COF\text{-}Re)^-$ charge separation state. In the presence of CO_2, the reduced $(COF\text{-}Re)^-$ species dissociates a Cl^- ligand to yield CO_2 adducts as typically reported for Re(I) tricarbonyl molecular catalysts (**Figure 36**). The studied COF comprises bipyridine as complexing building block and yields CO under visible light irradiation with a rate of 750 μmol g^{-1} h^{-1} with 98% selectivity. Notably, the hybrid performance is 22 times higher than that for the homogeneous *fac*-$[Re(CO)_3(bpy)(Cl)]$ molecular catalyst under the same conditions. Another COF bearing Re(I) moieties was reported by Fu and collaborators. The sp^2-C linked Re-modified COF showed better charge separation and transfer than the pristine COF, producing CO at a rate of 1040 μmol g^{-1} h^{-1} with 81% selectivity in acetonitrile/TEOA (30:1). Additional incorporation of Pt nanoparticles enabled the production of syngas, *i.e.*, the co-formation of H_2 and CO.

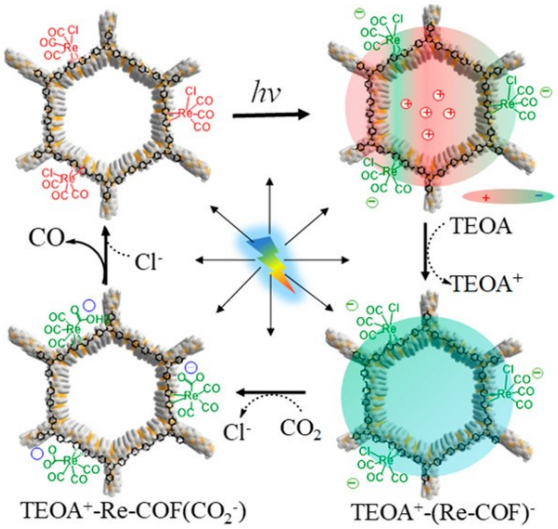


Figure 36. Proposed photocatalytic mechanism for the CO_2 reduction to CO using the Re(I)-decorated COF. Adapted with permission.[66] Copyright 2018, American Chemical Society.

Beyond the incorporation of metal carbonyl complexes, COFs also allow for anchoring other molecular catalysts.[255, 265, 269, 284] Yang *et. al*., for example, reported a 3,3′,5,5′-tetraformyl-4,4′-biphenyldiol-COF (TFBD-COF) modified with a Co^{2+} complex having salicylideneaniline (SA) as auxiliary ligand, Figure 10a. TFBD-COF-Co-SA showed a CO_2-to-CO reduction activity of 7400 μmol g^{-1} in 5 h and a 90% selectivity under visible light illumination in the presence of TEOA as sacrificial agent and $[Ru(bpy)_3]Cl_2$ as photosensitizer. This COF-hybrid performed better than the pristine COF and the TFBD-COF-Co without the auxiliary ligand and showed similar activities as the homogeneous catalyst $[Co(SA)_2]$. The TFBD-COF-Co-SA (**Figure 37a**), however, was considerably more stable than the homogeneous analogue, which evidences the benefits of the heterogenization. The proposed mechanism for the system is shown in **Figure 37b**.[285]

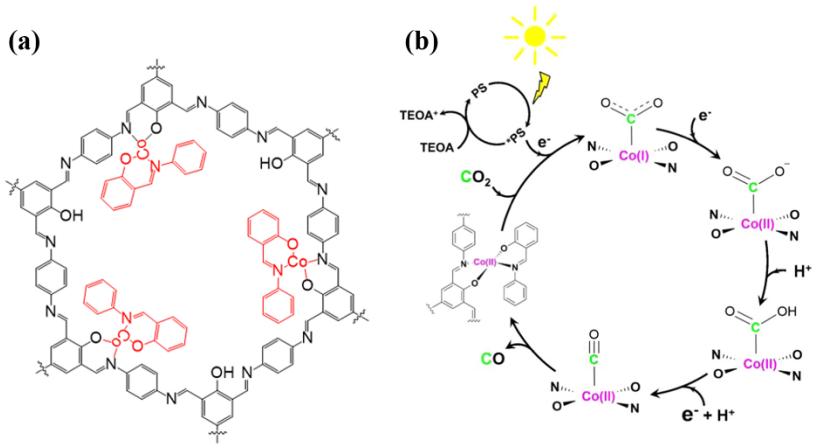


Figure 37. (a) Modified TFBD-Co-SA-COF and (b) proposed mechanism of the photocatalytic CO_2 reduction in the presence of TEOA as a hole scavenger. Adapted with permission.[285] Copyright 2021, American Chemical Society.

COF/metal nanoparticles (NP) hybrids

The use of metal nanoparticles as co-catalysts in photocatalytic systems is an effective approach to suppress recombination of charge carriers. Similar to homogeneous molecular catalysts, metal nanoparticles also suffer from unwanted physicochemical processes under photocatalytic conditions, most prominently aggregation, limiting their storage, processing and further use.[286-288] The spatially controlled incorporation of NP into COF templates promises beneficial synergistic effects, as the restricted space inside the pores of the highly ordered COFs prevents aggregation and promotes a homogeneous distribution of the metal nanoparticles. In terms of sustainability, this is also beneficial as the consumption of precious metals is drastically reduced when combined with COF templates, offering large surface areas and a high accessibility of the catalytic active centers. However, the nanoparticle loading should be monitored carefully, as an excessive amount of nanoparticles can block the pores of the COFs and shield the active sites during the photocatalytic reduction of CO_2. In addition, the

metallic islands can act as recombination centers for photogenerated charge carriers.

In COF/metal nanoparticle hybrids, the generally established mechanism involves the band gap excitation of the COF, followed by electron transfer to the metallic co-catalyst where the CO_2 reduction takes place, as exemplified in **Figure 38**.[289]

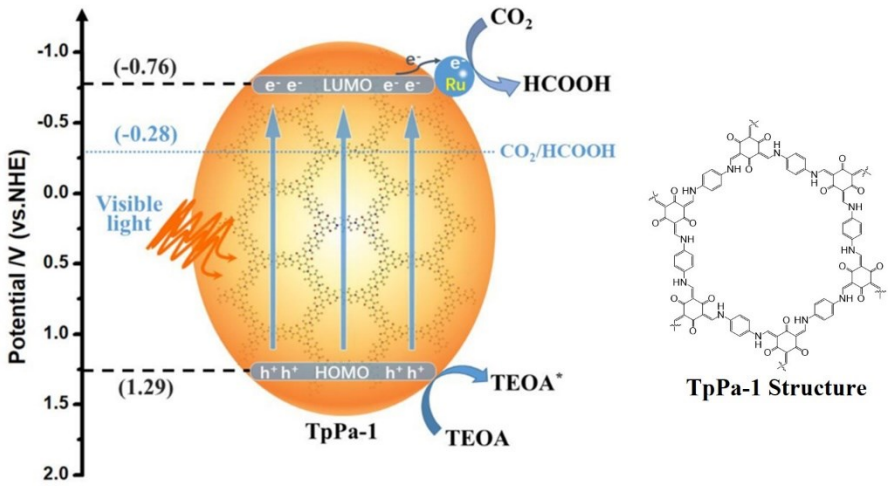


Figure 38. Schematic energy level diagram of a COF (TpPa-1) decorated with Ru nanoparticles for the conversion of CO_2 to formic acid. Adapted with permission.[289] Copyright 2021, Elsevier.

Similar to metal complexes, the incorporation of metal nanoparticles into COF pores can enhance the electron transfer and inhibit the recombination of photogenerated charge carriers. Key examples involve the incorporation of Ru^0 or Pd^0 nanoparticles, leading to the conversion of CO_2 to formic acid or CO, respectively, with traces of CH_4.[262, 274, 289, 290] An in-depth discussion of the product selectivity in COF-based photocatalysts is given at a later point in this review. Further examples involve the application of bimetallic clusters such as Pd_xIn_y@N3-COF composites reported by Huang *et al.* The bimetallic system is more efficient than those employing pristine Pd or In nanoparticles, which is

attributed to the improved electron mobility in the clusters. Moreover, as CO_2 reduction and H_2O oxidation occur simultaneously, the authors report the production of methanol and ethanol with a selectivity of 74 and 26%, respectively.[291]

COF/metal oxide hybrids

An intriguing strategy to create new photocatalysts is the combination of traditional inorganic semiconductors and COFs to form powerful hybrid systems with improved photocatalytic activity and stability.[292, 293] An organic-inorganic Z-scheme heterojunction for artificial photosynthesis was reported for the first time by Zhang *et al.*, who combined semiconductors able to oxidize water (TiO_2, Bi_2WO_6 and α-Fe_2O_3) with CO_2-reductive COFs (named as COF-316 and COF-318, respectively). The highest CO production rate of 69.67 μmol g^{-1} h^{-1} was achieved by the hybrid system COF-318-TiO_2 in a gas-solid system using H_2O as electron donor under simulated sunlight illumination (λ= 380-800 nm) in the absence of any additional sensitizer or co-catalyst. The CO production rate in this system was six times higher than that of the individual components. The covalent coupling between the organic framework and the metal oxide semiconductor is crucial, enabling photogenerated electrons to be transferred efficiently to the organic moiety following the bandgap excitation of the metal oxide (**Figure 39**). Hence, photoexcited electrons and holes accumulate in the COF and the metal oxide, respectively, and are available for simultaneous CO_2 reduction and H_2O oxidation.[248]

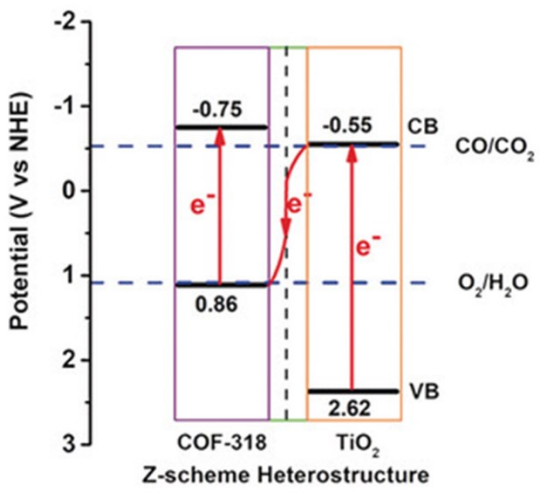


Figure 39. Schematic illustration of the charge carrier transfer in COF-318-TiO_2 under light illumination following the Z-scheme model. Adapted with permission.[248] Copyright 2020, John Wiley and Sons.

The importance of a covalent linkage between the inorganic semiconductor and the COF was highlighted by the work of Xu *et al.* TiO_2 nanoparticles were functionalized with -NH_2 groups for subsequent condensation with -OH sites of the selected COF, resulting in a covalently bonded heterojunction, **Figure 40**. This heterojunction showed a 2.18 times higher photocatalytic activity than the non-covalently bound analogue, due to the improved charge carrier separation and migration. When Co^{2+} ions were added, the hybrid system TiO_2@CTF-Py produced CO at a rate of 43.34 μmol g^{-1} h^{-1}, in aqueous solution and without the addition of photosensitizers or sacrificial electron donors, exceeding the rates of the pristine CTF-Py by 5 and that of TiO_2 by 7 times.[294] The proposed CO_2 photoreduction mechanism involves a Z-scheme, where electrons tend to remain on the CTF-Py surface for CO_2 reduction and holes on the TiO_2 surface for water oxidation. Similar hybrid systems using TiO_2 as inorganic platform have been reported in the literature, showing similar CO generation rates under photocatalytic conditions analogous to the COF-

hybrid systems described above.[290-293] In the **Table 7**, a summary of the photocatalytic activity of COF-based hybrids for CO_2 reduction is presented, including the aforementioned systems.

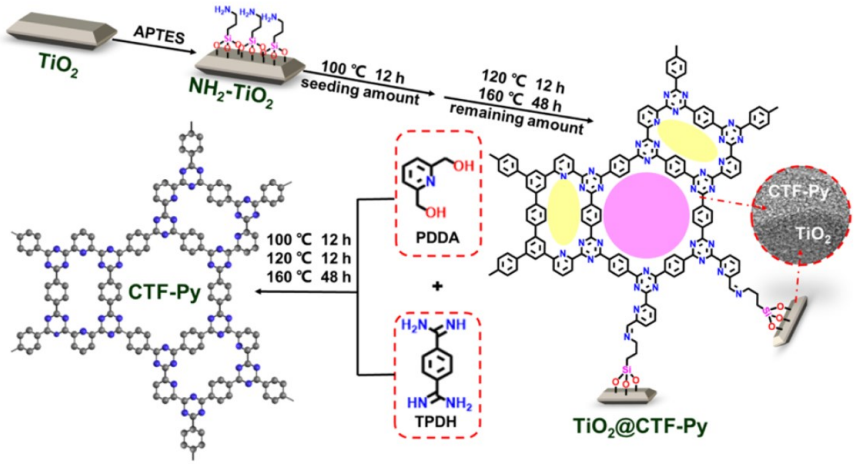
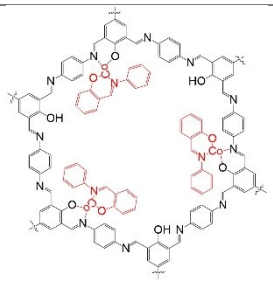
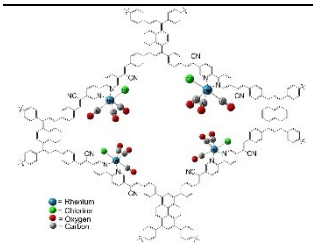
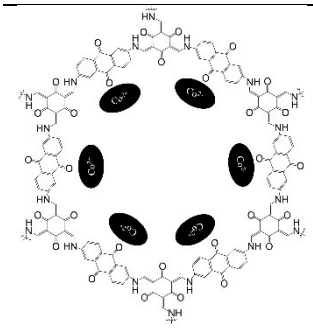
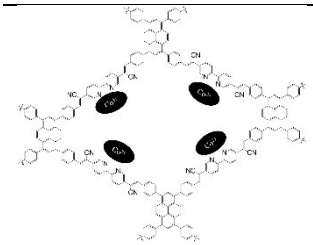
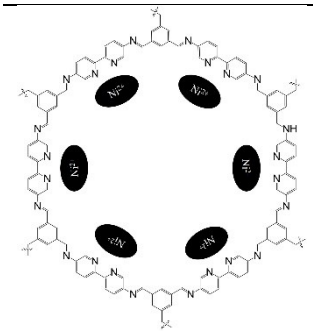


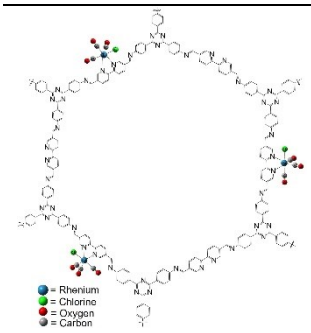
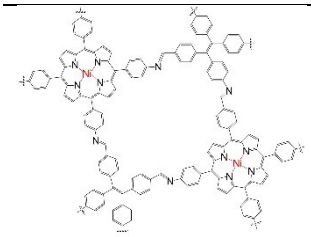
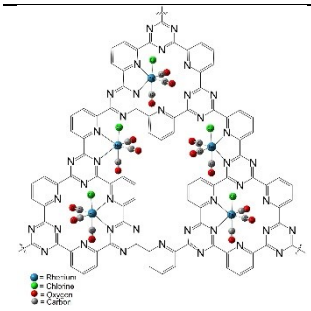
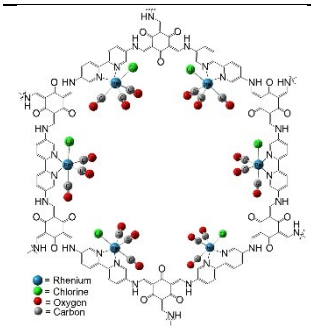
Figure 40. Synthesis route of the CTF-Py COF and the heterogeneous catalyst TiO_2@CTF-Py. Reproduced with permission.[294] Copyright 2021, Elsevier.

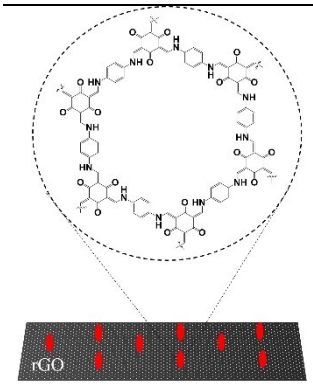
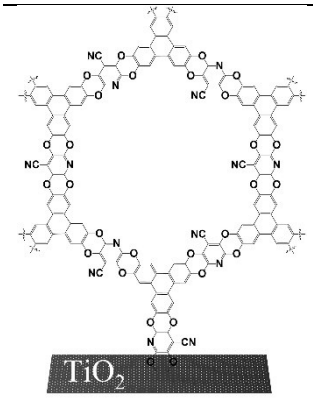
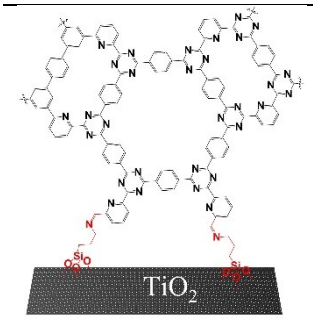
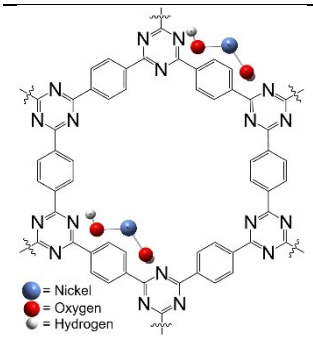
.

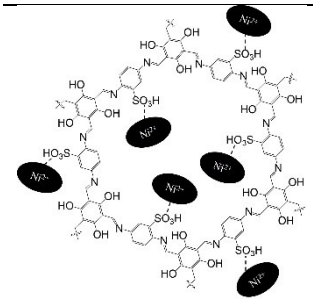
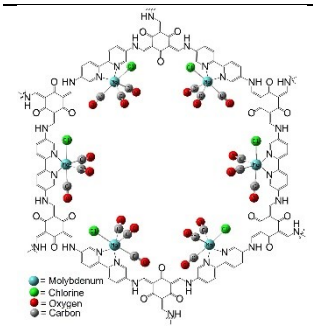
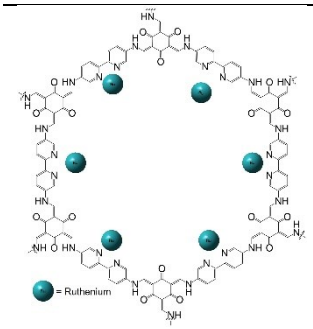
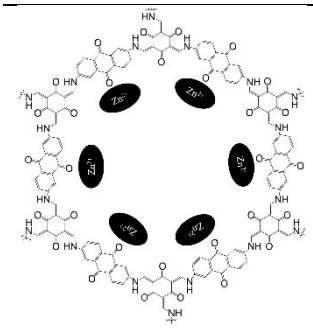
Table 7. Relevant examples of COFs- based hybrids applied for the CO_2 photoreduction.

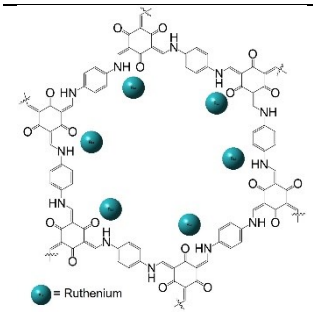
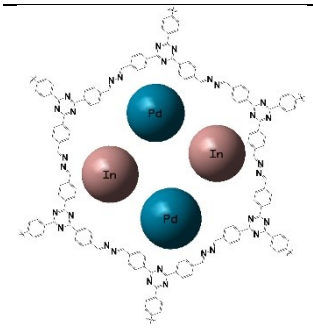
COF	Surface area ($m^2\ g^{-1}$)	Conversion rate ($\mu mol\ g^{-1}\ h^{-1}$)	Main product (selectivity)	Sacrificial agent / solvent	Light source	Ref.
 **TFBD-COF-Co-SA**	560.65	1480	CO (90%)	TEOA / CH_3CN[d]	>420 nm	282

 **Re-Bpy-sp^{2}c-COF**	323	1040	CO (86%)	TEOA / CH_3CN [d]	300 W (Xe) >420 nm	68
 **DQTP-COF-Co**	195.9	1020	CO (59%)	TEOA / CH_3CN [d]	300 W (Xe) >420 nm	279
 **COFdpy-Co**	192.8	1000	CO (81%)	TEOA / H_2O	300 W (Xe) >420 nm	255
 **Ni-TpBpy**	580	811.4	CO (96%)	TEOA / CH_3CN-H_2O [d]	300 W (Xe) >420 nm	249

 **Re-COF**	-	750	CO (98%)	TEOA / CH_3CN	225 W (Xe) >420 nm	66
 **NiP-TPE-COF**	1154	525	CO (93%)	TEOA / CH_3CN-H_2O [d]	300 W (Xe) >420 nm	278
 **Re-CTF-py**	693	353.05	CO (-)	TEOA / H_2O [a]	300 W (Xe)	268
 **Re-TpBpy-COF**	632	283	CO (-)	TEOA / CH_3CN-H_2O	200 W (Xe) >390 nm	280

 **rGOxTpPa-1**	882.4	198.97	CO (89%)	TEOA / CH_3CN [b]	- > 400 nm	293
 **COF-318-TiO_2**	196.3	69.67	CO (-)	H_2O	200 mW cm^{-2} >380 nm	248
 **TiO_2@CTF-Py**	332	43.34	CO (98%)	H_2O	300 W (Xe) >320 nm	294
	7.1	38.66	CO (-)	TEOA / CH_3CN-H_2O [d]	300 W (Xe) >420 nm	290

Ni(OH)$_2$-CTF-1						
 **TTCOF-Ni**	65.6	10.62	CO (95%)	H_2O [d]	400 mW cm^{-2} (Xe) >420 nm	295
 **Mo-COF**	322.8	6.19	CO (-)	H_2O	300 W (Xe) >420 nm	284
 **0.6 wt% Ru@TpBpy**	643	172	HCOOH (-)	TEOA / CH_3CN	300 W (Xe) >420 nm	274
	345.57	152.5	HCOOH (90%)	TEOA / CH_3CN [d]	300 W (Xe) >420 nm	279

DQTP-COF-Zn						
 **3.0 wt% Ru/TpPa-1**	385	108.8	HCOOH (-)	TEOA / CH_3CN	300 W (Xe) >420 nm	[289]
 **PdIn@N_3-COF**	100.5	33.2	CH_3OH (74%)	H_2O	300 W (Xe) >400 nm	[291]

[a]Gas-solid system; [b]co-catalyst; [d]photosensitizer.

Control of product selectivity with COF-based hybrids

A high product selectivity is aimed for an efficient CO_2 photoreduction, favoring the generation of carbonaceous species over H_2 and the simultaneous control over the CO_2-derived product. While the COF structure in heterogeneous COF/metal catalyst systems is key for light harvesting and charge carrier transport, the product selectivity is mainly controlled by the nature of the co-catalyst. Typically, when the metal centers act as π-donors to their respective ligands (*e.g.* Ni^{2+} and Co^{2+} complexes), CO is preferentially formed, while metal centers which act as π – acceptors lead to production of formic acid.[278, 279] The conversion of CO_2 into alcohols is yet more challenging. Huang and collaborators

developed a COF filled with bimetallic PdIn nanoparticles exhibiting dual active sites for the C-C bond coupling, hence, possessing great potential for the photosynthesis of the alcohols.[291] The synergistic effects between COF and nanoparticles facilitated the coupling of key intermediates and subsequent H-electron transfer.

The selective photoreduction of CO_2 in competition with H_2 is greatly dependent on the selective adsorption and activation of CO_2 on the framework or, in the case of modified COFs, on the metal active sites and the special reaction microenvironment.[249, 277] Chen *et al.* conducted DFT calculations, revealing that the adsorption energy of CO_2 on Ni single sites in the presence of polyimide PI-COF-TT was significantly lower than that of H_2O, **Figure 41**.[265] The authors have shown that the hydrogen bonding interactions between the H atoms of the COF structure and the CO_2 molecules reduced the adsorption energy and, hence, promoted CO_2 adsorption and further conversion.

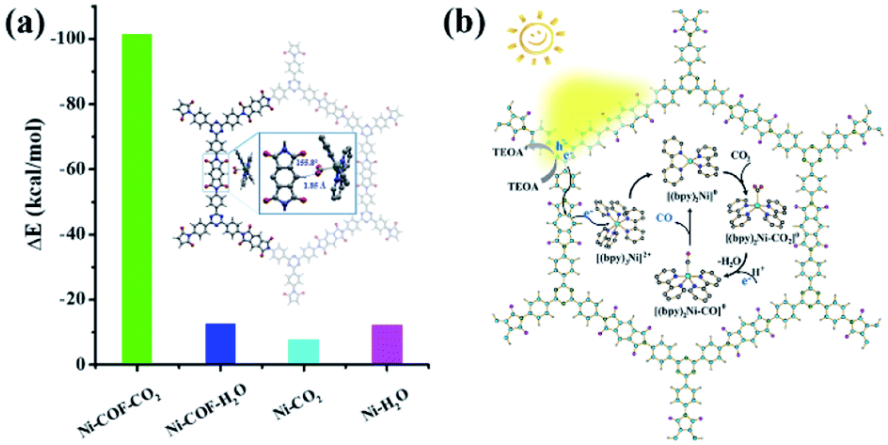


Figure 41. (a) DFT-calculated adsorption energy of CO_2 and H_2O on $[Ni(bpy)_2]^0$ with and without PI-COF-TT (inset: activation of CO_2 by $[Ni(bpy)_2]$). (b) Proposed mechanism for the CO_2 photoreduction over PI-COF-TT. Reproduced with permission.[265] Copyright 2020, Royal Society of Chemistry.

The sacrificial donor, often indispensable for photocatalytic reactions, has rarely been discussed, yet it exerts significant influence on the product selectivity. Among others, typical sacrificial donors for the photocatalytic CO_2 reduction are triethylamine, triethanolamine, and ascorbic acid. To date, the influence of sacrificial donors is not fully elucidated, as many parameters seem to play a role, such as the stability of the molecule under reaction conditions, the pH, the solvent mixture, and the concentration of the sacrificial donor. An interesting discussion about this topic is offered by Pellegrin and Odobel.[296] The polarity, dielectric constant, and metal bonding ability of different solvents and solvent mixtures can also have an effect on stabilizing a specific intermediate products in the photocatalytic process, greatly influencing the product selectivity.[279, 297]

3.2. Conclusions and perspectives

The continuous efforts towards the understanding of the correlation between the photocatalyst's constitution and the fundamental steps involved in the CO_2 photoreduction, namely, light absorption, internal and interfacial charge carrier dynamics, CO_2 adsorption, and reaction with the photogenerated charge carriers have enabled the development of materials with enhanced conversion efficiencies and selectivity. For conventional inorganic semiconductors, control of the surface defects and acidity as well as the formation of heterojunctions were found to be key strategies for the improvement of the light harvesting efficiency, charge carrier separation, and selectivity. Nevertheless, overall efficiency is often limited by the relatively low surface area and the absence of specific CO_2 adsorption sites, which impacts the product selectivity. The modification with metallic and molecular catalysts has improved the electron transfer rates and

selectivity, however, more research is required to overcome mass transport limitations. Additionally, the often-uncontrolled deposition of the metallic catalyst on the surface of inorganic semiconductors reduces the photocatalytic performance and increase the consumption of precious metals.

On the other hand, COFs offer well-ordered crystalline channels for structure-directed modifications with atomistic precision, large surface areas, and high synthetic tunability of structural and optoelectronic properties. These features enable the positioning of the light absorption units close to selected catalytic centers and can thus promote the CO_2 conversion. Moreover, the combination of electron rich and electron deficient linkers creates an internal driving force for efficient charge carrier separation. However, COFs still lack long-term stability under photocatalytic reaction conditions, and the synthesis of their linkers certainly increases the production costs. Further optimization in material design is therefore required to obtain up-scalable photocatalysts able to efficiently contribute to the mitigation of CO_2 emissions. In this context, the development of high-throughput synthesis and screening methods supported by robotic process automation is a promising approach for future COF-based materials development. In conclusion, the novel 2D and 3D COF materials constructed from diverse linkers and building units offer a high potential to become efficient photocatalysts for selective CO_2 reduction

Chapter 4

Unlocking CO_2 Photoreduction with Re(I) Single-Site COF-based Catalysts: Structure-Activity Relationships

.

4.1. Introduction

The excessively high concentration of CO_2 in the atmosphere (~425 ppm) has become a major environmental concern.[298] Carbon capture and storage (CCS) is one of the promising technologies that could be utilized to minimize and/or reduce CO_2 emissions from large industrial sources, such as fossil fuel-based power plants.[299, 300] The photochemical reduction of CO_2 to CO using renewable energy provides a green pathway to syngas and thereby a wide variety of chemicals and fuels via the Fischer−Tropsch process.[301]

fac-[$Re(CO)_3(NN)X$] complexes (where NN = 2,2′-bipyridine derivatives and X = halides) are well known for their (photo)electrochemical selective reduction of CO_2 into CO since the pioneering publications by Hawecker and co-workers in 1983 and 1986.[40, 41] Driven by their promising CO_2 reduction performance, the research has focused on optimizing these catalysts by elucidating the reaction mechanism and correlating the electronic structure with the photophysical and electrochemical properties.[20, 45, 47, 103, 302-305] While *fac*-[$Re(CO)_3(NN)X$] complexes represent an important class of CO_2 homogeneous reduction catalysts, it is well established that their stability is limited by deactivation via dimerization.[108, 118, 124, 125] To circumvent this limitation, several

studies have propose the use of sterically bulky NN ligands.[49, 103, 105, 306] Alternatively, immobilizing the molecular complexes onto solid state supports to create hybrid molecular-solid catalysts offer distinct advantages, as it enhances stability while facilitating both product separation and catalyst recyclability.[62]

Different hybrid CO_2 photcatalyst have been investigated with tricarbonyl rhenium derivatives as catalytic centers.[13, 60, 61, 307-312] While significant progress has been made in achieving high selectivity and stability, the structural environment of the catalytic centers often remains poorly defined such that the spatial orientation of the catalysis is unknown. This lack of atomistic control limits the potential of molecular design for optimizing performance and hinders a comprehensive understanding of the photocatalytic CO_2 reduction mechanism.

On the other hand, Covalent Organic Frameworks (COFs), a class of crystalline polymeric materials made from small molecular building blocks connected through covalent bonds, offer several advantages that include crystallinity, rich pore structure, and enhanced stability.[62, 251, 313] This modular approach allows for the incorporation of well-defined metal binding sites, such as bipyridine or porphyrin units, that effectively confine and stabilize molecular CO_2 reduction catalysts while providing precise structural control over hybrid photocatalysts.[66, 259, 280, 314]

Recently, we reported a rhenium modified 2D COF with well-ordered Re-sites distributed throughout the framework, enabling the design of an efficient hybrid photocatalyst for CO_2-to-CO reduction.[315] However, important aspects such as the influence of catalytic site loading and the catalytic mechanism remain underexplored. Furthermore, despite the literature show few examples of light absorption and charge-separation (CS) in rhenium-modified COFs using

transient optical and X-ray absorption spectroscopy,[66, 314] further complementary studies are needed to clarify the key intermediates involved in the catalytic cycle.

In this work, we investigate a highly conjugated 2D COF (**RebpyPyr COF**) for photocatalytic CO_2 reduction. This COF was synthesized from 1,3,6,8-tetrakis(4-aminophenyl)pyrene (**Pyr**) as a structure-directing building block combined with 2,2'-bipyridine (**bpy**) linker that provides coordination sites for tricarbonyl rhenium centers. The post-functionalized **RebpyPyr COF** was characterized using STEM-HAADF, allowing visualization of the atomistic distribution of the catalytic center within the COF structure. By systematically varying the Re(I) center loading, we aim to understand how it influences the COF structure and show that the COF architecture can accommodate a wide range of catalyst densities while maintaining increasing catalytic activity, thereby establishing a direct relationship between catalyst loading and photocatalytic performance. Photocatalytic experiments reveal efficient CO_2-to-CO conversion and improved operational stability compared with the molecular analogue in fluid solution, highlighting advantages of immobilizing Re catalysts within an ordered porous framework. Furthermore, FTIR spectroelectrochemical investigations provide insights into the CO_2 reduction mechanism.

4.2. Experimental section

Materials. All solvents were purchased from *Sigma Aldrich*, *Acros* or *TCI Europe* in the common purities *purum*, *puriss* or *reagent grade*. The materials were used as received without additional purification and handled in air unless otherwise noted.

Synthesis of bpyPyr COF In a 6 mL Schott-Duran culture tube, a solid mixture of 2,2'-bipyridine-5,5'-dicarbaldehyde, **bpy(CHO)$_2$** (8.5 mg, 0.03 mmol) and 1,3,6,8-tetrakis(4-aminophenyl)pyrene, **Pyr**, (11.3 mg, 0.015 mmol) was suspended in 1000 µL of 1,4-dioxane Subsequently, 100 µL of acetic acid (aqueous, 6 M) was added. The culture tube was tightly sealed and heated at 120°C for 3 days. The resulting suspension was filtered and the isolated orange-red solid was washed with acetone and THF. The final product was Soxhlet-extracted with THF for 3 h.

Synthesis of RebpyPyr COF. The obtained **bpyPyr COF** (30 mg) was refluxed with different amounts of [Re(CO)$_5$Cl] (10wt%, 25wt%, 50wt%, 75wt%, 100wt% and 200wt%) in 15 mL of toluene for 1 h. The resulting dark brown powder was filtered while hot and washed thoroughly with toluene and diethyl ether before drying under vacuum. ICP-OES analysis was conducted to determine the Re content along with their respective occupation of bpy sites (**Table B3**) (see calculation details in the Determination of the number of bpy sites coordinated to Re section).

Synthesis of sacrificial donor. The (1,3-dimethyl-2-phenyl-2,3dihydro-1H-benzo[d]imidazole) structure were prepared as previously reported.[18] First, 2-phenyl-1,3-dimethylbenzimidazolium iodide was obtained from a two-step methylation reaction of 2-phenylbenzimidazole. The solid was reduced in the presence of $NaBH_4$ to yield BIH, respectively. **BIH**: ^{1}H NMR (400 MHz, DMSO-d^6, δ): 7.55 (dd, J = 6.4, 1.9 Hz, 2H), 7.45 (dd, J = 5, 19 Hz, 3H), 6.62 (dd, J = 5.4, 3.3 Hz, 2H), 6.45 (dd, J = 5.4, 3.2 Hz, 2H), 4.87 (s, 1H), 2.48 (s, 6H).

Synthesis of *fac*-[Re(CO)$_3$(bpy)Cl]. The *fac*-[Re(CO)$_3$(bpy)Cl], (bpy = 2,2′-bipyridine) was carried following the procedure reported for other Re(I)

complexes.[92-95] $[Re(CO)_5Cl]$ (0.27 mmol) and the bpy ligand (0.33 mmol) were refluxed in toluene for 3 hours. The mixture was hot-filtered, washed with ethyl ether and the solid was dried under vacuum. Yield: 94%. ^1H NMR (400 MHz, $CDCl_3$, δ): 9.09 (d, J = 5.35, 2H), 8.20 (d, J = 8. 06, 2H), 8.08 (td, 7.97, 7.86, 1.60, 2H), 7.56 (td, J = 6.79, 6.13, 1.26, 2H).

Powder X-ray diffraction (PXRD) measurements were performed using a Bruker D8 Discover instrument with Ni-filtered Cu K_α radiation and a LynxEye position-sensitive detector.

Fourier-transform infrared spectroscopy (FTIR) measurements were performed with a Bruker Vertex 70 FTIR instrument by focusing the light of a globar as a MIR light source through a KBr beam splitter with integrated gold mirrors and an ATR sample stage with a Ge crystal. The spectra were recorded with an N_2 cooled MCT detector at a resolution of 2 cm^{-1} and averaged over 128 scans.

Scanning electron microscopy (SEM) micrographs were obtained with an FEI Helios NanoLab G3 UC microscope equipped with a Schottky field-emission electron source operated at 3 kV.

Transmission electron microscopy (TEM) and scanning TEM in high-angle annular dark-field mode (STEM-HAADF) were performed on a probe-corrected FEI Titan Themis instrument equipped with a field emission gun operated at 300 kV.

Nitrogen sorption isotherms were recorded with a Quantachrome Autosorb 1 instrument at 77 K. **Carbon dioxide sorption** measurements were conducted on a Quantachrome Autosorb iQ at 273 K and 298 K. The samples were outgassed for 24 h at 120°C under high vacuum prior to the measurements.

Pore size distributions based on the nitrogen sorption data were calculated using a QSDFT model with a carbon kernel for cylindrical pores.

Nuclear magnetic resonance (NMR) spectra were recorded on Bruker AV 400 and AV 400 TR spectrometers. Proton chemical shifts are expressed in parts per million (δ scale) and are calibrated using residual non-deuterated solvent peaks as internal reference (e.g., DMSO-d_6: 2.50 ppm).

UV-Vis-NIR spectra were recorded on a Perkin-Elmer Lambda 1050 spectrometer equipped with a 150 mm integrating sphere, photomultiplier tube (PMT) and InGaAs detector. **Diffuse reflectance spectra** were collected with a Praying Mantis (Harrick) accessory and were referenced to barium sulfate powder as 100%R standard. The specular reflection of the sample surface was removed from the signal using apertures that allow only light scatter at angles > 20° to pass. Diffuse reflectance data was smoothed using the LOWESS filter, integrated in the Origin 2022b data analysis software.

Steady-state photoluminescence (PL). PL measurements were performed with a FluoTime 300 from PicoQuant GmbH. The samples were photo-excited using a laser with a wavelength of 378 nm (LDH-P-C-375 from PicoQuant GmbH) pulsed at 500 kHz, with a pulse duration of ~100 ps and fluence of ~300 μJ cm^{-2} per pulse. The PL was collected using a high-resolution monochromator and photomultiplier detector assembly (PMAC 192-N-M, PicoQuant GmbH).

Photocatalytic experiments. For the photocatalytic experiments with COFs, 1.0 mg of photocatalyst and 5.0 mg of BIH was employed in the catalytic reaction. Distilled H_2O or C_6H_5OH (phenol) were used as Bronsted-acids. For catalytic experiments with *fac*-[$Re(CO)_3(bpy)Cl$], an acetonitrile solution containing 2.41 mol L^{-1} was used with 5.0 mg of BIH.

A quartz cuvette with a total volume of 41.5 mL was employed as the photocatalytic reaction and a final volume of 3.5 mL of solvent was used for all experiments, allowing 38 mL of headspace. A Newport Oriel 1 kW Solar Simulator (model 91191-1000; 900 W Xe lamp and LP370/LP420 long pass filter) connected in-line to the sample loop of a gas chromatograph (Agilent GC 8890). Gaseous products were separated with a carbonPLOT column and a molecular sieve column in series. The carbonPLOT column decelerated the elution of CO_2 relative to the other lighter gases (O_2, N_2, H_2, and CO), while the molecular sieves separated each gas with specific retention times. A thermal conductivity detector (TCD) was used to detect O_2, N_2, and H_2. A methanizer, equipped with a nickel hydrogenation catalyst, was paired with a flame ionization detector (FID) to detect CO_2 and CO. Argon (Ar) was used as the carrier gas.

FTIR Spectroelectrochemical (IR-SEC) experiments. ATR-IR-SEC cell containing a **Re bpyPyr COF/**MWNT modified glass carbon working electrode, platinum wire counter electrode, and silver wire pseudo-reference electrode in 0.1 M TBAH/acetonitrile solutions under an Ar/CO_2 atmosphere were employed in the SEC-IR experiments with **Re bpyPyr COF**. The experiment were performed by modifying the glass carbon electrode surface with a conductive suspension of **Re bpyPyr COF/**MWNT (see the details on Glass Carbon modification section) and put in close contact with the ZnSe prism of the ATR instrument, **Figure B10**. A PerkinElmer Frontier spectrometer was used to monitor glass carbon electrode surface coupled with a μAutolab PGSTAT204 potentiostat/galvanostat (Autolab). The spectral region was set to a range from 2060 to 1700 cm^{-1}. A total of 7 scans were co-added for a spectrum with a resolution of 8 cm^{-1} during a cyclic voltammetry with a scan rate of 5.0 mV s^{-1}.

Blank Ar and CO_2 saturated acetonitrile solutions with 0.1 M TBAH were used as background for experiments performed under Ar and CO_2 atmosphere, respectively.

For the Nernst analysis, the IR band intensities were fitted using a Boltzmann-type function (**Equation 12**).

$$y = A_2 + \frac{A_1 - A_2}{1+\exp(\frac{x-x_0}{dx})} \quad (\mathbf{12})$$

where A_1 and A_2 correspond to the limiting values, x_0 is the midpoint potential, and dx is related to the slope of the transition.

Glass Carbon modification. The dispersion was prepared using 1.0 mg of **Re bpyPyr COF**, 1.0 mg of multi-walled carbon nanotubes (MWNT), 20 mL of ionomer (Sustainion® XA-95% in Ethanol, Dioxide Materials Inc.) and 980 mL of acetonitrile. The mixture was submitted to an ultrasonic probe sonicator (Sonics & Materials INC, VCX130) with a power rating of 130 W for 5 min until get a stable dispersion. A glass carbon electrode was modified by drop-casting using 50 mL (5 layers of 10 mL each) of prepared dispersion. Between each 10 mL drop, an interval of 10 minutes was allowed completely modification dry before the next layer drop.

Determination of the number of bpy sites coordinated to Re. ICP-OES analysis was conducted to determine the Re content presented in the **Table B3** along with their respective occupation of bpy sites. The value obtained by ICP-OES is used to calculate the coverage of bpy sites similar to the reported method in our previous paper.[315] Firstly, the molecular weight of the bpyPyr COF is estimated by using a fragment reflecting the 2:1 ratio of the **bpy** to the **Pyr** linker (**Figure 42**).

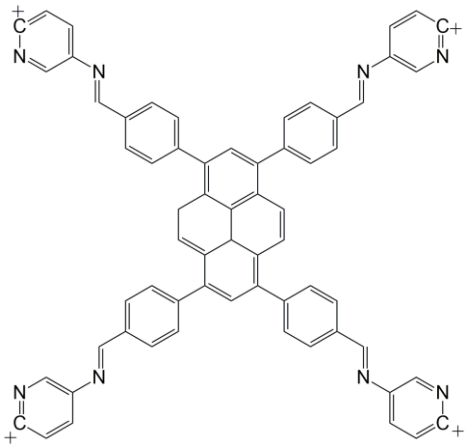


Figure 42. COF fragment reflecting the 2:1 ratio of bpy to Pyr.

The molecular weight of this $C_{64}H_{40}N_8^{4+}$ fragment is M = 921.072 g mol^{-1}. The weight percent of rhenium given by the ICP-OES can be expressed as the following **Equation 13**:

$$bpy\ loading\% = \frac{ICP * M\left(C_{64}H_{40}N_8^{4+}\right)}{M(\mathrm{Re}) - ICP * M(\mathrm{Re(CO)_3Cl})} \frac{100}{2} \quad (\mathbf{13})$$

where ICP is a number between 0 and 1, corresponding to the experimental ICP data (g of Re per g of material). The M(Re) and M(Re(CO)$_3$Cl corresponds to their molar weight of 182.21 and 305.69 g mol^{-1} respectively. The maximum value of bpy sites per fragment are 2 and 100 is used to convert the result to percentage.

4.3. Results and discussion

Structural and morphological characterization of bpyPyr COF and Re bpyPyr COF.

The imine-linked **bpyPyr COF** was synthesized solvothermally via an acid-catalyzed Schiff-base condensation between 2,2′-bipyridine-based (**bpy**) and

pyrene-based (**pyr**) building blocks **(Scheme B1)**. Powder X-ray diffraction (PXRD) of **bpyPyr COF** confirms the formation of an ordered structure **(Figure 43a**), with intense reflections at 2θ = 3.1°, 6.4°, 9.7°, and 12.3° along with a broad diffraction peak centered at 24.2° (2θ), which are attributed to the (001) reflection characteristic of interlayer pp stacking in 2D COFs.[316]

The structure (**Figure 43b**) was further elucidated through structural simulation using Materials Studio 2020 (BIOVIA), and the geometries were optimized using the Forcite module.[317-319] This model consists of two identical layers arranged in a stacked disposition. In this configuration, each bipyridyl sites are pointing toward different pores. As previously shown by Bandomo and co-authors, this isomer is more stable than the one in which bipyridyl groups are oriented toward the same pore.[320] The structural model was Pawley-refined using a triclinic cell (space group P1; a = 28.201 Å, b = 28.226 Å, c = 7.282 Å, and α = 103.2 ° , β = 104.3°, γ = 81.7°), yielding good agreement with the experimental pattern (**Figure 43a)** and consistent with a previous report.[320] Details of the Pawley-refinement are provided in **Table B1.**

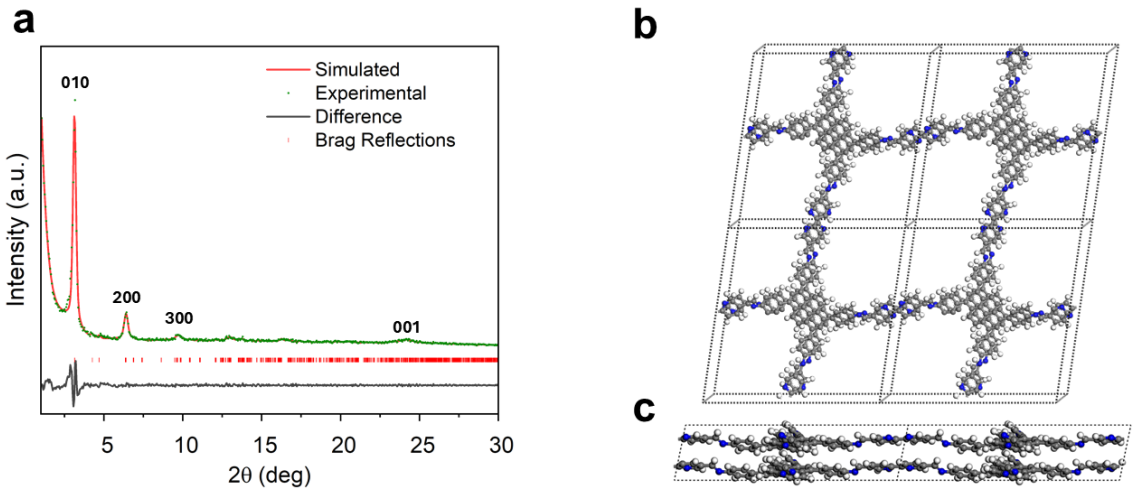


Figure 43. a) Experimental and indexed Pawley-refined PXRD pattern of **bpyPyr** and b) its crystal structure showing the unit cell used for Pawley-refinement and

its c) cross-sectional view. Lattice parameters: a = 28.201 Å, b = 28.226 Å, c = 7.282 Å, α = 103.2°, β = 104.3°, and γ = 81.7°. Powder refinement: R_p = 7.37%.

Immobilization of Re(I) tricarbonyl centers was achieved via post-synthetic modification by refluxing the pristine **bpyPyr COF** with $Re(CO)_5Cl$ in toluene under an inert atmosphere (**Scheme B1**). Fourier Transform Infrared (FTIR) spectroscopy of the resulting material denoted **Re bpyPyr COF,** confirms successful coordination of the Re(I) centers (**Figure B1**). The imine stretching vibration at 1492 cm^{-1} is preserved upon metalation, demonstrating retention of the COF backbone, and additionally, new absorptions at 2025 and 1894 cm^{-1} are observed exclusively for **Re bpyPyr COF** which are characteristic CO stretching modes (A_1 and E, molecular symmetry C_{3v}) evidencing the presence of *facial*-$Re(CO)_3$ units coordinated to bipyridine ligands.[60, 61, 117]

The PXRD pattern of **Re bpyPyr COF** was refined using a structural model containing 50% coverage of bpy sites by $Re(CO)_3Cl$ units and an experimental PXRD pattern obtained from a **Re bpyPyr COF** sample with 57% bpy site coverage, as determined by ICP-OES (see the SI for details on the method for conversion from wt% Re to bpy sites coverage). **Figure 44** shows the obtained Pawley refinement and the corresponding structural model. For the Pawley refinement, the lattice parameters were fixed at a = 28.201 Å, b = 28.226 Å, c = 7.282 Å, α = 103.2°, β = 104.3°, and γ = 81.7°, corresponding to the pristine **bpyPyr COF** structure. Details of the Pawley-refinement are provided in **Table B2.**

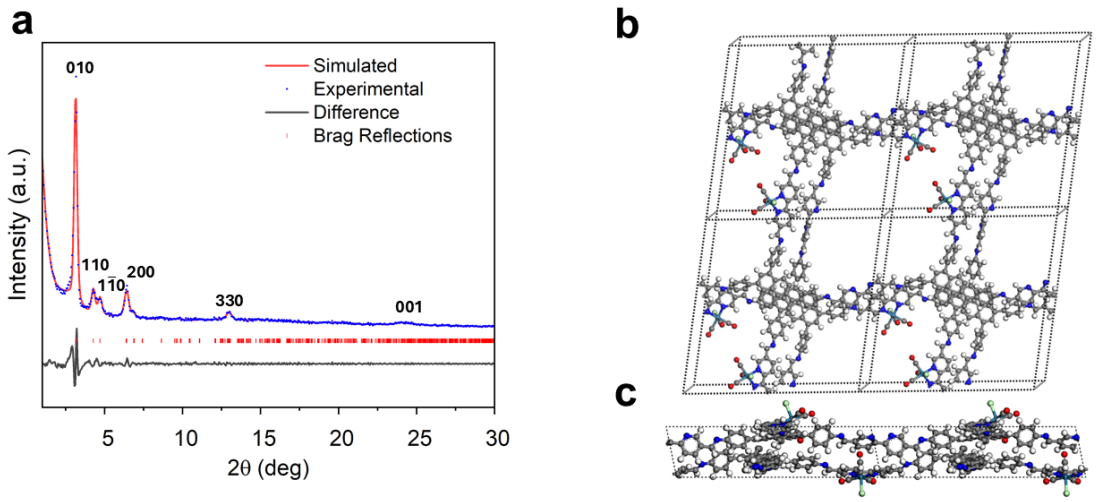


Figure 44. a) Experimental and indexed Pawley-refined PXRD pattern of **Re bpyPyr** and b) its crystal structure showing the unit cell used for Pawley-refinement and its c) cross-sectional view. The experimental PXRD spectrum contains 57% of the bpy sites covered with $Re(CO)_3Cl$ units while the crystal structure contains 50%. Lattice parameters: a = 28.201 Å, b = 28.226 Å, c = 7.282 Å, α = 103.2°, β = 104.3°, and γ = 81.7°. Powder refinement: R_p = 6.59%.

Long-range crystallinity is maintained after metalation, as evidenced by the preservation of the characteristic diffraction peaks of the parent COF. Upon increasing the Re(I) content, new low-intensity reflections emerge at 2q = 4.3° and 13.0°, while the lattice parameters remain essentially unchanged. However, based on the structural optimizations it is observed that the insertion of $Re(CO)_3Cl$ units strongly affects the interlayer stacking organization of the COF backbone, changing from an almost eclipsed arrangement in the pristine COF to a slipped stacking configuration in the Re-modified sample. Considering the large size of the Re atom and the expected bond distances for Re-Cl and Re-CO, neighboring layers separated by 3.641 Å are expected to undergo lateral offset to accommodate the $Re(CO)_3Cl$ units while minimizing steric hindrance. This effect can be better visualized in the cross-sectional view of the **Re bpyPyr COF** structure shown in **Figure 44c**. Furthermore, **Figure B2** illustrates the Miller

planes associated with the new reflections observed after Re modification, as identified from the Pawley refinement. As shown in **Figure B2**, the new reflections are influenced by the presence of $Re(CO)_3Cl$ units and changes in the pyrene-pyrene stacking.

Regarding the stacking nature of 2D COFs, the literature already shows various examples of slight slipped structures being more energetically favorable than the respective eclipsed stacking. Depending on the modification, treatment, or structural design, adjacent layers may become laterally offset, resulting in stacking arrangements that differ from the commonly assumed AA or AB configurations.[321-325]

To corroborate the studies on the structural influence of $Re(CO)_3Cl$ incorporation on **bpyPyr COF**, samples with bpy site coverages ranging from 3% to 85%, as determined by ICP-OES (**Table B3**) and computational models with discrete bpy site occupancies of 25%, 50%, 75%, and 100% were considered (**Figure B3a**). These occupancy levels are dictated by the structural model (**Figure 1b**), which consists of two stacked layers containing four unit cells. Since each unit cell contains two bpy coordination sites, the model provides a total of four equivalent sites available for functionalization. Consequently, only occupancies of 1/4, 2/4, 3/4, and 4/4 can be simulated, corresponding to 25%, 50%, 75%, and 100% site occupation, respectively. For geometry optimization, the unit cell parameters were fixed to those of the pristine **bpyPyr COF** (space group P1; a = 28.201 Å, b = 28.226 Å, c = 7.282 Å, a = 103.2°, b = 104.3°, and g = 81.7°). Based on these optimized models, theoretical PXRD patterns were generated (**Figure B3b**), showing similar trends as experimental data shows (**Figure B3c**). In particular, the simulated patterns reproduce the same reflections

and overall diffraction trends observed experimentally upon metalation, although in the experimental data, a clear loss of crystallinity can be observed at high (>70%) Re(I) loadings.

To better isolate the effect of interlayer stacking on the PXRD pattern, the same structural model presented in **Figure B4a** were recalculated after removal of the $Re(CO)_3Cl$ units while maintaining the slipped layer arrangement (**Figure B4a)** optimized in **Figure B3a**. The resulting simulated PXRD patterns (**Figure B4b**) exhibits reflections similar to those for the Re-modified COFs, with some slight differences. Firstly, no diffraction emerges at 2q = 4.3° in the absence of $Re(CO)_3Cl$ units, despite the layer offset, indicating that this reflection is primarily associated with the presence of $Re(CO)_3Cl$ units. In contrast, a new reflection at 2q = 13.0° appears when the pyrene-pyrene stacking becomes slipped, even in the absence of $Re(CO)_3Cl$ units, showing that the changes in this region are mainly related to the COF interlayer stacking arrangement.

Therefore, the structural modifications affect the PXRD pattern in two distinct ways. First, the presence of the heavy Re atom increases the intensity of the reflection at 2q = 4.3° associated with the (110) plane due to enhanced electron density. Second, the layer slippage induced by $Re(CO)_3Cl$ units incorporation generates the low-intensity reflection at 2q = 13.0° associated with the (330) plane, which is directly related to changes in the pyrene-pyrene stacking organization. Despite these structural rearrangements, the lattice parameters remain essentially unchanged.

Importantly, the exact degree of layer offset is not quantified here, as the experimental loading does not guarantee homogeneous bpy site occupation throughout all layers, unlike the idealized simulated structures. Under

experimental conditions, a perfectly uniform distribution of $Re(CO)_3Cl$ units across all crystallites and layers is unlikely because the post-synthetic modification is performed on the insoluble COF powder, where diffusion and particle agglomeration may limit homogeneous functionalization.

Nevertheless, the data provides important insights into how the incorporation of $Re(CO)_3Cl$ units affects the stacking organization of **bpyPyr COF** and how these changes are reflected in the PXRD pattern. A gradual loss of long-range crystallinity is also observed experimentally, particularly at high bpy site coverages, likely due to increasing structural distortions within the COF pores. Despite this loss of crystallinity, the reflection at 2q = 13.0°, associated with the slipped-layer arrangement, remains clearly observable and becomes increasingly pronounced as the $Re(CO)_3Cl$ units loading increases.

For the following characterizations, only the **Re bpyPyr COF** with 42% of covered bpy sites was used, as it shows a satisfactory Re amount and crystallinity ratio. Scanning Electron Microscope (SEM) analysis (**Figure B5**) of **bpyPyr COF** reveals uniformly shaped spheres with diameters of 1-2 μm covered with star-shaped platelets. Following metalation, coral-like surface features are formed, suggesting morphological modification after incorporation of Re centers.

Nitrogen adsorption measurements (**Figure 45a**) show that the pristine **bpyPyr COF** exhibits a high BET surface area of 1740 ± 174 $m^2 g^{-1}$, which is not significantly changed upon metalation (1800 ± 180 $m^2 g^{-1}$). Pore size distribution analysis (PSD) (**Figure 45b**) evidence a small decrease in the average pore diameter from 2.5 nm (**bpyPyr COF**) to 2.1 nm (**Re bpyPyr COF**), consisting with partial occupation of pore volume by $Re(CO)_3Cl$ units. The porous size for **Re bpyPyr COF** is further confirmed by the STEM-HAADF shown in **Figure 3d-f**.

Furthermore, this trend aligns well with the theoretical pore dimensions derived from the structural model (2.8 vs. 2.3 nm for **bpyPyr COF** and **Re bpyPyr COF**, respectively), supporting successful incorporation of molecular catalytic sites within the COF channels. Importantly, CO_2 adsorption measurements show an enhanced CO_2 uptake for **Re bpyPyr COF** relative to that for the pristine framework (**Figure 45c**), indicating stronger host–guest interactions likely promoted by the $Re(CO)_3Cl$ centers.[315]

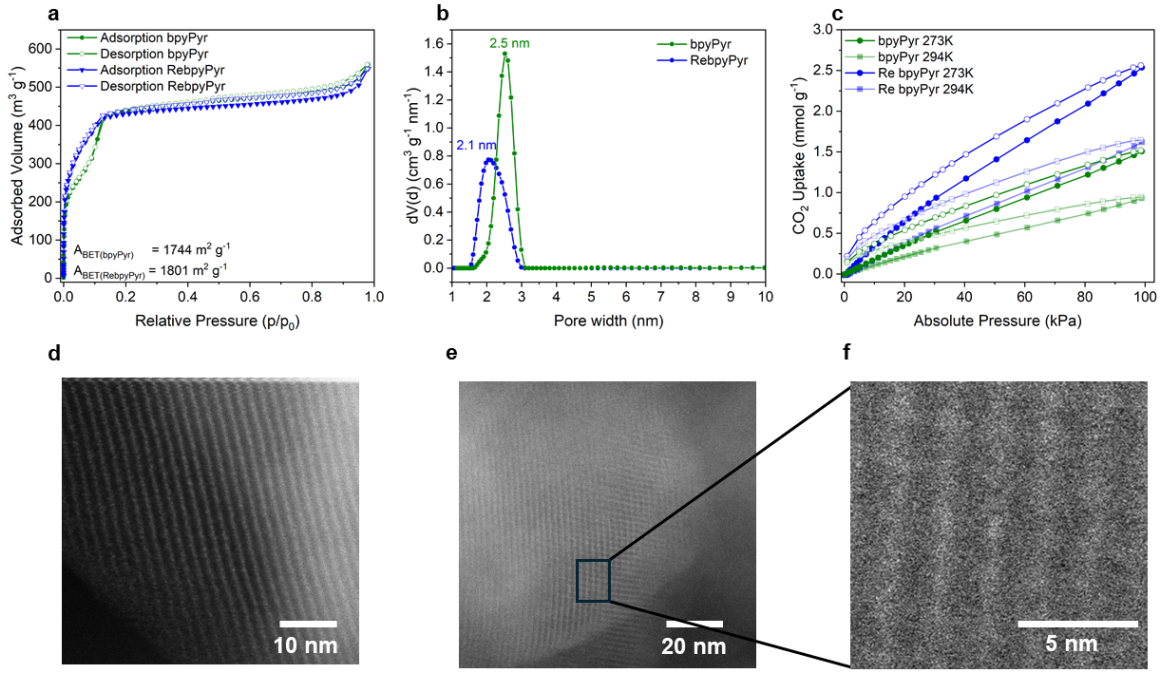


Figure 45. a) Nitrogen sorption isotherms of **bpyPyr COF** and **RebpyPyr COF**. b) Pore size distribution and cumulative pore volume of **bpyPyr COF** and **Re bpyPyr COF**. c) CO_2 sorption isotherms at 273 K (0 °C), indicating enhanced affinity of **Re bpyPyr COF** for CO_2 (filled symbols: adsorption, open symbols: desorption). d-f) STEM-HAADF images of **Re bpyPyr COF** showing the highly ordered Re sub-structure within the COF backbone: d) interlayer distance, e) In-plane lattice spacing, and f) magnified view of (e). The experimental data corresponds to 42% site occupation.

High-Resolution Transmission Electron Microscopy (HR-TEM) allows to experimentally determine d-spacing distances of 28.7 and 28.4 Å for **bpyPyr**

COF and **Re bpyPyr COF**, respectively, corresponding to in-plane lattice spacing (**Figure B6**) consistent with the (100) plane of the triclinic unit cell, which are in very good agreement with their simulated lattice (a = 28.2 Å, b = 28.1 Å and a = 28.0 Å, b = 28.2 Å for **bpyPyr COF** and **Re bpyPyr COF**, respectively). To directly probe the spatial distribution of Re centers, Scanning Transmission Electron Microscopy in High-Angle Annular Dark-Field mode (STEM-HAADF) was employed. Owing to Z-contrast imaging, Re atoms appear as bright atomic-scale features (**Figure 45d–f**). These features are homogeneously distributed throughout the framework. Interlayer separations are also observed consistent with a p-p stacking layered architecture, confirming preservation of the layered structure after metalation (**Figure 45d**).[326] Moreover, the periodic arrangement predicted by the structural model is observed in **Figure 45e-f**, demonstrating homogenous Re site distributions with porous size of 2.1 nm, corroborating with the porous size distribution determined by N_2 sorption measurements. The absence of detectable Re clustering supports site isolation within the COF lattice, a key structural feature for suppressing bimolecular deactivation pathways that are highly relevant to the catalytic behavior discussed below.

Photophysical properties

The optical properties of pristine and Re-functionalized COFs were investigated by UV–vis absorption and photoluminescence (PL) spectroscopies (**Figure 46**). The pristine **bpyPyr COF** exhibits absorption and PL maxima at 476 and 692 nm, respectively. Upon $Re(CO)_3Cl$ units incorporation, **Re bpyPyr COF** displays pronounced bathochromic shifts to 548 nm (absorption) and 808 nm (PL), compared to the pristine COF. In addition, the absorption spectrum

broadens substantially, extending across the entire visible region. Tauc plot analysis, assuming a direct transition (**Figure 46b**), reveals a substantial narrowing of the optical band gap from 2.31 eV for **bpyPyr COF** to 1.75 eV for **Re bpyPyr COF**. This spectral change is consistent with the pronounced color change from bright orange (**bpyPyr COF**) to black (**Re bpyPyr COF**) (**Figure B7**). Such change indicates a significant modification of the electronic structure, resulting in enhanced visible-light harvesting upon metalation.

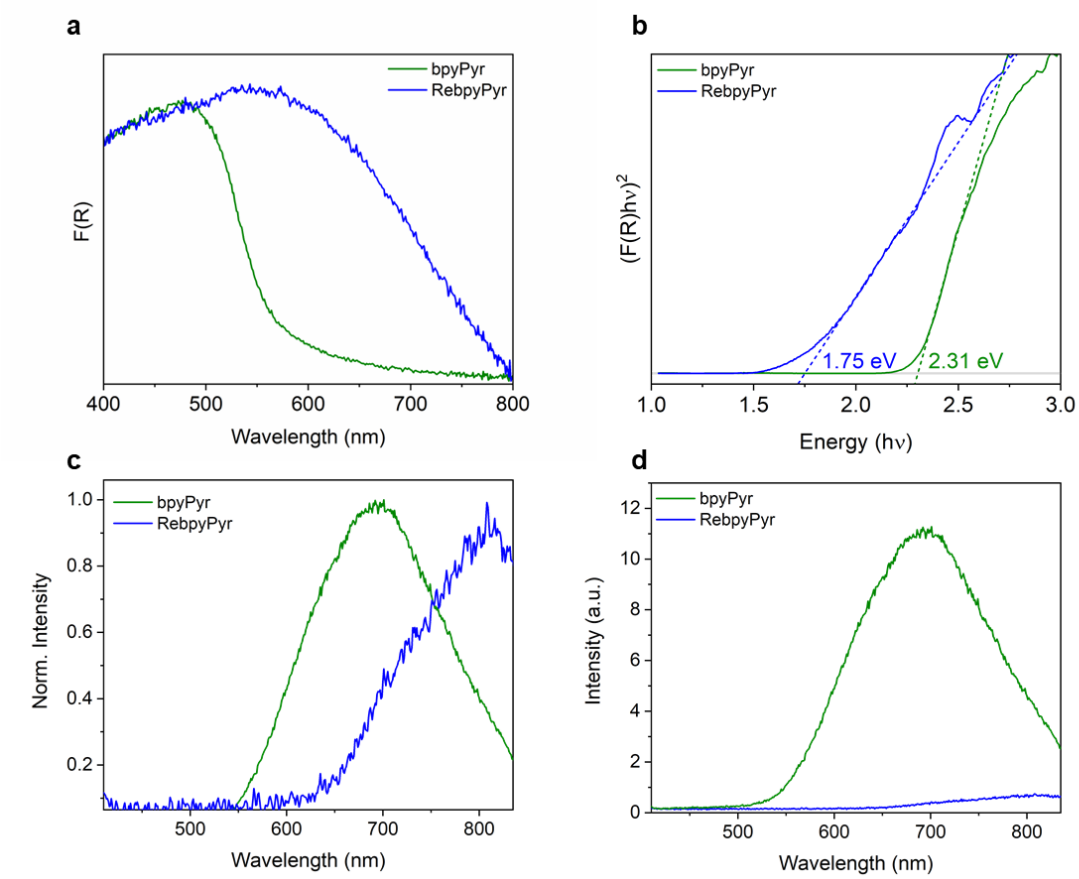


Figure 46. a) The UV-vis absorption spectra, b) Tauc plot analysis, c) PL spectra and d) normalized PL spectra (λ_{exc} = 375 nm) of **bpyPyr** and **RebpyPyr COFs.**

Photoluminescence measurements under same conditions further highlight the impact of metal incorporation. The PL intensity of **Re bpyPyr COF** is strongly decreased relative to the pristine **bpyPyr COF (Figure 46c)**,

consistent with efficient photoinduced charge transfer between the COF backbone and the Re(I)-sites.[315]

Collectively, these results indicate that post-synthetic metalation not only introduces catalytic centers but also significantly alters the photophysical landscape of the COF, promoting enhanced visible-light absorption and facilitating excited-state charge separation, both which are critical for photocatalytic CO_2 reduction.[315, 327]

Photocatalytic CO_2 Reduction

Photocatalytic CO_2 reduction experiments were conducted using a 300 W Xe lamp solar simulator that provides photon energies l > 370 nm with an irradiance of 100 mW cm^{-2}. Under some conditions a 420 nm long-pass filter was utilized to remove ultraviolet photons. Suspensions of the COF catalyst dispersed in acetonitrile initially containing triethanolamine (TEOA) as a sacrificial donor were irradiated under a CO_2-saturated atmosphere, and gaseous products were quantified by gas chromatography. While CO evolution was absent for photochemical measurements with the pristine **bpyPyr COF**, **Re bpyPyr COF** exhibited clear photocatalytic activity, indicating that the $Re(CO)_3Cl$ moieties act as the catalytic centers for CO_2-to-CO reduction. In addition, no detectable CO was observed for **Re bpyPyr COF** under argon atmosphere. This behavior is consistent with the well-established catalysis of molecular *fac*-$[Re(CO)_3(NN)X]$ (NN = 2,2'-bipyridine derivatives and X = halides) that typically exhibit high selectivity toward CO formation with minimal H_2 production, even in aqueous solutions.[20, 41]

The photocatalytic activity was optimized based on catalyst concentration by evaluating the rate of CO production for 0.3 and 0.6 mg mL^{-1} catalyst concentrations, (**Figure B8a**)**.** The catalytic experiments revealed that, under same experimental conditions, lower catalyst concentrations yield higher CO production rates, with a linear evolution of CO. As the experiments were conducted using catalyst suspension at different concentrations, several factors may contribute to observed behavior. This include particle agglomeration, light scattering, inner filter effects, consumption of sacrificial donor and others.[328-330] Consequently, a catalyst concentration of 0.3 mg mL^{-1} was selected for all subsequent experiments, as it is comparable to values commonly reported in similar studies (see **Table B4** for comparison).[66, 280, 315] Furthermore, post-catalysis FTIR spectra confirmed the persistence of the characteristic imine and CO stretching bands, indicating that both the COF backbone and the $Re(CO)_3$ moieties remain intact during the investigated irradiation time (**Figure B8b**)**.**

Following optimization of the reaction conditions, the influence of Re loading within the framework on photocatalytic CO production was investigated (**Figure 47**). The Re-modified COFs with 3 and 9% Re loading exhibited negligible CO formation under the tested conditions, whereas samples containing 42-85% Re loading displayed progressively higher CO production as the Re content increased. The total CO production after 8 h irradiation, together with the corresponding turnover number (TON), was plotted as a function of the percentage of bpy sites coordinated to $Re(CO)_3Cl$ units (**Figure 47b**).

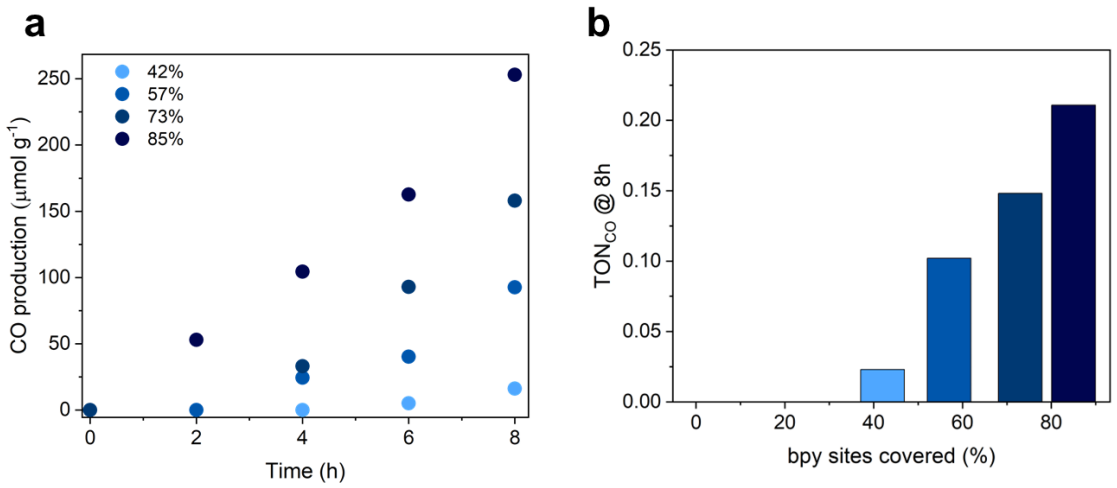


Figure 47. The CO production rate by **Re bpyPyr COFs** with 42-85% Re loadings over 8 hours under illumination with λ > 370 nm. d) Corresponding TON measured after 8 h. Experiments were performed in CO_2-saturated CH_3CN/TEOA (5:1) solutions. The TON were calculated by dividing the amount of CO produced by the actual amount of Re present during the photocatalytic experiments.

A nearly linear relationship was observed between CO production and Re loading in the range of 42-85% site occupation, indicating that a substantial fraction of the incorporated Re centers remains catalytically active within this loading regime. Interestingly, the TON values also increased with increasing Re loading. This trend demonstrates that enhanced catalytic performance cannot be solely attributed to the larger number of immobilized Re centers, as the catalytic efficiency per Re site also improves at higher loadings.

Notably, it is also clear from the TON values that the catalytic performance is limited by light scattering and aggregation. Such phenomena point out to the need to improve the COF dispersion in the reaction medium. As discussed above, PXRD analysis and structural simulations indicate that increasing Re loading progressively modifies the interlayer stacking, inducing lateral offset between adjacent COF layers. Such structural rearrangement may enhance the accessibility of catalytic sites by reducing steric constraints associated with the

nearly eclipsed stacking arrangement of the pristine framework. Enhanced TON suggests that structural reorganization of the framework plays an important role in determining the catalytic performance of the Re-modified COFs.

Previous studies on hybrid catalysts featuring *fac*-[$Re(CO)_3(bpy)Cl$] centers have documented that metal complex loading density significantly impacts the resulting TON. For example, Marinescu and Kubiak demonstrated that high catalyst loading on heterogenous supports causes a decrease in TON_{CO}.[4, 331] This trend is likely due to increased intermolecular interactions and the formation of inactive dimers, which represent the primary deactivation pathway for *fac*-[$Re(CO)_3(bpy)Cl$]. In contrast, our study shows that the COF accommodates high catalyst loading preventing detrimental dimerization and leading to an increase in catalytic performance with catalyst density. We attribute this behavior to the site isolation of catalytic centers within the highly ordered COF structure. Supporting this conclusion, Bandomo and co-authors reported the suppression of dimerization as a deactivation pathway for tricarbonyl manganese complexes immobilized within a COF structure.[320]

The choice of sacrificial electron donor (SED) proved critical to the framework's performance.[18, 74] Experiments using triethanolamine (TEOA) as SED resulted in modest CO production rates. However, Imidazole derivatives have received increasing attention in literature as sacrificial donors for CO_2 photoreduction reaction since the first report of Ishitani et. al. [74] Upon substituting TEOA with 1,3-dimethyl-2phenyl-2,3-dihydro-1H-benzimidazole (BIH), we observed a marked enhancement in catalytic activity. **Re bpyPyr COF** containing 42% of bpy sites coordinated to $Re(CO)_3Cl$ moieties was selected for catalytic assays using different SEDs. The CO production rate reached 389 μmol g^{-1} h^{-1},

corresponding to a 60-fold enhancement relative to the initial experiments using TEOA (**Figure 48a**). This enhancement is attributed to the stronger reducing power of BIH compared to TEOA (BIH, E_{ox}= 0.57 V *vs*. SHE; TEOA, E_{ox} = 1.06 V vs. SHE)[74] enabling more efficient quenching of the excited states of **Re bpyPyr COF** and facilitating access to the highly reducing Re site required for CO_2 activation.

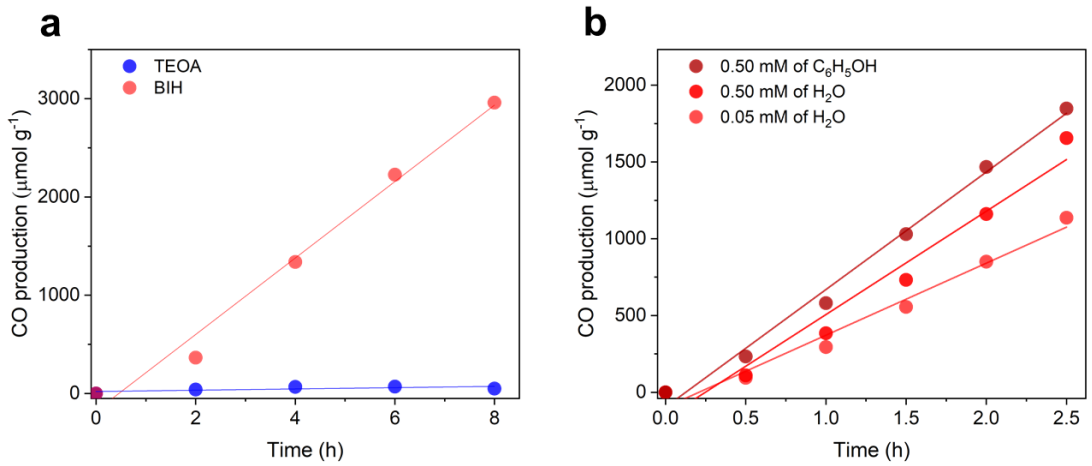


Figure 48. a) Photocatalytic CO production rates of **Re bpyPyr COF (42% occupancy of bpy sites)** using TEOA versus BIH as SEDs. b) Impact of protic additives such as 0.05 mM water and 0.50 mM phenol on the CO production rates. . All experiments were performed in CO_2-saturated CH_3CN/TEOA (5:1) or CH_3CN/BIH (6.7 mM of BIH) under illumination with λ > 370 nm.

Beyond the choice of sacrificial donor, the influence of proton activity on catalytic performance was investigated. Numerous studies have demonstrated that the addition of weak Brønsted acids (e.g. H_2O (pK_a = 26.6), and phenol, C_6H_5OH, (pK_a = 21.6) to the catalytic medium significantly enhances CO_2 reduction rate, a behavior attributed to the stabilization of intermediates, and to the acceleration of the C-O bond cleavage.[302, 332] To investigate the influence of additional protons sources on **Re byPyr COF system**, photocatalytic

experiments were performed with H_2O (0.05–0.50 mM) or phenol (C_6H_5OH) (0.50 mM) (**Figure 48b**). The introduction of these Brønsted acids led to a systematic increase in CO production rates. The highest activity was achieved with phenol reaching a CO production rate of 765 μmol g^{-1} h^{-1}. In contrast, the addition of 0.05 and 0.50 mM of water yielded rates of 469 and 673 μmol g^{-1} h^{-1}, respectively.

Long-term photocatalytic experiments were performed under two different illumination regimes: white light excitation which includes ultraviolet and visible light (l > 370 nm) and only with visible light excitation (l > 420 nm) (**Figure B9**). Under UV conditions, **Re bpyPyr COF** was more efficient but demonstrated lower long-term stability. In contrast, CO formation under visible light illumination was sustained for up to 16 hours. These photocatalytic results are comparable to those reported Re-hybrid-COFs for CO_2-to-CO reduction (**Table B4**).

To evaluate the COF efficacy in suppressing the undesired dimerization of *fac*-[$Re(CO)_3$(bpy)Cl], the performance of the Re-functionalized COF was compared directly to its molecular analogue. To ensure a rigorous comparison, experiments were conducted under identical reaction conditions using equivalent concentrations of catalytic sites. Both systems were tested under broad-spectrum excitation (including UV) and visible-light-only regimes to assess how the framework enhances the stability of the molecular complex. **Figure 49** shows the TON_{CO} for Re-functionalized COF and its molecular analogue over a 20 hours reaction period.

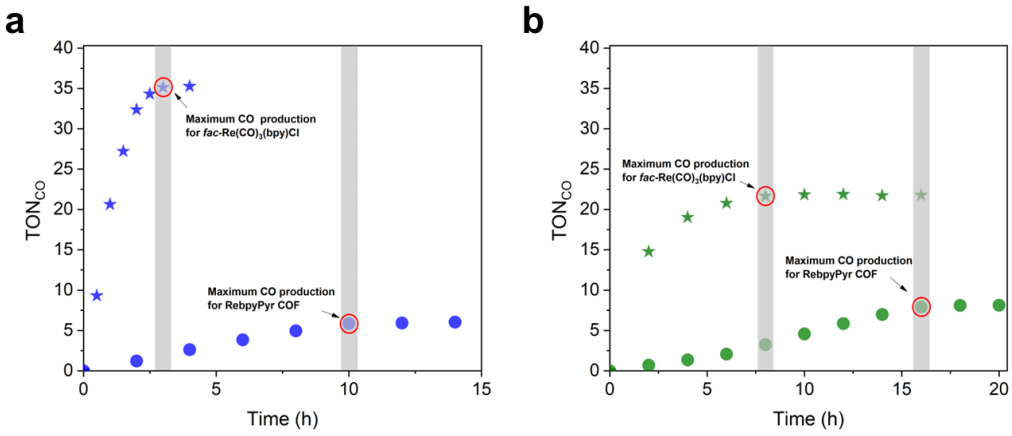


Figure 49. The TON_{CO} values of **Re bpyPyr COF** (circles) and *fac*-[$Re(CO)_3(bpy)Cl$] (stars) under white light illumination with a) I > 370 nm and illumination at b) I > 420 nm with BIH as sacrificial donor. The highlight regions show the maximum TON for *fac*-[$Re(CO)_3(bpy)Cl$] and **Re bpyPyr COF** for their respective illumination condition. Experiments were performed in CO_2-saturated CH_3CN/BIH (6.7 mM of BIH). To ensure a rigorous comparison, experiments were conducted using 0.84 mmol of catalytic sites for both **Re bpyPyr COF** and *fac*-[$Re(CO)_3(bpy)Cl$] complex.

The molecular catalyst *fac*-[$Re(CO)_3(bpy)Cl$] exhibited significant CO evolution for only the first 3 hours under I > 370 nm illumination (**Figure 49a**). Under visible light excitation (I > 420 nm), CO evolution was extended to 8 hours, though this was accompanied by a decrease in TON_{CO} values from 35 to 22 (**Figure 49b**). The higher TON observed during UV illumination compared to visible light, is attributed to the higher absorbance of the complex in the UV region relative to that in the visible region (**Figure B10**).

In contrast, the **Re bpyPyr COF** displayed no significant change in TON_{CO} values when switching from UV to visible irradiation, highlighting the role of the COF as a photosensitizer enabling efficient electron transfer to the Re(I) centers. In addition, **Re bpyPyr COF** exhibited enhanced operational stability, sustaining CO evolution for up to 10 hours (I > 370) and 16 hours (I > 420 nm). These results indicate that immobilization of *fac*-[$Re(CO)_3(bpy)Cl$] units within the ordered COF

architecture improves catalytic stability, most likely by suppressing bimolecular deactivation pathways such as Re-Re dimerization, which are well established as a primary deactivation mechanism in homogeneous *fac*-[$Re(CO)_3(NN)Cl$] systems.[20, 118, 124, 125]

The TON_{CO} values of **Re bpyPyr COF** were lower than that measured for the molecular analogue. This behavior is attributed to heterogeneous dispersion effects, including partial particle agglomeration in suspension, which can limit CO_2 access to active sites.[333, 334] Overall, these results highlight that the ordered COF architecture enables high densities of accessible Re catalytic centers while suppressing bimolecular deactivation pathways, leading to improved photocatalytic stability and efficient CO_2 reduction.

Mechanistic studies

Catalytic cycle for CO_2 to CO conversion has been extensively characterized for molecular *fac*-[$Re(CO)_3(bpy)Cl$ and its analogs using Fourier-Transform Infrared spectroelectrochemical (IR-SEC) measurements. This techniques monitors the characteristic CO stretching modes (A_1 and E, molecular symmetry C_{3v}) associated with the molecular symmetry of the complex under applied bias.[114, 117] Because carbonyl band frequencies are sensitive to the electronic environment of the metal center, governed by p back-bonding between the metal and the carbonyl ligands, they serve as reliable spectroscopic markers to identify key intermediates during the CO_2 catalytic cycle.[109, 115, 335] However, a fundamental question remains: does the rhenium complex operate via the same mechanism when embedded within a rigid COF structure. To address this, we designed a customized three-electrode attenuated total reflectance infrared

spectroelectrochemical (ATR-IR-SEC) cell to probe the catalytic mechanism(s) of the heterogeneous system in-situ. A **Re bpyPyr COF**/multiwall carbon nanotubes (MWNT) film deposited on a glassy carbon served as the working electrode and was placed in close contact with a ZnSe ATR crystal and a reference and a counter electrodes (**Figure B11**). In typical experiments the CO stretching frequencies were monitored during cyclic voltammetry (CV) measurements at low scan rates of 5 mV s^{-1} (**Figure 50**).

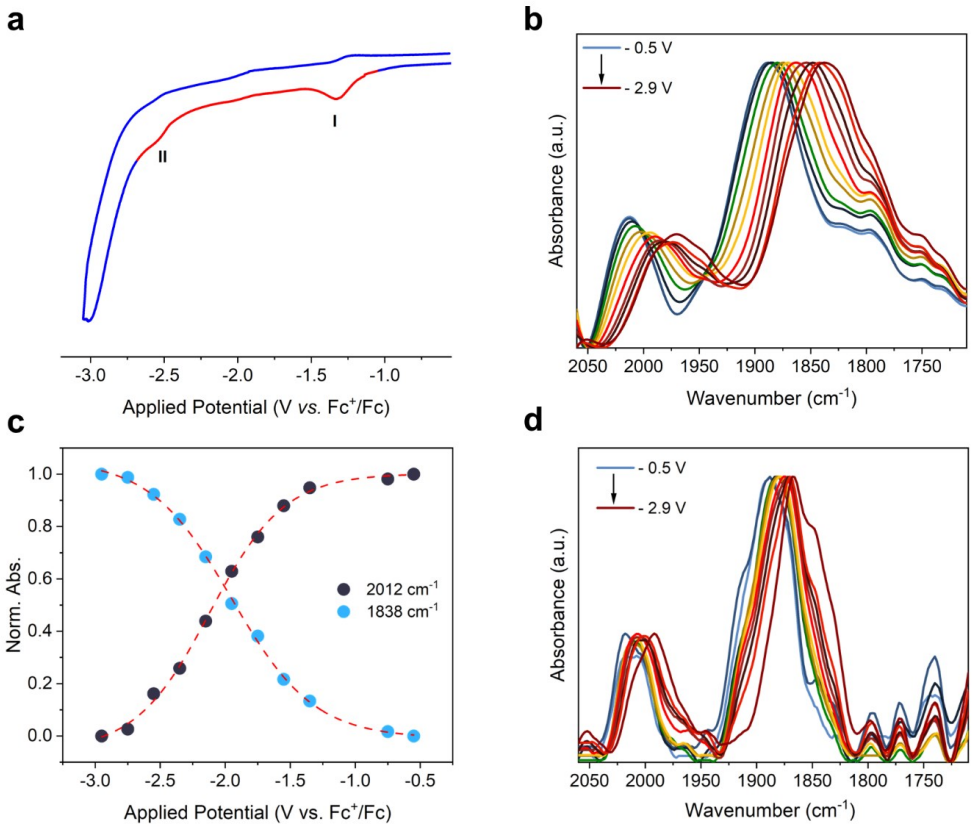


Figure 50. a) Cyclic voltammogram measured at a scan rate of 5.0 mV s^{-1} where I and II are the first and second reductions for **Re bpyPyr COF**. b) ATR-IR-SEC spectra of **Re bpyPyr COF** under an Ar atmosphere at the indicated potentials. c) A plot of the absorption measured at 2012 and 1838 cm^{-1} as a function of the applied potential. Overlaid on the data are fits to a modified Nernst equation. d) ATR-IR-SEC spectra measured under a CO_2 atmosphere at the indicated potentials. All potentials are reported *vs*. Fc^+/Fc (E_0 = 0.400 V *vs*. SHE) and all measurements were performed in a 0.1 M $TBAPF_6/CH_3CN$ electrolyte.

Cyclic voltammograms of the **Re bpyPyr COF** (**Figure 50a**) revealed only slights differences relative to the molecular analogue *fac*-[$Re(CO)_3$(bpy)Cl] complex (**Figure B12**). For the molecular complex, the first reduction is ligand based (E_{onset} = - 1.47 V vs Fc^+/Fc) and initiates chloride labilization. At more negative potentials, a metal-centered reduction forms the two-electron reduced species observed at E_{onset} = - 2.61 V vs Fc^+/Fc.[102-105] Therefore, for **Re bpyPyr COF**, we attribute the observed first reduction peak to a ligand-metal based reduction (E_{onset} = - 1.15 V vs Fc^+/Fc), i.e., the reduction of the bridging Re(I)-coordinated bipyridine units in the COF, followed by the metal-centered reduction creating the two-electron reduced species (E_{onset} = - 2.47 V vs Fc^+/Fc). Compared to the *fac*-[$Re(CO)_3$(bpy)Cl] complex, both potentials are more positive, likely due to stabilization of the ligand p orbitals within the extended conjugated **bpyPyr COF** structure.

During the electrochemical reduction of **Re bpyPyr COF**, the CO stretches shift from 2012 and 1888 cm^{-1} for the initial species to 1970 and 1838 cm^{-1} for the reduced species, respectively (**Figure 50b**). These results are consistent with the behavior reported for *fac*-[$Re(CO)_3$(bpy)Cl] derivatives, where reduction increases electron density at the Re center and enhances p-backbonding to the CO ligands, resulting in lower frequences.[109, 115]

Extensive IR-SEC studies by Kubiak and Fujita independently on *fac*-[$Re(CO)_3$(NN)Cl] (where NN = diamines ligands) have shown that the successive formation of one-and two-electron reduced species is accompanied by characteristic vCO shifts within the 2025 to 1860 cm^{-1} regium.[124, 125] These results also identified the formation of Re-Re bonded dimers, $[Re(CO)_3(NN)]_2$, generated following chloride dissociation and coupling of reduced monomeric species. The

resulting dimers exhibit four terminal carbonyl stretching modes distributed between approximately 1840 and 2000 cm^{-1}.[16, 18]

A Nernst analysis (**Figure 50c**), in which the relative intensities of selected IR bands were monitored as a function of the applied potential, allows correlation of spectral changes with redox processes and identification of the potential range where interconversion between species occurs. The potential-dependent evolution of the IR band intensities was fitted using a Boltzmann-type function (**Equation 12**). The extracted midpoint potentials (X_0) for the initial and reduced species are in reasonable agreement (**Table B5 and B6**), although a slight offset is observed, suggesting that the redox process is not a simple two-state equilibrium but may involve intermediate species or kinetic contributions. Moreover, while the expected dx (slope) values for a one- or two-electron process in an ideal Nernstian system are 25.7 and 12.9 mV, respectively, the obtained dx values (286 and 314 mV) are significantly larger.[336] This deviation from ideal Nernstian behavior indicates a distribution of redox environments or overlapping processes, consistent with the heterogeneous nature of the COF-based catalyst. Furthermore, monitoring the initial (2012 cm^{-1}) and final (1838 cm^{-1}) species reveals significant changes between -1.5 and -2.7 V *vs.* Fc^+/Fc corresponding to the potential window highlighted in red in **Figure 50a**.

From the IR-SEC experiments performed with the **Re bpyPyr COF/**MWNT modified electrodes, it is clear that the **Re bpyPyr COF** exhibits the same spectral shift trends along the reduction pathway as those observed for the molecular *fac*-$[Re(CO)_3(bpy)Cl]$ complex.[118, 124, 125] Therefore, we conclude that the reduction pathway in **Re bpyPyr COF** is centered on the $Re(CO)_3Cl$ moiety, proceeding through the formation of the pentacoordinated one-electron reduced species (*fac*-

[$Re^0(CO)_3(bpy)$]) and the two-electron reduced species (*fac*-[$Re(CO)_3(bpy)]^-$) between -1.5 and -2.7 V *vs.* Fc^+/Fc. The formation of the dimeric species *fac*-[$Re(CO)_3(bpy)]_2$ cannot be definitively ruled out due to the limited spectral resolution of the IR-SEC experiments performed with **Re bpyPyr COF/**MWNT modified electrode. However, it should be severally hindered due to the spatial separation of the catalytic centers within the **bpyPyr COF** structure.

Under a CO_2 atmosphere, a similar trend is observed upon the application of cathodic potentials (**Figure 50d**). However, the low-energy peaks at 1970 and 1838 cm^{-1}, attributed to the two-electron reduced species, do not accumulate under CO_2 as they do under Ar atmosphere. This behavior likely arises from the rapid reaction of the reduced species with CO_2, preventing detection under these experimental conditions.[337, 338] This observation further supports that the two-electron reduced species act as the active catalyst for CO_2 reduction.[49, 108, 123]

Taken together, the ATR-IR-SEC experiments indicated that the $Re(bpy)(CO)_3$ unit acts as the catalytic site in **Re bpyPyr COF**. The mechanism for CO_2 reduction closely resembles that of molecular *fac*-[$Re(CO)_3(bpy)Cl$] catalysts while benefiting from the spatial organization imposed by COF framework. Based on these observations, a catalytic cycle involving the discussed intermediates is proposed, **Figure 51**. Importantly, the catalytic mechanism proposed here is derived from spectroelectrochemical measurements, where reduction of the catalyst is achieved electrochemically. Under photocatalytic conditions, the same reduced species may be generated through photoinduced electron transfer with the sacrificial donor. Previous studies on *fac*-[$Re(CO)_3(bpy)Cl$] catalysts have demonstrated that electrochemical and photochemical pathways produce the same key intermediates, differing mainly in

the mode of electron delivery [20]. Consequently, the intermediates identified here by IR-SEC are expected to accurately represent the key species involved in the photocatalytic CO_2 reduction cycle.

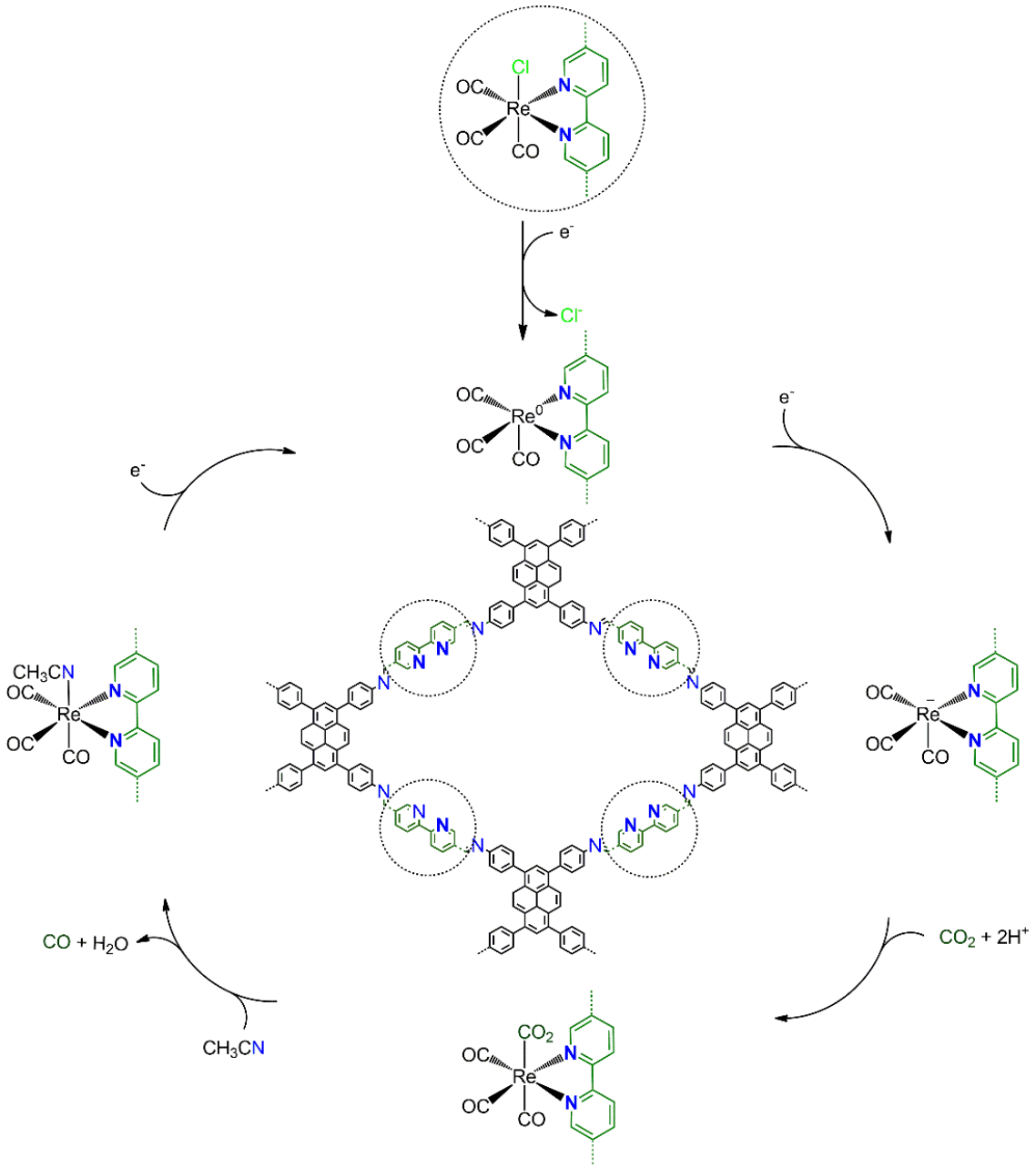


Figure 51. Proposed catalytic cycle for CO_2 reduction for **Re bpyPyr COF**.

4.4. Conclusions

In summary, an imine-linked bipyridine–pyrene COF was successfully functionalized with $Re(CO)_3Cl$ catalytic centers to produce a crystalline hybrid material capable of photocatalytic CO_2 reduction. Structural analysis, including the STEM-HAADF imaging, confirms that the incorporation of the rhenium(I) complex preserves the long-range order of the COF while introducing well-defined catalytic sites throughout the framework. Photophysical measurements reveal electronic communication between the COF backbone and the Re centers, resulting in broadened visible-light absorption and efficient quenching of the COF photoluminescence. Photocatalytic experiments demonstrate that **Re bpyPyr COF** effectively reduces CO_2 to CO under visible-light irradiation, with activity strongly influenced by the choice of electron donor and proton source. Importantly, systematic variation of the Re loading shows how the COF structure is affected and that high catalyst loadings can be utilized without the loss of catalytic activity found in other heterogeneous systems with *fac*-$[Re(CO)_3(bpy)Cl]$. Hence, this COF-based catalyst exhibits improved operational stability that is likely due to spatial isolation of catalytic sites within the ordered framework.

The ATR-FTIR spectroelectrochemical investigations revealed that the reduction pathway of the immobilized catalyst closely resemble that of the molecular analogue, indicating that the intrinsic catalytic mechanism is preserved upon immobilization. At the same time, the COF architecture appears to limit bimolecular deactivation processes that commonly affect homogeneous systems. These findings demonstrate that crystalline COF structures can serve as effective

platforms for organizing molecular catalysts while tuning their catalytic performance and stability. Such hybrid materials represent a promising strategy for the development of efficient and robust photocatalysts for solar-driven CO_2 conversion.

CHAPTER 5

Designing Atomically Precise and Robust COF Hybrids for Efficient Photocatalytic CO_2 Reduction

5.1. Introduction

Photocatalytic CO_2 reduction has attracted growing interest, as it enables direct conversion of CO_2 and solar energy into value-added chemicals.[19, 339, 340] A major breakthrough in this field was the development of the molecular *fac*-$[Re(CO)_3(bpy)Cl]$, where bpy = 2'2' bipyridine, catalyst by *Lehn* and co-workers, which opened a new avenue for designing CO_2 photocatalysts with high precision and molecular control over reactivity.[282] To leverage the tunability of molecular catalysts while addressing their inherent limitations regarding stability, hybrid photocatalytic systems have emerged in which molecular catalysts are immobilized on solid supports such as metal oxides, nanoparticles, carbon nanostructures, and polymeric materials like g-C_3N_4.[341-344] While significant progress has been made with hybrid systems in achieving high selectivity and stability, the structural environment of the catalytic centers often remains poorly-defined, with active sites randomly distributed across the substrate. This lack of atomistic control limits the potential of molecular design for optimizing the catalyst performance and hinders a comprehensive understanding of the photocatalytic CO_2 reduction mechanism.

Two-dimensional (2D) covalent organic frameworks (COFs) have been recognized as a promising platform for designing heterogeneous photocatalysts

due to their virtually unlimited structural, chemical, and optoelectronic tunability.[62, 313] COFs are crystalline porous frameworks built from organic building blocks that are connected *via* strong covalent bonds.[345] The rational design of the building blocks and the linkage motifs results in tailor-made materials with pre-defined features.[251] Specifically, this modular approach allows for the integration of well-defined metal binding sites, such as bipyridine or porphyrin, which can effectively confine and stabilize CO_2 molecular catalysts, thereby facilitating rigorous structural control over hybrid photocatalysts.[314] Furthermore, the choice of COF linkage motifs was shown to modify the microenvironment around catalytic centers and to influence the π-π conjugation and stability of the COFs and thus their performance in photocatalytic CO_2 reduction.[346] Despite these advantages, synthesizing highly crystalline and stable 2D COFs is challenging due to constraints related to reaction conditions and characteristics of the building blocks.[347] Achieving high crystallinity in COFs is essential not only for defining the spatial arrangement of catalytic sites but also for advancing the understanding and molecular design of hybrid photocatalysts.

Here, we introduce a novel 2D COF for photocatalytic CO_2 reduction, utilizing dibenzo[g,p]chrysenetetraamine (DBC) as a structure-directing building block for the synthesis of a highly crystalline and stable COF. For the first time, the detailed X-ray diffraction (XRD) and transmission electron microscopy (TEM) analysis allowed us to resolve the atomistic-level distribution and organization of the molecular catalyst within the COF structure. Additionally, the tight π-π stacking of the COF layers provides exceptional photostability under visible light illumination, maintaining performance for more than 50 hours.

DBC, a planar and rigid monomer with an extended π-conjugated structure, promotes tight, ordered stacking of COF layers with a high degree of conjugation. Imine-linked DBC-based COFs have been demonstrated to feature high crystallinity, as well as excellent thermal and chemical stability, along with long-lived excited states.[22,23] Despite these promising properties, DBC-COFs have not yet been explored for photocatalytic applications.

Here, we combine DBC with 2,2'-bipyridine-5,5'-dicarbaldehyde (bpy), forming the **bpyDBC COF**, **Figure 52**. The bpy unit (linkers) provides docking sites for the immobilization of $[Re(CO)_5Cl]$ yielding a model molecular CO_2 photocatalyst *fac*-$Re(CO)_3(bpy)Cl$ within porous, thereby forming the hybrid photocatalyst **Re bpyDBC** COF.

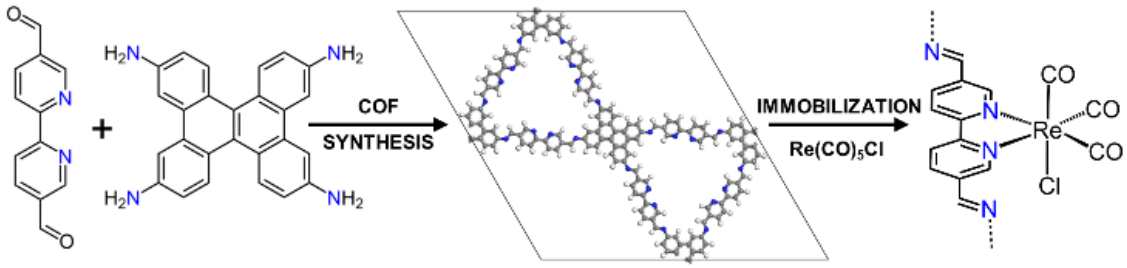


Figure 52. Synthesis of **bpyDBC** COF and immobilization of $Re(CO)_5Cl$, yielding **Re bpyDBC** COF.

5.2. Experimental Section

All solvents were purchased from *Sigma Aldrich*, *Acros* or *TCI Europe* in the common purities *purum*, *puriss* or *reagent grade*. The materials were used as received without additional purification and handled in air unless otherwise noted.

Synthesis of COF linker molecules. The COF linker 2,2'-bipyridine-5,5'-dicarbaldehyde (bpy) was purchased from BLDpharm. Dibenzo[g,p]chrysenetetraamine, (DBCTA) was synthesized according to the

literature. ^{1}H NMR (400 MHz, DMSO-d_6) δ (ppm): 8.15 (d, J = 8.8 Hz, 4H, C(1)H), 7.55 (d, J = 2.3 Hz, 4H, C(2)H), 6.9 (dd, J = 8.8, 2.3 Hz, 4H, C(3)H), 5.39 (s, 8H, NH_2).

Synthesis of bpyDBC COF. In a 6 mL Schott-Duran culture tube, a solid mixture of 2,2'-bipyridine-5,5'-dicarbaldehyde, bpy(CHO)$_2$ (6.38 mg, 0.03 mmol) and dibenzo[g,p]chrysenetetraamine, DBCTA (5.84 mg, 0.015 mmol) was suspended in 500 µL 1,4-dioxane and mesitylene (250 µL each). Subsequently, 50 µL of acetic acid (aqueous, 6 M) was added. The culture tube was tightly sealed and heated at 120°C for 4 days (**Scheme C1**). The resulting suspension was filtered and the isolated brown powder was Soxhlet-extracted with THF for 8 h, followed by extraction in supercritical CO_2 at 110 bar and 40°C for 1 hour.

Synthesis of RebpyDBC COF. BpyDBC COF (30 mg) and [Re(CO)$_5$Cl] (14.65 mg, 0.04 mmol) were dispersed in 15 mL toluene and heated to reflux for 40 min. The resulting dark brown powder was filtered hot and washed thoroughly with methanol. The resulting powder was dried under vacuum. ICP-OES analysis was conducted to determine the Re content to 15.87 ± 0.43 wt%, which equals an occupation of bpy sites of 43.5 ± 2.7 %. The percentage of bpy sites occupied by Re(CO)$_3$Cl is calculated based on the following considerations:

To estimate the molecular weight of the COF, a fragment reflecting the 2:1 ratio of the bpy to the DBC linker is considered (**Figure 53**). The molecular weight of this $C_{50}H_{28}N_8^{4+}$ fragment is M = 740.83 g mol^{-1}.

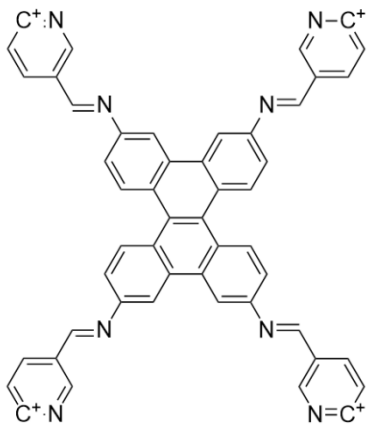


Figure 53. COF fragment reflecting the 2:1 ratio of bpy to DBC.

The weight percent y of rhenium given by the ICP-OES can be expressed as the following **Equation 14**:

$$y = \frac{x * M(\mathrm{Re})}{M(\mathrm{C_{50}H_{28}N_8^{4+}}) + x * M(\mathrm{Re(CO)_3Cl})} \quad (\mathbf{14})$$

where x is a number between 0 and 2, corresponding to the number of immobilized Re-complexes per fragment (max. value = 2, since only two bpy sites are available per fragment). A 100% coverage of the two available bpy sites of the fragment translates to two additional $Re(CO)_3Cl$ compounds, each with a weight of M = 305.69 g mol^{-1}, thus $x = 2$ in the equation. Insertion of the corresponding molecular weights (M(Re) = 182.21 g mol^{-1}) yields a value of $y = 0.269$, or 26.9 wt% for a 100% coverage of the bpy sites with Re-complex.

In reality, the value obtained by ICP-OES is used to calculate the coverage of bpy sites. For example, ICP-OES measures 16.2 wt% Re in the sample of interest. Replacing $y = 0.162$ in the above equation and solving it for x yields a value of $x = 0.878$. Applying the rule of three,if $x = 2$ corresponds to 100%, then $x = 0.878$ corresponds to coverage of 43.9% of the bpy sites.

Synthesis of sacrificial donor. The benzimidazolidine derivate, BIH (1,3-dimethyl-2-phenylbenzo[d]imidazolidine) was synthesized as previously reported.[348] H NMR ($CDCl_3$ 400 MHz) δ (ppm): 7.61-7.53 (m, 2H), 7.45-7.37 (m, 3H), 6.71 (dd, J = 5.4, 3.2 Hz, 2H), 6.43 (dd, J = 5.4, 3.2 Hz, 2H), 4.88 (s, 1H), 2.56 (s, 6H).

Powder X-ray diffraction (PXRD) measurements were performed using a Bruker D8 Discover instrument with Ni-filtered Cu K_α radiation and a LynxEye position-sensitive detector.

Fourier-transform infrared spectroscopy (FTIR) measurements were performed with a Bruker Vertex 70 FTIR instrument by focusing the light of a globar as a MIR light source through a KBr beam splitter with integrated gold mirrors and an ATR sample stage with a Ge crystal. The spectra were recorded with an N_2 cooled MCT detector at a resolution of 2 cm^{-1} and averaged over 128 scans.

Scanning electron microscopy (SEM) micrographs were obtained with an FEI Helios NanoLab G3 UC microscope equipped with a Schottky field-emission electron source operated at 3 kV.

Transmission electron microscopy (TEM) and scanning TEM in high-angle annular dark-field mode (STEM-HAADF) was performed on a probe-corrected FEI Titan Themis instrument equipped with a field emission gun operated at 300 kV.

Nitrogen sorption isotherms were recorded with a Quantachrome Autosorb 1 instrument at 77 K. **Carbon dioxide sorption** measurements were conducted on a Quantachrome Autosorb iQ at 273 K and 298 K. The samples were outgassed for 24 h at 120°C under high vacuum prior to the measurements.

Pore size distributions based on the nitrogen sorption data were calculated using a QSDFT model with a carbon kernel for cylindrical pores.

Nuclear magnetic resonance (NMR) spectra were recorded on Bruker AV 400 and AV 400 TR spectrometers. Proton chemical shifts are expressed in parts per million (δ scale) and are calibrated using residual non-deuterated solvent peaks as internal reference (e.g., DMSO-d_6: 2.50 ppm).

UV-Vis-NIR spectra were recorded on a Perkin-Elmer Lambda 1050 spectrometer equipped with a 150 mm integrating sphere, photomultiplier tube (PMT) and InGaAs detector. **Diffuse reflectance spectra** were collected with a Praying Mantis (Harrick) accessory and were referenced to barium sulfate powder as 100%R standard. The specular reflection of the sample surface was removed from the signal using apertures that allow only light scatter at angles > 20° to pass. Diffuse reflectance data was smoothed using the LOWESS filter, integrated in the Origin 2022b data analysis software.

Steady-state photoluminescence (PL) and time-correlated single-photon counting (TCSPC). A home-built confocal laser scanning microscope (CLSM) setup was used for characterizing the photoluminescence of the COF samples. The samples were measured in the epi-direction using an air objective (0.85 NA, Fluor 40, NIKON). A beamsplitter (MELLES GRIOT 03BTL005) and a 490 nm long-pass filter were utilized to separate the laser from the photoluminescence (PL) light. Excitation was provided by a sub-picosecond laser (iChrome TOPTICA) operating at 476 nm with a repetition rate of 40 MHz. The detection system was divided into two components. The first part featured an avalanche photodiode (APD, type: MPD PDM, with a detector size of 50 × 50 µm), which was used in combination with time-correlated single-photon counting

(TCSPC) electronics (BECKER UND HICKEL) to measure time-resolved PL transients. The second part comprised a spectrometer (ANDOR SHAMROCK SRi303) connected to a CCD camera (ANDOR NEWTON DU920) for capturing spectra. The data were recorded using a customized LABVIEW (National Instruments) program that integrated the manufacturers' software with our specific measurement requirements. Further data processing and analysis, including extracting PL spectra and TCSPC transients, were performed using MATLAB (MATHWORKS).

Thermogravimetric analysis (TGA) measurements were performed using a Netzsch Jupiter ST 449 C instrument equipped with a Netzsch TASC 414/4 controller. The samples were heated from room temperature to 900°C under a synthetic air flow (25 mL min^{-1}) at a heating rate of 10 K min^{-1}.

Cyclic Voltammetry was performed on a Metrohm Autolab Potentiostat using a three-electrode setup with Pt wire as counter electrode, Ag wire as pseudo-reference electrode and slurry-coated FTO glass as working electrode in 0.1M $TBAPF_6$ in acetonitrile. The electrolyte was prepared and stored under Ar. The Ag pseudo-reference electrode was referenced against the ferrocene redox couple. Measured potentials *vs.* the ferrocene redox couple Fc/Fc^+ were converted to the absolute electrode potential (E_{vac}) and to potentials *vs*. Standard Hydrogen Electrode (SHE) according to the following equations (i) and (ii), respectively. Note that the absolute potential scale equals to the negative physical scale. Potentials *vs*. Standard Calomel Electrode (SCE) were converted to potentials *vs.* SHE according to equation (iii).[349] Reduction potentials for the sacrificial donors retrieved from the literature were converted to SHE accordingly.

$$\text{(i)} \qquad E_{vac} = E_{Fc/Fc^+} + 4.8\ \text{eV}$$

(ii) $E_{vac} = E_{SHE} + 4.44\ \text{eV}$

(iii) $E_{SHE} = E_{SCE} + 0.241\text{V}$

Slurries for electrode coating were prepared by dispersing 21 mg of COF material, 4.5 mg Ketjen black and 4.5 mg PVDF (70:15:15) in 300 µL NMP. The mixture was repeatedly vortexed and ultrasonicated until the desired viscosity was achieved. 15 µL of the slurry was then drop-cast onto FTO glass and dried immediately using a heat gun.

Photocatalytic experiments were carried out in a quartz cuvette with a total volume of 5.08 mL. The reactor was loaded with 3.50 mL of acetonitrile, 1.0 mg of photocatalyst and 5.0 mg of BIH. The mixture was then purged with CO_2 until saturation was reached and exposed to a 300 W Xe lamp equipped with a water filter and a 370 or 400 nm long-pass filter. At given time intervals, 100 µL of the headspace atmosphere was sampled to quantify the amount of produced CO using a gastight syringe and analyzed using **Gas chromatography** (GC) (Shimadzu GC2014), equipped with a flame ionization detector (FID) and a methanizer. A PerkinElmer Clarus 580 – GC-TCD was employed to check potential H_2 production.

Stability experiments were conducted under the same conditions as the photocatalytic experiments. After 24 h, the COF powder was removed from the reaction suspension *via* filtration, washed with small amounts of THF and subsequently dried under vacuum.

Gas Chromatography-Mass Spectrometry (GC-MS). To reveal the carbon source in the photoreaction product, namely carbon monoxide (CO), ^{13}C isotope labelled CO_2 gas (Sigma Aldrich, 99 atom % ^{13}C, < 3 atom % ^{18}O) was used in the photocatalytic reaction following the same procedure described

above. In this case, a gas sample (500 μL) from the headspace of the cuvette was analysed by GC-MS Shimadzu QP2020-NX with electron ionisation (EI) equipped with a U-Bond column (30 m, ID 0.32 mm) for $^{13}CO_2$ separation and a Molsieve 5A column (30 m, ID 0.32mm) for ^{13}CO separation without N_2 interference. The standard gas mixture of CO_2, CO, CH_4, O_2, and N_2 as balance (All-in-gas GmbH) was used to set the instrument method and to identify the analytes' retention times (RT). The characteristic ions at RT_{CO} = 6.7 min with m/z 29 ($^{13}C^{16}O$), 28 ($^{12}C^{16}O$), 16 (^{16}O), and 13 (^{13}C) were detected in single ion monitoring mode (SIM). Shimadzu Postrun Data Analysis software was used to process the data.

5.3. Results and discussion

The synthesized **bpyDBC** COF was structurally analyzed using powder X-Ray diffraction (PXRD) and FTIR, **Figure 54a-b.** The experimental PXRD pattern, showing sharp reflections at 2.2°, 3.9°, 4.5°, 6.8°, 8.5°, 9.0° and 11.3° *2θ*, confirms the crystallinity of the pristine COF. The diffraction peak at 25° corresponds to the (001) plane, which is attributed to the π- π stacking of the as-formed structure.

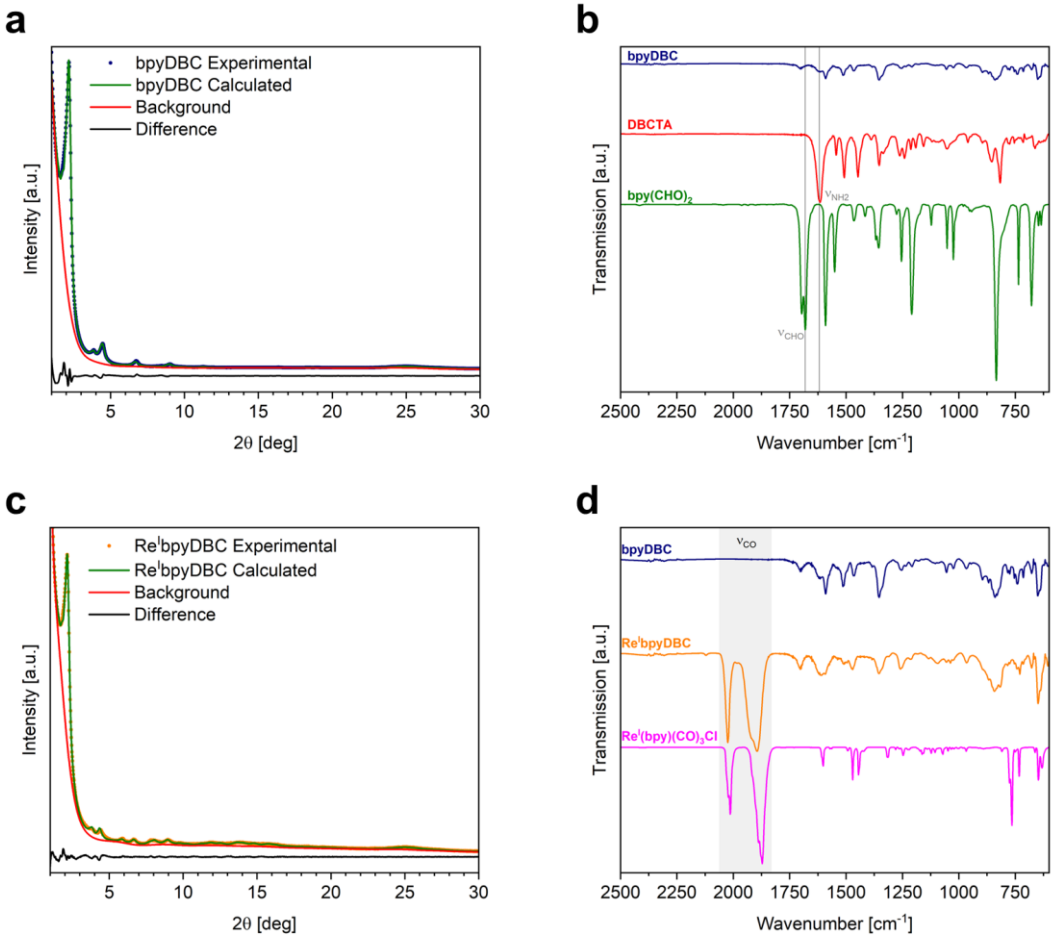


Figure 54. (a) Experimental and Rietveld refined PXRD patterns of **bpyDBC** COF, (b) FTIR spectra of the two linkers bpy(CHO)$_2$ and DBCTA together with the spectrum of the **bpyDBC** COF. c) Experimental and Rietveld refined PXRD patterns of **Re bpyDBC** COF and (d) FTIR spectra of **bpyDBC**, **Re bpyDBC** and the molecular analog Re(bpy)(CO)$_3$Cl.

Upon the introduction of Re(I), the crystallinity of the COF network is preserved and additional diffraction peaks appear at 5.9°, 8.0°, 9.9°, 12.0° and 13.9°, due to an increase of the corresponding structure factors (**Figure 54c**). The successful immobilization of $[Re(CO)_3Cl]$ by the **bpyDBC** COF was further evidenced by the three CO vibrational bands observed between 1800 and 2100 cm^{-1} in the FTIR, corresponding to the A_1 and the two E modes expected for the *facial* geometry of the $Re(CO)_3Cl$ moiety,[60, 99] and resembling those of the molecular catalyst $[Re(bpy)(CO)_3Cl]$ (**Figure 54d**).

For the Rietveld refinement[350] of these COFs, we considered a combination of four fixed structural variants of the unit cell content to account for the different possible orientations of the bpy unit, **Figure 55a**.

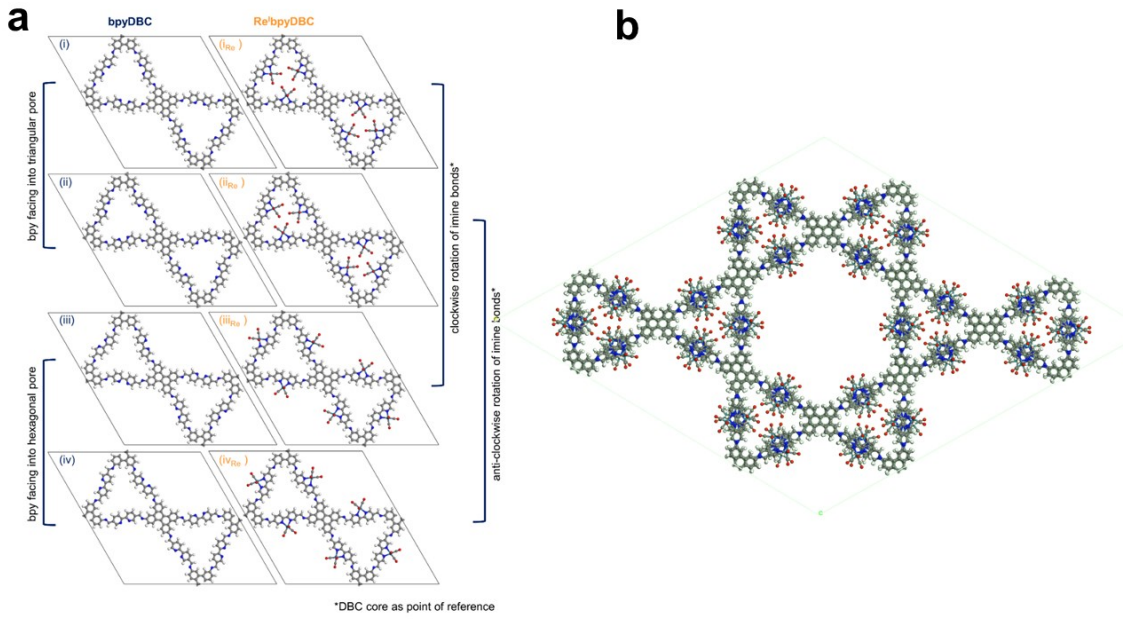


Figure 55. a) Structural variants of the two COFs and b) superposition of the four structural variants of the unit cell, illustrating how the threefold propeller contrast dominated by Re(I) is created.

The N atoms of the bpy unit can either point into the small triangular pore (*i* and *ii*) of the Kagomé structure, or into the large hexagonal pore (*iii* and *iv*). By

combining the four structural variants with equal weights of 0.25, we achieved a successful refinement of the COF in P6 symmetry, assuming AA stacking, which resulted in the structure illustrated in **Figure 55b**.

Therefore, the PXRD pattern of both COFs was then fully indexed with a hexagonal lattice with refined lattice constants of a = b = 44.7(1) Å, c = 3.56(1) Å with weighted R-value (wR) of 3.49 % and a = b = 44.8(1) Å, c = 3.65(1) Å with wR = 2.66 %, for **bpyDBC** and **Re bpyDBC**, respectively. For the model containing Re(I)-loaded, a refined occupation factor of the bpy sites with $Re(CO)_3Cl$ of 47% was considered. This is close to the value of 44% (16.2 wt% Re) obtained by ICP OES.

To investigate the distribution of the Re(I)-complex within the COF structure at the near atomic level we employed scanning TEM in high-angle annular dark field mode (STEM-HAADF), which we resolved, for the first time, the position of the metal centers in the crystalline COF network (**Figure 56**) and **Figures C1-C2**.

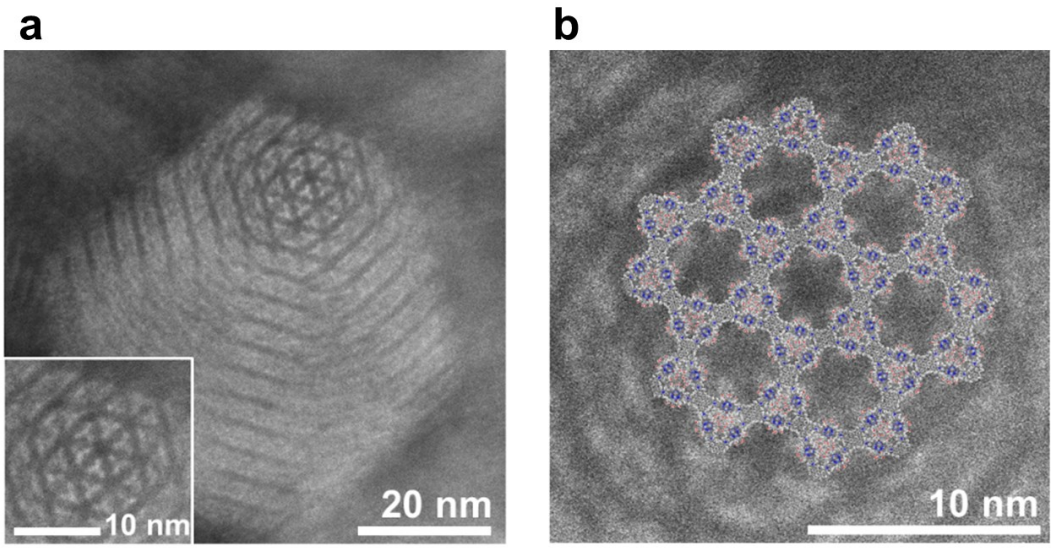


Figure 56. a) STEM-HAADF image showing the highly ordered Re(I) sub-structure within the COF lattice. b) Magnified section of a) with the COF lattice.

Here, the image contrast is approximately proportional to the atomic number squared, making heavy atoms such as Re(I) appear as bright spots. STEM-HAADF images of the **Re bpyDBC** COF reveal a highly ordered Re(I) sub-structure adopting the crystallographic positions defined by the bpy linker. The superposition of the four structural variants (**Figure 55b**) used for the Rietveld refinement illustrates how a statistical distribution of the Re(I) centers in the COF lattice creates the threefold propeller-type pattern visible in the STEM-HAADF image (**Figure 56b**).

On the other hand, TEM images of **bpyDBC** COF and **Re bpyDBC** COF are similar, showing a fully crystallized, homogenous material with crystallite sizes between 50 and 100 nm (**Figure 57**).

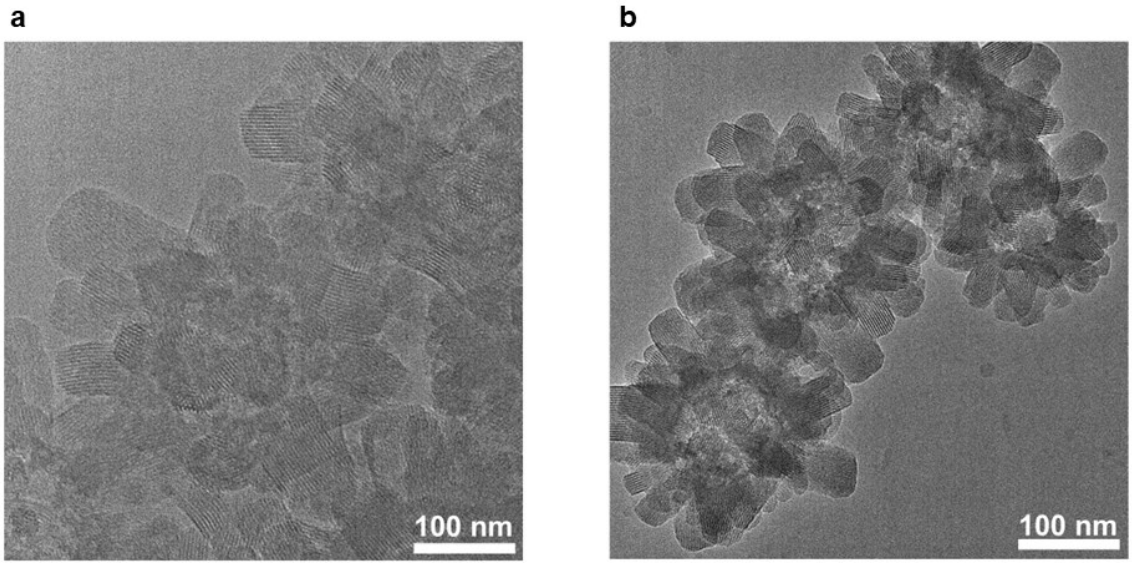


Figure 57. TEM images of the **bpyDBC** COF (a) and **Re bpyDBC** COF (b).

Moreover, nitrogen sorption at 77 K yielded a Brunauer-Emmett-Teller (BET) surface area of 1252 $m^2 g^{-1}$ and pore sizes of 1.9 nm and 3.5 nm of the dual-pore Kagomé **bpyDBC** COF structure, while upon metalation it decreases its BET surface area to 717 $m^2 g^{-1}$ and pore sizes to 1.9 nm and 3.3 nm in the **Re**

bpyDBC COF (**Figure 58**). The observed decreasing on surface area and pore sizes are expected once the Re(I) was loaded into **bpyDBC** COF pores. Furthermore, the incorporation of Re(I) centers into the COF significantly enhanced CO_2 uptake (**Figure C3**), thereby facilitating the interactions between the hybrid catalyst and the reactant.

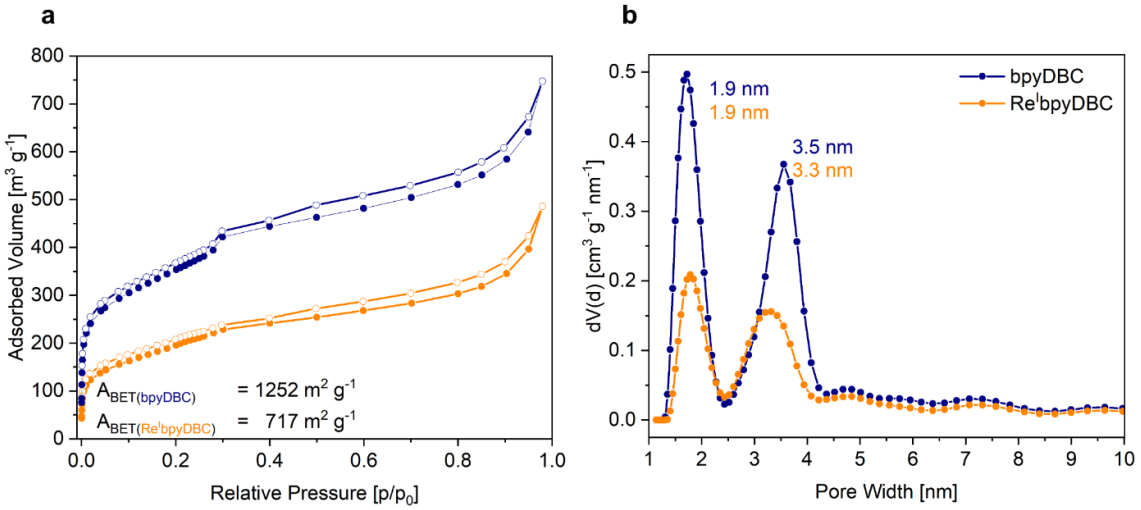


Figure 58. a) Nitrogen sorption isotherms of **bpyDBC** and **Re bpyDBC** COF and b) pore size distributions of both COFs.

Changes in the electronic structure of the COF upon immobilization of the Re(I) complex were investigated *via* UV-Vis and photoluminescence (PL) measurements along with cyclic voltammetry (CV). The optic characterizations (UV-vis and PL) are shown in **Figure 59** while their corresponding CVs are shown in **Figure C4**.

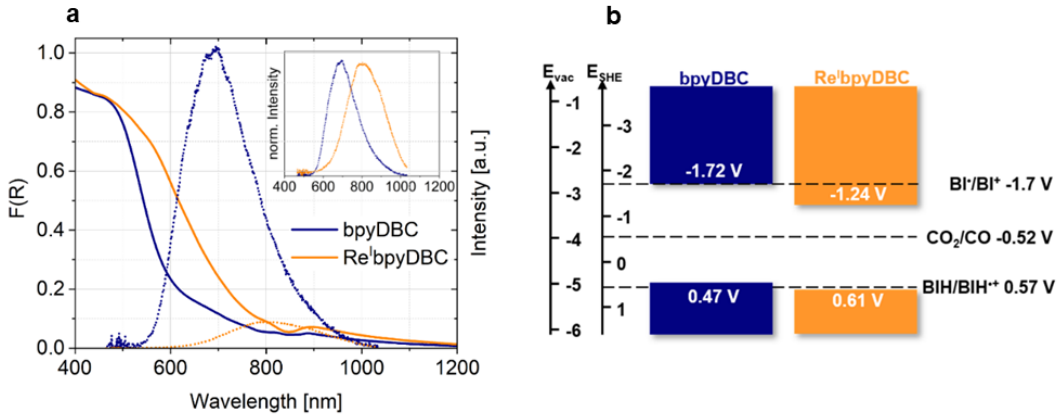


Figure 59. (a) UV-Vis absorption (continuous line) and PL emission (dotted line, λ_{exc} = 476 nm) of **bpyDBC** and **Re bpyDBC**. (b) Energy levels of the two COFs, and reduction potentials of the sacrificial donor BIH and the CO_2 to CO reduction.

The absorption onset of **Re bpyDBC** COF is red-shifted by approx. 150 nm compared to **bpyDBC**. Fitting this onset with a Tauc plot yields direct band gaps of 2.19 eV for **bpyDBC** and 1.85 eV for **Re bpyDBC** (**Figure C5**). However, it is well known that the incorporation of metal centers affects the electronic transition properties of organic frameworks.[65, 351] The PL emission of the pristine COF is characterized by a broad band with λ_{em}= 693 nm, which is significantly quenched in **Re bpyDBC**, indicating the efficient electronic interaction between the COF and the Re(I) center (**Figure 59a**). Time-resolved measurements with time-correlated single-photon counting (TCSPC) reveal a multi-component decay similar to those observed by Pan and coworkers for a different Re-COF hybrid (**Figure C6**).[314] Double exponential fits of the experimental signals reveal lifetimes of 32 (77%) and 241 ps (23%) for the pristine **bpyDBC** COF and 30 (82%) and 227 ps (18%) for **Re bpyDBC** COF. The precision of such values, especially the shortest lifetimes, is affected by the response function of the TCSPC setup, but the data suggest the increase of non-radiative processes in

the **Re bpyDBC** hybrid, likely due to the charge transfer from the COF to the Re(I) centers.

Using cyclic voltammetry (**Figure C4**), valence band (VB) energies of the pristine and metalated COF were determined to be 0.47 V and 0.61 V *vs.* SHE, respectively. Combining CV and UV-Vis results, the conduction band (CB) energies of the two materials were estimated (**Figure 59b**), establishing that both COFs are thermodynamically capable of reducing CO_2 to CO.

In the photocatalytic CO_2 reduction assays, 1,3-dimethyl-2-phenyl-2,3-dihydro-1H-benzimidazole (BIH) was used as sacrificial electron donor. BIH has a stronger reduction potential (E_{ox} = 0.57 V vs. SHE)[352] compared to other commonly used sacrificial electron donors such as TEA (triethylamine, E_{ox} = 0.693V vs. SHE)[75], TEOA (triethanolamine, E_{ox} = 1.06 V vs. SHE)[76] or BNAH (1-benzyl-1,4-dihydronicotinamide, E_{ox} = 0.81 V vs. SHE)[353] and, moreover, upon oxidation, BIH undergoes rapid deprotonation to form the radical BI$^{\bullet}$, which is an even stronger reducing agent (E_p = −1.7 V vs. SHE).[20] This allows BIH to donate two electrons and one proton during the photocatalytic process, boosting the CO_2 conversion.

The performance of **Re bpyDBC** in the photocatalytic CO_2 reduction was investigated using a 300 W Xe lamp as the illumination source equipped with 370 or 400 nm long-pass filters. In both cases the irradiance was set at 100 mW cm^{-2}. Acetonitrile suspensions containing the COF catalyst and an excess of BIH were exposed to light illumination under saturated CO_2 atmosphere. The gaseous products were monitored by gas chromatography.

Notably, in the photocatalytic experiments CO was identified as the only reduction product. Control experiments conducted under argon atmosphere, in

the dark, and in the absence of catalyst did not yield any CO. These results establish that the reduction product CO originates from the purged CO_2 and is formed only when the **Re bpyDBC** is present. **Figure 60a** displays the CO evolution using **Re bpyDBC** COF as photocatalyst under UV-Vis (>370 nm) illumination.

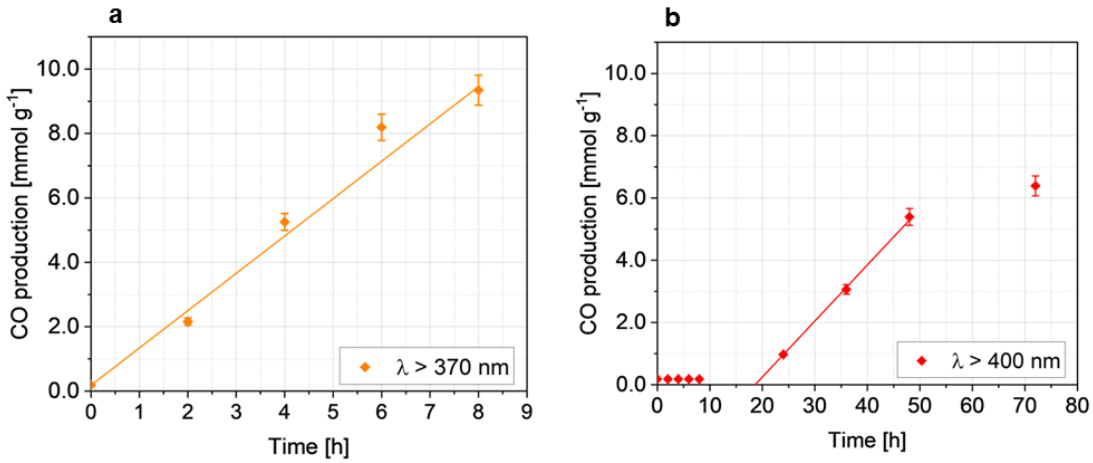


Figure 60. CO production of the **Re bpyDBC** COF under illumination with (a) λ >370 nm and (b) λ >400 nm. Solid lines represent the linear fitting of the data to extract CO production rates.

A remarkably high rate of 1.16 mmol g^{-1} h^{-1} was achieved, which ranks amongst the highest CO rates reported in the literature for similar systems without the use of an additional photosensitizer (**Table 8**).[66, 68, 280] However, comparing rates from different groups is non-intuitive and should be approached with caution, as differences in the photocatalytic setup (e.g. wavelength of source, photon flux, reactor geometry, catalyst concentration, stirring, and others) can significantly influence the catalyst performance.[354, 355] In contrast, the pristine **bpyDBC** COF did not show any CO evolution under these conditions, underlining the importance of the Re(I) center serving as the active site in the COF structure.

This fact is also evident when looking at the kinetic profile at different illumination conditions.

Table 8. COF-based hybrid Re(I) complexes applied in the photoreduction of CO_2 to CO.

COF	CO production rate [μmol $g^{-1}h^{-1}$]	Sacrificial agent/ solvent	Conc. [mg mL^{-1}]	Amount of Re(I) active sites [μmol]*	TON_{CO}	Light source	Ref.
Re bpyDBC	1160	BIH/CH_3CN	0.3	0.93	35 (24h, after two additional purges with CO_2)	300 W (Xe) >370 nm	[This work]
Re-Bpy-sp^2-c-COF	1040 1400[a]	TEOA/ CH_3CN	0.2	0.97	18.7 (17.5 h)	300 W (Xe) >420 nm	[68]
Re-COF	750	TEOA/ CH_3CN	0.3	0.27	48	225 W (Xe) >420 nm	[66]
Re-TpBpy-COF	282	TEOA/ CH_3CN-H_2O	1.3	21.3	-	200 W (Xe) >390 nm	[280]
Re bpyDBC	180	BIH/CH_3CN	0.3	0.93	7.0 (72 h)	300 W (Xe) >420 nm	[This work]

[a] In the presence of a photosensitizer

* The Re(I) content was calculated based on the wt% given by ICP OES. For example, in this work, 1 mg of COF used in the photocatalytic experiments contains 16.91 wt% Re, or 169.1 μmol. Divided by the molar mass of Re (182.21 g mol^{-1}), a Re content of 0.93 μmol is determined.

Recycling studies carried out under UV-Vis light reveal that after 8 h illumination, a new purging with CO_2 leads to the production of more CO (**Figure C7**) leading to a maximum turnover number (TON_{CO}) of 35.

Under visible light (>400 nm) illumination (**Figure 60b**), an evolution rate of 0.18 mmol g^{-1} h^{-1} was achieved but an induction period of 20 h was observed. The different behavior under different illumination conditions indicates distinct

mechanisms of CO_2 conversion. UV-vis light can directly induce MLCT excitation of the molecular catalyst followed by reductive quenching through BIH and the release of the Cl^--ligand. This yields the well-known penta-coordinated 18-electron-species driving the CO_2 to CO conversion.[123] In contrast, under (only) visible light excitation, light harvesting occurs through internal $\pi\pi^*$ transitions in the highly conjugated **bpyDBC** COF structure. The relatively long induction period observed under visible-light excitation suggests that the catalytically active species is gradually built up until an effective concentration is reached. The formation of the active species is expected to rely on electron transfer from the COF acting as antenna to the catalytic Re(I) centers.

We do not attribute the onset of CO production after the induction period to any structural changes or degradation of the COF material. Post-reaction PXRD and FTIR measurements (**Figure 61**) collected after 24h of illumination (i.e. after the onset of CO production) show no evidence of changes in the chemical structure of the COF or the coordination environment of the Re centers.

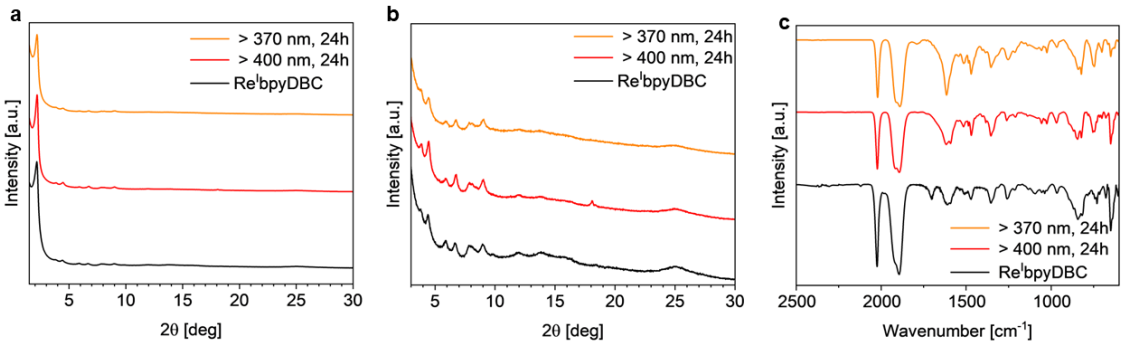


Figure 61. PXRD pattern (a and b) and IR spectra (c) of the **Re bpyDBC** COF before and after 24 h of photocatalysis under illumination with λ > 370 nm and λ > 400 nm.

Additionally, the ^{13}CO labeling experiments validate that the CO product originates from CO_2 reduction rather than decomposition of the material (**Figure C8-9**).

The outstanding stability of the **Re bpyDBC** COF is further evidenced by its continuous CO production for 72 hours under visible light. In contrast, a homogeneous catalyst, released through degradation of the hybrid COF-catalyst, would be unlikely to sustain such prolonged activity.

Unlike previously reported COFs, where the loss of crystallinity led to ceased photoactivity,[68] the **Re bpyDBC** COF exhibits exceptional stability, maintaining its catalytic performance for 72 h – approx. three times longer than the longest-reported Re-COF system under standard photocatalytic conditions (**Table 9**).

Table 9. Comparison of the duration of the photocatalytic experiments for several COF-based CO_2 photocatalysts.

COF	**Duration of photocatalytic experiment [h]**	**Ref.**
Re bpyDBC (> 400 nm)	72	[This work]
PdIn@N_3-COF	24	[291]
Re-COF	22.5	[66]
COFdpy-Co	18	[255]
Re-Bpy-sp^2c-COF	17.5	[68]
Re-TpBpy-COF	12	[280]

This outstanding stability can be directly correlated to the extremely high crystallinity, the precise definition of the local coordination environment as well as excellent electronic delocalization achieved through the use of the structure-directing DBC-node.

5.4. Conclusion

Concluding, in this study we demonstrate that the favorable low curvature and large conjugated structure of the dibenzochrysene-based building unit are key factors for enhancing both the crystallinity and stability of the novel hybrid photocatalyst, **Re bpyDBC** COF, for CO_2 reduction. The **bpyDBC** COF serves as a molecular framework with predefined binding sites for the molecular model catalyst $Re(CO)_5Cl$. For the first time, we successfully resolved the highly ordered substructure adopted by the Re(I) centers within the COF using STEM-HAADF analysis, providing valuable insights regarding the molecular design of hybrid catalysts. In the photocatalytic conversion of CO_2 to CO, the **Re bpyDBC** COF exhibited a remarkable CO production rate of 1.16 mmol g^{-1} h^{-1} under UV-Vis illumination with BIH serving as a sacrificial electron donor. Under visible light, the Re-COF maintained catalytic activity for over 50 hours at a reduced rate of 0.18 mmol h^{-1} h^{-1}, competing with the longest operational lifetime of other COF-based CO_2 photocatalyst reported to date (Table S2). Our work highlights that COFs can function as effective platforms for the hybridization of molecular catalysts, offering atomistic control over structure and exceptional stability.

Part II

Chapter 6

Electrochemical CO_2 conversion: towards scalability

6.1. From Photocatalytic to Electrocatalytic Systems

Photocatalytic systems represent an elegant approach to artificial photosynthesis. However, their overall performance is often limited by inefficient light harvesting, charge recombination, photon penetration through the reaction medium, and the inherent difficulties associated with scaling photochemical reactors while maintaining uniform light distribution.[356, 357] In contrast, electrocatalytic systems employ electricity as the driving force, which can also be direct integrated with renewable energy sources such as photovoltaic and wind power while offering precise control over reaction conditions through the applied potential or current.[358-360] Consequently, electrocatalytic CO_2 reduction has emerged as one of the most promising technologies for the practical and scalable production of carbon-neutral fuels and chemicals. **Figure 62** shows a schematic representation of practical CO_2RR systems where the electricity is driven from renewable energy sources.

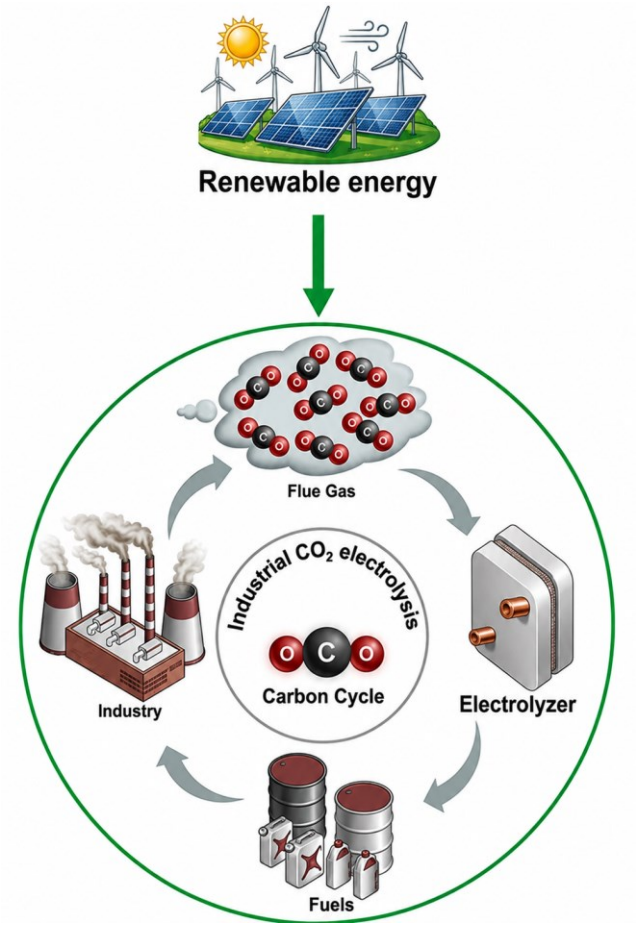


Figure 62. Schematic Diagram of CO_2 Electrolysis Driven by Renewable Electrical Energy.

The large-scale deployment of CO_2 reduction processes also depends on the design of efficient electrochemical reactors capable of operating under industrially relevant conditions.[361] Consequently, catalyst development and reactor engineering have become increasingly interconnected fields in the pursuit of sustainable carbon utilization. **Figure 63** illustrates the main electrochemical cells used for CO_2 electroreduction studies.

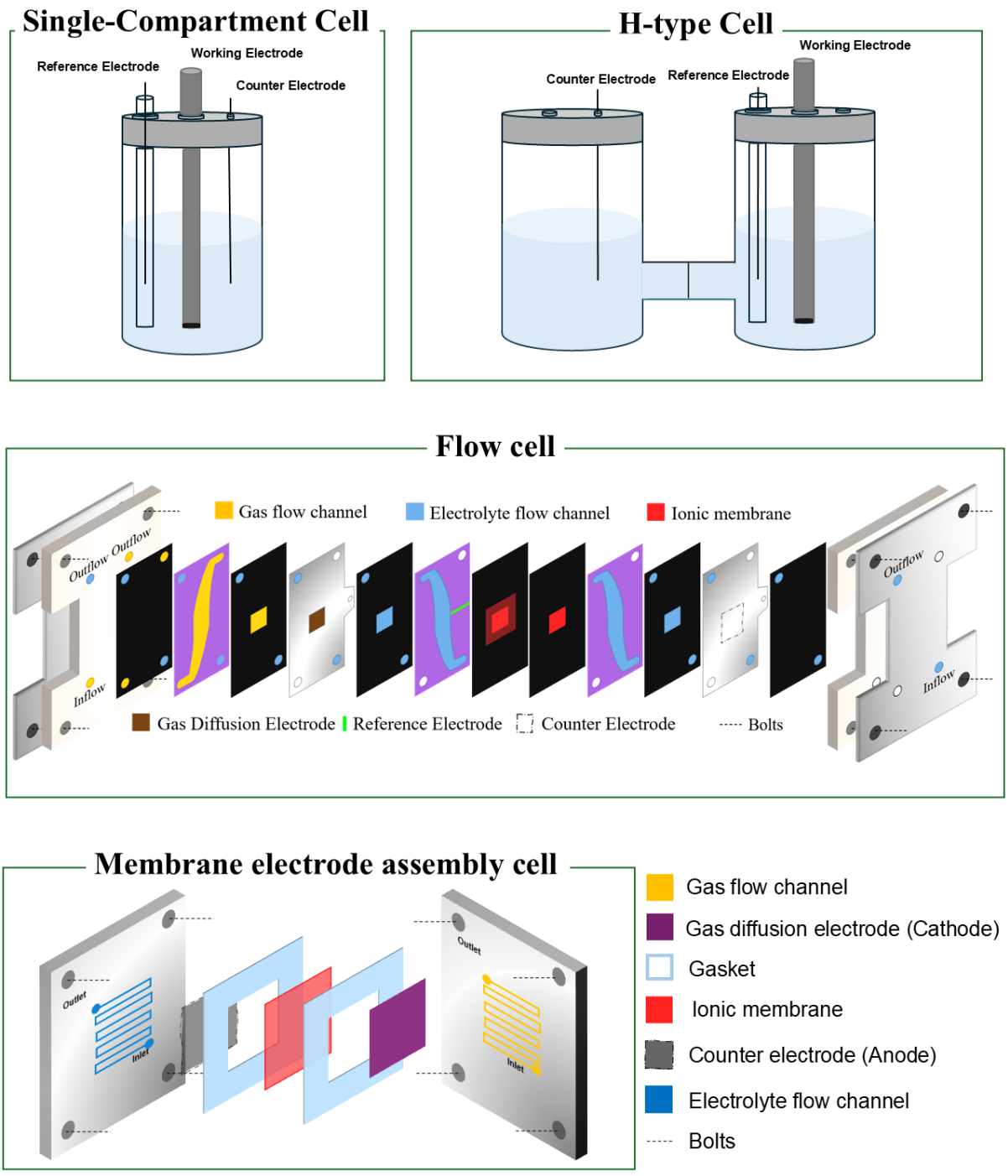


Figure 63. Schematic representation of different types of electrochemical cells used for CO_2 reduction studies.

The earliest investigations of molecular electrocatalysts were generally carried out using conventional single-compartment electrochemical cells, in which the working, counter, and reference electrodes are immersed in the same

electrolyte solution. The working electrode can be selected from bulk catalysts (e.g. Cu foil) to powder catalysts supported on glassy carbon or carbon paper/cloth.[362] These simple reactor configurations offer straightforward operation and are particularly suitable for fundamental electrochemical studies, catalyst screening and spectroelectrochemical investigations.[363, 364] However, because oxidation products generated at the counter electrode remain in the same electrolyte as the reduction products, undesirable side reactions and product crossover can occur, limiting their applicability for quantitative CO_2 reduction studies.

To overcome these limitations, H-type electrochemical cells became the standard laboratory configuration for CO_2 reduction research.[362, 365] In these reactors, the cathodic and anodic compartments are separated by an ion-exchange membrane, allowing the reduction and oxidation reactions to occur independently while minimizing product crossover. During electrolysis, CO_2 is continuously supplied to the cathodic compartment through a glass frit, and the outlet gas stream is directed to a gas chromatograph (GC) for the analysis of gaseous products. The CO_2 flow rate is typically regulated using a mass flow controller positioned at either the inlet or outlet of the electrochemical cell. To ensure accurate determination of the Faradaic efficiency (FE), the electrochemical reactor must remain completely gastight throughout the experiment. Following electrolysis, the electrolyte is collected and analyzed for liquid products, which are commonly quantified by proton Nuclear Magnetic Resonance (^{1}H NMR) spectroscopy or High-Performance Liquid Chromatography (HPLC). The H-cell configuration has become the benchmark reactor for evaluating catalytic activity, Faradaic efficiency, product selectivity,

and mechanistic pathways of both molecular and heterogeneous catalysts. Nevertheless, its performance remains limited by the relatively low solubility, typically around 33 mM, and slow diffusion of CO_2 in aqueous electrolytes, which impose severe mass transport limitations and restrict the achievement of industrial-relevant current density levels.[366]

The introduction of flow-cell reactors represented a significant step toward practical CO_2 electrolysis.[367] Unlike conventional H-cells, flow cells continuously deliver fresh electrolyte and gaseous CO_2 to the electrode surface, improving reactant transport and facilitating continuous operation. The incorporation of gas-diffusion electrodes (GDEs) further enhanced reactor performance by supplying CO_2 directly through a porous hydrophobic layer to the catalyst interface, substantially reducing diffusion limitations associated with CO_2 solubilization.[32] These improvements enable current densities exceeding several hundred mA cm^{-2} approaching those required for industrial implementation.

More recently, Membrane Electrode Assemblies (MEAs) have emerged as one of the most promising reactor architectures for scalable CO_2 electroreduction.[31 368] In MEA configurations, the catalyst layers are deposited directly onto gas-diffusion electrodes positioned in intimate contact with an ion-conducting membrane, eliminating the need for large catholyte volumes and significantly reducing ohmic resistance. This compact architecture facilitates efficient gas transport, minimizes carbonate formation, improves carbon utilization, and enables continuous operation at commercially relevant current densities.

6.2. Earth-abundant catalyst as promising candidates for replacing noble-metal catalysts.

Transition-metal complexes have played a central role in the development of molecular catalysts selective CO_2RR.[369] Historically, catalysts based on second and third row transition metals have demonstrated superior catalytic stability compared with their first-row analogues, owing to their favorable electronic structures and greater chemical stability. Some of the most efficient electrocatalysts reported to date are based on Pd, Ru, Rh, and particularly here mentioned Re complexes. Nevertheless, numerous first-row transition-metal complexes have also been explored as CO_2 reduction catalysts, including metal phthalocyanines (M = Ni, Co, Mn, Cu, Fe), metalloporphyrins (M = Fe, Co, Ni), polypyridine complexes (M = Cr, Fe, Co, Ni),[81] and cyclam derivatives (M = Ni, Co) demonstrating that earth-abundant metals can exhibit significant catalytic activity when incorporated into appropriate ligand environments. [369, 370]

Among these alternatives, Mn(I) tricarbonyl complexes have attracted particular attention because they closely resemble the well-established and here previously discussed Re(I) catalysts while replacing one of the scarcest transition metals with one of the most abundant.[47, 283, 371] Mn is approximately 1.3 million times more abundant than Re in the Earth's crust, with an average abundance of 950 mg kg^{-1} compared to only 7 x 10^{-4} mg kg^{-1} for Re.

This remarkable difference has important economic and environmental implications, particularly for the large-scale implementation of CO_2 reduction technologies, where catalyst cost, resource availability, and the environmental impact associated with mining become critical considerations.

Since the pioneering work of Bourrez and co-workers, the complex *fac*-[Mn(bpy)(CO)$_3$Br] has become one of the benchmark molecular electrocatalysts for the selective reduction of CO_2 to CO, demonstrating that efficient molecular catalysis can be achieved using an earth-abundant metal center.[283]

The Mn(I) complex and its synthetic analogs are capable of reducing CO_2 to CO at lower applied potentials than the corresponding Re-based counterparts, without significantly compromising catalytic activity.[371] Mechanistic investigations of this class of Mn(I)-tricarbonyl complexes have shown that the homogeneous catalysts rapidly lose Br^- after a one-electron reduction, forming the pentacoordinated Mn^0 species.[335, 372] The rate at which these complexes lose Br^- is higher than that of the Re-tricarbonyl analogues, enabling access to higher TOF for the CO_2 to CO conversion. However, similar to the Re(I) tricarbonyl complexes, the singly reduced Mn^0 complex tends to easily form Mn^0-Mn^0 dimeric species, which are unable to catalyze the CO_2 reduction reaction, thereby limiting its electrocatalytic performance (**Figure 64**).[47, 373]

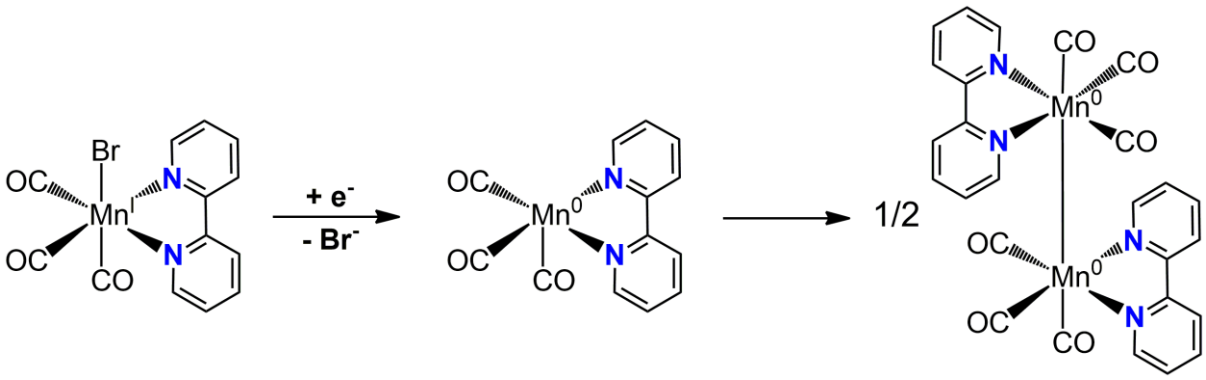


Figure 64. Reduction pathway for *fac*-[Mn(bpy)(CO)$_3$Br] based on previous reports.[47, 373]

Various strategies have been developed to stabilize the Mn^0 species and prevent dimerization, including the incorporation of bulky or electron-donating ligands to provide steric hindrance, as well as the heterogenization of the

homogeneous catalyst onto solid supports such as carbon nanotubes or TiO_2.[306, 374-378] While significant progress has been made with such hybrid systems in achieving excellent selectivity and high current densities, this approach suffers from several limitations. Poor control over spatial catalyst distribution, due to a lack of well-defined binding sites on the solid support, along with a limited structural tunability, restricts the ability to precisely tailor the local environment around the catalytic centers.[379-382]

As we also have seen for Re(I) analogues, the Covalent Organic Frameworks (COFs) are promising platforms for immobilizing molecular electro- and photocatalysts due to their synthetic versatility, structural robustness and well-defined crystalline and porous structure.[62, 322] However, aiming at have a greater rigidity compared to bipyridine, which enhances the stability of coordinated metal centers, the incorporation of a more conjugated phenanthroline as a metal-coordinating building block have shown promissor results in the literature. [383-387] Additionally, its higher degree of electron delocalization can facilitate charge transfer and improve catalytic efficiency.[388, 389]

López-Magano and co-workers demonstrated the potential of phenanthroline-containing imine-linked COFs (Phen-COFs) by immobilizing Ni^{II} and Ir^{III} sites to create a heterogeneous dual photocatalyst for C–C cross-coupling reactions between aryl bromides and radical precursors.[383, 384] The phenanthroline moiety played a crucial role in stabilizing the metal centers, preventing leaching of metal fragments into the reaction medium, thereby enhancing both activity and recyclability. Recently, Lloret-Fillol and co-workers conducted a systematic mechanistic study on a Mn-based COF incorporating a phenanthroline building block.[386] Despite its potential, poor crystallinity and low

porosity of the phenanthroline-based COF limited the catalytic performance, including its ability to suppress undesired dimerization. These findings underscore the need for further research to advance the design and synthesis of phenanthroline-based COFs containing Mn(I) complexes, aiming to improve their crystallinity, porosity, and catalytic properties to fully harness the potential of phenanthroline in electrocatalytic CO_2 reduction.

To date, the performance of COF-based electrodes for CO_2 reduction has been evaluated using traditional liquid-phase electrochemical cells such as H-cells.[390, 391] However, in such studies, the current density is often limited by the CO_2 solubility in the liquid electrolytes and its poor diffusion. The catholyte-free membrane-electrode-assembly (MEA) represents an elegant alternative offering several advantages for the development of electrochemical CO_2 reduction processes. By enabling direct contact between the catalyst and CO_2 gas while avoiding interaction with aqueous electrolytes, this architecture mitigates mass transport limitations, enhances CO_2 availability at the catalytic sites, reduces parasitic H_2 reactions, and decreases ionic resistance due to the zero-gap design.[392, 393] The combination of this advanced electrochemical cell design with COF-based electrocatalysts, featuring highly porous structures and high specific surface areas (~800 to 2000 $m^2\ g^{-1}$), opens new opportunities for the precise control over catalytic properties and offers a powerful strategy for developing next-generation electrocatalysts with improved performance and stability for sustainable CO_2 reduction applications.[394, 395]

6.3. Mn(I) - Functionalized Covalent Organic Framework as Efficient Electrocatalyst for CO_2 Reduction in a Catholyte-Free Zero-Gap Electrolyzed

Therefore, in this section, we present the design and synthesis of a crystalline imine-linked 2D COF constructed from 4,4′-(1,10-phenanthroline-3,8-diyl)dibenzaldehyde (Phen) and 4,4′,4″,4‴-(pyrene-1,3,6,8-tetrayl)tetraaniline (Py). Post-functionalization of the resulting **PhenPy** framework with $[Mn(CO)_5Br]$ yields the heterogeneous electrocatalyst **Mn PhenPy** COF, in which the nitrogen atoms of Phen serve as predefined coordination sites for the metal centers (**Figure 66a**). Gas diffusion electrodes (GDEs) based on conductive carbon paper were fabricated using **Mn PhenPy** COF and integrated into a catholyte-free MEA cell for the electrochemical reduction of CO_2 to CO. This study represents the first example of a COF-based material utilized as an active CO_2 reduction electrocatalyst in an industry-relevant MEA cell architecture, thus providing a proof of principle for the successful integration of COF-based materials into scalable and efficient CO_2 reduction technologies. Furthermore, we demonstrate that the **Mn PhenPy** COF mitigates the formation of detrimental dimeric Mn^0−Mn^0 species, in contrast to previously reported studies on similar COFs.[386] The high crystallinity and porosity of **Mn PhenPy** are identified as the key factors in suppressing dimerization and enhancing electrocatalytic performance. As a result, **Mn PhenPy** outperforms both the molecular Mn catalyst and previously reported bipyridine (bpy) - and phenanthroline-based Mn COF hybrids in terms of turnover number and frequency.

6.4. Experimental Section

Materials. All solvents were purchased from *Sigma Aldrich*, *Acros* or *TCI Europe* in the common purities *purum*, *puriss* or *reagent grade*. The materials were used as received without additional purification and handled in air unless otherwise noted.

Synthesis of COF building block 4,4′-(1,10-phenanthroline-3,8-diyl)dibenzaldehyde (Phen). This synthesis involved a three step synthesis. Firstly, the linker 2,2-Dimethylpropane-1,3-diol (4 eq., 4155.6 mg, 40 mmol), p-toluenesulfonic acid (0.09 eq., 171.2 mg, 0.9 mmol) and (4-formylphenyl)-boronic acid (1 eq., 1497.9 mg, 10 mmol) were mixed in a Schlenk flask under argon atmosphere. The solids were dissolved in 100 mL toluene and heated to reflux for 1.5 h. The reaction solution was poured into a saturated aqueous solution of sodium hydrogen carbonate (300 mL), and CH_2Cl_2 (3 x 150 mL) was added. The organic layer was separated and dried over sodium sulphate. *In vacuo* removal of all solvents yielded colourless platelet-like crystals of **1** (3022.3 mg, 9.9 mmol, 99%). **^{1}H-NMR (400 MHz, $CDCl_3$): δ (ppm)** = 7.80 (d, *J* = 6.4 Hz, 2H, H-3), 7.48 (d, *J* = 6.3 Hz, 2H, H-4), 5.40 (s, H-5), 3.76 (d, *J* = 11.94 Hz, 2H, H-9), 3.76 (s, 4H, H-2,10), 3.64 (d, *J* = 10.6 Hz, 2H, H-6), 1.29 (s, 3H, H-11), 1.00 (s, 6H, H-7,8), 0.80 (s, 3H, H-1). In the second step the 3,8-Dibromophenanthroline (1 eq., 338 mg, 1 mmol), **1** (3 eq., 912.6 mg, 3 mmol), aqueous sodium carbonate solution (2.6 eq., 1 M, 2.6 mL, 2.6 mmol) and tetrakis-(tri-phenylphosphine)palladium(0) (15 mol%, 173.33 mg) were mixed in a Schlenk flask and dissolved in a degassed THF/toluene mixture (7.4 mL, 1:1) under argon atmosphere. The reaction mixture was heated to reflux for 72 h. After cooling to

room temperature, an aqueous solution of sodium hydroxide (1 M, 10 mL) and brine (sat. aq. NaCl, 20 mL) was added to the reaction mixture. The aqueous layer was extracted with CH_2Cl_2 (3 x 50 mL). The combined organic phases were dried over sodium sulphate and the solvents removed *in vacuo*. The crude product was recrystallized from hot MeOH and the solvents removed *in vacuo*. A yellow poder **2** was obtained (450.5 mg, 80%). **^{1}H-NMR (400 MHz, $CDCl_3$):** δ (ppm) = 9.81 (d, *J* = 2.1 Hz, 2H, H-6), 8.75 (d, *J* = 2.1 Hz, H-8), 8.13 (s, 2H, H-7), 7.83 (d, *J* = 8.6 Hz, 4H, H-5), 7.75 (d, *J* = 9.1 Hz, 4H, H-4), 5.50 (s, 2H, H-3), 3.83 (d, *J* = 11.3 Hz, 4H, H-2/9), 3.71 (d, *J* = 10.5 Hz, 4H, H-2/9), 1.33 (s, 6H, H-1/10), 0.84 (s, 6H, H-1/10). Finally, for the phen ligand synthesis, the obtained **2** (1 eq., 265.5 mg, 0.476 mmol) was dissolved in degassed THF (50 mL). Hydrochloric acid (5%, 6.44 mL) was added and the solution heated to reflux for 18 h. The reaction mixture was cooled to room temperature and all solvents removed *in vacuo*. The residual solid was thoroughly washed with water (40 mL) and small amounts of THF. 4,4′-(1,10-phenanthroline-3,8-diyl)dibenzaldehyde (Phen) was obtained as a light yellow powder (**phen**) (160.4 mg, 0.423 mmol, 87%). **^{1}H-NMR (400 MHz, $CDCl_3$):** δ (ppm) = 10.20 (s, 2H, H-1), 9.51 (d, *J* = 2.2 Hz, 2H, H-4), 8.51 (d, *J* = 2.4 Hz, 2H, H-6), 8.10 (d, *J* = 8.5 Hz, 4H, H-2), 7.99 (d, *J* = 8.4 Hz, 4H, H-3), 7.97 (s, 2H, H-5)

Synthesis of PhenPy COF. In a 6 mL Schott-Duran culture tube, a solid mixture of 4,4′-(1,10-phenanthroline-3,8-diyl)dibenzaldehyde Phen (3.88 mg, 0.01 mmol, see SI for synthesis, NMR spectra of intermediates and main product are shown in Figure S1-S3) and 4,4′,4″,4‴-(pyrene-1,3,6,8-tetrayl)tetraaniline Py (2.83 mg, 0.005 mmol, 98%, BLD Pharm, CAS: 1610471-69-6) was suspended in 500 µL 1,4-dioxane and mesitylene (1:3). Subsequently, 50 mL of acetic acid

(aqueous, 6 M) was added. The culture tube was tightly sealed and heated to 120 °C for 4 days. The resulting suspension was filtrated and the isolated brown powder was Soxhlet extracted with EtOAc for 6 h, followed by treatment in supercritical CO_2 at 110 bar and 40 °C for 2 h. Elemental analysis for $(C_{68}H_{42}N_8)_n$, calculated: C, 84.4 ; H, 4.4 ; N, 11.5. Found: C, 74.9 ; H, 4.3 ; N, 7.1. Calculations for the elemental analysis were based on an infinite structure, ignoring the presence of undefined end-groups or possible residues in the pore system.

Synthesis of Mn PhenPy COF. PhenPy COF (30 mg) and $[Mn(CO)_5Br]$ (30 mg) were dispersed in 10 mL EtOAc and heated to reflux for 1 h under Ar atmosphere. The resulting powder was filtrated, thoroughly washed with EtOAc and dried under reduced pressure. ICP-OES analysis was conducted to determine the Mn content to be 2.2 wt%, corresponding to 28 % of the Phen sites occupied. The percentage of Phen sites immobilizing $[Mn(CO)_3Br]$ is calculated as detailed in the SI (*Mn-occupation of Phen*).

Synthesis of fac-[Mn(Phen)(CO)$_3$Br]. Phen (1.1 eq., 30 mg, 0.077 mmol) and $Mn(CO)_5Br$ (1 eq., 24.7 mg, 0.07 mmol) were dissolved in 10 mL EtOAc and heated to reflux for 3 h under Ar atmosphere. The resulting powder was thoroughly washed with EtOAc and dried under reduced pressure. Yield: 71%. FTIR: $\nu_{C\equiv O}$ s(2025, 1952 and 1917 cm^{-1}). ^1H NMR (400 MHz, Acetone-d_6) δ (ppm) = 10.11 (s, 2H), 9.56 (d, J = 1.9 Hz, 2H), 8.68 (d, J = 2.0 Hz, 2H), 8.10 (d, J = 8.3 Hz, 4H), 8.09 (s, 2H), 7.94 (d, J = 8.2 Hz, 4H).

Synthesis of fac-[Mn(bpy)(CO)$_3$Br]. Bpy (110 mg, 0.71 mmol) and $Mn(CO)_5Br$ (200 mg, 0.72 mmol) were dissolved in 30 mL EtOAc and heated to reflux for 1 h under Ar atmosphere. The resulting powder was thoroughly washed with Et_2O and dried under reduced pressure. Yield: 85%. FTIR: $\nu_{N\text{-}H}$ m(3068 cm^{-}

[1]), $\nu_{C\equiv O}$ s(2017, 1910 and 1883 cm^{-1}). ^1H NMR (400 MHz, Acetone-d_6) δ (ppm) = 9.31 (d, J = 5.5 Hz, 2H), 8.58 (d, J = 8.1 Hz, 2H), 8.23 (t, J = 7.7 Hz, 2H), 7.75 (t, J = 6.4 Hz, 2H).

Powder X-ray diffraction (PXRD) measurements were performed using a Bruker D8 Discover instrument with Ni-filtered Cu K_α radiation and a LynxEye position-sensitive detector.

Theoretical structure simulations. The COF structure was constructed using the Accelrys Materials Studio software package. A *P1* symmetry was applied and the structure model optimized using the Forcite module with the Universal Force-Field. Structure refinement using the Pawley method was carried out as implemented in the Reflex module of the Materials Studio software. Thompson-Cox-Hastings peak profiles were used, and peak asymmetry was corrected using the Berar-Baldinozzi method.

Fourier-transform infrared spectroscopy (FTIR) measurements were performed with a Bruker Vertex 70 FTIR instrument by focusing the light of a globar as a MIR light source through a KBr beam splitter with integrated gold mirrors and an ATR sample stage with a Ge crystal. The spectra were recorded by a N_2 cooled MCT detector with a resolution of 2 cm^{-1} and averaged over 128 scans.

Scanning electron microscopy (SEM) images were obtained with an FEI Helios NanoLab G3 UC microscope equipped with a Schottky field-emission electron source operated at 3 kV. Before measuring, the samples were coated with a 10 nm thick carbon layer. **Energy-dispersive X-ray spectroscopy** (EDX) mapping was performed at an acceleration voltage of 12 kV. The primary electron beam current was optimized as a compromise between achievable resolution and

a good signal-to-noise ratio at the EDX detector. The mapping acquisition time was 15–20 minutes, with drift correction applied during the process. The acceleration voltage for **back-scattered electron** (BSE) images was 4 kV. The beam current was adjusted as a compromise between the required image resolution and the signal-to-noise ratio at the CBS detector. The CBS detector is a doped Si detector where back-scattered electrons generate electron-hole pairs.

Transmission electron microscopy (TEM) was performed with a probe-corrected FEI Titan Themis instrument equipped with a field emission gun operated at 300 kV.

Thermogravimetric analysis (TGA) measurements were performed using a Netzsch Jupiter ST 449 C instrument equipped with a Netzsch TASC 414/4 controller. The samples were heated from room temperature to 900°C under a synthetic air flow (25 mL min^{-1}) at a heating rate of 10 K min^{-1}.

Nitrogen sorption isotherms were recorded with a Quantachrome Autosorb 1 or Autosorb iQ instrument at 77 K. **Carbon dioxide sorption** measurements were conducted on a Quantachrome Autosorb iQ at 273 K and 298 K. The sample was outgassed for 24 h at 120°C under high vacuum prior to the measurements. Pore size distributions from nitrogen sorption data were calculated using the QSDFT model with a carbon kernel for cylindrical pores.

Nuclear magnetic resonance (NMR) spectra were recorded on Bruker AV 400 and AV 400 TR spectrometers. Proton chemical shifts are expressed in parts per million (δ scale) and are calibrated using residual non-deuterated solvent peaks as internal reference (e.g. DMSO-d_6: 2.50 ppm).

UV-Vis-NIR spectra were recorded on a Perkin-Elmer Lambda 1050 spectrometer equipped with a 150 mm integrating sphere, photomultiplier tube

(PMT) and InGaAs detectors. **Diffuse reflectance spectra** were collected with a Praying Mantis (Harrick) accessory and were referenced to barium sulfate powder as 100 %R standard. The specular reflection of the sample surface was removed from the signal using apertures that allow only light scatter at angles > 20° to pass.

TON_{CO} calculations. For the TON_{CO} calculations, the moles of CO produced at each potential were divided by the moles of catalytic centers (Mn) present in the catalyst deposited on the carbon paper electrode. For **Mn PhenPy** COF, ICP-OES was used to determine the amount of Mn. The parameters used in these calculations, along with the TON_{CO} values at each potential, are summarized in **Table D1**.

TOF_{CO} calculations. The turnover frequency for CO production (TOF_{CO}) was calculated by dividing the TON_{CO} by the time (i.e. 30 min) the potential was held at each potential step.

Mn-occupation of Phen sites. To estimate the molecular weight of the COF, a fragment reflecting the 2:1 ratio of the Phen to the Py linker is considered (**Figure 65**). The molecular weight of this $C_{92}H_{54}N_8^{12\bullet}$ fragment is M = 1271.50 g mol^{-1}.

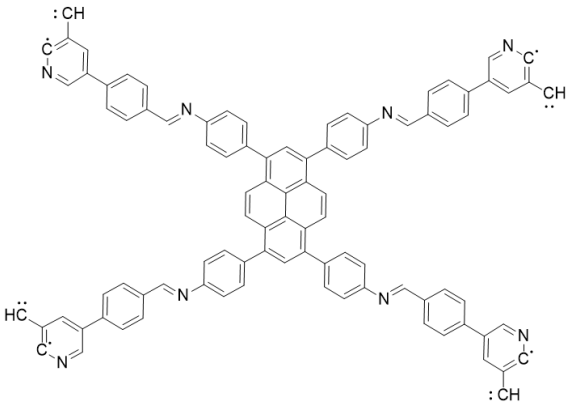


Figure 65. **PhenPy** COF fragment reflecting the 2:1 ratio of Phen to Py.

The weight percent y of Mn given by the ICP-OES can be expressed as the following **Equation 15**.

$$y = \frac{x * M(\mathrm{Mn})}{M(\mathrm{C_{92}H_{54}N_8^{12\bullet}}) + x * M(\mathrm{Mn(CO)_3Br})} \quad (\mathbf{15})$$

where x is a number between 0 and 2, corresponding to the number of immobilized Mn-complexes per fragment (max. value = 2, since only two Phen sites are available per fragment). A 100% coverage of the two available Phen sites of the fragment translates to two additional $Mn(CO)_3Br$ compounds, each with a weight of M = 218.87 g mol^{-1}, thus $x = 2$ in the equation. Insertion of the corresponding molecular weights (M(Mn) = 54.94 g mol^{-1}) yields a value of $y = 0.064$, or 6.4 wt% for a 100% coverage of the Phen sites with Mn-complex.

In reality, a value given by ICP-OES is used to calculate the coverage of Phen sites. For example, ICP-OES measures 2.2 wt% Mn in the sample of interest. Replacing y =0.022 in the above equation and solving it for x yields a value of $x = 0.558$. Applying the rule of three, if $x = 2$ corresponds to 100%, then $x = 0.558$ corresponds to a coverage of 28% of the Phen sites.

Cyclic voltammetry (CV) was performed on a Metrohm Autolab potentiostat using a three-electrode setup with Pt wire as counter electrode, Ag wire as

pseudo-reference electrode and slurry-coated FTO glass as working electrode in 0.1 M $TBAPF_6$ in acetonitrile. The electrolyte was prepared and stored under Ar. The Ag pseudo-electrode was referenced against the ferrocene redox couple. Measured potentials vs. the ferrocene redox couple Fc/Fc^+ were converted to the absolute electrode potential (E_{vac}) and to potentials vs. Standard Hydrogen Electrode (SHE) according to the following equations (i) and (ii), respectively. Note that the absolute potential scale is equal to the negative physical scale.[396] Potentials vs. Standard Calomel Electrode (SCE) were converted to potentials vs. SHE according to equation (iii).[349] Reduction potentials for the sacrificial donors retrieved from the literature were converted to SHE accordingly.

(iv) $E_{vac} = E_{Fc/Fc^+} + 4.8\ \text{eV}$

(v) $E_{vac} = E_{SHE} + 4.44\ \text{eV}$

(vi) $E_{SHE} = E_{SCE} + 0.241\text{V}$

Slurries were prepared by dispersing 14.1 mg of COF material, 11.3 mg Super C65 carbon black and 2.8 mg PVDF (50:40:10) in 400 µL NMP. The mixture was ultrasonicated for 30 minutes and stirred at room temperature for a minimum of 2 days to guarantee homogeneous dispersion of all components. 20 µL of the slurry was then drop-cast onto FTO glass, covering an area of ~ 1 cm^2 and dried overnight at 60 °C.

Preparation of gas diffusion electrodes. Gas diffusion electrodes (GDEs) were prepared by spray coating an ink on a carbon paper substrate (GDL-Sigracet, 39B) using an airbrush (Vonder). The ink was composed of 2.0 mg of Mn PhenPy COF catalyst or 1.0 mg of *fac*-$[Mn(Phen)(CO)_3Br]$ catalyst, 1.0 mg of carbon black (amorphous carbon, CAS 1333-86-4), 10.0 µL of ionomer

(Sustainion XA-95% in Ethanol, Dioxide Materials Inc.) and 2.0 mL of dimethylformamide (Aldrich 99.8 %). The mixture was submitted to an ultrasonic probe sonicator (Sonics & Materials INC, VCX130) with a power rating of 130 W for 15 minutes. The homogenized solution was then deposited onto a 1.0 cm^2 area of carbon paper using the airbrush, with approximately 50% of the slurry mass lost during deposition, as determined by the difference between the initial and final mass of the carbon paper electrode. The electrode was subsequently dried in an oven at 80 °C for 24 h. Finally, the prepared electrode was applied as cathode for the electrochemical reduction of CO_2.

Electrochemical CO_2 reduction in MEA cell. All electrochemical measurements were carried out on a potentiostat/galvanostat (Autolab PGSTAT204, Metrohm). CO_2 reduction performance was evaluated in a commercial catholyte-free Membrane Electrode Assembly (MEA) cell (Dioxide Materials®). GDEs containing Mn PhenPy or *fac*-[Mn(bpy)$(CO)_3$Br] were used as cathodes, Ni foam as anode and 1 M KOH was used as anolyte, circulating at 5 mL min^{-1}. The half-cells were connected with an anion exchange membrane (Sustainion®) and CO_2 gas was directly fed to the cathode at 30 mL min^{-1}, excluding the use of an aqueous electrolyte. Measurements were carried out under potentiostatic conditions applying a full-cell potential range from 2.6 to 3.2 V for 30 minutes for each potential step. The current density was monitored to assess the electrode's performance. Gaseous products leaving the cell were transported by the continuous CO_2 flow cell to a gas sampling bag, where aliquots of 500 µL were collected with a gas-tight syringe and injected into a gas chromatograph equipped with thermal conductivity detection (GC-TCD, PerkinElmer Clarus 580) for the quantification of CO. The GC-TCD is equipped

with two columns (Porapak N 2 mm and molecular sieve) and a detector for thermal conductivity. The measurements were performed at 120 °C on the injector and 150 °C on the detector, with a thermal ramp of 35–120 °C. Ar was used as carrier gas at 30 mL min^{-1}.

6.5. Results and Discussion

Design and Structural Characterization.

Under solvothermal conditions, the building blocks **Phen** and **Py** were linked *via* a *Schiff-base* acid-catalyzed imine condensation reaction, resulting in the formation of the crystalline **PhenPy** COF (**Figure 66a**).

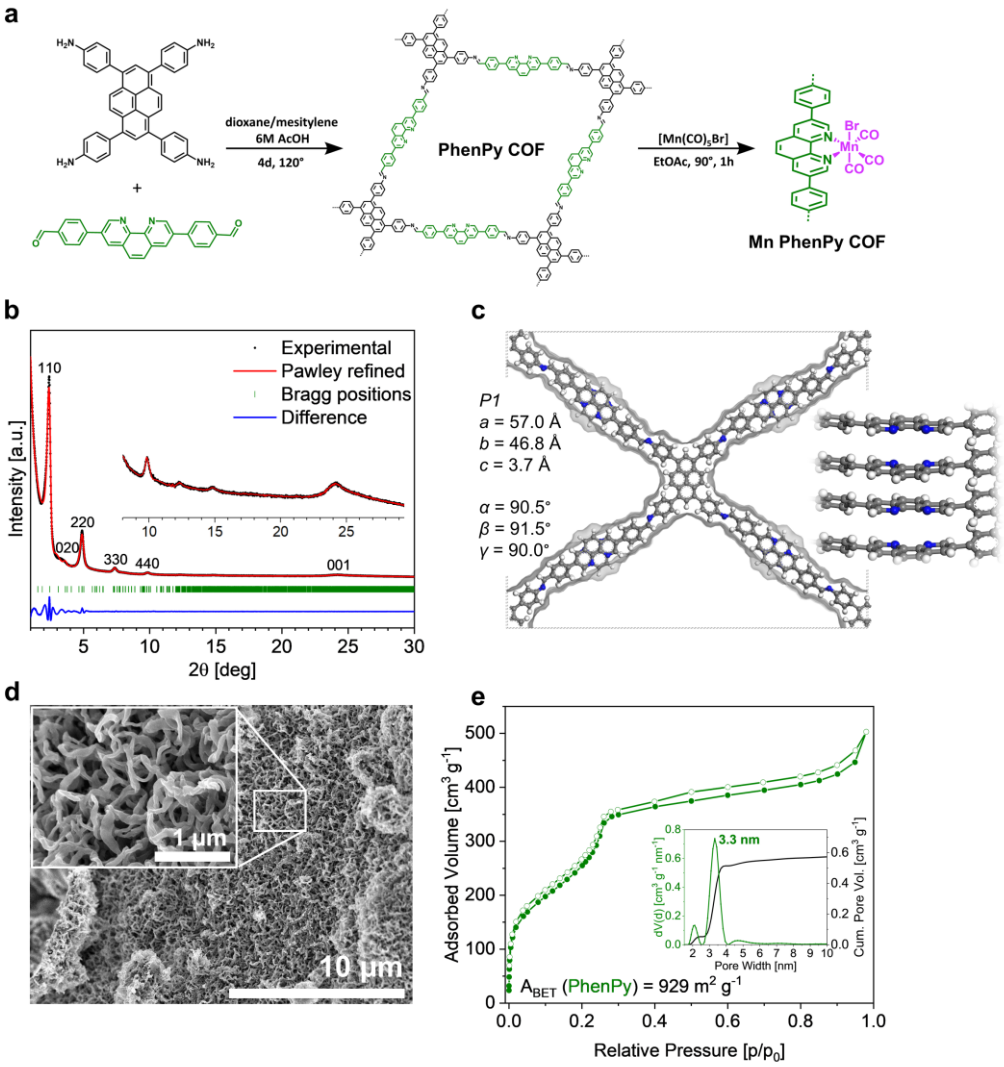


Figure 66. (a) Synthesis of **PhenPy** COF and immobilization of $[Mn(CO)_5Br]$, yielding **Mn PhenPy** COF (schematic). (b) Experimental and indexed Pawley-refined PXRD pattern of **PhenPy** COF. Pawley refinement was conducted using the simulated structure model of **PhenPy**, based on the triclinic space group *P1.* (c) Unit cell of **PhenPy** COF. Alternating phenanthroline moieties in adjacent layers face towards different pores (inset). The cell parameters of the refined structure are provided in the Section S7. (d) SEM micrograph of the **PhenPy** COF powder, indicating a fibrillar morphology. (e) Nitrogen sorption measurements reveal high porosity with a BET surface area of 929 m^2g^{-1}. Inset: pore size distribution and cumulative pore volume of **PhenPy**

The crystallinity of the synthesized COF was confirmed by powder X-ray diffraction (PXRD) analysis, **Figure 66b**, which shows sharp reflections at 2.4°, 4.9°, 7.5° and 10.0° *2θ*. The reflection at 24° corresponds to the (001) plane,

which is attributed to the π-π stacking of the two-dimensional COF sheets with a stacking distance of 3.7 Å. A simulated structure model of the **PhenPy** COF was Pawley-refined based on the triclinic space group *P1*. In line with the structure of the previously reported, structurally similar COF_{bpy} (bpy = bipyridine), an AB stacking model was chosen where one layer is rotated by 180° about the *b* axis, orienting the stacked phenanthroline groups toward different pores (inset in **Figure 66c**).[320] The refined pattern shows good agreement with the experimentally obtained data, with the refined unit cell parameters *a* = 57.0 Å, *b* = 46.8 Å, *c* = 3.7 Å and *α* = 90.5°, *β* = 91.5° and *γ* = 90.0°.

Scanning electron microscopy (SEM) images of the **PhenPy** COF powder in **Figure 66d** reveal a uniform, fibrillar morphology of interconnected ribbon-like structures. The morphological features suggest a highly porous structure beneficial for gas diffusion and adsorption. The morphology is also reflected in transmission electron microscopy (TEM) images, with fully crystallized ribbon-like structures visible in **Figure D1.**

Nitrogen sorption experiments at 77 K yielded a Brunauer-Emmett-Teller (BET) surface area of 929 $m^2 g^{-1}$, significantly higher than those reported for other **Phen**-based COFs,[383, 384, 386] further confirming the high crystallinity and porosity of the **PhenPy** COF (**Figure 66e**). Pore sizes were analysed using the quenched solid density-functional theory (QSDFT) model for 1D cylindrical pores, revealing a pore size of 3.3 nm, which closely matches the simulated value of about 3.4 nm (inset, **Figure 66e**).

The successful formation of the COF network was further confirmed by Fourier-transform infrared (FTIR) spectroscopy. The absence of the aldehyde vibration of the **Phen** building block at 1690 cm^{-1} and the amine vibrations of the

Py building block at 1614, 3352 and 3454 cm^{-1} in the FTIR spectrum of the COF in **Figure D2** agree with the formation of the imine bond, which appears as a shoulder at 1624 cm^{-1}. Hence, PXRD, FTIR, and nitrogen sorption analysis evince the formation of the COF network with well-defined structural and textural properties that closely align with the simulated model.

Post-functionalization of the **PhenPy** COF with $[Mn(CO)_5Br]$ was conducted at 85°C in ethyl acetate for 1 h under Ar atmosphere, following a well-established procedure preserving the chemical nature of the complex (**Figure 66a**).[386] Due to the light-sensitivity of the Mn(I) complex, functionalization reactions were carried out in the dark. The PXRD of **Mn PhenPy** COF displays diffraction peaks analogous to the pristine **PhenPy** COF, evincing that the crystalline structure of the material is retained (**Figure 68a**). The amount of Mn incorporated into the COF was obtained by ICP-OES, resulting in 2.2 wt% of Mn, which corresponds to 28% of the COF phenanthroline moieties being coordinated to Mn(I) centers (see Mn-occupation of Phen sites section for calculation details).

X-ray photoelectron spectroscopy (XPS) of the **Mn PhenPy** COF confirms the presence of Mn(I) and Br within the COF structure (**Figure 67**).

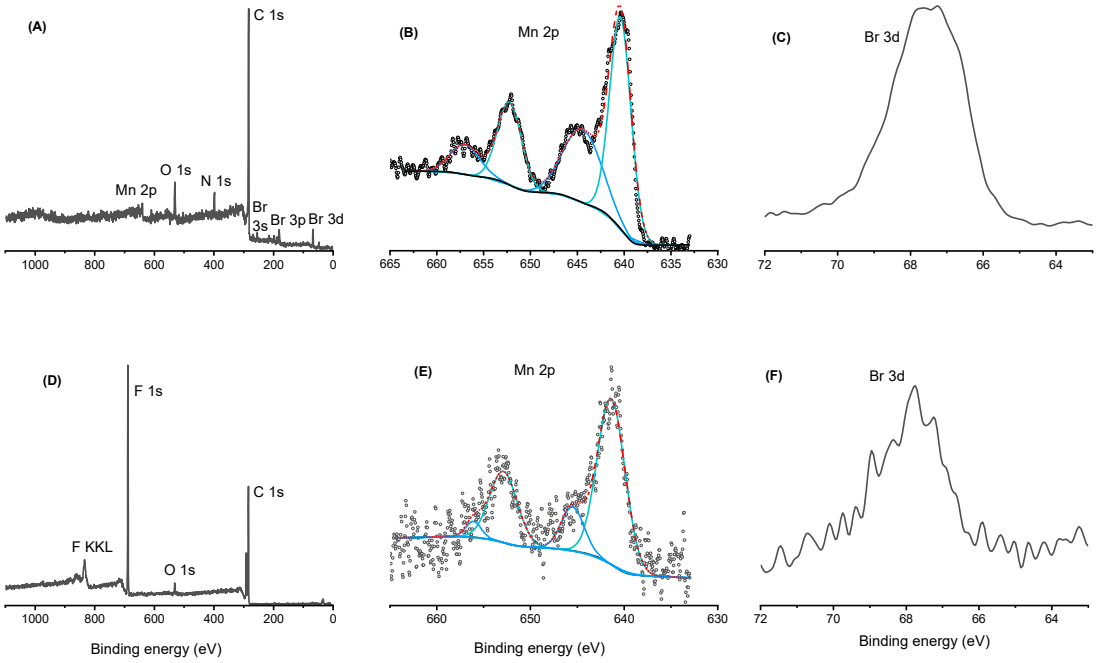


Figure 67. XPS spectra of **Mn PhenPy** COF (a-c) and **Mn PhenPy** COF applied to a gas diffusion electrode (d-f).

A high resolution scan of the Mn 2p peak reveals the main doublet at binding energies of 640.4 and 652.2 eV, which is characteristic of Mn(I) tricarbonyl complexes.[397-399] Additional shoulders at binding energies of 644.4 and 657.0 eV are also clearly observed and have been attributed to the formation of solvated species due to Br labilization as reported elsewhere[45].

The three characteristic CO vibration bands observed between 1850 and 2050 cm^{-1} in the FTIR spectrum provide further evidence of the successful immobilization of the tricarbonyl Mn(I) complex within the porous COF structure (**Figure 68b**). These bands correspond to the A_1 and two E vibrational modes expected for the *facial* geometry of the $Mn(CO)_3Br$ moiety and closely resemble

those of the molecular analog *fac*-[Mn(**Phen**)$(CO)_3$Br], in which the **Phen** building block acts as ligand to the Mn(I) center.

SEM images in **Figure 68c** reveal a uniform and fibrillar morphology similar to that of the pristine **PhenPy**, featuring ribbon-like structures. SEM-EDX (energy dispersive X-ray spectroscopy) spectra collected at various spots on the powder surface confirm the presence of Mn and Br (**Figure D3**). As shown in **Figure D4**, SEM-EDX mapping indicates a homogeneous distribution of the Mn(I) complex in the **Mn PhenPy** COF structure. The nitrogen sorption experiments of **Mn PhenPy** COF reveal a reduced BET surface area of 306 $m^2\ g^{-1}$ (**Figure D5**) compared to the pristine COF, a trend commonly observed following post-modification of COFs with metal centers.[68, 99, 249, 320]

Physical Properties

Efficient electrocatalysis requires a high affinity of the catalyst for CO_2 adsorption; therefore, CO_2 sorption experiments were performed at temperatures of 273 K and 294 K and pressures of up to 1000 mbar (100 kPa). **Mn PhenPy** COF exhibited a maximum CO_2 uptake of 2.5 mmol g^{-1} at 273 K, whereas its pristine counterpart **PhenPy** adsorbed only 1.6 mmol g^{-1} at the same temperature (1.5 mmol g^{-1} and 1.0 mmol g^{-1} at 294 K, respectively, **Figure 68d** and **D6**). Despite the reduced surface area, the results indicate an enhanced affinity of the COF for CO_2 following the incorporation of Mn(I) centers. Similar enhancement in affinity following incorporation of metal centers has also been reported in previous studies.[68, 147]

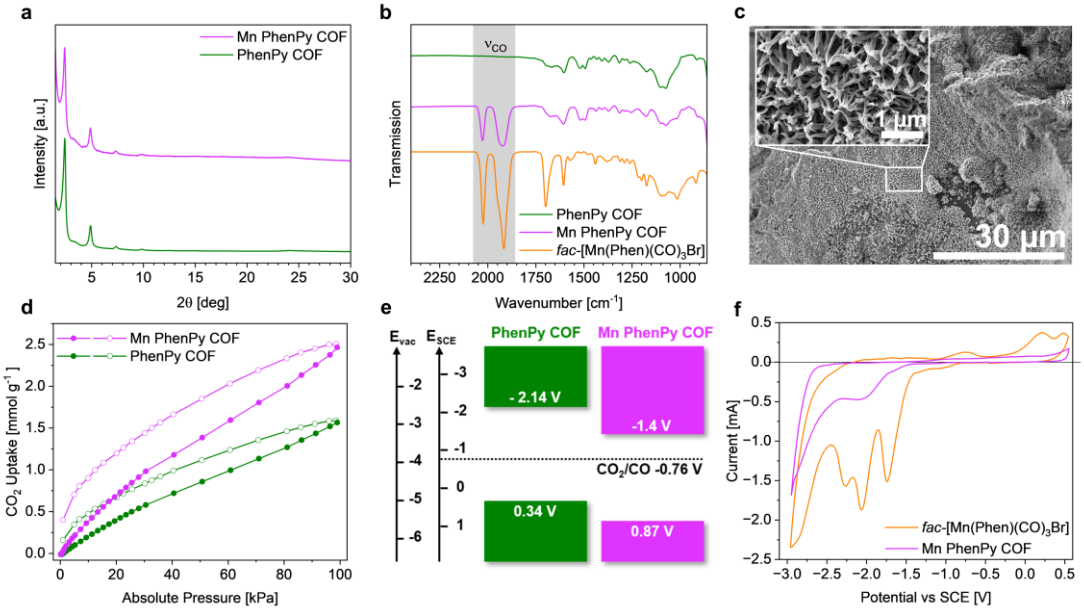


Figure 68. (a) PXRD patterns of the **PhenPy** and the **Mn PhenPy** COFs. (b) FTIR spectra of **PhenPy** and **Mn PhenPy** COF, as well as of the molecular analog *fac*-[Mn(**Phen**)$(CO)_3$Br]. (c) SEM micrographs of the **Mn PhenPy** COF. (d) CO_2 sorption measurements at 273 K (0 °C) indicating an enhanced affinity of **Mn PhenPy** COF for CO_2 (filled dots: adsorption, open dots: desorption). (e) Energy levels of the two COFs obtained from Tauc plot fitting of the optical absorption onsets and CV measurements (Figures S13, S14), and the CO_2 to CO reduction potential. (f) Cyclic Voltammetry of **Mn PhenPy** COF and *fac*-[Mn(**Phen**)$(CO)_3$Br] measured in a three-electrode setup in acetonitrile ($TBAPF_6$, 0.1M) under Ar at a scan speed of 10 mV s^{-1}. The colours are assigned as follows: **PhenPy** (green)**, Mn PhenPy** (pink), *fac*-[Mn(**Phen**)$(CO)_3$Br] (orange).

It is well established that the incorporation of metal centers influences the electronic properties of organic frameworks. Hence, changes in electronic structure of the COF upon immobilization of Mn were investigated using UV-vis measurements. **Figure D7** shows that the absorption onset of **Mn PhenPy** is red-shifted by approx. 120 nm compared to its pristine counterpart. Similar red-shifts upon incorporation of metal centers have been reported in the literature.[68, 351, 383] Supported by band structure calculations, Kamiya *et al.* assigned the optical shift to the presence of metal 3*d* orbitals introduced below the conduction band of the

COF.[400] Direct band gaps of 2.48 eV for **PhenPy** and 2.23 eV for **Mn PhenPy**, respectively, were determined by Tauc plot analysis (**Figure D8**).[401] Consistent with previously reported studies,[402-404] cyclic voltammetry (CV) measurements under oxidative conditions were performed, enabling the determination of the valence band (VB) energies of the pristine COF and the Mn(I)-decorated COF at -5.02 eV and -5.51 eV, respectively, relative to the vacuum level (**Figure D9**). Combining CV and UV-vis results, the conduction band (CB) energies of the two materials were estimated. The resulting energy levels diagram (**Figure 68e**) indicates that both COFs are thermodynamically capable of reducing CO_2 to CO.

To access the ability of the COF structure to inhibit the formation of the undesirable Mnº-Mnº dimer species upon electroreduction, CV curves were recorded for **Mn PhenPy** and its molecular analog *fac*-[Mn(**Phen**)$(CO)_3$Br] at negative applied potentials (**Figure D10**). Under Ar atmosphere with anhydrous CH_3CN as the electrolyte, *fac*-[Mn(**Phen**)$(CO)_3$Br] displayed prominent peaks at -1.73 V and -2.05 V *vs*. SCE in the forward scan and two peaks at -0.75 and 0.21 V *vs.* SCE during the reverse CV scan, which were absent in **Mn PhenPy** COF (**Figure 68f**). The electrochemical behavior of molecular and immobilized Mn(I) complexes has been extensively studied applying a wide range of spectroscopic and electrochemical techniques.[373, 377, 378] Accordingly, the observed CV peaks can be attributed to the formation and respective reoxidation of the Mnº-Mnº dimer and the mononuclear $[Mn(L)(CO)_3]^-$, formed by the two-electron reduction of the dimer.[283] A more detailed analysis of the redox features of the molecular analog *fac*-[Mn(**Phen**)$(CO)_3$Br] is presented in **Figure D10**. The absence of these redox processes in the CV profile of **Mn PhenPy** COF indicates that anchoring the Mn(I) complex to the COF framework *via* its phenanthroline moieties effectively

suppresses the formation of the undesired dimer. Lloret-Fillol *et al.* reported on the ability of a bipyridine-based COF to impose structural constraints on the Mn(I) complex, thereby preventing dimerization. However, they were unable to achieve a similar complete suppression of Mn^0-Mn^0 formation using a phenantroline-based COF, in contrast to our findings. [386] We propose that the high crystallinity and porosity of the herein synthesized **PhenPy** COF plays a crucial role in effectively constraining the Mn(I) centers within the COF framework, thereby effectively preventing dimerization.[320]

Electrocatalytic CO_2 Reduction.

Given its promising electrochemical properties for CO_2 reduction, the **Mn PhenPy** COF was tested as an electrocatalyst for CO_2 reduction to CO in a MEA cell. Gas diffusion electrodes were fabricated by spray-coating an ink containing the COF as the active material onto carbon paper. XPS measurements were conducted to confirm the presence of characteristic Mn(I) and Br peaks in the electrode (**Figure 67d–f**). After immobilization of the **Mn PhenPy** COF onto the GDE, the COF-related peaks decrease, likely due to the low COF loading used during electrode preparation. Additionally, F peak is detected as a result of the PTFE coating on the carbon paper, which is used to impart hydrophobicity. While Mn(I) and Br signals are barely visible in the survey spectrum, high-resolution scans allow for their unequivocal identification. The Mn 2p doublet exhibits a similar pattern to that observed for the **Mn PhenPy** COF bulk material, although the peaks are slightly shifted to lower binding energies indicating electronic interactions between the COF and the electrode surface.

To evaluate the CO_2 reduction activity, selectivity and stability of the **Mn PhenPy** COF, measurements were conducted under potentiostatic conditions applying a full-cell potential ranging between 2.6 and 3.2 V, with each potential step maintained for 30 minutes, while monitoring the current density and CO production. The gaseous products exiting the cell were carried by the continuous CO_2 flow into a gas sampling bag, from which aliquots were collected using a gas-tight syringe and injected into a gas chromatograph for CO and H_2 quantification.

To benchmark the catalytic performance of the **Mn PhenPy** COF, comparative measurements were carried out under identical conditions using the well-established complex d *fac*-[Mn(bpy)$(CO)_3$Br] as a reference catalyst.[283]Like the **Mn PhenPy** COF, the molecular catalyst was spray-coated onto carbon paper and integrated as GDE into the MEA cell. First reported in 2011 by Chardon-Noblat, Deronzier, and co-workers as an active and selective catalyst for CO_2 reduction to CO, fac-[Mn(bpy)$(CO)_3$Br] has since been extensively investigated as both an electro- and photocatalyst.[283, 399] The catalytic performances of **Mn PhenPy** COF and the reference complex are presented in **Figure 69b-c**.

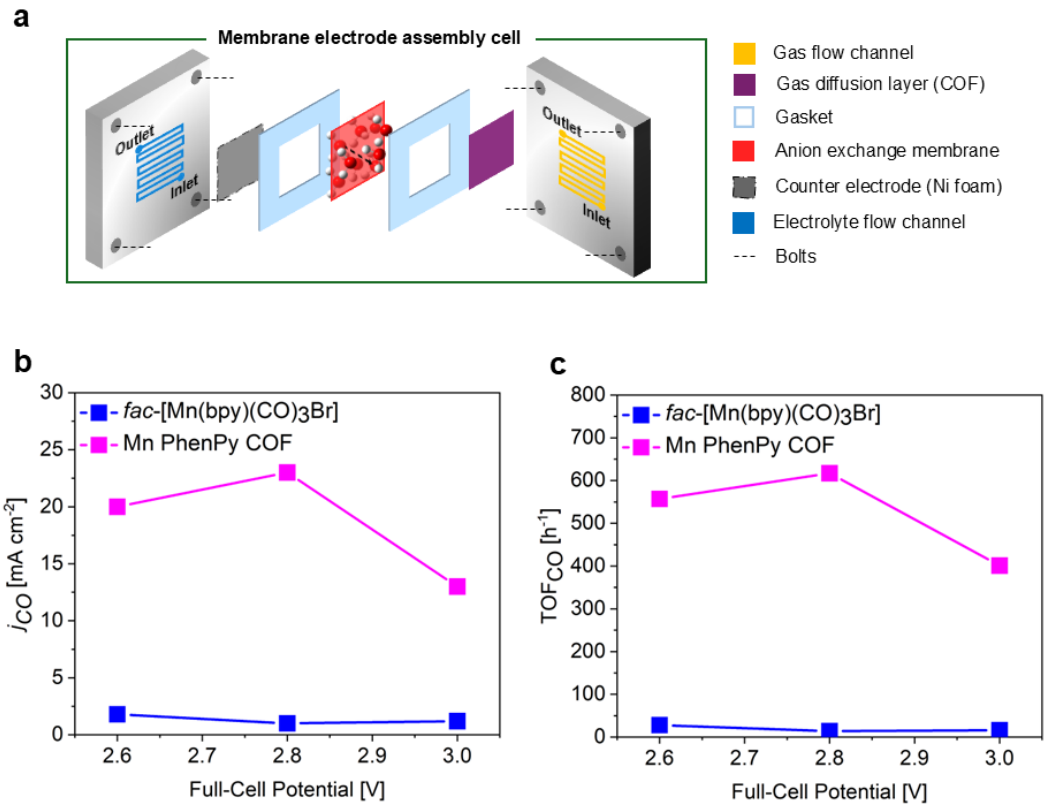


Figure 69. (a) Schematic representation of the catholyte-free MEA cell architecture employing a GDE with **Mn PhenPy** COF as active electrocatalyst. (b) Partial current densities for CO formation j_{CO} (chronoamperometry) and (c) the respective TOF for CO, TOF_{CO}, of **Mn PhenPy** COF and *fac*-[Mn(bpy)(CO)$_3$Br] at different applied full-cell potentials (details in Table S1) measured using a catholyte-free MEA cell with 1 M KOH as anolyte and a *Sustainion*® anion-exchange-membrane.

Using the pristine **PhenPy** COF as an electrocatalyst in this cell configuration resulted in no detectable CO formation. In contrast, **Mn PhenPy** demonstrated high partial current densities for CO production, reaching j_{CO} = 23 mA cm^{-2} at 2.8 V, before declining at higher potentials (**Figure 69b**). The benchmark catalyst, *fac*-[Mn(bpy)(CO)$_3$Br], showed a decrease in partial CO current density with increasing potential, dropping from 1.8 mA cm^{-2} at 2.6 V to 1.2 mA cm^{-2} at 3.0 V (**Table 10**). The GC-analysis of the product stream revealed that **Mn PhenPy** COF demonstrated high CO_2 to CO conversion, producing 222

μmol cm^{-2} of CO within 30 minutes under an applied cell voltage of 2.8 V, resulting in a maximum turnover number (TON_{CO}) of 308, and a turnover frequency (TOF_{CO}) of 617 h^{-1} (see **Table D1** for details on the TON_{CO} and TOF_{CO} calculations). This confirms that the Mn(I) centers act as catalytically active sites within the COF.

Table 10. Comparison of performance of a selection of Mn-based CO_2 reduction electrocatalysts.

catalyst		**electrolyte**	**cell type**	n_{CO} **[μmol cm^{-2}]**	j_{CO} **[mA cm^{-2}]**	TOF_{CO} **[h^{-1}][a)]**	FE_{CO}**(%)**	**Ref.**
Mn PhenPy COF	2.6 V	catholyte-free anolyte: 1M KOH	MEA cell	189	20	557	8	**This work**
	2.8 V			222	23	617	17	
	3.0 V			128	13	401	11	
fac-[Mn(bpy)$(CO)_3$Br]	2.6 V	catholyte-free anolyte: 1M KOH	MEA cell	19	1.8	28	3	**This work**
	2.8 V			10	1	14	1	
	3.0 V			11	1.2	16	1	
COF_{bpyMn} |NT[b)]		$NaHCO_3$ (0.5 M) pH 7.4	H-cell	114	15	190	55	[320]

COF_{PTMn}|NT[c)]	$NaHCO_3$ (0.5 M) pH 7.4	H-cell	10	8[d)]	10	30	[386]
Mn-MOF	CH_3CN + 0.25% acetic acid	H-cell	0.03	-	3.5	-	[405]
CNT|Mn(pyr)	$KHCO_3$ (0.5 M) pH 7.4	three-electrode setup	46	2	175	34	[377]
[Mn-CH_3CN]|MWCNT	$K_2B_4O_7$ (0.1 M), K_2SO_4 (0.2 M) pH 6.6	three-electrode setup, flow reactor	74	5.2	70	84	[406]
Mn(bpy)|MWCNT	PB (0.06 M) pH 7.4	three-electrode setup	3	1	25	51	[378]
[Mn(bpy)$(CO)_3$Br]|GC	CH_3CN + 8% MeOH	three-electrode setup	0.45	-	362		[407]

[a)] TOF ($n_{CO}/(n_{Mn,total} \cdot time)$).[b), c)] Total amount of Mn deposited: 225 nmol cm^{-2} and 900 nmol cm^{-2}, respectively. [d)] Value calculated from information provided in the reference. PB, NT and GC stand for phosphate buffer, nanotubes and glassy carbon, respectively.

At an applied potential of 2.8 V, the benchmark molecular catalyst achieved a maximum TON_{CO} of only 8 and TOF_{CO} of 14 h^{-1}. In other words, immobilizing the Mn(I) complex within the porous COF structure led to a 40-fold enhancement in TOF (**Figure 69c**). Furthermore, the **Mn PhenPy** COF outperforms previously reported Mn-based hybrid electrocatalysts for CO_2 reduction (**Table 10**).[320, 377, 378, 386, 405-407] Notably, our analysis is based on the total amount of catalytic sites embedded in the COF. This approach may underestimate the true TON and TOF values, as other studies often report values normalized to the estimated electroactive sites, typically less than 25% of the total catalyst loading in COFs, yielding significantly higher apparent activities.[231, 320, 386] However, quantifying the electroactive sites in a MEA cell is particularly challenging, requiring significant modifications to the cell architecture. Addressing this remains a key direction for future research.

Furthermore, we measured the Faradaic efficiencies for CO and H_2 evolution (FE_{CO} and FE_{H2}, respectively) as a function of the applied potential (**Figure 70a**). H_2 generated *via* the competing cathodic hydrogen evolution reaction, is the dominant product, with a FE_{H2} of 83%, likely due to the high carbon loading in the GDE. As indicated by the Faradaic efficiency results, the current values may not represent the highest reported in the literature. However, the achieved H_2/CO ratio is well-aligned with the requirements of important downstream applications, such as Fischer-Tropsch synthesis and related processes.

Additionally, j_{CO} values (23 mA cm^{-2}) achieved in this study rank among the highest reported in the literature for COF based materials, further emphasizing the exceptional performance of the Mn-COF catalyst. To further

assess the system's stability, we conducted long-term electrolysis over 6 hours at 2.8 V (**Figure 70b**). While H_2 remains the primary product, the FE_{CO} decreases only slightly from 17% to 12% during the experiment, and TOF remains at approximately 73% of its initial value. These results strongly support the stability of the Mn PhenPy COF under the tested conditions and indicate that Mn^0-Mn^0 dimer formation is not significant in the MEA system. Consequently, the sustained Faradaic efficiency evinces that the catalyst remains both active and selective for CO_2 reduction throughout the duration of the experiment.

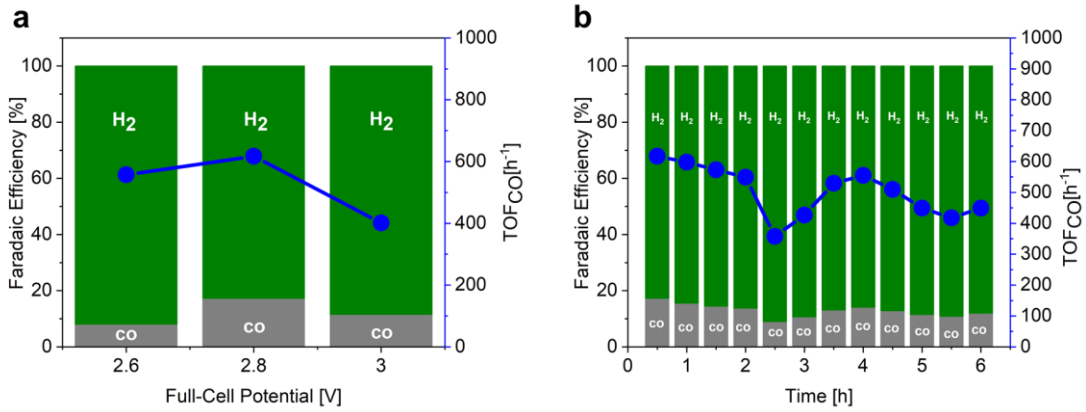


Figure 70. (a) Faradaic efficiencies (left scales) and TOF (blue dots, right scales) values as a function of different applied potentials along with (b) long-term stability experiments conducted at applied full-cell potential of 2.8 V recorded for **Mn PhenPy** COF.

The results discussed above indicate that the COF framework not only enhances the catalytic performance of the Mn(I) complex but also improves its stability, enabling operation at higher potentials. This enhanced stability can be attributed to the immobilization of Mn(I) centers within the porous COF structure, which effectively suppresses the formation of the detrimental Mn^0–Mn^0 dimer. We propose that the CO_2 electrocatalytic cycle of the **Mn PhenPy** COF aligns with previously reported mechanisms for similar Mn-based COF hybrids, wherein the formation of a pentacoordinated Mn(I) intermediate facilitates the reduction of

CO_2 to CO.[386] [320]Furthermore, we attribute the outstanding catalytic performance to the high crystallinity of the **Mn PhenPy** COF, which stabilizes catalytically active Mn single sites within an accessible porous framework. Additionally, the MEA cell architecture plays a crucial role by enhancing mass transport, increasing CO_2 availability at the active sites, and improving catalyst integration into the electrochemical environment, thereby maximizing overall efficiency.

6.6. Conclusion

In conclusion, we report the successful design and synthesis of a highly crystalline COF-based electrocatalyst, **Mn PhenPy**, for the efficient reduction of CO_2 to CO in a catholyte-free MEA cell. The porous and highly ordered **PhenPy** COF serves as a robust scaffold for immobilizing Mn(I) centers, offering pre-defined coordination sites through its phenanthroline moieties. The resulting **Mn PhenPy** hybrid exhibits enhanced CO_2 affinity and excellent electrochemical properties, making it a highly effective material for use in GDEs within MEA electrolyzers. Compared to the molecular benchmark catalyst fac-[Mn(bpy)$(CO)_3$Br], **Mn PhenPy** demonstrates superior catalytic performance, achieving a 40-fold enhancement in turnover number (TON = 308) and turnover frequency (TOF = 617 h^{-1}) at an applied cell potential of 2.8 V. Notably, **Mn PhenPy** also outperforms previously reported Mn-based hybrid electrodes used in H-cell configurations, particularly in terms of TOF. In addition to its high activity, **Mn PhenPy** displays enhanced operational stability. Unlike the molecular catalyst, which shows declining current densities at elevated potentials, **Mn PhenPy** reaches a peak partial CO current density of 23 mA cm^{-2} at 2.8 V. Long-term electrolysis experiments reveal only a modest decrease in CO Faradaic

efficiency from 17% to 12% over 6 hours. These advances can be attributed to the structural advantages of the COF framework, including the stabilization of active Mn intermediates and effective suppression of deactivation pathways such as Mn^0–Mn^0 dimer formation. Importantly, this work represents the first successful application of a COF-based electrocatalyst in a catholyte-free MEA configuration, highlighting the potential of crystalline porous frameworks for advancing CO_2 electroreduction technologies.

Part III

Chapter 7

Towards Multi-site Cascade Catalysts for Sequential CO_2 Reduction

7.1. Introduction

One of the major challenges in catalytic CO_2 reduction is the selective production of highly reduced carbon-based products. Although remarkable advances have been achieved in the development of molecular and heterogeneous catalysts capable of selectively converting CO_2 into two-electron products such as CO and $HCOO^-$, extending these reactions toward more reduced compounds including CH_3OH, CH_4, and multicarbon products (C_{2+}), remains more challenging. [408-410]

As was shown in the previous chapter, this work has advanced on the development of catalysts for selective reduction of CO_2 into CO, which opens the possibility to the subsequent conversion of CO into more highly reduced products. Such topic is a matter of extensive discussions in the literature.[411] CO is not only an important industrial feedstock but also represents a key intermediate in numerous catalytic CO_2 reduction pathways.[412] Consequently, the selective production of CO may be viewed not as the final objective, but rather as the first step toward the synthesis of more energy-dense liquid fuels, through the so-called CO reduction reaction (CORR).[12, 413-415]

Among them, methanol (CH_3OH) is a high value-added chemical/fuel with high energy density and easy storage. Currently, CH_3OH is produced from

syngas. Alternatively, recapturing CO_2/and directly converting it into CH_3OH would help to mitigate CO_2 emissions and achieve full carbon cycling. The integration of CO_2 capture with in-situ reduction of CO_2 into CH_3OH in the liquid phase is thus attractive.

Therefore, inspired by natural processes where, rather than employing multifunctional enzymes that catalyzes every single reaction step, highly specialized enzymes are organized into sequential metabolic pathways, in which the product generated by one catalyst immediately becomes the substrate for the next catalytic center. This is the basic concept of cascade catalysis, also referred to as *tandem* catalysis. The implementation of cascade systems enables the designing of multi-site catalysts that synergize different active sites for promoting the reduction of CO_2 to *CO intermediates and further multielectron reactions to generate high valued liquid products.

Cascade catalytic reactions are typically divided into three different types (**Figure 71a-c**), which are referred as orthogonal, assisted or self- cascade catalytic reactions. [416]

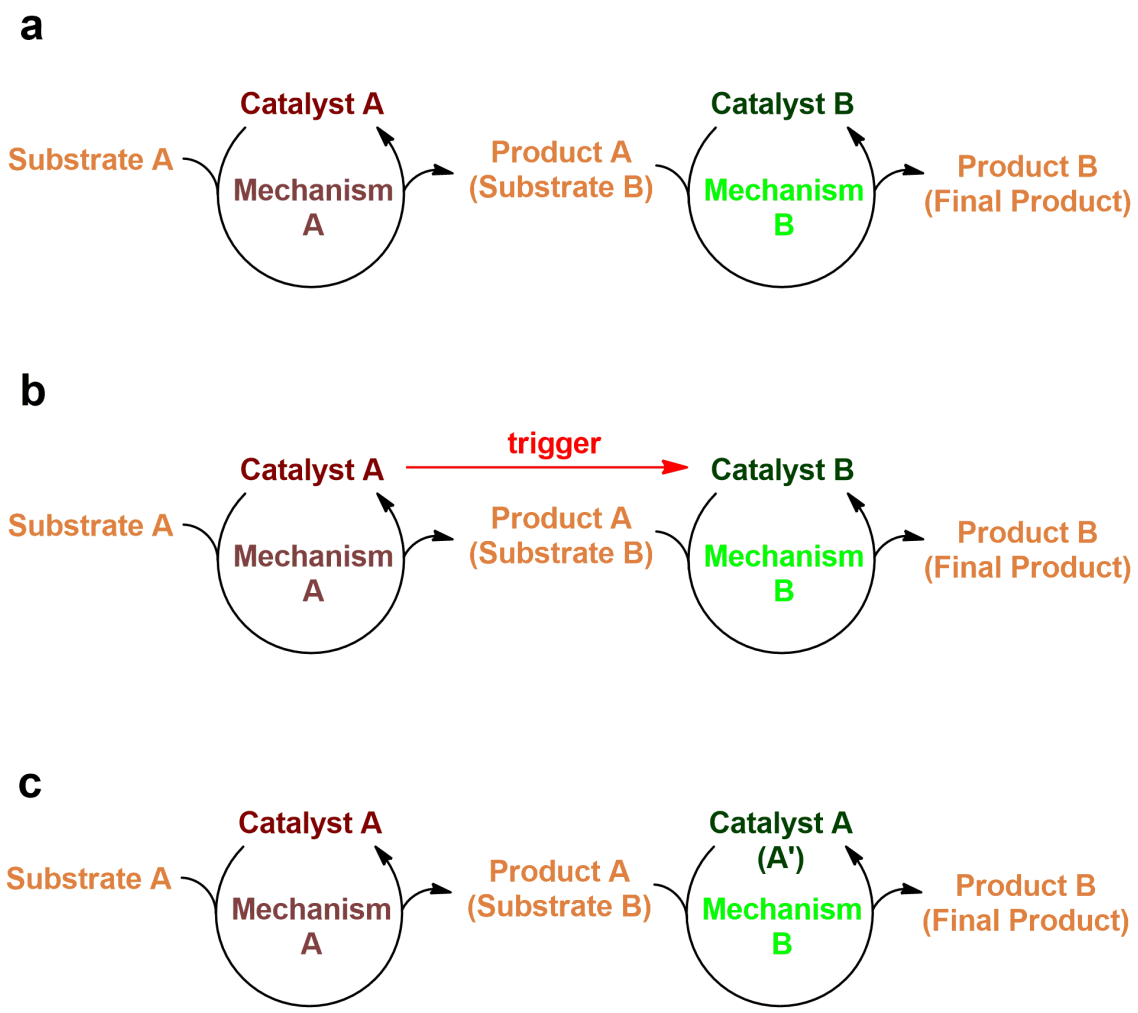


Figure 71. Schematic illustration of an a) Orthogonal, b) Assisted and c) Self-cascade Catalytic Reactions.

Orthogonal reactions, **Figure 71a**, are characterized by their mutual independence, which involves two or more functionality distinct and noninterfering catalysts in which the starting substrate (A) undergoes preferential reaction with Catalyst A to generate Product A, which in turn functions as Substrate B (the substrate for Catalyst B). For the assisted cascade catalytic reactions, **Figure 71b**, the principle is very similar, however there is a trigger that transforms the catalyst A into catalyst B. In contrast with the orthogonal systems, the two catalytic processes cannot occur simultaneously, as the two catalysts do not coexist. For the self- cascade catalytic reaction, the catalyst A acts on

Substrate A to convert it to Product A. Product A functions as Substrate B, entering the second type of catalytic transformation mediated by Catalyst A (or A'). The reaction selectivity is determined by the local concentration of the Substrate A and Substrate B, i.e. Product A.

Different thermocatalytic, electrocatalytic and enzymatic/biocatalytic strategies have been successfully reported as cascade systems for synthesizing multielectron reduction products and it is anticipated that cascade catalytic systems will progressively emerge as preferred approach for CO_2RR.[417] However, as the cascade system involves diverse catalytic reactions, it can be challenging to identify an operational window compatible with all catalysts due to significant differences in reaction conditions, as compartmentalization and compatibility, intermediates separation and purification after each reaction, leading to complications such as loss of intermediates and reduced catalyst reuse efficiency. [418-420]

One strategy to overcome these limitations is the organization of complementary catalytic sites within a single material. Rather than physically separating individual catalysts into different reactors or reaction compartments, multifunctional catalytic platforms seek to co-localize distinct active sites within the same solid framework, thereby minimizing intermediate diffusion distances while facilitating sequential catalytic transformations.

The above-mentioned design has recently begun to emerge in the literature.[420, 421]Two examples are shown in **Figure 72a** and are included in the class of self-cascade catalysts.[422] [423] O'Mara and co-workers developed a nanoconfined catalyst consisting of a silver core surrounded by a porous copper

shell, where the two catalytic domains cooperatively promoted the formation of n-propanol and propionaldehyde from CO_2 at potentials as low as −0.6 V *vs*. RHE.

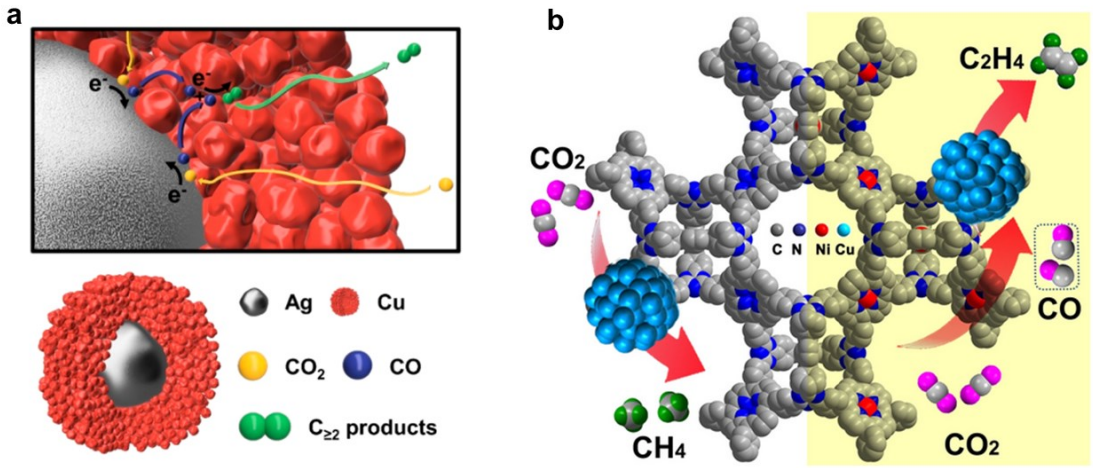


Figure 72. Schematic illustration of Cascade Reaction on a) Ag−Cu Nanozyme and b) PTF(Ni)/Cu for CO_2RR showing the *CO intermediate diffusing through the interface of the hybrid materials for the formation of C2+ products. Adapted from O'Mara[422] and Meng[423].

Meng and collaborators have developed and prepared an earth abundant elements-based tandem catalyst PTF(Ni)/Cu (**Figure 72b**).[423] This structure is basically a class of COF, with a porphyrinic triazine framework (PTF), which they uniformly dispersed Cu NPs on PTF(Ni). The synergistic ensemble of PTF(Ni) and Cu NP sites facilitate large generation of CO from PTF(Ni) sites and followed efficient transfer to the nearby Cu NPs with a high coverage of *CO intermediates, which is beneficial for their further dimerization and reduction to C_2H_4. A significantly enhanced selectivity of C_2H_4 was obtained on PTF(Ni)/Cu, achieving 57.3% of FEC_2H_4, which is about 6 times higher than that of the non-tandem contrast catalyst PTF/Cu. The operando ATR-FTIR and DFT calculations elucidated the great significance of the high concentration of local CO on Cu sites

during C_2H_4 formation, while a low CO concentration was favorable for the formation of CH_4.

Porous materials, like Covalent Organic Frameworks (COFs) or Conjugated Microporous Polymers (CMPs), are particularly attractive for implementing this concept. Their modular architecture enables the precise incorporation of multiple molecular catalytic sites at predetermined positions within the same framework while preserving permanent porosity and structural order. Such characteristics make them promising platforms for constructing cascade catalytic systems, in which reaction intermediates generated by one active site can be sequentially transformed by neighboring catalytic centers within a single porous material. To date, however, most cascade CO_2 reduction systems rely on heterogeneous nanostructures or physically coupled catalysts.[417, 420] The development of molecularly defined porous materials capable of integrating complementary catalytic functions within a single crystalline framework remains largely unexplored.

For clarity, the term *multi-site cascade catalyst* is used throughout this chapter to describe catalytic architectures in which two or more functionally complementary active sites are incorporated within the same porous framework to promote sequential reaction pathways. Such general nomenclature is actually due to the fact that the mechanism of the catalytic reactions is not fully uncovered and therefore it is not possible yet to classify them based on the concepts discussed in **Figure 71**.

Motivated by this concept, this chapter explores preliminary strategies for constructing *multi-site cascade catalyst* COFs for sequential CO_2 reduction. Two distinct architectures are investigated. The first combines Lehn-type Re(I)

tricarbonyl catalysts ([$Re(CO)_3(bpy)Cl$]), which selectively reduce CO_2 to CO under photocatalytic conditions, with Tanaka-type molecular catalysts (*cis*-$[Ru(bpy)_2(CO)_2]^{2+}$) for promote further reduction toward CH_3OH. The second explores an electrocatalytic analogue in which Mn(I)-bipyridine catalytic centers are integrated with cobalt phthalocyanine units within the same COF architecture, able respectively to reduce CO_2 to CO and sequentially reduce CO to CH_3OH. Although still at the proof-of-concept stage, these systems establish a new design strategies for *multi-site cascade catalyst* based on COFs for sequential CO_2 reduction capable of integrating complementary molecular functions within a single material.

7.2. Experimental Section

Materials. All solvents were purchased from *Sigma Aldrich*, *Acros* or *TCI Europe* in the common purities *purum*, *puriss* or *reagent grade*. The materials were used as received without additional purification and handled in air unless otherwise noted.

Synthesis of bpyPyr COF. In a 6 mL Schott-Duran culture tube, a solid mixture of 2,2'-bipyridine-5,5'-dicarbaldehyde, **bpy(CHO)$_2$** (8.5 mg, 0.03 mmol) and 1,3,6,8-tetrakis(4-aminophenyl)pyrene, **Pyr**, (11.3 mg, 0.015 mmol) was suspended in 1000 µL of 1,4-dioxane Subsequently, 100 µL of acetic acid (aqueous, 6 M) was added. The culture tube was tightly sealed and heated at 120°C for 3 days. The resulting suspension was filtered and the isolated orange-red solid was washed with acetone and THF. The final product was Soxhlet-extracted with THF for 3 h.

Synthesis of Re bpyPyr. The obtained **bpyPyr COF** (50 mg) was refluxed with different amounts of [$Re(CO)_5Cl$] (50wt%, 100wt%) in 15 mL of toluene for 1 h. The resulting dark powder was filtered while hot and washed thoroughly with toluene and diethyl ether before drying under vacuum overnight.

Synthesis of [$Ru(bpy)(CO)_2(OTf)_2$]. It was prepared as previously reported.[415] The [$Ru(CO)_2Cl_2$] (1.0 g, 4.33 mmol) and 2,2′-bipyridine (1.03 g, 6.66 mmol) were dissolved in methanol (50 mL) and heated at reflux under Ar atmosphere for 1 h. The reaction flask was cooled to room temperature, the pale-yellow solid was collected by filtration, washed with cold methanol and diethyl ether, and dried under vacuum. The resulting solid was redissolved in CH_3CN and refluxed in the presence of silver trifluoromethanesulfonate (AgOTf) under an Ar atmosphere. The precipitate (AgCl) was filtered off, and the resulting filtrate was roto vapored, affording the final dark-yellow powder. Yield: 1.01 g (1.6 mmol, 38%). ^{1}H NMR (400 MHz, CD_3CN) δ 9.17 (ddd, J = 5.5, 1.6, 0.9 Hz, 2H), 8.47 (dt, J = 8.2, 1.1 Hz, 2H), 8.25 (td, J = 7.9, 1.5 Hz, 2H), 7.75 (ddd, J = 7.7, 5.5, 1.3 Hz, 2H).

Synthesis of Ru bpyPyr. The previously synthesized [$Ru(bpy)(CO)_2(OTf)_2$] (50 mg, 0.08 mol) was refluxed with 50 mg of bpyPyr COF in 15 mL of a 2:1 water/ethanol mixture under an Ar atmosphere for 12 h. The resulting dark powder was filtered hot and washed thoroughly with water before drying under vacuum overnight.

Synthesis of Re Ru bpyPyr. The obtained **Re bpyPyr COF** (50 mg) was refluxed with [$Ru(bpy)(CO)_2(OTf)_2$] (50 mg, 0.08 mol) in 15 mL of toluene for 1 h. The resulting dark powder was filtered hot and washed thoroughly with water before drying under vacuum overnight.

Synthesis of BIH. The (1,3-dimethyl-2-phenyl-2,3dihydro-1H-benzo[d]imidazole) was prepared as previously reported.[18] First, 2-phenyl-1,3-dimethylbenzimidazolium iodide was obtained from a two-step methylation reaction of 2-phenylbenzimidazole. The solid was reduced in the presence of $NaBH_4$ to yield BIH. **BIH**: ^{1}H NMR (400 MHz, DMSO-d^6, δ): 7.55 (dd, J = 6.4, 1.9 Hz, 2H), 7.45 (dd, J = 5, 19 Hz, 3H), 6.62 (dd, J = 5.4, 3.3 Hz, 2H), 6.45 (dd, J = 5.4, 3.2 Hz, 2H), 4.87 (s, 1H), 2.48 (s, 6H).

Fourier-transform infrared spectroscopy (FTIR) measurements were performed with a Bruker VERTEX 80v FTIR spectrometer equipped with a liquid nitrogen-cooled MCT detector and a 4000 cm^{-1} low-pass filter, with a spectral resolution of 2 cm^{-1}.

Photocatalytic Studies. Photocatalytic experiments were performed using 1.0 mg of **Re-Ru bpyPyr** or **Re bpyPyr** with 50 mg of BIH (0.22 mmol) and 31 mg of LiOTf (0.022 mmol) in toluene under CO_2 or Ar (control experiments) atmosphere. The photocatalytic reactor was illuminated with a Newport Oriel 1 kW Solar Simulator (model 91191-1000; 900 W Xe lamp and LP420 long pass filter) connected in-line to the sample loop of a gas chromatograph (Agilent GC 8890). Gaseous products were separated with a carbonPLOT column and a molecular sieve column in series. The carbonPLOT column decelerated the elution of CO_2 relative to the other lighter gases (O_2, N_2, H_2, and CO), while the molecular sieves separated each gas with specific retention times. A thermal conductivity detector (TCD) was used to detect O_2, N_2, and H_2. A methanizer, equipped with a nickel hydrogenation catalyst, was paired with a flame ionization detector (FID) to detect CO_2 and CO. Argon (Ar) was used as the carrier gas.

The liquid products from **Re bpyPyr** and **Re-Ru bpyPyr** catalysts were detected after photocatalysis using Bruker 400 MHz Nuclear Magnetic Resonance (^{1}H NMR) spectroscopy with solvent (toluene) suppression by mixing ^{1}H NMR analysis. The peak of CH_3OH was detected at δ = 3.06 ppm.

Preparation of gas diffusion electrodes. Gas diffusion electrodes (GDEs) were prepared by spray coating an ink on a carbon paper substrate (GDL-Sigracet, 39B) using an airbrush (Vonder). The ink was composed of 2.0 mg of **Mn bpyCoPc** catalyst, 1.0 mg of multi-walled carbon nanotubes (MWNT), 10.0 µL of ionomer (5% wt Nafion solution) and 2.0 mL of ethanol (Aldrich 99.0 %). The mixture was submitted to an ultrasonic probe sonicator (Sonics & Materials INC, VCX130) with a power rating of 130 W for 30 minutes. The homogenized solution was then deposited onto a 1.0 cm^2 area of carbon paper using the airbrush, with approximately 50% of the slurry mass lost during deposition, as determined by the difference between the initial and final mass of the carbon paper electrode. The electrode was subsequently dried in an oven at 80 °C for 24 h. Finally, the prepared electrode was applied as working electrode for the electrochemical reduction of CO_2.

Electrochemical CO_2 reduction in flow cell. All electrochemical measurements were carried out on a potentiostat/galvanostat (Autolab PGSTAT204, Metrohm). CO_2 reduction performance was evaluated in a commercial flow cell. GDEs containing **Mn bpyCoPc** (1.0 cm^2) were used as working electrode, Ni foam as anode, leek-free $Ag/AgCl/KCl_{(sat)}$ as the reference electrode and 0.5 M $KHCO_3$ was used as electrolyte, circulating at 5 mL mim^{-1}. The half-cells were connected with an anion exchange membrane (Fumasep®, 110-140 µm thick) and CO_2 gas was directly fed to the cathode at 30 mL min^{-1}.

Measurements were carried out under potentiostatic conditions applying -2.0 V for 90 minutes. The current density was monitored to assess the electrode's performance. Gaseous products leaving the cell were transported by the continuous CO_2 flow cell to a gas sampling bag, where aliquots of 500 µL were collected with a gas-tight syringe and injected into a gas chromatograph equipped with thermal conductivity detection (GC-TCD, PerkinElmer Clarus 580) for the quantification of CO. The GC-TCD is equipped with two columns (Porapak N 2 mm and molecular sieve) and a detector for thermal conductivity. The measurements were performed at 120 °C on the injector and 150 °C on the detector, with a thermal ramp of 35–120 °C. Ar was used as carrier gas at 30 mL min^{-1}. and CO. Argon (Ar) was used as the carrier gas.

The liquid products of **Mn bpyCoPc** catalyst were detected after electrocatalysis using Bruker 400 MHz Nuclear Magnetic Resonance (^{1}H NMR) spectroscopy with solvent (H_2O) suppression by mixing 560 µL of electrolyte with 80 µL of a solution of 10 mM dimethylsulfoxide (DMSO) as internal standard and 160 µL D_2O. Concentration of CH_3OH and HCOOH were calculated using the ratio of the area of the CH_3OH (δ = 3.4 ppm) or $HCOO^-$ (δ = 8.5 ppm) peak to that of the DMSO internal standard (δ = 2.8 ppm).

FTIR Spectroelectrochemical (IR-SEC) experiments. ATR-IR-SEC cell containing a **Mn bpyPyr COF/**MWNT modified glass carbon working electrode, platinum wire counter electrode, and silver wire pseudo-reference electrode in 0.1 M TBAH/acetonitrile solutions under an Ar/CO_2 atmosphere were employed in the SEC-IR experiments with **Mn bpyPyr COF**. The experiment was performed by modifying the glass carbon electrode surface with a conductive suspension of **Mn bpyPyr COF/**MWNT (see the details on Glass Carbon modification section)

and put in close contact with the ZnSe prism of the ATR instrument, **Figure B10**. A PerkinElmer Frontier spectrometer was used to monitor glass carbon electrode surface coupled with a μAutolab PGSTAT204 potentiostat/galvanostat (Autolab). The spectral region was set to a range from 2100 to 1600 cm^{-1}. A total of 7 scans were co-added for a spectrum with a resolution of 8 cm^{-1} during a cyclic voltammetry with a scan rate of 5.0 mV s^{-1}. Blank Ar and CO_2 saturated acetonitrile solutions with 0.1 M TBAH were used as background for experiments performed under Ar and CO_2 atmosphere, respectively.

Glass Carbon modification. The dispersion was prepared using 1.0 mg of **Mn bpyPyr COF**, 1.0 mg of multi-walled carbon nanotubes (MWNT), 20 mL of ionomer (5% wt Nafion solution) and 980 mL of acetonitrile. The mixture was submitted to an ultrasonic probe sonicator (Sonics & Materials INC, VCX130) with a power rating of 130 W for 30 min until get a stable dispersion. A glass carbon electrode was modified by drop-casting using 100 mL (10 layers of 10 mL each) of prepared dispersion. Between each 10 mL drop, an interval of 5 minutes was allowed completely modification dry before the next layer drop.

7.3. Results and Discussion

7.3.1. Multi-site cascade Re-RubpyPyr catalyst

In Chapter 4, we have shown that the post-synthetic incorporation of $Re(CO)_3$ moieties into the **bpyPyr COF** significantly enhanced the photocatalytic stability for CO_2 reduction compared to its homogeneous counterpart, *fac*-$Re(CO)_3(bpy)Cl$. The immobilized catalyst exhibited improved stability together

with strong visible-light absorption allowing for use λ > 420 nm during the photocatalytic experiments showing selective CO production.

On the other hand, the molecular catalyst originally developed by Tanaka and co-workers,[424] has been recognized as one of the few molecular systems capable of promoting the reduction of CO to CH_3OH under mild reaction conditions.[425] Muller and co-authors showed the sequential conversion of coordinated CO into methanol under a single step using recyclable organic hydride donors, such as BIH, in CH_3CN solution **Figure 73**.[415] Under room-temperature, the rapid quantitative conversion of the initial carbonyl complex into the corresponding formyl intermediate (Ru-CHO^+) was first observed. After three days, the hydroxymethyl species (Ru-CH_2OH^+) became the predominant product, reaching a yield of 47 ± 3% relative to the starting Ru-CO^{2+} complex. Finally, a subsequent irradiation of the reaction mixture with a 505 nm LED for an additional three days induced CH_3OH release, affording an overall CH_3OH yield of 23 ± 1% based on the initial Ru-CO^{2+} concentration, corresponding to a 50 ± 1% conversion of the Ru-CH_2OH^+ intermediate into free CH_3OH.

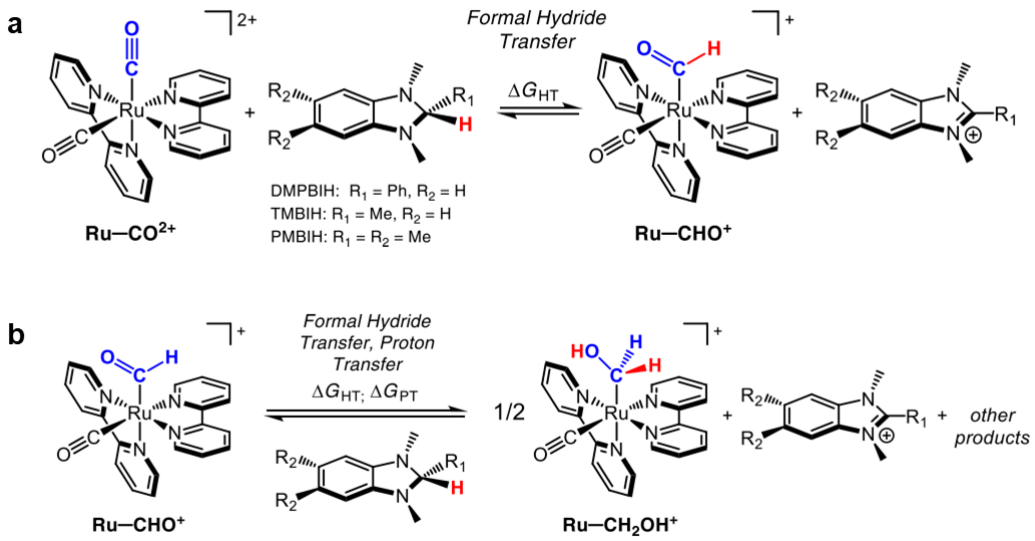


Figure 73. Reaction of *cis*-$[Ru(bpy)_2(CO)_2]^{2+}$ ($Ru-CO^{2+}$) and *cis*-$[Ru(bpy)_2(CO)(CHO)]^{+}$ ($Ru-CHO^{+}$) with organohydride donors (BIHs).

Inspired by these studies, the present work explores whether the catalytic functions responsible for CO formation and its subsequent hydrogenation can be integrated within the same porous structure. In this strategy, Lehn-type Re(I) tricarbonyl catalytic sites, which exhibit high selectivity toward CO_2-to-CO conversion, are combined with Tanaka-type Ru catalytic centers, which are expected to promote the subsequent reduction of CO to CH_3OH. The **Figure 74a** illustrates the chemical structures of the **Re bpyPyr** and **Re Ru bpyPyr** catalysts.

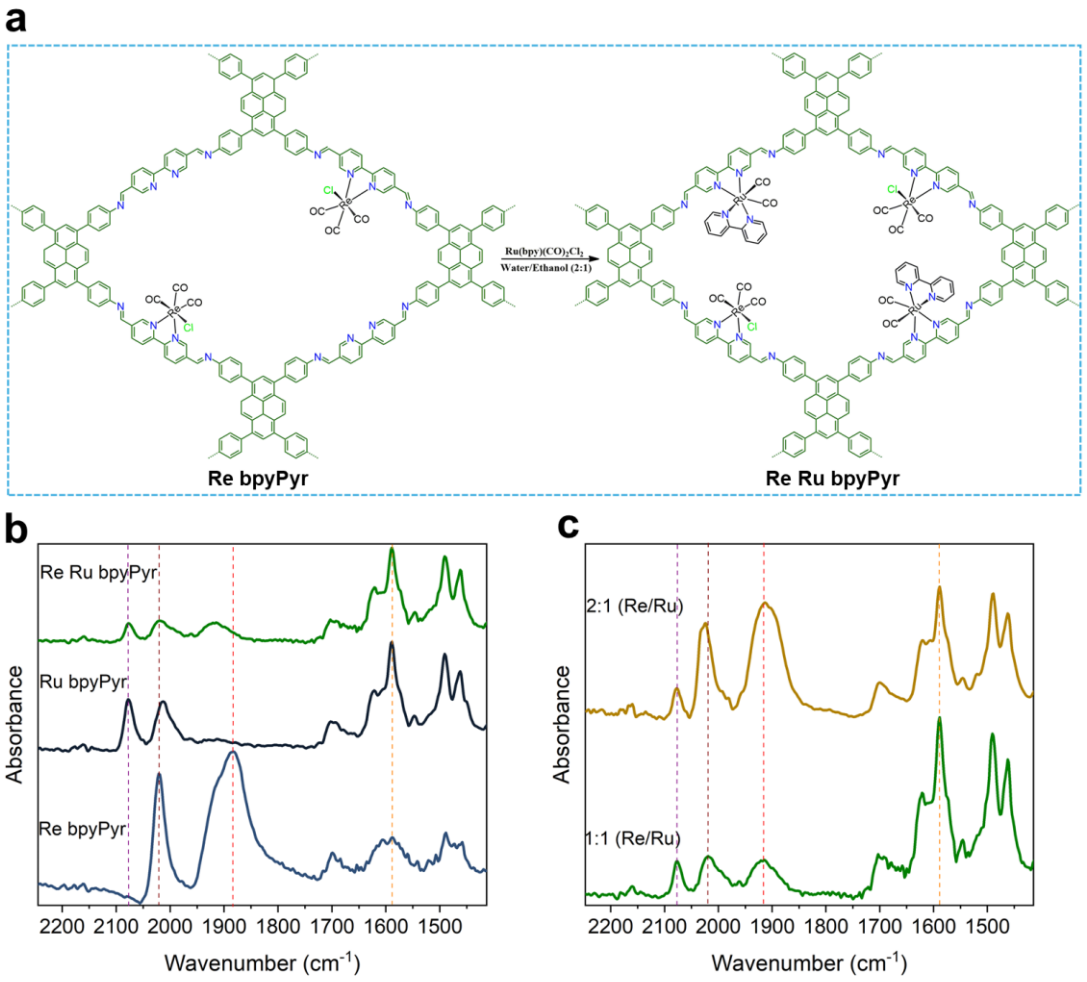


Figure 74. a) Chemical structures of the **Re bpyPyr** and **Re-Ru bpyPyr** materials together with the post-synthetic immobilization strategy for incorporates the $Ru(bpy)_2(CO)_2$ moiety, b) FTIR spectra of **Re bpyPyr, Ru bpyPyr** and **Re Ru bpyPyr** 1:1 (Re/Ru), c) FTIR spectra of **Re Ru bpyPyr** prepared using different Re/Ru molar ratios of 2:1 and 1:1. The **Ru bpyPyr** structure contain only the Ru sites without any Re sites.

The successful incorporation of both molecular catalytic centers into the COF framework was initially investigated by FTIR spectroscopy (**Figure 74b**). The vibrational mode assigned to the imine linkage, ν(C=N), appears at 1590 cm^{-1} and remains unchanged after both post-synthetic metalation, while new absorption bands appear for **Re bpyPyr**, **Ru bpyPyr** and **Re Ru bpyPyr**.

The FTIR spectrum of **Re bpyPyr** presents three characteristics ν(CO) stretching bands at 2021, 1915 and 1885 cm^{-1}, assigned to the facially coordinated $Re(CO)_3$ moiety. In contrast, **Ru bpyPyr** exhibits two ν(CO) stretching bands at 2077 and 2011 cm^{-1}, corresponding to the cis-coordinated $Ru(CO)_2$ moiety.

For the dual-functionalized **Re Ru bpyPyr,** three characteristics ν(CO) stretching bands are observed at 1914, 2024 and 2078 cm^{-1}, which correspond to the overlapping of the characteristic ν(CO) observed for the individual **Re bpyPyr** and **Ru bpyPyr** materials. However, the ν(CO) stretching frequences associated with the Re centers shift toward higher wavenumbers in the presence of the Ru centers. It suggests that the incorporation of both metal centers within the same conjugated **bpyPyr** framework results in a slight reduction in electron density at the Re(I) center after incorporation of the Ru site, indicating efficient electronic communication between the two metal sites though the π-conjugated framework.

Both metal centers were immobilized within the same COF framework using different Re/Ru molar ratios (1:1 and 2:1), which resulted in different relative intensities of the ν(CO) stretching bands associated with the $Re(CO)_3$ moieties, as shown in **Figure 74c**.

The **Re Ru bpyPyr** catalyst was evaluated under photocatalytic CO_2 reduction conditions. The experiments were performed in toluene using BIH as the sacrificial donor in the presence of LiOTf under visible-light irradiation (λ > 420 nm). Toluene was selected as the reaction medium because of its non-coordinating nature, thereby minimizing solvent coordination to the Ru center and potentially facilitating the catalytic turnover required for the subsequent reduction

of CO. The gaseous products were continuously monitored by gas chromatography, whereas the liquid phase was analyzed by ^{1}H NMR spectroscopy to detect the possible formation of CH_3OH.

Control experiments using **Re Ru bpyPyr** under an Ar atmosphere showed no detectable CO evolution throughout the irradiation period and only trace, non-quantifiable amounts of CH_3OH after 24 h of irradiation. This observation is consistent with that previously reported by Muller and co-authors, in which the Tanaka catalyst produces CH_3OH trough the reduction of its coordinated CO ligands under the selected reaction conditions. On the other hand, the control experiment using **Re bpyPyr** showed only the expected CO evolution, while no products in the liquid phase were detected.

In contrast, when the photocatalytic experiments using **Re Ru bpyPyr** were carried out under a CO_2 atmosphere, significant CO evolution was detected after 12 h of irradiation, accompanied by the appearance of a well-defined singlet at δ = 3.06 ppm in the ^{1}H NMR spectrum of the liquid phase, assigned to the methyl (CH_3) protons of CH_3OH (**Figure 75**).

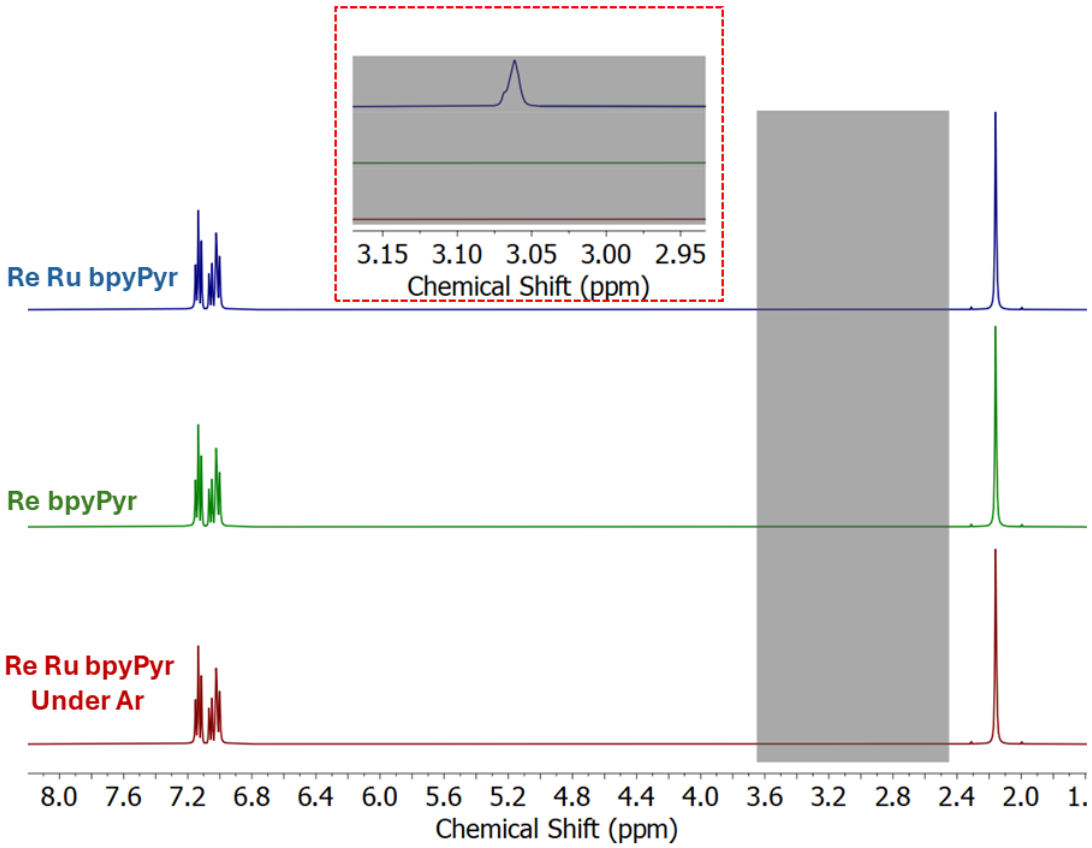


Figure 75. ^{1}H NMR spectra of the liquid phase collected during the light-induced (λ > 420 nm) reaction of **Re-Ru bpyPyr** (under Ar atmosphere), **Re bpyPyr** (under CO_2 atmosphere) and **Re-Ru bpyPyr** (under CO_2 atmosphere) in the presence of BIH (0.22 mmol) and LiOTf (0.22 mmol) in toluene. The highlighted peak is attributed to CH_3OH.

As discussed in Chapter 4, the *fac*-$Re(CO)_3(bpy)Cl$ catalytic centers are highly selective for the visible-light-driven reduction of CO_2 to CO. Consequently, the CO generated at the Re sites is expected to serve as the reaction intermediate for the neighboring Ru catalytic centers. The simultaneous observation of CO in the gas phase together with CH_3OH formation in the liquid phase is therefore consistent with the proposed cascade catalytic mechanism, in which the Re(I) sites promote the initial CO_2-to-CO conversion, followed by the subsequent reduction of CO at the Ru catalytic centers.

Although the present results do not unequivocally demonstrate direct substrate transfer between the two active sites, they provide encouraging preliminary evidence that complementary molecular catalysts can be spatially integrated within a single porous framework to promote sequential CO_2 reduction reactions. Beyond demonstrating the feasibility of this catalyst design, this architecture also provides an attractive platform for mechanistic investigations. By immobilizing the Tanaka catalytic center within a porous framework, the transformation of the coordinated Ru-CO species into the subsequent reaction intermediates may be monitored under heterogeneous photocatalytic conditions using *in-situ* and operando spectroscopic techniques.

As mentioned above, methanol formation proceeds through the sequential transformation of the coordinated carbonyl ligand according to the pathway, Ru-CO → Ru-CHO → M−CH_2OH followed by one more protonation and CH_3OH release.[425]. These intermediates exhibit characteristic ν(CO) stretching vibrations in the FTIR and have previously been identified by FTIR spectroscopy.[426]

Therefore, additional photocatalytic experiments were performed using **Ru bpyPyr** in order to monitor changes in the Ru catalytic center by FTIR spectroscopy and investigate whether the same sequence of intermediates reported for the molecular Tanaka catalyst could also be observed after immobilization within the porous framework. **Figure 76** compares the FTIR spectra recorded before and after photocatalysis under Ar atmosphere. Following irradiation, the two original ν(CO) stretching bands at 2077 and 2017 cm^{-1} converted into three new bands centered at 2017, 1977, and 1933 cm^{-1}.

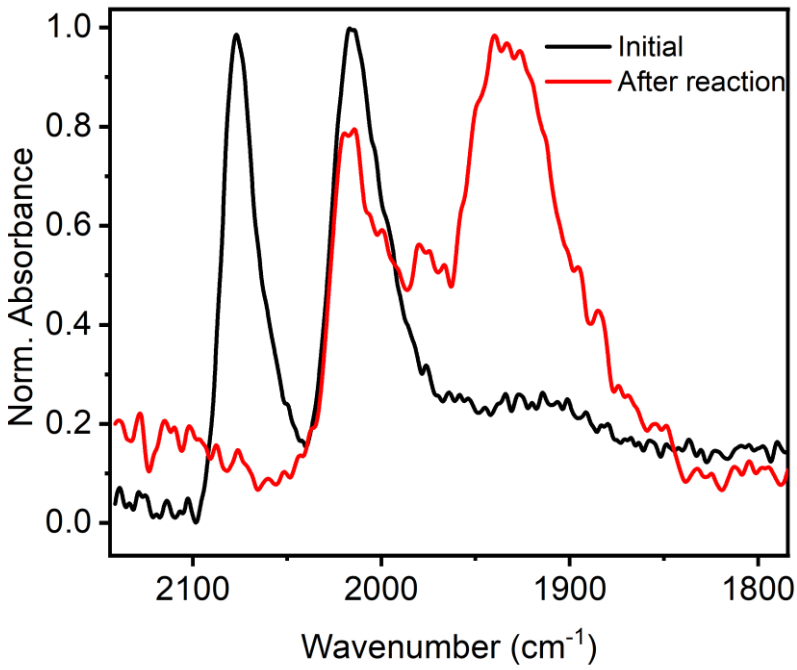


Figure 76. FTIR spectra of **Ru bpyPyr** recorded before and after photocatalytic irradiation under an Ar atmosphere.

The new absorption band centered at 1933 cm^{-1} is particularly noteworthy because it falls within the spectral region previously assigned to the Ru-CH_2OH intermediate (1925-1932 cm^{-1}). This observation suggests the possible formation of the hydroxymethyl intermediate during photocatalysis, providing preliminary spectroscopic evidence that the immobilized Ru catalytic center follows a reaction pathway analogous to that reported for the homogeneous Tanaka catalyst. Besides the new band at 1933 cm^{-1}, a small peak at 1980 cm^{-1} is also observed along with a peak at 2020 cm^{-1}, which cannot be fully assigned with the current data.

Although additional studies are required to fully quantify the efficiency of the new system towards CO2 conversion into CH_3OH and also to fully elucidate the elementary reaction pathway, the present results establish an important proof

of concept for the development of multi-site cascade catalysts for sequential CO_2-to-CO-to-CH_3OH conversion within a single porous architecture.

7.3.2. Multi-site cascade Mn bpyCoPc catalyst

In Chapter 6, we have shown that the post-synthetic incorporation of $Mn(CO)_3$ moieties into the phenPy COF significantly enhances the electrocatalytic performance for CO_2 reduction compared to its homogeneous counterpart, *fac*-$Mn(CO)_3$(bpy)Br. The immobilized catalyst exhibited improved stability together with a high TOF_{CO} toward the selective production of CO, evidencing the potential of COFs as molecularly defined platforms for electrocatalytic CO_2 reduction.

Building upon these findings, we sought to investigate whether this molecularly precise architecture could be further exploited to construct a multi-site cascade catalyst capable of promoting sequential carbon reduction reactions within a single framework. For this purpose, cobalt phthalocyanine (CoPc), a well-established catalyst for the reduction of CO_2 and, more importantly, CO toward CH_3OH under appropriate reaction conditions,[427, 428] was incorporated together with the Mn(I) catalytic centers into the same COF architecture (**Figure 77a**). The rationale behind this design is that the Mn(I) sites selectively catalyze the initial reduction of CO_2 to CO, thereby increasing the local concentration of CO in the vicinity of neighboring CoPc sites, which are expected to promote its subsequent reduction toward CH_3OH.

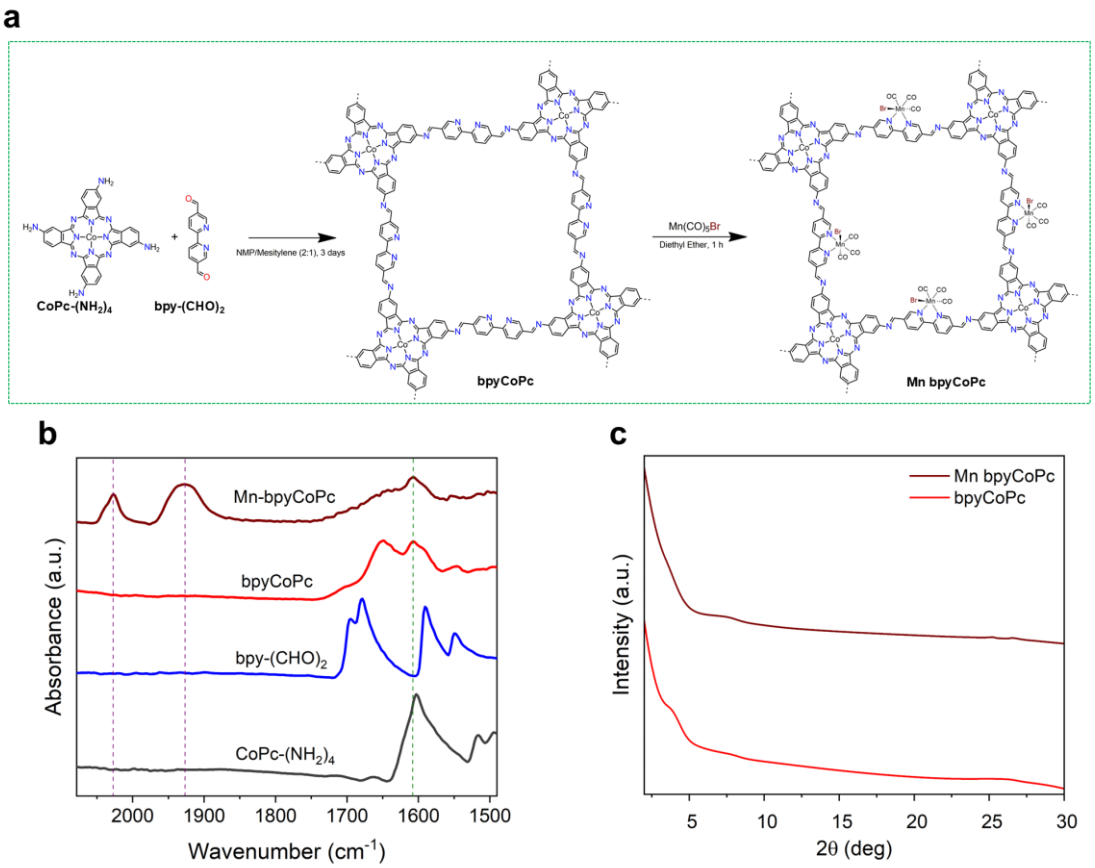


Figure 77. a) Synthesis of **bpyCoPc** and immobilization of $Mn(CO)_5Br$, yielding **Mn bpyCoPc**, b) FTIR spectra of **Mn bpyCoPc**, **bpyCoPc** and their precursors, c) PXRD spectra of **Mn bpyCoPc**, **bpyCoPc**.

The imine-linked **bpyCoPc** polymer was synthesized under solvothermal conditions via an acid-catalyzed Schiff-base condensation between 2,2′-bipyridine-based (bpy) dialdehyde and cobalt phthalocyanine-based (CoPc) tetraamine building blocks. The successful condensation synthesis was evidenced by FTIR spectroscopy (**Figure 77b**). We can note the absence of the characteristic stretching vibrations of the aldehydes groups (1679-1694 cm^{-1}) and amine groups (1602 cm^{-1}), while the formation of a new absorption band assigned to the imine stretching vibration (1607 cm^{-1}) confirms the successful Schiff-base condensation.

Moreover, its PXRD pattern (**Figure 77c**) exhibits only broad diffraction features, characteristic of an amorphous porous polymer. Due to the absence of crystallinity, **bpyCoPc** cannot be classified as a COF. Instead, it is described as an amorphous porous polymer containing well-defined coordination sites throughout its framework.

Following post-synthetic metalation to add Mn(I) centers, the imine bonds remain unmodified while new absorption bands appear in the carbonyl stretching region (1800–2100 cm^{-1}) in the FTIR spectrum of **Mn bpyCoPc (Figure 77b)**, which are characteristic of coordinated $Mn(CO)_3$ moieties, as discussed previously in Chapter 6. On the other hand, the PXRD pattern also shows only very broad diffraction features, corresponding to the formation of an amorphous porous polymer.

Mn bpyCoPc and **bpyCoPc** were both employed as electrocatalysts for CO_2 reduction using a conventional H-type cell using $KHPO_4$ (0.5 M) as electrolyte (**Figure 78a**). The electrocatalysts were mixed with MWCNT (multi-walled carbon nanotubes) and Nafion and then spray-coated onto carbon paper.

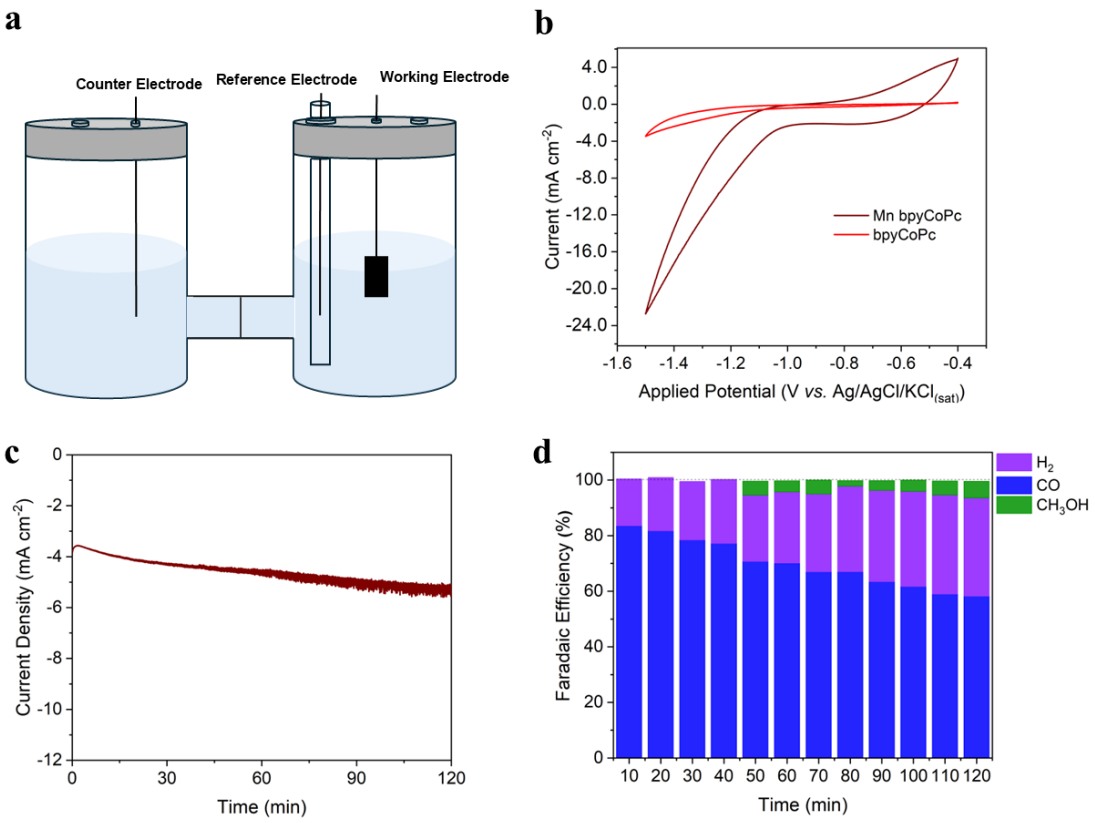


Figure 78. a) Schematic representation of the H-type cell architecture employing a GDE with **Mn bpyCoPc** as active electrocatalyst. b) Cyclic Voltammetry (CV) of **Mn bpyCoPc** and **bpyCoPc** measured right before the bulk electrocatalysis in CO_2-saturated $KHPO_4$ (0.5 M) at a scan rate of 100 mV s^{-1}. c) Chronoamperometric responses during the bulk electrocatalysis of **Mn bpyCoPc** at 1.5 V *vs*. Ag/AgCl and d) Faradaic Efficiencies (FE) values as function of time at applied potential of 1.5 V *vs*. $Ag/AgCl/KCl_{(sat)}$.

The cyclic voltammetry (CV) (**Figure 78b**) under a CO_2-saturated electrolyte showed a significant increase in the catalytic current (I_{cat}) for **Mn bpyCoPc**, reaching a current value 6.7-fold higher than that of **bpyCoPc** at 1.5 V *vs*. Ag/AgCl. When the bulk electrolysis was performed at 1.5 V vs. Ag/AgCl using **bpyCoPc**, no CO or CH_3OH was detected during 120 min of experiment.

The employment of **Mn bpyCoPc** as the electrocatalyst at 1.5 V vs. Ag/AgCl initially produced only CO and H_2 with Faradaic Efficiencies (FE) of 84 and 17%, respectively, after 10 min of electrolysis, with the absence of any

product in the liquid phase. However, after 50 min of reaction, CH_3OH was detected in the liquid phase with a FE of 5%, while the FEs for CO and H_2 changes to 71 and 24%, respectively. The FE for CH_3OH fluctuated between 2 and 6% until the end of the experiment (120 min).

Interestingly, the delayed appearance of CH_3OH, accompanied by a simultaneous decrease in the FE for CO, is consistent with the proposed cascade catalytic mechanism, in which CO initially produced at the Mn(I) catalytic sites is subsequently consumed by neighboring CoPc sites for further reduction toward CH_3OH. Although additional mechanistic studies are required to unequivocally confirm this pathway, these preliminary observations support the feasibility of the proposed catalyst design.

Given its promising electrocatalytic performance in the H-cell configuration, **Mn bpyCoPc** was subsequently evaluated in a flow cell reactor to investigate its behavior under enhanced mass-transport conditions. Unlike conventional H-cells, flow cells continuously deliver fresh electrolyte and gaseous CO_2 to the electrode surface, improving reactant transport and enabling operation at substantially higher current densities.[32] Therefore, a GDE was employed as the work electrode in a flow cell (Electro-Cell®) with an geometric area of $1cm^2$. The anodic and cathodic compartments were separated by an anion-exchange membrane (Fumasep®, 110-140 μm thick). A Ni foam electrode was used as the anode, while a leak-free Ag/AgCl electrode was employed as the reference electrode and 0.5 M of $KHCO_3$ was used as the electrolyte. The design of this setup is schematically illustrated in **Figure 79a**.

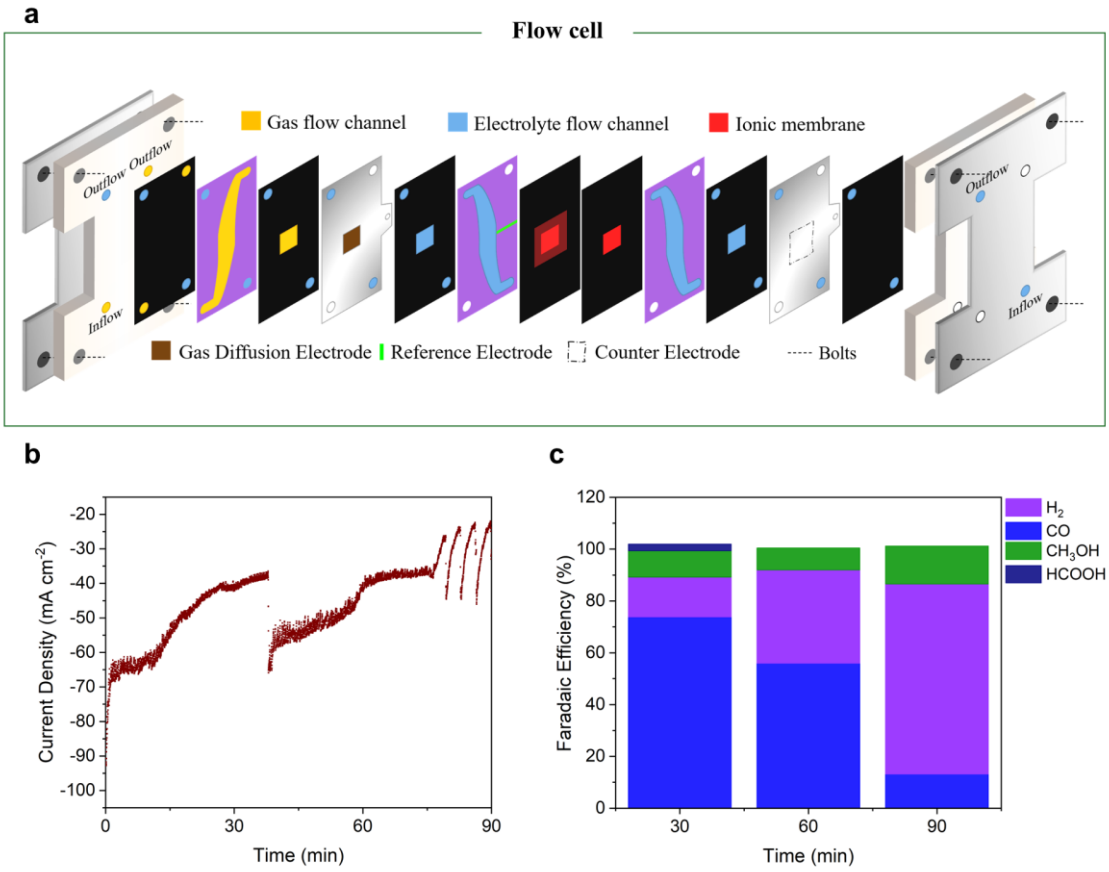


Figure 79. (a) Schematic representation of the flow-cell architecture employing a GDE with **Mn bpyCoPc** as the electrocatalyst. (b) Chronoamperometric response during bulk electrolysis of **Mn bpyCoPc** at −2.0 V *vs.* Ag/AgCl/$KCl_{(sat)}$. (c) Faradaic efficiencies (FE) for CO, H_2, CH_3OH and HCOOH as a function of electrolysis time in the flow-cell configuration under a CO_2 flow rate of 30 mL min^{-1} using 0.5 M $KHCO_3$ as the electrolyte.

During bulk electrolysis (**Figure 79b**) at -2.0 V *vs.* Ag/AgCl, the current density initially reached approximately -65 mA cm^{-2} for the first 15 min. Subsequently, the current density progressively decreased, reaching approximately - 30 mA cm^{-2} after 90 min of electrolysis. This decrease indicates a progressive loss of electrochemical performance during prolonged operation, which may be associated with changes in the catalyst layer, electrode wetting or catalyst deactivation. Despite this decrease in current density, CO_2 reduction products continued to be detected throughout the electrolysis. The FE (**Figure**

79c) for CH_3OH increased from 10% after 30 min to 15% after 90 min, whereas the FE for CO decreased substantially from 77% to 13% over same period. In parallel, the FE for H_2 increased from 16% to 71%. Thus, prolonged electrolysis resulted in a progressive shift in product selectivity from CO_2 reduction towards the competing hydrogen evolution reaction (HER), accompanied by a relative increase in the contribution of CH_3OH to the carbon-containing products.

The persistence of CH_3OH formation, better illustrated in **Figure 80**, despite the substantial decrease in CO production is consistent with the proposed cascade architecture, in which CO generated at Mn sites may undergo subsequent reduction at neighboring CoPc centers.

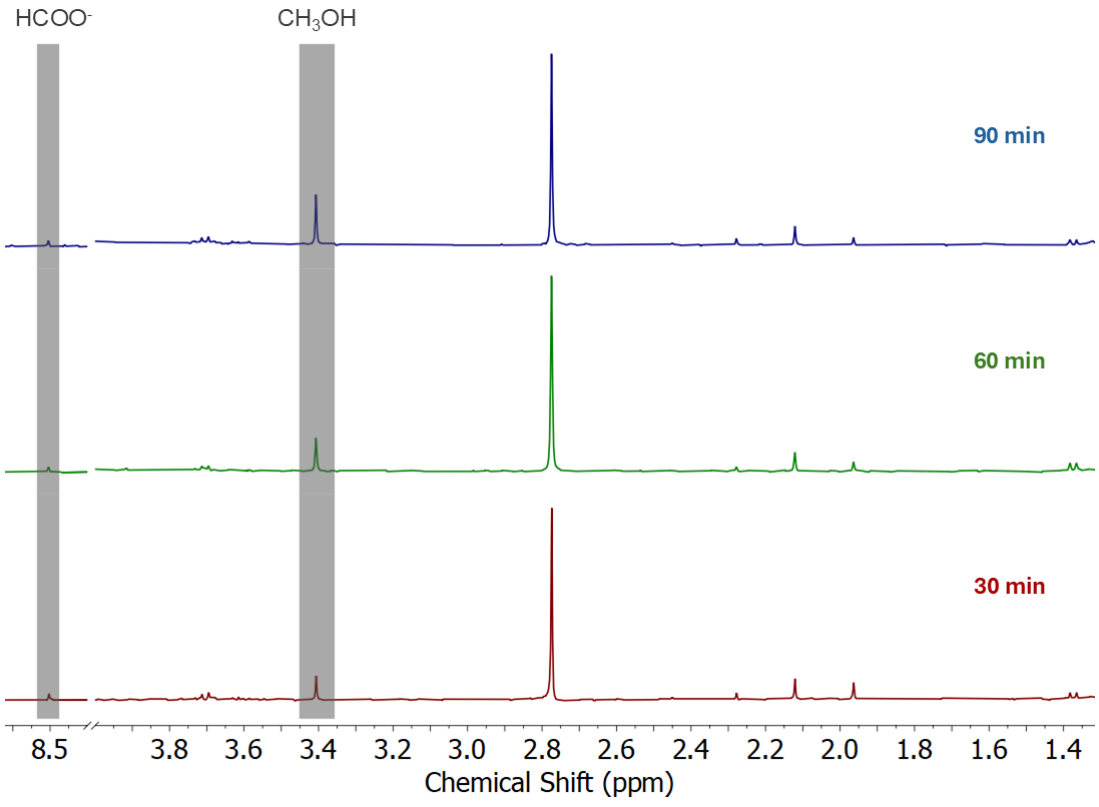


Figure 80. ^1H NMR spectra of the liquid phase collected after 30, 60, and 90 min of bulk electrolysis performed at an applied potential of −2.0 V *vs.* Ag/AgCl under a CO_2 atmosphere. The samples were prepared by mixing the electrocatalytic solution with D_2O and DMSO as the internal standard (δ = 2.78 ppm).

As shown in **Figure 79c** and **Figure 80**, formate production was observed only during the initial stage of electrolysis and was no longer detected after 60 and 90 min. This behavior suggests that HCOOH is most likely a competing reduction product formed during the early stages of catalysis rather than a key intermediate in the CH_3OH formation pathway. For Mn(I) tricarbonyl CO_2 reduction catalysts, CO and $HCOO^-$ are generally produced through distinct mechanistic pathways, with $HCOO^-$ formation involving hydride transfer reactions and CO formation proceeding through CO_2 activation followed by C-O bond cleavage.[47, 48, 371, 372] Therefore, the formation of $HCOO^-$ is most likely due to the presence of parallel Mn-centered reaction pathways during the initial stages of electrolysis.

Mechanistic studies

Carbonyl band frequencies are sensitive to the electronic environment of the metal center, governed by metal-to-CO π back-bonding between the metal and the carbonyl ligands, and therefore they serve as reliable spectroscopic markers to identify and monitor key intermediates during the CO_2 catalytic cycle.[109, 115, 335, 371] Therefore, we used a customized three-electrode attenuated total reflectance infrared spectroelectrochemical (ATR-IR-SEC) cell to probe the catalytic mechanism(s) of the heterogeneous system *in-situ*. A **Mn bpyCoPc COF/**multi-walled carbon nanotubes (MWNT) film deposited on a glassy carbon electrode served as the working electrode and was placed in close contact with a ZnSe ATR crystal, together with a reference and a counter electrode (the same configuration used in Chapter 4). The FTIR spectrum was monitored in the range of 1600-2100 cm^{-1} during cyclic voltammetry (CV) measurements at a low scan

rate of 5 mV s^{-1} (**Figure 81**). Due to the concomitant catalytic HER observed previously, we performed the ATR-IR-SEC measurements in an anhydrous organic electrolyte (0.1 M $TBAPF_6/CH_3CN$).

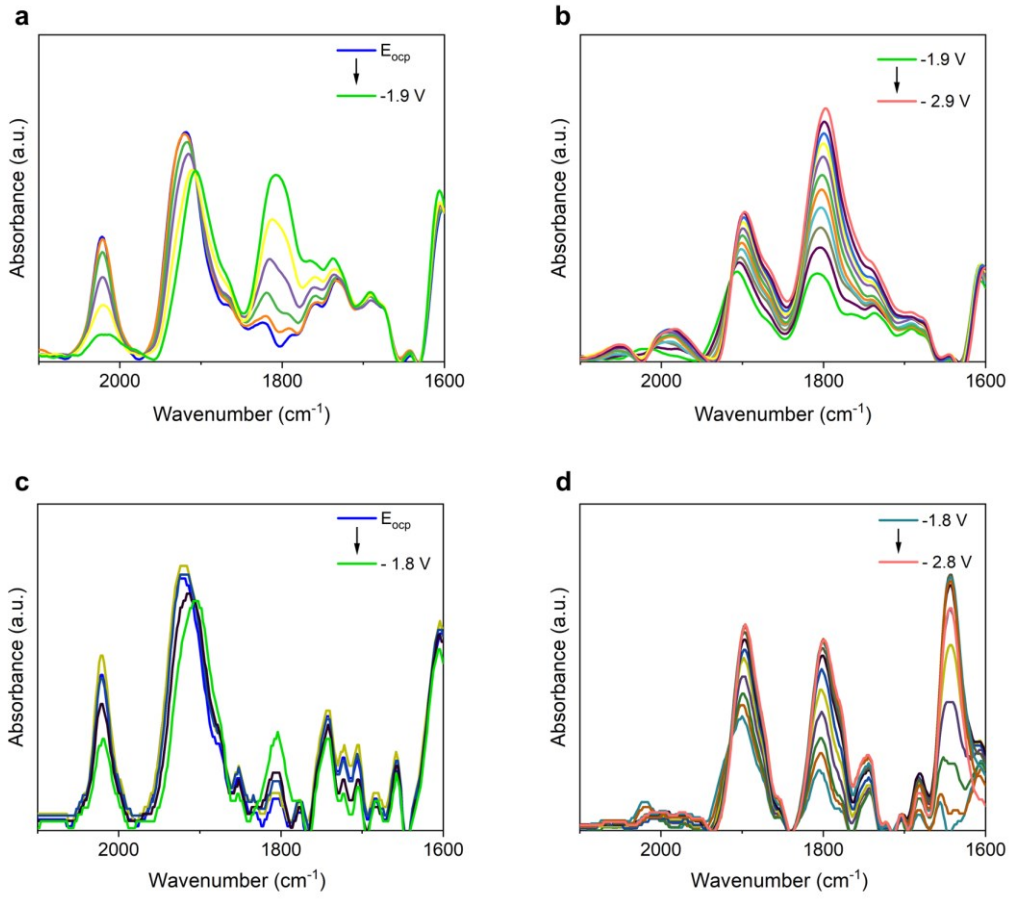


Figure 81. Infrared spectroelectrochemistry (IR-SEC) of **Mn bpyCoPc** in 0.1 M $TBAPF_6/CH_3CN$ electrolyte during the first and second reduction process under (a-b) Ar and (c-d) CO_2 atmospheres. The graphs on the left (a and c) corresponds to the first electron reduction process while the graphs on the right (b and d) are from the second electron reduction process. All potential are reported vs. Fc/Fc^+.

The spectral changes were monitored both under Ar (**Figure 81a-b**) and CO_2 (**Figure 81c-d**) atmosphere. A proposed catalytic pathway is presented in **Figure 82**, where each assigned species is highlighted. Under Ar, the initial species (2022 and 1921 cm^{-1}) present at the open-circuit potential (E_{ocp}) is converted during the first reduction potential getting its maximum (species b) at -

1.9 V *vs.* Fc/Fc^+, showing a spectral change characterized by a systematic red shift of the v(CO) bands together with the appearance of new low-frequency carbonyl absorptions (2013, 1906 and 1808 cm^{-1}), indicating increased metal-to-CO π-backbonding after reduction. The absence of a well-defined isosbestic point suggests that this process involves multiple consecutive steps, which is consistent with the sequential formation of the one-electron reduced species followed by bromide dissociation to generate a five-coordinate Mn radical intermediate.[320, 335, 386, 429]

In contrast, the second transformation exhibits a well-defined isosbestic point, indicating a direct interconversion between the second and third species. The appearance of additional v(CO) bands in the low-frequency region (1988, 1898 and 1798 cm^{-1}) indicates the formation of a new reduced Mn(I) carbonyl species. The lower-frequency shift is consistent with the formation of the two-electron reduced species (species c). Additional and overlapping carbonyl absorptions, particularly the band at 2050 cm^{-1}, suggest that the reduced Mn center may exist in more than one electronic or coordination environment under these conditions. This band could be associated with a solvent coordinated Mn carbonyl species, a distinct reduced Mn intermediate, or electronic perturbations imposed by the COF backbone and neighboring CoPc sites. At present, the available IR-SEC data do not allow an unambiguous assignment of these overlapping carbonyl bands, being necessary, for instance, experiments using **bpyCoPc** aiming at more precise assignments.

Under CO_2 atmosphere, a very similar spectral evolution is observed. However, after formation of the five-coordinate, two-electron reduced species, a absorption band at 1646 cm^{-1} is observed, which might be due to the formation

of a Mn-COOH (species d) or alternatively to the formation of carbonate or bicarbonate species resulting from direct CO_2 reaction with water impurities at strongly negative potentials.[430, 431] However, additional experiments are required to distinguish between these possible assignments. Therefore, the proposed reduction catalytic mechanism at the Mn(I) center is presented in the **Figure 82**.

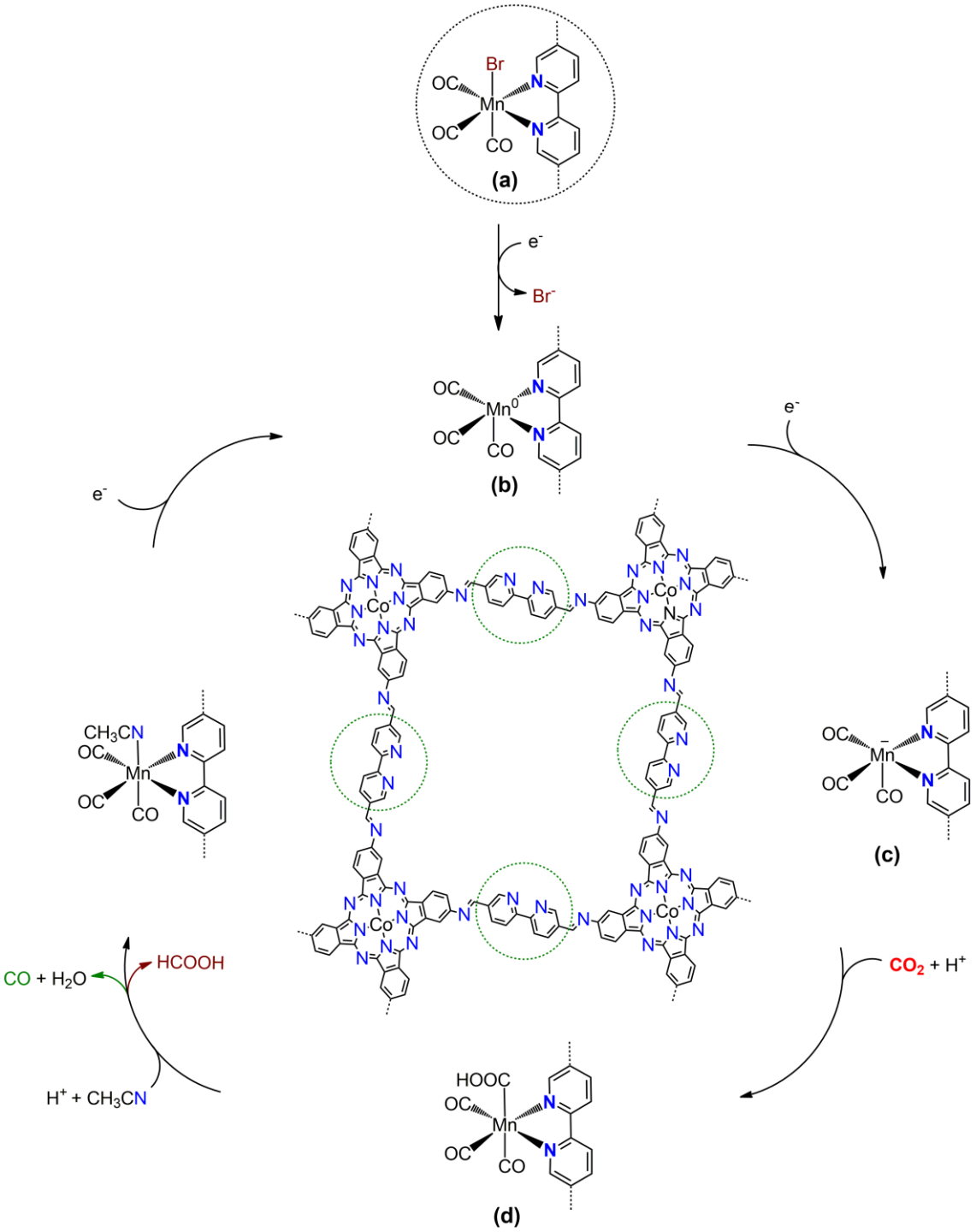


Figure 82. Proposed electrocatalytic catalytic pathway for **Mn bpyCoPc.** The Mn-COOH adduct (species d) can undergo reduction to produce either CO (green pathway) or HCOOH (red pathway).

Taken together, these observations indicate that the Mn centers undergo sequential reduction processes and participate in the electrochemical activation

of CO_2. The formation of CO and HCOOH during bulk electrolysis is consistent with the involvement of these reduced Mn intermediates in CO_2 reduction.

Chapter 8

Conclusions and Perspectives

8.1. General Conclusions

This thesis investigated the rational design of molecular and hybrid catalytic systems for selective CO_2 reduction through both photocatalytic and electrocatalytic approaches. Beginning with fundamental mechanistic investigations of homogeneous molecular catalysts, the work progressively advanced towards the development of atomically defined porous catalytic platforms and, finally, the proposal of multi-site cascade catalysts that integrate complementary catalytic functions within a single material for the selective production of liquid fuels.

A central contribution of this thesis was demonstrating that mechanistic understanding at the molecular level provides the foundation for the rational design of hybrid catalytic systems. The investigation of proton-responsive Re(I) tricarbonyl complexes revealed how the ligand environment influences excited-state dynamics, electron-transfer processes, and catalyst deactivation pathways. The combination of IR spectroelectrochemistry and *in-situ* FTIR spectroscopy enabled the identification of key catalytic intermediates and showed that catalyst deactivation proceeds through dimerization involving carbonyl-bridged species. These studies established important mechanistic principles for understanding the behavior of molecular CO_2 reduction catalysts and highlighted the importance of controlling intermolecular interactions during catalysis.

The second major conclusion of this thesis is that Covalent Organic Frameworks provide an effective platform for preserving the molecular nature of catalytic centers while substantially improving their operational stability. The incorporation of [$Re(CO)_3$] units into bipyridine-based COFs demonstrated that immobilized catalysts retain the fundamental reduction pathway of their molecular analogues while suppressing the bimolecular deactivation processes that commonly limit homogeneous systems. More importantly, the results showed that catalytic performance is governed not only by the molecular catalyst itself but also by the structural characteristics of the surrounding framework. Framework architecture, catalyst loading, and interlayer organization were found to directly influence catalytic activity and stability, establishing framework engineering as a fundamental design parameter for hybrid molecular catalysts.

Furthermore, this thesis has shown that molecularly defined porous catalysts can be successfully translated from photocatalytic systems to electrocatalytic devices operating under technologically relevant conditions. The incorporation of Mn(I) catalytic centers into porous bipyridine-based frameworks produced highly active CO_2 reduction catalysts that remained compatible with gas-diffusion electrodes, catholyte-free zero-gap electrolyzer systems. These studies evidence that porous molecular materials are not only mechanistically informative model systems but also promising catalytic platforms for scalable CO_2 conversion technologies.

Finally, this work introduced the concept of multi-site cascade catalysts for sequential CO_2 reduction. By spatially integrating complementary molecular catalytic centers within the same porous architecture, both photocatalytic and electrocatalytic systems were developed to explore sequential CO_2-to-CO-to-

CH_3OH conversion. Although these systems remain at a proof-of-concept stage, they demonstrate the feasibility of organizing multiple catalytic functions within a single molecularly defined framework and establish a new strategy for promoting multistep CO_2RR. This approach extends the role of COFs beyond catalyst immobilization toward the construction of multifunctional catalytic architectures that facilitate intermediate transfer and cooperative catalytic processes.

Taken together, the results presented in this thesis establish a progressive evolution of catalyst design principles that extend from molecular ligand engineering to catalyst immobilization, framework engineering, scalable electrocatalytic devices, and finally multi-site cascade catalyst architectures. More importantly, the work demonstrates that molecular catalyst design and porous framework engineering are complementary and interconnected strategies for developing advanced catalytic systems. The integration of molecular precision, structural organization, and multifunctional catalyst architecture provides a foundation for the next generation of hybrid catalysts for the efficient and selective conversion of CO_2 into increasingly complex and energy-dense solar fuels.

8.2. Perspectives

Although significant progress has been achieved in understanding the behavior of molecular catalysts immobilized within Covalent Organic Frameworks (COFs), several elementary reaction steps occurring inside porous catalytic architectures remain only partially understood. Future investigations combining operando FTIR spectroscopy, transient absorption spectroscopy, X-ray absorption spectroscopy (XAS), isotopic labeling experiments, and density

functional theory calculations will be essential for identifying catalytic intermediates and elucidating the electron-, proton-, and hydride-transfer processes involved in CO_2 reduction. In this context, the recently developed colloidal COFs represent a particularly promising opportunity.[432] Their improved dispersibility and reduced particle aggregation may increase the accessibility of catalytic sites under solution conditions while enabling mechanistic investigations with a level of spectroscopic detail that has been difficult to achieve with conventional bulk COFs. Such studies are expected to provide the molecular-level understanding necessary for the rational design of increasingly efficient catalytic systems.

This thesis also showed that catalytic performance is governed not only by the molecular catalyst itself but also by the structural and electronic characteristics of the porous framework. Future developments should therefore focus on the simultaneous optimization of both components. Rational control over pore size, topology, crystallinity, electronic conjugation, hydrophobicity, and catalyst distribution within COFs offers opportunities to improve charge transport, substrate diffusion, catalyst accessibility, and long-term operational stability. These studies may ultimately establish general design principles for molecularly defined porous catalysts. In addition, the results obtained in this thesis indicate that immobilized catalytic sites can influence the stacking arrangement of neighboring COF layers. A deeper understanding of interlayer interactions and strategies to control stacking distance, such as the growth of oriented COF films on conductive carbon nanotube substrates,[433] may provide new routes for enhancing charge transport and catalytic activity.

One of the most promising outcomes of this work is the proposal of multi-site cascade catalyst COFs containing complementary molecular catalytic centers driving sequential CO_2-to-CO-to-CH_3OH conversion. The development of these multi-site cascade catalysts opens a new direction for CO_2 reduction research by integrating multiple catalytic functions within a single molecularly defined porous architecture. Future studies should focus on demonstrating the existence of true cascade reaction pathways through isotopic labeling and operando spectroscopic characterization. The confirmation of substrate channeling or intermediate transfer between neighboring catalytic sites would establish a fundamentally new strategy for the selective production of liquid fuels from CO_2.

Finally, future catalyst development should move beyond maximizing the activity of isolated catalytic sites and instead focus on constructing integrated catalytic platforms that simultaneously combine stability, selectivity, and multifunctionality within a single catalyst architecture. In this context, COFs represent a unique class of materials that combines structural order, synthetic versatility, and molecular-level control, making them particularly attractive for the development of next-generation artificial photosynthetic systems.

References

1. Green, F.; Bois von Kursk, O.; Muttitt, G.; Pye, S., No new fossil fuel projects: The norm we need. Science 2024, 384 (6699), 954-957. https://doi.org/10.1126/science.adn6533

2. Wang, C.; Song, J.; Shi, D.; Reyna, J. L.; Horsey, H.; Feron, S.; Zhou, Y.; Ouyang, Z.; Li, Y.; Jackson, R. B., Impacts of climate change, population growth, and power sector decarbonization on urban building energy use. Nature Communications 2023, 14 (1), 6434. https://doi.org/10.1038/s41467-023-41458-5

3. IEA, World Energy Statistics & Balances, IEA, Paris. . https://www.iea.org/data-and-statistics/data-product/world-energy-statistics-balances (accessed Licence: Terms of Use for Non-CC Material).

4. Zhanaidarova, A.; Jones, S. C.; Despagnet-Ayoub, E.; Pimentel, B. R.; Kubiak, C. P., Re(tBu-bpy)(CO)(3)Cl Supported on Multi-Walled Carbon Nanotubes Selectively Reduces CO(2) in Water. Journal of the American Chemical Society 2019, 141 (43), 17270-17277. https://doi.org/10.1021/jacs.9b08445

5. Deshmukh, M. K. G.; Sameeroddin, M.; Abdul, D.; Abdul Sattar, M., Renewable energy in the 21st century: A review. Materials Today: Proceedings 2023, 80, 1756-1759. https://doi.org/10.1016/j.matpr.2021.05.501

6. Houghton, J. T.; Ding, Y.; Griggs, D. J.; Noguer, M.; van der Linden, P. J.; Dai, X.; Maskell, K.; Johnson, C. A., Climate change 2001: the scientific basis: contribution of Working Group I to the third assessment report of the Intergovernmental Panel on Climate Change. Cambridge university press: 2001.

7. Mukherji, A., Climate change 2023 synthesis report. 2023.

8. Wang, Z.; Sun, Y.; Kong, H.; Xia-Bauer, C., An in-depth review of key technologies and pathways to carbon neutrality: classification and assessment of decarbonization technologies. Carbon Neutrality 2025, 4 (1). https://doi.org/10.1007/s43979-025-00129-8

9. Yin, Y.; Luo, B.; Li, K.; Moskowitz, B. M.; Mosevitzky Lis, B.; Wachs, I. E.; Zhu, M.; Sun, Y.; Zhu, T.; Li, X., Plasma-assisted manipulation of vanadia nanoclusters for efficient selective catalytic reduction of NOx. Nature Communications 2024, 15 (1), 3592. https://doi.org/10.1038/s41467-024-47878-1

10. Yuan, M.; Kummer, M. J.; Minteer, S. D., Strategies for Bioelectrochemical CO2 Reduction. Chemistry - A European Journal 2019, 25 (63), 14258-14266. https://doi.org/10.1002/chem.201902880

11. Li, K.; Peng, B.; Peng, T., Recent Advances in Heterogeneous Photocatalytic CO2 Conversion to Solar Fuels. ACS Catalysis 2016, 6 (11), 7485-7527. https://doi.org/10.1021/acscatal.6b02089

12. Jouny, M.; Luc, W.; Jiao, F., High-rate electroreduction of carbon monoxide to multi-carbon products. Nature Catalysis 2018, 1 (10), 748-755. https://doi.org/10.1038/s41929-018-0133-2

13. White, J. L.; Baruch, M. F.; Pander Iii, J. E.; Hu, Y.; Fortmeyer, I. C.; Park, J. E.; Zhang, T.; Liao, K.; Gu, J.; Yan, Y.; Shaw, T. W.; Abelev, E.; Bocarsly, A. B., Light-Driven Heterogeneous Reduction of Carbon Dioxide: Photocatalysts and Photoelectrodes. Chemical Reviews 2015, 115 (23), 12888-935. https://doi.org/10.1021/acs.chemrev.5b00370

14. Gao, J.; Choo Sze Shiong, S.; Liu, Y., Reduction of CO2 to chemicals and Fuels: Thermocatalysis versus electrocatalysis. Chemical Engineering Journal 2023, 472, 145033. https://doi.org/10.1016/j.cej.2023.145033

15. Berardi, S.; Drouet, S.; Francàs, L.; Gimbert-Suriñach, C.; Guttentag, M.; Richmond, C.; Stoll, T.; Llobet, A., Molecular artificial photosynthesis. Chemical Society Reviews 2014, 43 (22), 7501-7519. https://doi.org/10.1039/C3CS60405E

16. Knör, G., Recent progress in homogeneous multielectron transfer photocatalysis and artificial photosynthetic solar energy conversion. Coordination Chemistry Reviews 2015, 304-305, 102-108. https://doi.org/10.1016/j.ccr.2014.09.013

17. Desai, D. K., The Artificial Photosynthesis System: An Engineering Approach. In Artificial Photosynthesis, 2005; pp 291-300. https://doi.org/10.1002/3527606742.ch16

18. Sampaio, R. N.; Grills, D. C.; Polyansky, D. E.; Szalda, D. J.; Fujita, E., Unexpected Roles of Triethanolamine in the Photochemical Reduction of CO(2) to Formate by Ruthenium Complexes. Journal of the American Chemical Society 2020, 142 (5), 2413-2428. https://doi.org/10.1021/jacs.9b11897

19. Fang, S.; Rahaman, M.; Bharti, J.; Reisner, E.; Robert, M.; Ozin, G. A.; Hu, Y. H., Photocatalytic CO2 reduction. Nature Reviews Methods Primers 2023, 3 (1), 61. https://doi.org/10.1038/s43586-023-00243-w

20. Kuramochi, Y.; Ishitani, O. I., Hitoshi., Reaction mechanisms of catalytic photochemical CO2 reduction using Re(I) and Ru(II) complexes. Coordenation Chemistry Review 2018, 373, 333-356. https://doi.org/10.1016/j.ccr.2017.11.023

21. Takeda, H. K., Hiroki

Okamoto, Kouhei

Ishitani, Osamu Photocatalytic CO2 reduction using a Mn complex as a catalyst. ChemComm. 2014, 50, 1491-1493. https://doi.org/10.1039/C3CC48122K

22. Takeda, H.; Ishitani, O., Development of efficient photocatalytic systems for CO2 reduction using mononuclear and multinuclear metal complexes based on mechanistic studies. Coordenation Chemistry Review 2010, 254 (3-4), 346-354. https://doi.org/10.1016/j.ccr.2009.09.030

23. Mundada, V. V.; Devi, M.; Das, B.; T, V.; Thangavel, R., Review on Electrocatalytic CO2 Reduction: From Molecular Mechanisms to Scalable Systems. Energy & Fuels 2025, 39 (36), 17192-17233. https://doi.org/10.1021/acs.energyfuels.5c03120

24. Francke, R.; Schille, B.; Roemelt, M., Homogeneously Catalyzed Electroreduction of Carbon Dioxide-Methods, Mechanisms, and Catalysts. Chemical Reviews 2018, 118 (9), 4631-4701. https://doi.org/10.1021/acs.chemrev.7b00459

25. Qiao, J.; Liu, Y.; Hong, F.; Zhang, J., A review of catalysts for the electroreduction of carbon dioxide to produce low-carbon fuels. Chemical Society Reviews 2014, 43 (2), 631-675. https://doi.org/10.1039/C3CS60323G

26. Geskes, C.; Heinze, J., A spectroelectrochemical cell for measurements in highly purified solvents. Journal of Electroanalytical Chemistry 1996, 418 (1-2), 167-173. https://doi.org/10.1016/S0022-0728(96)04762-6

27. Zhang, X.; Zwanziger, J. W., Design and applications of an in situ electrochemical NMR cell. Journal of Magnetic Resonance 2011, 208 (1), 136-

147.
https://doi.org/10.1016/j.jmr.2010.10.013

28. Dias, M.; Hudhomme, P.; Levillain, E.; Perrin, L.; Sahin, Y.; Sauvage, F.-X.; Wartelle, C., Electrochemistry coupled to fluorescence spectroscopy: a new versatile approach. Electrochemistry communications 2004, 6 (3), 325-330. https://doi.org/10.1016/j.elecom.2004.01.010

29. Murray, P. R.; Collison, D.; Daff, S.; Austin, N.; Edge, R.; Flynn, B. W.; Jack, L.; Leroux, F.; McInnes, E. J.; Murray, A. F., An in situ electrochemical cell for Q-and W-band EPR spectroscopy. Journal of magnetic resonance 2011, 213 (1), 206-209. https://doi.org/10.1016/j.jmr.2011.09.041

30. Ashley, K.; Pons, S., Infrared Spectroelectrochemistry. Chemical Reviews 1988, 88 (4), 673-695. https://doi.org/10.1021/cr00086a006

31. Zhang, Z.; Huang, X.; Chen, Z.; Zhu, J.; Endrődi, B.; Janáky, C.; Deng, D., Membrane electrode assembly for electrocatalytic CO2 reduction: principle and application. Angewandte Chemie 2023, 135 (28), e202302789. https://doi.org/10.1002/ange.202302789

32. Rabiee, H.; Ma, B.; Yang, Y.; Li, F.; Yan, P.; Wu, Y.; Zhang, X.; Hu, S.; Wang, H.; Ge, L.; Zhu, Z., Advances and Challenges of Carbon-Free Gas-Diffusion Electrodes (GDEs) for Electrochemical CO2 Reduction. Advanced Functional Materials 2025, 35 (1), 2411195. https://doi.org/10.1002/adfm.202411195

33. Wang, Y.; He, T., Recent advances in and comprehensive consideration of the oxidation half reaction in photocatalytic CO2 conversion. Journal of Materials Chemistry A 2021, 9 (1), 87-110. https://doi.org/10.1039/D0TA09011E

34. Schwarz, H.; Dodson, R., Reduction potentials of CO2-and the alcohol radicals. The Journal of Physical Chemistry A 1989, 93 (1), 409-414. https://doi.org/10.1021/j100338a079

35. Vu, N. N.; Kaliaguine, S.; Do, T. O., Critical Aspects and Recent Advances in Structural Engineering of Photocatalysts for Sunlight-Driven Photocatalytic Reduction of CO2 into Fuels. Advanced Functional Materials 2019, 29 (31). https://doi.org/10.1002/adfm.201901825

36. Kutal., C.; Weber., M. A.; Ferraudi., G.; Geiger, D., A mechanistic investigation of the photoinduced reduction of-carbon dioxide mediated by.

Organometallics 1985, 4, 2161-2166. https://doi.org/10.1021/om00131a016

37. Das, R.; Chakraborty, S.; Peter, S. C., Systematic Assessment of Solvent Selection in Photocatalytic CO2 Reduction. ACS Energy Letters 2021, 6 (9), 3270-3274. https://doi.org/10.1021/acsenergylett.1c01522

38. Wagner, A.; Sahm, C. D.; Reisner, E., Towards molecular understanding of local chemical environment effects in electro- and photocatalytic CO2 reduction. Nature Catalysis 2020, 3 (10), 775-786. https://doi.org/10.1038/s41929-020-00512-x

39. Yamazaki, Y.; Takeda, H.; Ishitani, O. J. J. o. P.; Reviews, P. C. P., Photocatalytic reduction of CO2 using metal complexes. Journal of Photochemistry and Photobiology C: photochemistry Reviews 2015, 25, 106-137. https://doi.org/10.1016/j.jphotochemrev.2015.09.001

40. Hawecker, J.; Lehn, J. M. Z., Raymond, Efficient photochemical reduction of CO2 to CO by visible light irradiation of systems containing Re(bipy)(CO)3X or Ru(bipy) 32+-Co2+ combinations as homogeneous catalysts. Chemical Communications 1983, 9, 536-538. https://doi.org/10.1039/C39830000536

41. Hawecker, J. L., Jean-Marie. Ziessel, Raymond Photochemical and Electrochemical Reduction of Carbon Dioxide to Carbon Monoxide Mediated by (2,2'-Bipyridine)tricarbonylchlororhenium(I) and Related Complexes as Homogeneous Catalysts. Helvetica Chimica Acta 1986, 69, 1990-2012. https://doi.org/10.1002/hlca.19860690824

42. Sullivan, B.; Bolinger, C.; Conrad, D.; Vining, W.; Meyer, T. J. J. C. S., Chem. Commun, One-and two-electron pathways in the electrocatalytic reduction of CO, by fac-Re (bpy)(CO), Cl (bpy= 2, 2'-bipyridine). Chemical Communications 1985, 1414-1416. https://doi.org/10.1039/C39850001414

43. Hori, H., Johnson, F. P., Koike, K., Ishitani, O., & Ibusuki, T., Efficient photocatalytic COz reduction using [Re (bpy) (CO) 3{P(OEt) 3 }] Journal of photochemistry and photobiology A: chemistry 1996, 96, 171-174. https://doi.org/10.1016/1010-6030(95)04298-9

44. Sahara, G.; Ishitani, O., Efficient photocatalysts for CO2 reduction. Inorganic Chemistry 2015, 54, 5096-5104. https://doi.org/10.1021/ic502675a

45. Sato, S.; Matubara, Y.; Koike, K.; Falkenstrom, M.; Katayama, T.; Ishibashi, Y.; Miyasaka, H.; Taniguchi, S.; Chosrowjan, H.; Mataga, N.; Fukazawa, N.; Koshihara, S.; Onda, K.; Ishitani, O., Photochemistry of fac-[Re(bpy)(CO)3Cl]. Chemistry - A European Journal 2012, 18 (49), 15722-34. https://doi.org/10.1002/chem.201202734

46. Andrew, V. J. J. o. t. C. S., Dalton Transactions, An in situ infrared study of CO 2 reduction catalysed by rhenium tricarbonyl bipyridyl derivatives. Dalton Transitions 1992, (9), 1455-1463. https://doi.org/10.1039/dt9920001455

47. Riplinger, C. S., Matthew D. Ritzmann, Andrew M. Kubiak, Clifford P. Carter, Emily A. , Mechanistic contrasts between manganese and rhenium bipyridine electrocatalysts for the reduction of carbon dioxide. Journal of the American Chemical Society 2014, 136, 16285-16298. https://doi.org/10.1021/ja508192y

48. Mukherjee, J. S., Inke, Manganese and Rhenium Tricarbonyl Complexes Equipped with Proton Relays in the Electrochemical CO2 Reduction Reaction. European Journal of Inorganic Chemistry 2020, 2020, 4319-4333. https://doi.org/10.1002/ejic.202000738

49. Müller, A. V.; Faustino, L. A.; de Oliveira, K. T.; Patrocinio, A. O. T.; Polo, A. S., Visible-Light-Driven Photocatalytic CO2 Reduction by Re(I) Photocatalysts with N-Heterocyclic Substituents. ACS Catalysis 2022, 13 (1), 633-646.
https://doi.org/10.1021/acscatal.2c05521

50. Dattelbaum, D. M.; Omberg, K. M.; Schoonover, J. R.; Martin, R. L.; Meyer, T. J., Application of Time Resolved Infrared Spectroscopy to Electronic Structure in Metal to Ligand Charge Transfer Excited. Inorganic Chemistry 41, 6071-6079.
https://doi.org/10.1021/ic020400i

51. Ran, J.; Jaroniec, M.; Qiao, S. Z., Cocatalysts in Semiconductor-based Photocatalytic CO2 Reduction: Achievements, Challenges, and Opportunities. Advanced Materials 2018, 30 (7), 1-31. https://doi.org/10.1002/adma.201704649

52. Zhao, G.; Huang, X.; Wang, X.; Wang, X., Progress in catalyst exploration for heterogeneous CO2 reduction and utilization: a critical review. Journal of Materials Chemistry A 2017, 5 (41), 21625-21649. https://doi.org/10.1039/C7TA07290B

53. Huo, H.; Wu, F.; Kan, E.; Li, A., Overall Photocatalytic CO2 Reduction over Heterogeneous Semiconductor Photocatalysts. Chemistry - A European

Journal 2023, 29 (40), e202300658. https://doi.org/10.1002/chem.202300658

54. Liu, C.; Dubois, K. D.; Louis, M. E.; Vorushilov, A. S.; Li, G., Photocatalytic CO2 reduction and surface immobilization of a tricarbonyl Re (I) compound modified with amide groups. ACS Catalysis 2013, 3 (4), 655-662. https://doi.org/10.1021/cs300796e

55. Cecchet, F.; Alebbi, M.; Bignozzi, C. A.; Paolucci, F. J. I. C. A., Efficiency enhancement of the electrocatalytic reduction of CO2: fac-[Re (v-bpy)(CO) 3Cl] electropolymerized onto mesoporous TiO2 electrodes. Inorganica Chimica Acta 2006, 359 (12), 3871-3874. https://doi.org/10.1016/j.ica.2006.04.037

56. Anfuso, C. L.; Snoeberger III, R. C.; Ricks, A. M.; Liu, W.; Xiao, D.; Batista, V. S.; Lian, T. J. J. o. t. A. C. S., Covalent attachment of a rhenium bipyridyl CO2 reduction catalyst to rutile TiO2. Journal of the American Chemical Society 2011, 133 (18), 6922-6925. https://doi.org/10.1021/ja2013664

57. Cheong, H.-Y.; Kim, S.-Y.; Cho, Y.-J.; Cho, D. W.; Kim, C. H.; Son, H.-J.; Pac, C.; Kang, S. O. J. I. C., Photosensitization behavior of Ir (III) complexes in selective reduction of CO2 by Re (I)-complex-anchored TiO2 hybrid catalyst. Inorganic Chemistry 2017, 56 (19), 12042-12053. https://doi.org/10.1021/acs.inorgchem.7b01963

58. Schreier, M.; Luo, J.; Gao, P.; Moehl, T.; Mayer, M. T.; Grätzel, M., Covalent immobilization of a molecular catalyst on Cu2O photocathodes for CO2 reduction. Journal of the American Chemical Society 2016, 138 (6), 1938-1946.
https://doi.org/10.1021/jacs.5b12157

59. Windle, C. D.; Pastor, E.; Reynal, A.; Whitwood, A. C.; Vaynzof, Y.; Durrant, J. R.; Perutz, R. N.; Reisner, E., Improving the Photocatalytic Reduction of CO2 to CO through Immobilisation of a Molecular Re Catalyst on TiO2. Chemistry - A European Journal 2015, 21 (9), 3746-3754. https://doi.org/10.1002/chem.201405041

60. Faustino, L. A.; Souza, B. L.; Nunes, B. N.; Duong, A. T.; Sieland, F.; Bahnemann, D. W.; Patrocinio, A. O. T., Photocatalytic CO2 Reduction by Re(I) Polypyridyl Complexes Immobilized on Niobates Nanoscrolls. ACS Sustainable Chemistry & Engineering 2018, 6, 6073-6083. https://doi.org/10.1021/acssuschemeng.7b04713

61. Silva, G. N.; Faustino, L. A.; Nascimento, L. L.; Lopes, O. F.; Patrocinio, A. O. T., Visible light-driven CO2 photoreduction by a Re(I) complex immobilized onto CuO/Nb2O5 heterojunctions. The Journal of Chemical Physics

2024, 160 (3). https://doi.org/10.1063/5.0178945

62. Carmo, M. E. G.; Spies, L.; Silva, G. N.; Lopes, O. F.; Bein, T.; Schneider, J.; Patrocinio, A. O. T., From conventional inorganic semiconductors to covalent organic frameworks: advances and opportunities in heterogeneous photocatalytic CO2 reduction. Journal of Materials Chemistry A 2023, 11 (26), 13815-13843. https://doi.org/10.1039/D3TA01470C

63. Côté, A. P.; Benin, A. I.; Ockwig, N. W.; O'Keeffe, M.; Matzger, A. J.; Yaghi, O. M., Porous, Crystalline, Covalent Organic Frameworks. Science 2005, 310 (5751), 1166-1170. https://doi.org/10.1126/science.1120411

64. Wang, S.; Wei, X.; Li, Z.; Liu, Y.; Wang, H.; Zou, L.; Lu, D.; Akhtar, F. H.; Wang, X.; Wu, C., Recent advances in developing mixed matrix membranes based on covalent organic frameworks. Separation Purification Technology 2022, 301, 122004. https://doi.org/10.1016/j.seppur.2022.122004

65. Xu, R.; Wang, X.-S.; Zhao, H.; Lin, H.; Huang, Y.-B.; Cao, R., Rhenium-modified porous covalent triazine framework for highly efficient photocatalytic carbon dioxide reduction in a solid-gas system. Catalysis Science and Technology 2018, 8 (8), 2224-2230. https://doi.org/10.1039/C8CY00176F

66. Yang, S.; Hu, W.; Zhang, X.; He, P.; Pattengale, B.; Liu, C.; Huang, J., 2D Covalent Organic Frameworks as Intrinsic Photocatalysts for Visible Light-Driven CO2 Reduction. Journal of the American Chemical Society 2018, 140, 14614-14618. https://doi.org/10.1021/jacs.8b09705

67. Lu, M.; Liu, J.; Li, Q.; Zhang, M.; Liu, M.; Wang, J. L.; Yuan, D. Q.; Lan, Y. Q., Rational design of crystalline covalent organic frameworks for efficient CO2 photoreduction with H2O. Angewandte Chemie International Edition 2019, 58 (36), 12392-12397. https://doi.org/10.1002/anie.201906890

68. Fu, Z.; Wang, X.; Gardner, A. M.; Wang, X.; Chong, S. Y.; Neri, G.; Cowan, A. J.; Liu, L.; Li, X.; Vogel, A.; Clowes, R.; Bilton, M.; Chen, L.; Sprick, R. S.; Cooper, A. I., A stable covalent organic framework for photocatalytic carbon dioxide reduction. Chemical Science 2020, 11 (2), 543-550. https://doi.org/10.1039/C9SC03800K

69. Faustino, L. A.; Hora Machado, A. E.; Patrocinio, A. O. T., Photochemistry of fac-[Re(CO)3(dcbH2)(trans-stpy)]+: New Insights on the

Isomerization Mechanism of Coordinated Stilbene-like Ligands. Inorganic Chemistry 2018, 57 (5), 2933-2941. https://doi.org/10.1021/acs.inorgchem.8b00093

70. Crudo, N. R.; Sonea, A.; Karn, L. M.; Leznoff, D. B.; Warren, J. J., Modifying the Rate of Rhenium (Diimine)-Mediated Electrochemical Carbon Dioxide Reduction via the Addition of a Redox-Active Functional Group Near the Active Site. ACS Catalysis 2025, 15 (16), 14293-14304. https://doi.org/10.1021/acscatal.5c04063

71. Abudayyeh, A. M.; De Kreijger, S.; Grau, S.; Eryılmaz, E.; Robeyns, K.; Ertem, M. Z.; Llobet, A.; Elias, B.; Troian-Gautier, L., Enhanced Electrocatalytic and Selective CO2-to-CO Reduction by a Rhenium (I) Complex Bearing 6, 6′-Substituted 2, 2′-Bipyridines. ACS Catalysis 2025, 16 (1), 542-554. https://doi.org/10.1021/acscatal.5c06871

72. Qiu, L. Q.; Chen, K. H.; Yang, Z. W.; Ren, F. Y.; He, L. N., Prolonging the Triplet State Lifetimes of Rhenium Complexes with Imidazole-Pyridine Framework for Efficient CO2 Photoreduction. Chemistry - A European Journal 2021, 27 (62), 15536-15544. https://doi.org/10.1002/chem.202102837

73. Kurz, P.; Probst, B.; Spingler, B.; Alberto, R., Ligand Variations in [ReX(diimine)(CO)3] Complexes: Effects on Photocatalytic CO2 Reduction. European Journal of Inorganic Chemistry 2006, 2006 (15), 2966-2974. https://doi.org/10.1002/ejic.200600166

74. Tamaki, Y.; Koike, K.; Morimoto, T.; Ishitani, O., Substantial improvement in the efficiency and durability of a photocatalyst for carbon dioxide reduction using a benzoimidazole derivative as an electron donor. Journal of Catalysis 2013, 304, 22-28. https://doi.org/10.1016/j.jcat.2013.04.002

75. Chow, Y. L.; Danen, W. C.; Nelsen, S. F.; Rosenblatt, D. H., Nonaromatic aminium radicals. Chemical Reviews 1978, 78 (3), 243-274. https://doi.org/10.1021/cr60313a003

76. Manke, A.-M.; Geisel, K.; Fetzer, A.; Kurz, P., A water-soluble tin(IV) porphyrin as a bioinspired photosensitiser for light-driven proton-reduction. Physical Chemistry Chemical Physics 2014, 16 (24), 12029-12042. https://doi.org/10.1039/C3CP55023K

77. Hasegawa, E.; Takizawa, S.; Seida, T.; Yamaguchi, A.; Yamaguchi, N.; Chiba, N.; Takahashi, T.; Ikeda, H.; Akiyama, K., Photoinduced electron-transfer systems consisting of electron-donating pyrenes or anthracenes and benzimidazolines for reductive transformation of carbonyl compounds.

Tetrahedron 2006, 62 (27), 6581-6588. https://doi.org/10.1016/j.tet.2006.03.061

78. Rotundo, L.; Grills, D. C.; Gobetto, R.; Priola, E.; Nervi, C.; Polyansky, D. E.; Fujita, E., Photochemical CO2 Reduction Using Rhenium (I) Tricarbonyl Complexes with Bipyridyl-Type Ligands with and without Second Coordination Sphere Effects. ChemPhotoChem 2021, 5 (6), 526-537. https://doi.org/10.1002/cptc.202000307

79. Agarwal, J.; Fujita, E.; Schaefer III, H. F.; Muckerman, J. T., Mechanisms for CO production from CO2 using reduced rhenium tricarbonyl catalysts. Journal of the American Chemical Society 2012, 134 (11), 5180-5186. https://doi.org/10.1021/ja2105834

80. Gibson, D. H.; Yin, X.; He, H.; Mashuta, M. S., Synthesis and Reactions of fac-[Re (dmbpy)(CO) 3X](dmbpy= 4, 4 '-Dimethyl-2, 2 '-bipyridine; X= COOH, CHO) and Their Derivatives. Journal of Organometallic Chemistry 2003, 22 (2), 337-346. https://doi.org/10.1021/om020677q

81. Costentin, C.; Drouet, S.; Robert, M.; Savéant, J.-M., A local proton source enhances CO2 electroreduction to CO by a molecular Fe catalyst. Science 2012, 338 (6103), 90-94. https://doi.org/10.1126/science.1224581

82. Franco, F.; Cometto, C.; Vallana, F. F.; Sordello, F.; Priola, E.; Minero, C.; Nervi, C.; Gobetto, R., A local proton source in a [Mn(bpy-R)(CO)3Br]-type redox catalyst enables CO2 reduction even in the absence of Brønsted acids. Chemical Communications 2014, 50 (93), 14670-14673. https://doi.org/10.1039/C4CC05563B

83. Agarwal, J.; Shaw, T. W.; Schaefer III, H. F.; Bocarsly, A. B., Design of a catalytic active site for electrochemical CO2 reduction with Mn (I)-tricarbonyl species. Inorganic Chemistry 2015, 54 (11), 5285-5294. https://doi.org/10.1021/acs.inorgchem.5b00233

84. Ngo, K. T.; McKinnon, M.; Mahanti, B.; Narayanan, R.; Grills, D. C.; Ertem, M. Z.; Rochford, J., Turning on the protonation-first pathway for electrocatalytic CO2 reduction by manganese bipyridyl tricarbonyl complexes. Journal of the American Chemical Society 2017, 139 (7), 2604-2618. https://doi.org/10.1021/jacs.6b08776

85. Barlow, J. M.; Gupta, N.; Glusac, K. D.; Tiede, D. M.; Kaphan, D. M., Proton-Responsive Ligands Promote CO2 Capture and Accelerate Catalytic CO2/HCO2-Interconversion. Inorganic Chemistry 2024, 63 (42), 19527-19535. https://doi.org/10.1021/acs.inorgchem.4c02092

86. Wilting, A.; Stolper, T.; Mata, R. A.; Siewert, I., Dinuclear Rhenium Complex with a Proton Responsive Ligand as a Redox Catalyst for the Electrochemical CO(2) Reduction. Inorganic Chemistry 2017, 56 (7), 4176-4185.
https://doi.org/10.1021/acs.inorgchem.7b00178

87. Wilting, A.; Siewert, I., A Dinculear Rhenium Complex with a Proton Responsive Ligand in the Electrochemical-Driven CO2-Reduction Catalysis. ChemistrySelect 2018, 3 (17), 4593-4597. https://doi.org/10.1002/slct.201800772

88. Du, J. P.; Wilting, A.; Siewert, I., Are Two Metal Ions Better than One? Mono-and Binuclear α-Diimine-Re (CO) 3 Complexes with Proton-Responsive Ligands in CO2 Reduction Catalysis. European Journal of Inorganic Chemistry 2019, 25 (21), 5555-5564. https://doi.org/10.1002/chem.201806398

89. Hanson, S. S.; Warren, J. J., Syntheses, characterization, and electrochemical behavior of alkylated 2-(2′-quinolylbenzimidazole) complexes of rhenium (I). Canadian Journal of Chemistry 2018, 96 (2), 119-123. https://doi.org/10.1139/cjc-2017-0320

90. Sinha, S.; Sonea, A.; Gibbs, C. A.; Warren, J. J., Heterogeneous aqueous CO(2) reduction by rhenium(i) tricarbonyl diimine complexes with a non-chelating pendant pyridyl group. Dalton Transitions 2020, 49 (21), 7078-7083.
https://doi.org/10.1039/D0DT01300E

91. Sinha, S. B., Ellan K. ; Warren, J. J., Electrocatalytic CO2 reduction using rhenium(I) complexes with modified 2-(2'-pyridyl)imidazole ligands. Inorganic Chemica Acta 2017, 460, 63-68. https://doi.org/10.1016/j.ica.2016.09.019

92. Souza, B. L.; Faustino, L. A.; Prado, F. S.; Sampaio, R. N.; Maia, P. I. S.; Machado, A. E. H.; Patrocinio, A. O. T., Spectroscopic characterization of a new Re(i) tricarbonyl complex with a thiosemicarbazone derivative: Towards sensing and electrocatalytic applications. Dalton Transitions 2020, 49 (45), 16368-16379.
https://doi.org/10.1039/D0DT01078B

93. Ramos, L. D.; da Cruz, H. M.; Morelli Frin, K. P., Photophysical properties of rhenium (I) complexes and photosensitized generation of singlet oxygen. Photochemical & Photobiological Sciences 2017, 16, 459-466. https://doi.org/10.1039/c6pp00364h

94. Ramos, L. D.; Sampaio, R. N.; De Assis, F. F.; De Oliveira, K. T.; Homem-De-Mello, P.; Patrocinio, A. O. T.; Frin, K. P. M., Contrasting

photophysical properties of rhenium(i) tricarbonyl complexes having carbazole groups attached to the polypyridine ligand. Dalton Transitions 2016, 45 (29), 11688-11698.
https://doi.org/10.1039/C6DT01112H

95. Sousa, S. F.; Sampaio, R. N.; Barbosa Neto, N. M.; Machado, A. E. H.; Patrocinio, A. O. T., The photophysics of fac-[Re(CO)3(NN)(bpa)]+ complexes: A theoretical/experimental study. Photochemical & Photobiological Sciences 2014, 13 (8), 1213-1224. https://doi.org/10.1039/c4pp00074a

96. Patrocinio, A. O. T.; Brennaman, M. K.; Meyer, T. J.; Murakami Iha, N. Y., Excited-state dynamics in fac- [Re(CO)3(Me4phen)(L)] +. The Journal of Physical Chemistry A 2010, 114, 12129-12137. https://doi.org/10.1021/jp104692w

97. Tomasi, J.; Mennucci, B.; Cammi, R., Quantum mechanical continuum solvation models. Chemical Reviews 2005, 105, 2999-3093. https://doi.org/10.1021/cr9904009

98. do Carmo, M. E. G.; de Matos, P. A.; Maia, P. I. S.; Machado, A. E. H.; Beletti, M. E.; Tsubone, T. M.; Patrocinio, A. O. T., The photophysics of Ir(III) cyclometalated complexes containing the 2-(2-pyridyl)benzimidazole ancillary ligand: Protonation effect and their potential as specific lysosome probes in cells. Photochemistry and Photobiology A: Chemistry 2024, 448. https://doi.org/10.1016/j.jphotochem.2023.115339

99. Itokazu, M. K.; Polo, A. S.; de Faria, D. L. A.; Bignozzi, C. A.; Iha, N. Y. M., Syntheses and spectroscopic characterization of fac-[Re (CO) 3 (phen)(L)] PF6, L= trans-and cis-1, 2-bis (4-pyridyl) ethylene. Inorganica Chimica Acta 2001, 313 (1-2), 149-155. https://doi.org/10.1016/S0020-1693(00)00380-7

100. Mamud, J. F.; Biazolla, G.; Marques, C. S.; Cerchiaro, G.; de Queiroz, T. B.; Keppler, A. F.; Polo, A. S., Z to E light-activated isomerization of α-pyridyl-N-arylnitrone ligands sensitized by rhenium (I) polypyridyl complexes. Inorganic Chemica Acta 2021, 514, 120009. https://doi.org/10.1016/j.ica.2020.120009

101. Lees, A. J., The Luminescence Rigidochromic Effect Exhibited by Organometailic Complexes: Rationale and Applications. Comments on Inorganic Chemistry 1995, 17 (6), 319-346. https://doi.org/10.1080/02603599508032711

102. Müller, A. V.; Wierzba, W. M.; do Nascimento, L. G. A.; Concepcion, J. J.; Nikolaou, S.; Polyansky, D. E.; Polo, A. S., Tuning the Photocatalytic CO2 Reduction through para-Substituents in Bipyridyl Rhenium Complexes. Artificial

Photosynthesis 2025, 1, 214-225. https://doi.org/10.1021/aps.4c00026

103. Grice, K. A.; Kubiak, C. P., Recent Studies of Rhenium and Manganese Bipyridine Carbonyl Catalysts for the Electrochemical Reduction of CO2. In Advances in Inorganic Chemistry 2014; Vol. 66, pp 163-188. https://doi.org/10.1016/B978-0-12-420221-4.00005-6

104. Roell, S. A.; Schrage, B. R.; Ziegler, C. J.; White, T. A., Isolating substituent effects in Re(I)-phenanthroline electrocatalysts for CO2 reduction. Inorganic Chemica Acta 2020, 503, 119397. https://doi.org/10.1016/j.ica.2019.119397

105. Clark, M. L.; Cheung, P. L.; Lessio, M.; Carter, E. A.; Kubiak, C. P., Kinetic and Mechanistic Effects of Bipyridine (bpy) Substituent, Labile Ligand, and Brønsted Acid on Electrocatalytic CO2 Reduction by Re(bpy) Complexes. ACS Catalysis 2018, 8 (3), 2021-2029. https://doi.org/10.1021/acscatal.7b03971

106. Lovrić, M., Square-wave voltammetry. In Electroanalytical methods: guide to experiments, 2010; pp 121-145. https://doi.org/10.1007/978-3-642-02915-8_6

107. Scholz, F.; Inzelt, G.; Stojek, Z., Seminal publications in electrochemistry and electroanalysis. In Electroanalytical Methods: Guide to Experiments, 2010; pp 339-342. https://doi.org/10.1007/978-3-642-02915-8_18

108. Smieja, J. M.; Kubiak, C. P., Re(bipy-tBu)(CO)3Cl-improved catalytic activity for reduction of carbon dioxide: IR-spectroelectrochemical and mechanistic studies. Inorganic Chemistry 2010, 49 (20), 9283-9289. https://doi.org/10.1021/ic1008363

109. Johnson, F. P.; George, M. W.; Hartl, F.; Turner, J. J., Electrocatalytic Reduction of CO2 Using the Complexes [Re (bpy)(CO) 3L] n (n=+ 1, L= P (OEt) 3, CH3CN; n= 0, L= Cl-, Otf-; bpy= 2, 2 '-Bipyridine; Otf-= CF3SO3) as Catalyst Precursors: Infrared Spectroelectrochemical Investigation. Journal of Organometallic Chemistry 1996, 15 (15), 3374-3387. https://doi.org/10.1021/om960044+

110. Sullivan, B.; Bolinger, C.; Conrad, D.; Vining, W.; Meyer, T., One-Electrocn and 2-Electron Pathways in the Electrocatalytic Reduction of CO2 by fac-Re (2, 2 0-bipyridine)-(CO) 3Cl. Journal of the Chemical Society, Chemical Communications 1985, 1414-1415. https://doi.org/10.1039/C39850001414

111. Sastre, S.; Casasnovas, R.; Munoz, F.; Frau, J., Isodesmic reaction for accurate theoretical pKa calculations of amino acids and peptides. Physical Chemistry Chemical Physics 2016, 18 (16), 11202-12. https://doi.org/10.1039/C5CP07053H

112. Matsubara, Y.; Grills, D. C.; Kuwahara, Y., Thermodynamic Aspects of Electrocatalytic CO2 Reduction in Acetonitrile and with an Ionic Liquid as Solvent or Electrolyte. ACS Catalysis 2015, 5 (11), 6440-6452. https://doi.org/10.1021/acscatal.5b00656

113. Matsubara, Y., Standard Electrode Potentials for the Reduction of CO2 to CO in Acetonitrile-Water Mixtures Determined Using a Generalized Method for Proton-Coupled Electron-Transfer Reactions. ACS Energy Letters 2017, 2 (8), 1886-1891. https://doi.org/10.1021/acsenergylett.7b00548

114. Cotton, F. A.; Kraihanzel, C. S., Vibrational Spectra and Bonding in Metal Carbonyls. I. Infrared Spectra of Phosphine-substitutedGroupVI Carbonyls in the CO Stretching Region. Journal of the American Chemical Society 1962, 84.23, 4432-4438. https://doi.org/10.1021/ja00882a012

115. Stor, G. J.; Hartl, F.; Van Outersterp, J. W. M.; Stufkens, D. J., Spectroelectrochemical (IR, W/Vis) Determination of the Reduction Pathways for a Series of [Re(CO)3(a=diimine)L']O/+ (L' = Halide, Otf, THF, MeCN, n-PrCN, PPh3, P(OMe)3) Complexes. Organometallics 1995, 14, 1115-1131. https://doi.org/10.1021/om00003a013

116. Yoke Foo Lee; Jon R. Kirchhoff; Robert M. Bergerb; Gosztola, D., Spectroelectrochemistry and excited-state absorption spectroscopy of rhenium (I) α, α′-diimine complexes. Dalton Transitions 1995, 22, 3677-3682.

117. Howell, S. L.; Gordon., K. C., Vibrational spectroscopy of reduced Re (I) complexes of 1, 10-phenanthroline and substituted analogues. The Journal of Physical Chemistry A 2006, 110, 4880-4887. https://doi.org/10.1021/jp056614d

118. Yukiko Hayashi; Shouichi Kita; Bruce S. Brunschwig; Fujita, E., Involvement-of-a-binuclear-species-with-the-re-c(o)o-re-moiety-in-co2-reduction-catalyzed-by-tricarbonyl-rhenium(i). Journal of the American Chemical Society 2003, 125, 11976-11987. https://doi.org/10.1021/ja035960a

119. Klein, A.; Vogler, C.; Kaim, W., The-δ-in-18-δ-electron-complexes-importance-of-the-metal-ligand-interface-for-the-substitutional-reactivity-of-re(0). Organometallics 1996, 15, 236-244. https://doi.org/10.1021/om950500e

120. Kaim, W.; Kohlmann., S., Epr evidence for related electronic structures of α-diimine complexes with [Ru (bpy) 2] 2+ and re (CO) 3 (halide) fragments. Chemical Physics Letters 1987, 139, 365-369. https://doi.org/10.1016/0009-2614(87)80574-2

121. Hayashi, Y.; Kita, S.; Brunschwig, B. S.; Fujita, E., Involvement of a Binuclear Species with the Re-C(O)O-Re Moiety in CO2 Reduction Catalyzed by Tricarbonyl Rhenium(I) Complexes with Diimine Ligands: Strikingly Slow Formation of the Re-Re and Re-C(O)O-Re Species from Re(dmb)(CO)3S (dmb) 4,4′-Dimethyl-2,2′-bipyridine, S) Solvent). Journal of the American Chemical Society 2003, 125 11976-11987. https://doi.org/10.1021/ja035960a

122. Frank, P.; MichaeláHodges, Excited-state properties and reactivity of [ReCL (CO) 3 (2, 2′-bipy)](2, 2′-bipy= 2, 2′-bipyridyl) studied by time-resolved infrared spectroscopy. Dalton Transitions 1993, (19), 2977-2979.

123. Takeda, H., Koike, K., Inoue, H., Ishitani, O., Development of an efficient photocatalytic system for CO2 reduction using rhenium (I) complexes based on mechanistic studies. Journal of the American Chemical Society 2008, 130, 2023-2031. https://doi.org/10.1021/ja077752e

124. Fujita, E.; Muckerman, J. T., Why Is Re−Re Bond Formation Cleavage in [Re(bpy)(CO)3]2 Different. Inorganic Chemistry 2004, 43 (24), 7636-7647. https://doi.org/10.1021/ic048910v

125. Benson, E. E.; Kubiak, C. P., Structural investigations into the deactivation pathway of the CO2 reduction electrocatalyst Re(bpy)(CO)3Cl. Chemical Communications 2012, 48 (59), 7374-6. https://doi.org/10.1039/c2cc32617e

126. Mestroni, G.; Camus, A.; Mestroni., E., Cobalt complexes of 2, 2′-bipyridine and 1, 10-phenanthroline: I. Reaction with alkyl halides and π-acids. Journal of Organic Chemistry 1970, 24, 775-781. https://doi.org/10.1016/S0022-328X(00)84510-6

127. Keene, F. R.; Creutz, C.; Sutin., N., Reduction of carbon dioxide by tris (2, 2′-bipyridine) cobalt (I). Coordenation Chemistry Review 1985, 64, 247-260. https://doi.org/10.1016/0010-8545(85)80053-9

128. Zhang, Z.; Li, Q.-s.; Xie, Y.; King, R. B.; Schaefer, H. F., Binuclear and Trinuclear Chromium Carbonyls with Linear Bridging Carbonyl Groups: Isocarbonyl versus Carbonyl Bonding of Carbon Monoxide Ligands. Journal of

Physical Chemistry A 2010, 114 4672-4679. https://doi.org/10.1021/jp911120y

129. Shehzad, N.; Tahir, M.; Johari, K.; Murugesan, T.; Hussain, M., A critical review on TiO2 based photocatalytic CO2 reduction system: Strategies to improve efficiency. Journal of CO2 Utilization 2018, 26, 98-122. https://doi.org/10.1016/j.jcou.2018.04.026

130. Li, X.; Kawai, K.; Fujitsuka, M.; Osakada, Y., COF-based photocatalyst for energy and environment applications. Surfaces and Interfaces 2021, 25, 101249-101249. https://doi.org/10.1016/j.surfin.2021.101249

131. Guo, J.; Jiang, D., Covalent Organic Frameworks for Heterogeneous Catalysis: Principle, Current Status, and Challenges. ACS Central Science 2020, 6 (6), 869-879. https://doi.org/10.1021/acscentsci.0c00463

132. Verma, P.; Le Brocq, J. J. M.; Raja, R., Rational Design and Application of Covalent Organic Frameworks for Solar Fuel Production. Molecules 2021, 26 (14), 4181-4181. https://doi.org/10.3390/molecules26144181

133. Wang, H.; Wang, H.; Wang, Z.; Tang, L.; Zeng, G.; Xu, P.; Chen, M.; Xiong, T.; Zhou, C.; Li, X.; Huang, D.; Zhu, Y.; Wang, Z.; Tang, J., Covalent organic framework photocatalysts: structures and applications. Chemical Society Reviews 2020, 49 (12), 4135-4165. https://doi.org/10.1039/D0CS00278J

134. Yang, Q.; Luo, M.; Liu, K.; Cao, H.; Yan, H., Covalent organic frameworks for photocatalytic applications. Applied Catalysis B: Environmental 2020, 276, 119174-119174. https://doi.org/10.1016/j.apcatb.2020.119174

135. Li, J.; Zhao, D.; Liu, J.; Liu, A.; Ma, D., Covalent Organic Frameworks: A Promising Materials Platform for Photocatalytic CO2 Reductions. Molecules 2020, 25 (10), 2425-2425. https://doi.org/10.3390/molecules25102425

136. Halmann, M., Photoelectrochemical reduction of aqueous carbon dioxide on p-type gallium phosphide in liquid junction solar cells. Nature 1978, 275, 115-116. https://doi.org/10.1038/275115a0

137. Inoue, T.; Fujishima, A.; Konishi, S.; Honda, K., Photoelectrocatalytic reduction of carbon dioxide in aqueous suspensions of semiconductor powders.

Nature 1979, 277, 637-638. https://doi.org/10.1038/277637a0

138. Lee, Y. Y.; Jung, H. S.; Kang, Y. T., A review: Effect of nanostructures on photocatalytic CO2 conversion over metal oxides and compound semiconductors. Journal of CO2 Utilization 2017, 20 (May), 163-177. https://doi.org/10.1016/j.jcou.2017.05.019

139. Kočí, K.; Obalová, L.; Matějová, L.; Plachá, D.; Lacný, Z.; Jirkovský, J.; Šolcová, O., Effect of TiO2 particle size on the photocatalytic reduction of CO2. Applied Catalysis B: Environmental 2009, 89 (3-4), 494-502. https://doi.org/10.1016/j.apcatb.2009.01.010

140. Liao, Y.; Cao, S. W.; Yuan, Y.; Gu, Q.; Zhang, Z.; Xue, C., Efficient CO2 capture and photoreduction by amine-functionalized TiO2. Chemistry - A European Journal 2014, 20 (33), 10220-10222. https://doi.org/10.1002/chem.201403321

141. Varghese, O. K.; Paulose, M.; Latempa, T. J.; Grimes, C. A., High-rate solar photocatalytic conversion of CO2 and water vapor to hydrocarbon fuels. Nano Letters 2009, 9 (2), 731-737. https://doi.org/10.1021/nl803258p

142. Zangeneh, H.; Zinatizadeh, A. A. L.; Habibi, M.; Akia, M.; Hasnain Isa, M., Photocatalytic oxidation of organic dyes and pollutants in wastewater using different modified titanium dioxides: A comparative review. Journal of Industrial and Engineering Chemistry 2015, 26, 1-36. https://doi.org/10.1016/j.jiec.2014.10.043

143. Xin, C.; Hu, M.; Wang, K.; Wang, X., Significant Enhancement of Photocatalytic Reduction of CO2 with H2O over ZnO by the Formation of Basic Zinc Carbonate. Langmuir 2017, 33 (27), 6667-6676. https://doi.org/10.1021/acs.langmuir.7b00620

144. Akrami, S.; Murakami, Y.; Watanabe, M.; Ishihara, T.; Arita, M.; Guo, Q.; Fuji, M.; Edalati, K., Enhanced CO2 conversion on highly-strained and oxygen-deficient BiVO4 photocatalyst. Chemical Engineering Journal 2022, 442 (P2), 136209-136209. https://doi.org/10.1016/j.cej.2022.136209

145. Liu, X.; Ye, L.; Liu, S.; Li, Y.; Ji, X., Photocatalytic reduction of CO2 by ZnO micro/nanomaterials with different morphologies and ratios of {0001} facets. Scientific Reports 2016, 6 (June), 1-9. https://doi.org/10.1038/srep38474

146. Zhang, L.; Wang, W.; Jiang, D.; Gao, E.; Sun, S., Photoreduction of CO2 on BiOCl nanoplates with the assistance of photoinduced oxygen

vacancies. Nano Research 2015, 8 (3), 821-831. https://doi.org/10.1007/s12274-014-0564-2

147. Li, P.; Zhu, S.; Hu, H.; Guo, L.; He, T., Influence of defects in porous ZnO nanoplates on CO2 photoreduction. Catalysis Today 2019, 335 (December 2018), 300-305. https://doi.org/10.1016/j.cattod.2018.11.068

148. Li, P.; Hu, H.; Luo, G.; Zhu, S.; Guo, L.; Qu, P.; Shen, Q.; He, T., Crystal Facet-Dependent CO2Photoreduction over Porous ZnO Nanocatalysts. ACS Applied Materials and Interfaces 2020, 12 (50), 56039-56048. https://doi.org/10.1021/acsami.0c17596

149. Liu, L.; Zhao, H.; Andino, J. M.; Li, Y., Photocatalytic CO2 reduction with H2O on TiO2 nanocrystals: Comparison of anatase, rutile, and brookite polymorphs and exploration of surface chemistry. ACS Catalysis 2012, 2, 1817-1828.
https://doi.org/10.1021/cs300273q

150. Valášková, M.; Tokarský, J.; Pavlovský, J.; Prostějovský, T.; Kočí, K., α-Fe2O3 nanoparticles/vermiculite clay material: Structural, optical and photocatalytic properties. Materials 2019, 12 (11), 1-16. https://doi.org/10.3390/ma12111880

151. Hegazy, I. M.; Geioushy, R. A.; El-Sheikh, S. M.; Shawky, A.; El-Sherbiny, S.; Kandil, A. H. T., Influence of oxygen vacancies on the performance of ZnO nanoparticles towards CO2 photoreduction in different aqueous solutions. Journal of Environmental Chemical Engineering 2020, 8 (4). https://doi.org/10.1016/j.jece.2020.103887

152. Mao, J.; Peng, T.; Zhang, X.; Li, K.; Zan, L., Selective methanol production from photocatalytic reduction of CO 2 on BiVO 4 under visible light irradiation. Catalysis Communications 2012, 28, 38-41. https://doi.org/10.1016/j.catcom.2012.08.008

153. Kar, P.; Zeng, S.; Zhang, Y.; Vahidzadeh, E.; Manuel, A.; Kisslinger, R.; Alam, K. M.; Thakur, U. K.; Mahdi, N.; Kumar, P.; Shankar, K., High rate CO2 photoreduction using flame annealed TiO2 nanotubes. Applied Catalysis B: Environmental 2019, 243 (May 2018), 522-536. https://doi.org/10.1016/j.apcatb.2018.08.002

154. Ávila-López, M. A.; Gavrielides, S.; Luo, X.; Ojoajogwu, A. E.; Tan, J. Z. Y.; Luévano-Hipólito, E.; Torres-Martínez, L. M.; Maroto-Valer, M. M., Comparative study of CO2photoreduction using different conformations of CuO photocatalyst: Powder, coating on mesh and thin film. Journal of CO2 Utilization 2021, 50, 1-9. https://doi.org/10.1016/j.jcou.2021.101588

155. Nogueira, A. E.; Oliveira, J. A.; da Silva, G. T. S. T.; Ribeiro, C., Insights into the role of CuO in the CO2 photoreduction process. Scientific Reports 2019, 9 (1), 1-11. https://doi.org/10.1038/s41598-018-36683-8

156. Nogueira, A. E.; da Silva, G. T. S. T.; Oliveira, J. A.; Torres, J. A.; da Silva, M. G. S.; Carmo, M.; Ribeiro, C., Unveiling CuO role in CO2 photoreduction process - Catalyst or reactant? Catalysis Communications 2020, 137 (January), 105929-105929. https://doi.org/10.1016/j.catcom.2020.105929

157. Li, X.; Pan, H.; Li, W.; Zhuang, Z., Photocatalytic reduction of CO 2 to methane over HNb 3O 8 nanobelts. Applied Catalysis A: General 2012, 413-414 (301), 103-108. https://doi.org/10.1016/j.apcata.2011.10.044

158. Xiao, L.; Lin, R.; Wang, J.; Cui, C.; Wang, J.; Li, Z., A novel hollow-hierarchical structured Bi2WO6 with enhanced photocatalytic activity for CO2 photoreduction. Journal of Colloid and Interface Science 2018, 523, 151-158. https://doi.org/10.1016/j.jcis.2018.03.064

159. Wang, L.; Wang, Y.; Cheng, Y.; Liu, Z.; Guo, Q.; Ha, M. N.; Zhao, Z., Hydrogen-treated mesoporous WO3 as a reducing agent of CO2 to fuels (CH4 and CH3OH) with enhanced photothermal catalytic performance. Journal of Materials Chemistry A 2016, 4 (14), 5314-5322. https://doi.org/10.1039/C5TA10180H

160. Huang, C. y.; Guo, R. t.; Pan, W. g.; Tang, J. y.; Zhou, W. g.; Liu, X. y.; Qin, H.; Jia, P. y., One-dimension TiO2 nanostructures with enhanced activity for CO2 photocatalytic reduction. Applied Surface Science 2019, 464, 534-543. https://doi.org/10.1016/j.apsusc.2018.09.114

161. Chen, X.; Zhou, Y.; Liu, Q.; Li, Z.; Liu, J.; Zou, Z., Ultrathin, single-crystal WO 3 nanosheets by two-dimensional oriented attachment toward enhanced photocatalystic reduction of CO 2 into hydrocarbon fuels under visible light. ACS Applied Materials and Interfaces 2012, 4 (7), 3372-3377. https://doi.org/10.1021/am300661s

162. Zhou, Y.; Tian, Z.; Zhao, Z.; Liu, Q.; Kou, J.; Chen, X.; Gao, J.; Yan, S.; Zou, Z., High-yield synthesis of ultrathin and uniform Bi2WO6 square nanoplates benefitting from photocatalytic reduction of CO2 into renewable hydrocarbon fuel under visible light. ACS Applied Materials and Interfaces 2011, 3 (9), 3594-3601. https://doi.org/10.1021/am2008147

163. Kong, X. Y.; Choo, Y. Y.; Chai, S. P.; Soh, A. K.; Mohamed, A. R., Oxygen vacancy induced Bi2WO6 for the realization of photocatalytic CO2 reduction over the full solar spectrum: from the UV to the NIR region. Chemical Communications 2016, 52 (99), 14242-14245. https://doi.org/10.1039/C6CC07750A

164. Dong, L.; Xiong, Z.; Zhou, Y.; Zhao, J.; Li, Y.; Wang, J.; Chen, X.; Zhao, Y.; Zhang, J., Photocatalytic CO2 reduction over postcalcinated atomically thin TiO2 nanosheets: Residual carbon removal and structure transformation. Journal of CO2 Utilization 2020, 41, 101262. https://doi.org/10.1016/j.jcou.2020.101262

165. Xie, Y. P.; Liu, G.; Yin, L.; Cheng, H. M., Crystal facet-dependent photocatalytic oxidation and reduction reactivity of monoclinic WO3 for solar energy conversion. Journal of Materials Chemistry 2012, 22, 6746-6751. https://doi.org/10.1039/c2jm16178h

166. Liu, Y.; Huang, B.; Dai, Y.; Zhang, X.; Qin, X.; Jiang, M.; Whangbo, M. H., Selective ethanol formation from photocatalytic reduction of carbon dioxide in water with BiVO4 photocatalyst. Catalysis Communications 2009, 11 (3), 210-213. https://doi.org/10.1016/j.catcom.2009.10.010

167. Sun, S.; Watanabe, M.; Wu, J.; An, Q.; Ishihara, T., Ultrathin WO3·0.33H2O Nanotubes for CO2 Photoreduction to Acetate with High Selectivity. Journal of the American Chemical Society 2018, 140 (20), 6474-6482.
https://doi.org/10.1021/jacs.8b03316

168. da Silva, G. T. S. T.; Nogueira, A. E.; Oliveira, J. A.; Torres, J. A.; Lopes, O. F.; Ribeiro, C., Acidic surface niobium pentoxide is catalytic active for CO2 photoreduction. Applied Catalysis B: Environmental 2019, 242 (July 2018), 349-357.
https://doi.org/10.1016/j.apcatb.2018.10.017

169. Ovcharov, M. L.; Mishura, A. M.; Shcherban, N. D.; Filonenko, S. M.; Granchak, V. M., Photocatalytic reduction of CO2 using nanostructured Cu2O with foam-like structure. Solar Energy 2016, 139, 452-457. https://doi.org/10.1016/j.solener.2016.10.010

170. Yu, H.; Yan, S.; Zhou, P.; Zou, Z., CO 2 photoreduction on hydroxyl-group-rich mesoporous single crystal TiO 2. Applied Surface Science 2018, 427, 603-607.
https://doi.org/10.1016/j.apsusc.2017.08.073

171. Nunes, B. N.; Lopes, O. F.; Patrocinio, A. O. T.; Bahnemann, D. W., Recent advances in niobium-based materials for photocatalytic solar fuel

production. Catalysts 2020, 10 (1), 126. https://doi.org/10.3390/catal10010126

172. Prado, A. C. F.; Malafatti, J. O. D.; Oliveira, J. A.; Ribeiro, C.; Joya, M. R.; Luz, A. P.; Paris, E. C., Preparation and application of Nb2O5 nanofibers in CO2 photoconversion. Nanomaterials 2021, 11 (12), 1-14. https://doi.org/10.3390/nano11123268

173. Wang, P. Q.; Bai, Y.; Liu, J. Y.; Fan, Z.; Hu, Y. Q., One-pot synthesis of rutile TiO2 nanoparticle modified anatase TiO2 nanorods toward enhanced photocatalytic reduction of CO 2 into hydrocarbon fuels. Catalysis Communications 2012, 29, 185-188. https://doi.org/10.1016/j.catcom.2012.10.010

174. Galli, F.; Compagnoni, M.; Vitali, D.; Pirola, C.; Bianchi, C. L.; Villa, A.; Prati, L.; Rossetti, I., CO2 photoreduction at high pressure to both gas and liquid products over titanium dioxide. Applied Catalysis B: Environmental 2017, 200, 386-391. https://doi.org/10.1016/j.apcatb.2016.07.038

175. Low, J.; Cheng, B.; Yu, J., Surface modification and enhanced photocatalytic CO 2 reduction performance of TiO 2 : a review. Applied Surface Science 2017, 392, 658-686. https://doi.org/10.1016/j.apsusc.2016.09.093

176. Yang, M.-Q.; Xu, Y.-J., Photocatalytic conversion of CO2 over graphene-based composites: Current status and future perspective. Nanoscale Horizons 2016, 1 (3), 185-200. https://doi.org/10.1039/C5NH00113G

177. Pan, Y. X.; You, Y.; Xin, S.; Li, Y.; Fu, G.; Cui, Z.; Men, Y. L.; Cao, F. F.; Yu, S. H.; Goodenough, J. B., Photocatalytic CO2 Reduction by Carbon-Coated Indium-Oxide Nanobelts. Journal of the American Chemical Society 2017, 139 (11), 4123-4129. https://doi.org/10.1021/jacs.7b00266

178. Ehsan, M. F.; He, T., In situ synthesis of ZnO/ZnTe common cation heterostructure and its visible-light photocatalytic reduction of CO2 into CH4. Applied Catalysis B: Environmental 2015, 166-167, 345-352. https://doi.org/10.1016/j.apcatb.2014.11.058

179. Tseng, I. h.; Chang, W.-c.; Wu, J. C. S., Photoreduction of CO2 using sol-gel derived titania and titania-supported copper catalysts. Applied Catalysis B: Environmental 2002, 37, 37-48. https://doi.org/10.1016/S0926-3373(01)00322-8

180. Teramura, K.; Wang, Z.; Hosokawa, S.; Sakata, Y.; Tanaka, T., A doping technique that suppresses undesirable H2 evolution derived from overall water splitting in the highly selective photocatalytic conversion of CO2 in and by water. Chemistry - A European Journal 2014, 20, 9906-9909. https://doi.org/10.1002/chem.201402242

181. Zhao, G.; Zhou, W.; Sun, Y.; Wang, X.; Liu, H.; Meng, X.; Chang, K.; Ye, J., Efficient photocatalytic CO2 reduction over Co(II) species modified CdS in aqueous solution. Applied Catalysis B: Environmental 2018, 226 (November 2017), 252-257. https://doi.org/10.1016/j.apcatb.2017.12.054

182. Jia, P.-y.; Guo, R.-t.; Pan, W.-g.; Huang, C.-y.; Tang, J.-y.; Liu, X.-y.; Qin, H.; Xu, Q.-y., The MoS2/TiO2 heterojunction composites with enhanced activity for CO2 photocatalytic reduction under visible light irradiation. Colloids and Surfaces A: Physicochemical and Engineering Aspects 2019, 570, 306-316. https://doi.org/10.1016/j.colsurfa.2019.03.045

183. Qaraah, F. A.; Mahyoub, S. A.; Hezam, A.; Qaraah, A.; Xin, F.; Xiu, G., Synergistic effect of hierarchical structure and S-scheme heterojunction over O-doped g-C3N4/N-doped Nb2O5 for highly efficient photocatalytic CO2 reduction. Applied Catalysis B: Environmental 2022, 315, 121585-121596. https://doi.org/10.1016/j.apcatb.2022.121585

184. Sharma, P.; Kumar, S.; Tomanec, O.; Petr, M.; Zhu Chen, J.; Miller, J. T.; Varma, R. S.; Gawande, M. B.; Zbořil, R., Carbon Nitride-Based Ruthenium Single Atom Photocatalyst for CO2 Reduction to Methanol. Small 2021, 17 (16), 1-7. https://doi.org/10.1002/smll.202006478

185. Zhou, M.; Wang, S.; Yang, P.; Huang, C.; Wang, X., Boron Carbon Nitride Semiconductors Decorated with CdS Nanoparticles for Photocatalytic Reduction of CO2. ACS Catalysis 2018, 8 (6), 4928-4936. https://doi.org/10.1021/acscatal.8b00104

186. Wang, Y.; Li, B.; Zhang, C.; Cui, L.; Kang, S.; Li, X.; Zhou, L., Ordered mesoporous CeO2-TiO2 composites: Highly efficient photocatalysts for the reduction of CO2 with H2O under simulated solar irradiation. Applied Catalysis B: Environmental 2013, 130-131, 277-284. https://doi.org/10.1016/j.apcatb.2012.11.019

187. Chen, R.; Yin, H.; Zhang, Z.; Ding, J.; Zhang, J.; Wan, H., Enwrapping g-C3N4 on In2O3 hollow hexagonal tubular for photocatalytic CO2 conversion: Construction, characterization, and Z- scheme mechanism insight. Journal of Colloid And Interface Science 2023, 631, 122-132. https://doi.org/10.1016/j.jcis.2022.11.006

188. Wang, L.; Dong, Y.; Zhang, J.; Tao, F.; Xu, J., Construction of NiO/g-C3N4 p-n heterojunctions for enhanced photocatalytic CO2 reduction. Journal of Solid State Chemistry 2022, 308, 122878-122889. https://doi.org/10.1016/j.jssc.2022.122878

189. Kumar, P.; Joshi, C.; Barras, A.; Sieber, B.; Addad, A.; Boussekey, L.; Szunerits, S.; Boukherroub, R.; Jain, S. L., Core-shell structured reduced graphene oxide wrapped magnetically separable rGO@CuZnO@Fe3O4 microspheres as superior photocatalyst for CO2 reduction under visible light. Applied Catalysis B: Environmental 2017, 205, 654-665. https://doi.org/10.1016/j.apcatb.2016.11.060

190. Xiang, T.; Xin, F.; Zhao, C.; Lou, S.; Qu, W.; Wang, Y.; Song, Y.; Zhang, S.; Yin, X., Fabrication of nano copper oxide evenly patched on cubic sodium tantalate for oriented photocatalytic reduction of carbon dioxide. Journal of Colloid and Interface Science 2018, 518, 34-40. https://doi.org/10.1016/j.jcis.2018.01.109

191. Zhang, L.; Li, N.; Jiu, H.; Qi, G.; Huang, Y., ZnO-reduced graphene oxide nanocomposites as efficient photocatalysts for photocatalytic reduction of CO2. Ceramics International 2015, 41 (5), 6256-6262. https://doi.org/10.1016/j.ceramint.2015.01.044

192. Kumar, P.; Joshi, C.; Labhsetwar, N.; Boukherroub, R.; Jain, S. L., A novel Ru/TiO2 hybrid nanocomposite catalyzed photoreduction of CO2 to methanol under visible light. Nanoscale 2015, 7 (37), 15258-15267. https://doi.org/10.1039/C5NR03712C

193. Li, X.; Wang, Q.; Zhao, Y.; Wu, W.; Chen, J.; Meng, H., Green synthesis and photo-catalytic performances for ZnO-reduced graphene oxide nanocomposites. Journal of Colloid and Interface Science 2013, 411, 69-75. https://doi.org/10.1016/j.jcis.2013.08.050

194. Cheng, S. P.; Wei, L. W.; Wang, H. P., Photocatalytic reduction of CO2 to methanol by Cu2 O/TiO2 heterojunctions. Sustainability 2022, 14 (1), 1-13.
https://doi.org/10.3390/su14010374

195. Tahir, M.; Amin, N. A. S., Indium-doped TiO2 nanoparticles for photocatalytic CO2 reduction with H2O vapors to CH4. Applied Catalysis B: Environmental 2015, 162, 98-109. https://doi.org/10.1016/j.apcatb.2014.06.037

196. Li, M.; Li, P.; Chang, K.; Wang, T.; Liu, L.; Kang, Q.; Ouyang, S.; Ye, J., Highly efficient and stable photocatalytic reduction of CO2 to CH4 over Ru loaded NaTaO3. Chemical Communications 2015, 51 (36), 7645-7648. https://doi.org/10.1039/C5CC01124H

197. Song, Y.; Ye, C.; Yu, X.; Tang, J.; Zhao, Y.; Cai, W., Electron-induced enhanced interfacial interaction of the CuO/BiOCl heterostructure for boosted CO2 photoreduction performance under simulated sunlight. Applied Surface Science 2022, 583 (December 2021), 152463-152463. https://doi.org/10.1016/j.apsusc.2022.152463

198. Wan, Z.; Wang, J.; Wang, K.; Hu, M.; Wang, X., Photocatalytic reduction of CO2 with H2O vapor into solar fuels over Ni modified porous In2O3 nanosheets. Catalysis Today 2021, 374 (September 2020), 44-52. https://doi.org/10.1016/j.cattod.2020.10.008

199. Wang, F.; Wu, J.; Chen, S.; Duan, L., Ball-flower like CoS/g-C3N4 heterojunction photocatalyst for efficient and selective reduction of CO2 to CH4. Journal of CO2 Utilization 2023, 69, 102402-102413. https://doi.org/10.1016/j.jcou.2023.102402

200. Mehregan, S.; Hayati, F.; Mehregan, M.; Isari, A. A.; Jafari, A. J.; Giannakis, S.; Kakavandi, B., Exploring the visible light-assisted conversion of CO2 into methane and methanol, using direct Z-scheme TiO2@g-C3N4 nanosheets: synthesis and photocatalytic performance. Environmental Science and Pollution Research 2022, 29, 74951-74966. https://doi.org/10.1007/s11356-022-21048-6

201. Chen, C.; Jin, J.; Chen, S.; Wang, T.; Xiao, J.; Peng, T., In-situ growth of ultrafine ZnO on g-C3N4 layer for highly active and selective CO2 photoreduction to CH4 under visible light. Materials Research Bulletin 2021, 137 (August 2020), 111177-111177. https://doi.org/10.1016/j.materresbull.2020.111177

202. Zhu, X.; Deng, H.; Cheng, G., Facile construction of g-C3N4-W18O49 heterojunction with improved charge transfer for solar-driven CO2 photoreduction. Inorganic Chemistry Communications 2021, 132, 108814. https://doi.org/10.1016/j.inoche.2021.108814

203. Zhang, Z.; Wang, Z.; Cao, S.-w.; Xue, C., Au/Pt Nanoparticle-Decorated TiO 2 Nano fi bers with Plasmon- Enhanced Photocatalytic Activities for Solar-to-Fuel Conversion. The Journal of Physical Chemistry C 2013, 2. https://doi.org/10.1021/jp409311x

204. Qin, S.; Xin, F.; Liu, Y.; Yin, X.; Ma, W., Photocatalytic reduction of CO2 in methanol to methyl formate over CuO-TiO2 composite catalysts. Journal of Colloid and Interface Science 2011, 356 (1), 257-261. https://doi.org/10.1016/j.jcis.2010.12.034

205. Habisreutinger, S. N.; Schmidt-Mende, L.; Stolarczyk, J. K., Photocatalytic reduction of CO2 on TiO2 and other semiconductors.

Angewandte Chemie - International Edition 2013, 52 (29), 7372-7408. https://doi.org/10.1002/anie.201207199

206. Torres, J. A.; Nogueira, A. E.; Da Silva, G. T. S. T.; Lopes, O. F.; Wang, Y.; He, T.; Ribeiro, C., Enhancing TiO2 activity for CO2 photoreduction through MgO decoration. Journal of CO2 Utilization 2020, 35 (September 2019), 106-114.
https://doi.org/10.1016/j.jcou.2019.09.008

207. Nogueira, A. E.; Silva, G. T. S. T.; Oliveira, J. A.; Lopes, O. F.; Torres, J. A.; Carmo, M.; Ribeiro, C., CuO Decoration Controls Nb2O5 Photocatalyst Selectivity in CO2 Reduction. ACS Applied Energy Materials 2020, 3, 7629-7636. https://doi.org/10.1021/acsaem.0c01047

208. Shen, H.; Peppel, T.; Strunk, J.; Sun, Z., Photocatalytic Reduction of CO2 by Metal-Free-Based Materials: Recent Advances and Future Perspective. Solar RRL 2020, 4 (8). https://doi.org/10.1002/solr.201900546

209. Chang, X.; Wang, T.; Gong, J., CO 2 photo-reduction: insights into CO 2 activation and reaction on surfaces of photocatalysts. Energy Environmental Science 2016, 9 (7), 2177-2196. https://doi.org/10.1039/C6EE00383D

210. Tu, W.; Zhou, Y.; Zou, Z., Photocatalytic conversion of CO2 into renewable hydrocarbon fuels: State-of-the-art accomplishment, challenges, and prospects. Advanced Materials 2014, 26 (27), 4607-4626. https://doi.org/10.1002/adma.201400087

211. Karthikeyan, C.; Arunachalam, P.; Ramachandran, K.; Al-Mayouf, A. M.; Karuppuchamy, S., Recent advances in semiconductor metal oxides with enhanced methods for solar photocatalytic applications. Journal of Alloys and Compounds 2020, 828, 154281-154281. https://doi.org/10.1016/j.jallcom.2020.154281

212. Furukawa, H.; Yaghi, O. M., Storage of Hydrogen, Methane, and Carbon Dioxide in Highly Porous Covalent Organic Frameworks for Clean Energy Applications. Journal of the American Chemical Society 2009, 131 (25), 8875-8883.
https://doi.org/10.1021/ja9015765

213. Doonan, C. J.; Tranchemontagne, D. J.; Glover, T. G.; Hunt, J. R.; Yaghi, O. M., Exceptional ammonia uptake by a covalent organic framework. Nature Chemistry 2010, 2 (3), 235-238. https://doi.org/10.1038/nchem.548

214. Ding, S.-Y.; Wang, W., Covalent organic frameworks (COFs): from design to applications. Chemical Society Reviews 2013, 42 (2), 548-568. https://doi.org/10.1039/C2CS35072F

215. Guan, X.; Li, H.; Ma, Y.; Xue, M.; Fang, Q.; Yan, Y.; Valtchev, V.; Qiu, S., Chemically stable polyarylether-based covalent organic frameworks. Nature Chemistry 2019, 11 (6), 587-594. https://doi.org/10.1038/s41557-019-0238-5

216. Han, X.; Zhang, J.; Huang, J.; Wu, X.; Yuan, D.; Liu, Y.; Cui, Y., Chiral induction in covalent organic frameworks. Nature Communications 2018, 9 (1), 1294-1294. https://doi.org/10.1038/s41467-018-03689-9

217. Yusran, Y.; Fang, Q.; Valtchev, V., Electroactive Covalent Organic Frameworks: Design, Synthesis, and Applications. Advanced Materials 2020, 32 (44), 2002038-2002038. https://doi.org/10.1002/adma.202002038

218. DeBlase, C. R.; Hernández-Burgos, K.; Silberstein, K. E.; Rodríguez-Calero, G. G.; Bisbey, R. P.; Abruña, H. D.; Dichtel, W. R., Rapid and Efficient Redox Processes within 2D Covalent Organic Framework Thin Films. ACS Nano 2015, 9 (3), 3178-3183. https://doi.org/10.1021/acsnano.5b00184

219. Yang, H.; Zhang, S.; Han, L.; Zhang, Z.; Xue, Z.; Gao, J.; Li, Y.; Huang, C.; Yi, Y.; Liu, H.; Li, Y., High Conductive Two-Dimensional Covalent Organic Framework for Lithium Storage with Large Capacity. ACS Applied Materials & Interfaces 2016, 8 (8), 5366-5375. https://doi.org/10.1021/acsami.5b12370

220. Hu, Y.; Dunlap, N.; Wan, S.; Lu, S.; Huang, S.; Sellinger, I.; Ortiz, M.; Jin, Y.; Lee, S.-h.; Zhang, W., Crystalline Lithium Imidazolate Covalent Organic Frameworks with High Li-Ion Conductivity. Journal of the American Chemical Society 2019, 141 (18), 7518-7525. https://doi.org/10.1021/jacs.9b02448

221. Wang, D.-G.; Qiu, T.; Guo, W.; Liang, Z.; Tabassum, H.; Xia, D.; Zou, R., Covalent organic framework-based materials for energy applications. Energy & Environmental Science 2021, 14 (2), 688-728. https://doi.org/10.1039/D0EE02309D

222. Bessinger, D.; Ascherl, L.; Auras, F.; Bein, T., Spectrally Switchable Photodetection with Near-Infrared-Absorbing Covalent Organic Frameworks. Journal of the American Chemical Society 2017, 139 (34), 12035-12042. https://doi.org/10.1021/jacs.7b06599

223. Jin, E.; Asada, M.; Xu, Q.; Dalapati, S.; Addicoat, M. A.; Brady, M. A.; Xu, H.; Nakamura, T.; Heine, T.; Chen, Q.; Jiang, D., Two-dimensional sp2 carbon-conjugated covalent organic frameworks. Science 2017, 357 (6352), 673-676.
https://doi.org/10.1126/science.aan0202

224. Fang, Q.; Zhuang, Z.; Gu, S.; Kaspar, R. B.; Zheng, J.; Wang, J.; Qiu, S.; Yan, Y., Designed synthesis of large-pore crystalline polyimide covalent organic frameworks. Nature Communications 2014, 5 (1), 4503-4503. https://doi.org/10.1038/ncomms5503

225. Dogru, M.; Handloser, M.; Auras, F.; Kunz, T.; Medina, D.; Hartschuh, A.; Knochel, P.; Bein, T., A Photoconductive Thienothiophene-Based Covalent Organic Framework Showing Charge Transfer Towards Included Fullerene. Angewandte Chemie International Edition 2013, 52 (10), 2920-2924. https://doi.org/10.1002/anie.201208514

226. Waller, P. J.; Lyle, S. J.; Osborn Popp, T. M.; Diercks, C. S.; Reimer, J. A.; Yaghi, O. M., Chemical Conversion of Linkages in Covalent Organic Frameworks. Journal of the American Chemical Society 2016, 138 (48), 15519-15522.
https://doi.org/10.1021/jacs.6b08377

227. Haase, F.; Troschke, E.; Savasci, G.; Banerjee, T.; Duppel, V.; Dörfler, S.; Grundei, M. M. J.; Burow, A. M.; Ochsenfeld, C.; Kaskel, S.; Lotsch, B. V., Topochemical conversion of an imine- into a thiazole-linked covalent organic framework enabling real structure analysis. Nature Communications 2018, 9 (1), 2600-2600. https://doi.org/10.1038/s41467-018-04979-y

228. Zhao, C.; Lyu, H.; Ji, Z.; Zhu, C.; Yaghi, O. M., Ester-linked crystalline covalent organic frameworks. Journal of the American Chemical Society 2020, 142 (34), 14450-14454. https://doi.org/10.1021/jacs.0c07015

229. Li, X., sp2 carbon-conjugated covalent organic frameworks: synthesis, properties, and applications. Materials Chemistry Frontiers 2021, 5 (7), 2931-2949. https://doi.org/10.1039/D1QM00015B

230. Lu, M.; Zhang, M.; Liu, J.; Chen, Y.; Liao, J.-P.; Yang, M.-Y.; Cai, Y.-P.; Li, S.-L.; Lan, Y.-Q., Covalent Organic Framework Based Functional Materials: Important Catalysts for Efficient CO2 Utilization. Angewandte Chemie International Edition 2022, 61 (15), e202200003-e202200003. https://doi.org/10.1002/anie.202200003

231. Lin, S.; Diercks, C. S.; Zhang, Y. B.; Kornienko, N.; Nichols, E. M.; Zhao, Y.; Paris, A. R.; Kim, D.; Yang, P.; Yaghi, O. M.; Chang, C. J., Covalent organic frameworks comprising cobalt porphyrins for catalytic CO2 reduction in water. Science 2015, 349 (6253), 1208-1213. https://doi.org/10.1126/science.aac8343

232. Yadav, R. K.; Kumar, A.; Park, N. J.; Kong, K. J.; Baeg, J. O., A highly efficient covalent organic framework film photocatalyst for selective solar fuel production from CO2. Journal of Materials Chemistry A 2016, 4 (24), 9413-9418.
https://doi.org/10.1039/C6TA01625A

233. Guo, L.; Jin, S., Stable Covalent Organic Frameworks for Photochemical Applications. ChemPhotoChem 2019, 3 (10), 973-983. https://doi.org/10.1002/cptc.201900089

234. Ozdemir, J.; Mosleh, I.; Abolhassani, M.; Greenlee, L. F.; Beitle, R. R.; Beyzavi, M. H., Covalent Organic Frameworks for the Capture, Fixation, or Reduction of CO2. Frontiers in Energy Research 2019, 7. https://doi.org/10.3389/fenrg.2019.00077

235. Li, H.; Wang, L.; Yu, G., Covalent organic frameworks: Design, synthesis, and performance for photocatalytic applications. Nano Today 2021, 40, 101247-101247. https://doi.org/10.1016/j.nantod.2021.101247

236. Xu, N.; Diao, Y.; Qin, X.; Xu, Z.; Ke, H.; Zhu, X., Donor-acceptor covalent organic frameworks of nickel(ii) porphyrin for selective and efficient CO2reduction into CO. Dalton Transactions 2020, 49 (44), 15587-15591. https://doi.org/10.1039/D0DT03205K

237. Zhong, H.; Hong, Z.; Yang, C.; Li, L.; Xu, Y.; Wang, X.; Wang, R., A Covalent Triazine-Based Framework Consisting of Donor-Acceptor Dyads for Visible-Light-Driven Photocatalytic CO2 Reduction. ChemSusChem 2019, 12 (19), 4493-4499. https://doi.org/10.1002/cssc.201901997

238. Lei, K.; Wang, D.; Ye, L.; Kou, M.; Deng, Y.; Ma, Z.; Wang, L.; Kong, Y., A Metal-Free Donor-Acceptor Covalent Organic Framework Photocatalyst for Visible-Light-Driven Reduction of CO2 with H2O. ChemSusChem 2020, 13 (7), 1725-1729. https://doi.org/10.1002/cssc.201903545

239. Kim, T. W.; Jun, S.; Ha, Y.; Yadav, R. K.; Kumar, A.; Yoo, C.-Y.; Oh, I.; Lim, H.-K.; Shin, J. W.; Ryoo, R., Ultrafast charge transfer coupled with lattice phonons in two-dimensional covalent organic frameworks. Nature

Communications 2019, 10 (1), 1-10. https://doi.org/10.1038/s41467-019-09872-w

240. Feng, X.; Chen, L.; Honsho, Y.; Saengsawang, O.; Liu, L.; Wang, L.; Saeki, A.; Irle, S.; Seki, S.; Dong, Y.; Jiang, D., An Ambipolar Conducting Covalent Organic Framework with Self-Sorted and Periodic Electron Donor-Acceptor Ordering. Advanced Materials 2012, 24 (22), 3026-3031. https://doi.org/10.1002/adma.201201185

241. Li, X.; Gao, Q.; Aneesh, J.; Xu, H.-S.; Chen, Z.; Tang, W.; Liu, C.; Shi, X.; Adarsh, K. V.; Lu, Y.; Loh, K. P., Molecular Engineering of Bandgaps in Covalent Organic Frameworks. Chemistry of Materials 2018, 30 (16), 5743-5749.
https://doi.org/10.1021/acs.chemmater.8b02560

242. Miró, P.; Audiffred, M.; Heine, T., An atlas of two-dimensional materials. Chemical Society Reviews 2014, 43 (18), 6537-6554. https://doi.org/10.1039/C4CS00102H

243. Lukose, B.; Kuc, A.; Frenzel, J.; Heine, T., On the reticular construction concept of covalent organic frameworks. Beilstein Journal of Nanotechnology 2010, 1, 60-70. https://doi.org/10.3762/bjnano.1.8

244. Ghosh, S.; Nakada, A.; Springer, M. A.; Kawaguchi, T.; Suzuki, K.; Kaji, H.; Baburin, I.; Kuc, A.; Heine, T.; Suzuki, H.; Abe, R.; Seki, S., Identification of Prime Factors to Maximize the Photocatalytic Hydrogen Evolution of Covalent Organic Frameworks. Journal of the American Chemical Society 2020, 142 (21), 9752-9762.
https://doi.org/10.26434/chemrxiv.8957039.v2

245. Jakowetz, A. C.; Hinrichsen, T. F.; Ascherl, L.; Sick, T.; Calik, M.; Auras, F.; Medina, D. D.; Friend, R. H.; Rao, A.; Bein, T., Excited-state dynamics in fully conjugated 2D covalent organic frameworks. Journal of the American Chemical Society 2019, 141 (29), 11565-11571. https://doi.org/10.1021/jacs.9b03956

246. Fu, Y.; Zhu, X.; Huang, L.; Zhang, X.; Zhang, F.; Zhu, W., Azine-based covalent organic frameworks as metal-free visible light photocatalysts for CO2 reduction with H2O. Applied Catalysis B: Environmental 2018, 239, 46-51. https://doi.org/10.1016/j.apcatb.2018.08.004

247. Cui, J. X.; Wang, L. J.; Feng, L.; Meng, B.; Zhou, Z. Y.; Su, Z. M.; Wang, K.; Liu, S., A metal-free covalent organic framework as a photocatalyst for CO2reduction at low CO2concentration in a gas-solid system. Journal of Materials Chemistry A 2021, 9 (44), 24895-24902. https://doi.org/10.1039/D1TA07686H

248. Zhang, M.; Lu, M.; Lang, Z. L.; Liu, J.; Liu, M.; Chang, J. N.; Li, L. Y.; Shang, L. J.; Wang, M.; Li, S. L., Semiconductor/covalent-organic-framework Z-scheme heterojunctions for artificial photosynthesis. Angewandte Chemie International Edition 2020, 132 (16), 6562-6568. https://doi.org/10.1002/ange.202000929

249. Zhong, W.; Sa, R.; Li, L.; He, Y.; Li, L.; Bi, J.; Zhuang, Z.; Yu, Y.; Zou, Z., A covalent organic framework bearing single Ni sites as a synergistic photocatalyst for selective photoreduction of CO2 to CO. Journal of the American Chemical Society 2019, 141 (18), 7615-7621. https://doi.org/10.1021/jacs.9b02997

250. Frey, L.; Jarju, J. J.; Salonen, L. M.; Medina, D. D., Boronic-acid-derived covalent organic frameworks: from synthesis to applications. New Journal of Chemistry 2021, 45 (33), 14879-14907. https://doi.org/10.1039/D1NJ01269J

251. Keller, N.; Bein, T., Optoelectronic processes in covalent organic frameworks. Chemical Society Reviews 2021, 50 (3), 1813-1845. https://doi.org/10.1039/D0CS00793E

252. Uribe-Romo, F. J.; Hunt, J. R.; Furukawa, H.; Klöck, C.; O'Keeffe, M.; Yaghi, O. M., A Crystalline Imine-Linked 3-D Porous Covalent Organic Framework. Journal of the American Chemical Society 2009, 131 (13), 4570-4571.
https://doi.org/10.1021/ja8096256

253. Kandambeth, S.; Mallick, A.; Lukose, B.; Mane, M. V.; Heine, T.; Banerjee, R., Construction of Crystalline 2D Covalent Organic Frameworks with Remarkable Chemical (Acid/Base) Stability via a Combined Reversible and Irreversible Route. Journal of the American Chemical Society 2012, 134 (48), 19524-19527.
https://doi.org/10.1021/ja308278w

254. Waller, P. J.; AlFaraj, Y. S.; Diercks, C. S.; Jarenwattananon, N. N.; Yaghi, O. M., Conversion of Imine to Oxazole and Thiazole Linkages in Covalent Organic Frameworks. Journal of the American Chemical Society 2018, 140 (29), 9099-9103.
https://doi.org/10.1021/jacs.8b05830

255. Xiang, Y.; Dong, W.; Wang, P.; Wang, S.; Ding, X.; Ichihara, F.; Wang, Z.; Wada, Y.; Jin, S.; Weng, Y.; Chen, H.; Ye, J., Constructing electron delocalization channels in covalent organic frameworks powering CO2 photoreduction in water. Applied Catalysis B: Environmental 2020, 274, 119096-119096.
https://doi.org/10.1016/j.apcatb.2020.119096

256. Jiang, D., Covalent Organic Frameworks: An Amazing Chemistry Platform for Designing Polymers. Chem 2020, 6 (10), 2461-2483. https://doi.org/10.1016/j.chempr.2020.08.024

257. Ding, X.; Guo, J.; Feng, X.; Honsho, Y.; Guo, J.; Seki, S.; Maitarad, P.; Saeki, A.; Nagase, S.; Jiang, D., Synthesis of Metallophthalocyanine Covalent Organic Frameworks That Exhibit High Carrier Mobility and Photoconductivity. Angewandte Chemie International Edition 2011, 50 (6), 1289-1293.
https://doi.org/10.1002/anie.201005919

258. Er, D.; Dong, L.; Shenoy, V. B., Mechanisms for Engineering Highly Anisotropic Conductivity in a Layered Covalent-Organic Framework. The Journal of Physical Chemistry C 2016, 120 (1), 174-178. https://doi.org/10.1021/acs.jpcc.5b11928

259. Liu, W.; Li, X.; Wang, C.; Pan, H.; Liu, W.; Wang, K.; Zeng, Q.; Wang, R.; Jiang, J., A Scalable General Synthetic Approach toward Ultrathin Imine-Linked Two-Dimensional Covalent Organic Framework Nanosheets for Photocatalytic CO2 Reduction. Journal of the American Chemical Society 2019, 141 (43), 17431-17440. https://doi.org/10.1021/jacs.9b09502

260. Gao, Z.-Z.; Wang, Z.-K.; Wei, L.; Yin, G.; Tian, J.; Liu, C.-Z.; Wang, H.; Zhang, D.-W.; Zhang, Y.-B.; Li, X.; Liu, Y.; Li, Z.-T., Water-Soluble 3D Covalent Organic Framework that Displays an Enhanced Enrichment Effect of Photosensitizers and Catalysts for the Reduction of Protons to H2. ACS Applied Materials & Interfaces 2020, 12 (1), 1404-1411. https://doi.org/10.1021/acsami.9b19870

261. Li, H.; Chang, J.; Li, S.; Guan, X.; Li, D.; Li, C.; Tang, L.; Xue, M.; Yan, Y.; Valtchev, V.; Qiu, S.; Fang, Q., Three-Dimensional Tetrathiafulvalene-Based Covalent Organic Frameworks for Tunable Electrical Conductivity. Journal of the American Chemical Society 2019, 141 (34), 13324-13329. https://doi.org/10.1021/jacs.9b06908

262. Guo, S.; Xiao, Y.; Jiang, B., Encapsulation of Pd Nanoparticles in Covalent Triazine Frameworks for Enhanced Photocatalytic CO2 Conversion. ACS Sustainable Chemistry & Engineering 2021, 9 (37), 12646-12654. https://doi.org/10.1021/acssuschemeng.1c04176

263. Pachfule, P.; Acharjya, A.; Roeser, J.; Langenhahn, T.; Schwarze, M.; Schomäcker, R.; Thomas, A.; Schmidt, J., Diacetylene functionalized covalent organic framework (COF) for photocatalytic hydrogen generation. Journal of the American Chemical Society 2018, 140 (4), 1423-1427. https://doi.org/10.1021/jacs.7b11255

264. Wheatley, P. S., Gas Storage in Nanoporous Materials. Angewandte Chemie International Edition 2008, 47, 4966-4981. https://doi.org/10.1002/anie.200703934

265. Chen, X.; Dang, Q.; Sa, R.; Li, L.; Li, L.; Bi, J.; Zhang, Z.; Long, J.; Yu, Y.; Zou, Z., Integrating single Ni sites into biomimetic networks of covalent organic frameworks for selective photoreduction of CO2. Chemical Science 2020, 11 (26), 6915-6922. https://doi.org/10.1039/D0SC01747G

266. Yuan, F.; Yang, Z.; Zhang, X.; Tong, C.; Gahungu, G.; Li, W.; Zhang, J., Judicious design functionalized 3D-COF to enhance CO2 adsorption and separation. Journal of Computational Chemistry 2021, 42 (13), 888-896. https://doi.org/10.1002/jcc.26510

267. Zhang, M.; Zheng, R.; Ma, Y.; Chen, R.; Sun, X.; Sun, X., N-rich covalent organic frameworks with different pore size for high-pressure CO2 adsorption. Microporous and Mesoporous Materials 2019, 285, 70-79. https://doi.org/10.1016/j.micromeso.2019.04.021

268. Xu, R.; Wang, X. S.; Zhao, H.; Lin, H.; Huang, Y. B.; Cao, R., Rhenium-modified porous covalent triazine framework for highly efficient photocatalytic carbon dioxide reduction in a solid-gas system. Catalysis Science and Technology 2018, 8 (8), 2224-2230. https://doi.org/10.1039/C8CY00176F

269. You, S.-Q.; Zhou, J.; Chen, M.-M.; Sun, C.-Y.; Qi, X.-J.; Yousaf, A.; Wang, X.-L.; Su, Z.-M., A hydrazone-based covalent organic framework/iridium (III) complex for photochemical CO2 reduction with enhanced efficiency and durability. Journal of Catalysis 2020, 392, 49-55. https://doi.org/10.1016/j.jcat.2020.09.029

270. Wang, L.; Wang, R.-l.; Zhang, X.; Mu, J.-l.; zhou, Z.-Y.; Su, Z.-m., Tuning the VB of COF to improve the efficiency of photoreduction of CO2 with water. ChemSusChem 2020.

271. Zhong, H.; Hong, Z.; Yang, C.; Li, L.; Xu, Y.; Wang, X.; Wang, R., A Covalent Triazine-Based Framework Consisting of Donor-Acceptor Dyads for Visible-Light-Driven Photocatalytic CO2 Reduction. ChemSusChem 2019, 12 (19), 4493-4499. https://doi.org/10.1002/cssc.201901997

272. Hazra Chowdhury, I.; Hazra Chowdhury, A.; Das, A.; Khan, A.; Islam, S. M., A nanoporous covalent organic framework for the green-reduction of CO2under visible light in water. New Journal of Chemistry 2020, 44 (27),

11720-11726.
https://doi.org/10.1039/D0NJ01147A

273. Peng, L.; Chang, S.; Liu, Z.; Fu, Y.; Ma, R.; Lu, X.; Zhang, F.; Zhu, W.; Kong, L.; Fan, M., Visible-light-driven photocatalytic CO2reduction over ketoenamine-based covalent organic frameworks: role of the host functional groups. Catalysis Science and Technology 2021, 11 (5), 1717-1724. https://doi.org/10.1039/D0CY02061C

274. Liu, Z.; Huang, Y.; Chang, S.; Zhu, X.; Fu, Y.; Ma, R.; Lu, X.; Zhang, F.; Zhu, W.; Fan, M., Highly dispersed Ru nanoparticles on a bipyridine-linked covalent organic framework for efficient photocatalytic CO2reduction. Sustainable Energy and Fuels 2021, 5 (11), 2871-2876. https://doi.org/10.1039/D1SE00358E

275. Tang, J.; Su, C.; Shao, Z., Covalent Organic Framework (COF)-Based Hybrids for Electrocatalysis: Recent Advances and Perspectives. Small Methods 2021, 5 (12), 2100945-2100945. https://doi.org/10.1002/smtd.202100945

276. Gong, Y.-N.; Zhong, W.; Li, Y.; Qiu, Y.; Zheng, L.; Jiang, J.; Jiang, H.-L., Regulating photocatalysis by spin-state manipulation of cobalt in covalent organic frameworks. Journal of the American Chemical Society 2020, 142 (39), 16723-16731.
https://doi.org/10.1021/jacs.0c07206

277. Zhong, H.; Sa, R.; Lv, H.; Yang, S.; Yuan, D.; Wang, X.; Wang, R., Covalent Organic Framework Hosting Metalloporphyrin-Based Carbon Dots for Visible-Light-Driven Selective CO2 Reduction. Advanced Functional Materials 2020, 30 (35). https://doi.org/10.1002/adfm.202002654

278. Lv, H.; Sa, R.; Li, P.; Yuan, D.; Wang, X.; Wang, R., Metalloporphyrin-based covalent organic frameworks composed of the electron donor-acceptor dyads for visible-light-driven selective CO2 reduction. Science China Chemistry 2020, 63 (9), 1289-1294. https://doi.org/10.1007/s11426-020-9801-3

279. Lu, M.; Li, Q.; Liu, J.; Zhang, F. M.; Zhang, L.; Wang, J. L.; Kang, Z. H.; Lan, Y. Q., Installing earth-abundant metal active centers to covalent organic frameworks for efficient heterogeneous photocatalytic CO2 reduction. Applied Catalysis B: Environmental 2019, 254 (May), 624-633. https://doi.org/10.1016/j.apcatb.2019.05.033

280. Li, S. Y.; Meng, S.; Zou, X.; El-Roz, M.; Telegeev, I.; Thili, O.; Liu, T. X.; Zhu, G., Rhenium-functionalized covalent organic framework photocatalyst for efficient CO2 reduction under visible light. Microporous and Mesoporous

Materials 2019, 285 (February), 195-201. https://doi.org/10.1016/j.micromeso.2019.05.026

281. Johnson, E. M.; Haiges, R.; Marinescu, S. C., Covalent-Organic Frameworks Composed of Rhenium Bipyridine and Metal Porphyrins: Designing Heterobimetallic Frameworks with Two Distinct Metal Sites. ACS Applied Materials & Interfaces 2018, 10 (44), 37919-37927. https://doi.org/10.1021/acsami.8b07795

282. Hawecker, J.; Lehn, J.-M.; Ziessel, R., Efficient photochemical reduction of CO2 to CO by visible light irradiation of systems containing Re(bipy)(CO)3X or Ru(bipy)32+-Co2+ combinations as homogeneous catalysts. Journal of the Chemical Society, Chemical Communications 1983, (9), 536-538.
https://doi.org/10.1039/C39830000536

283. Bourrez, M.; Molton, F.; Chardon-Noblat, S.; Deronzier, A., [Mn (bipyridyl)(CO) 3Br]: an abundant metal carbonyl complex as efficient electrocatalyst for CO2 reduction. Angewandte Chemie International Edition 2011, 50 (42), 9903-9906. https://doi.org/10.1002/anie.201103616

284. Kou, M.; Liu, W.; Wang, Y.; Huang, J.; Chen, Y.; Zhou, Y.; Chen, Y.; Ma, M.; Lei, K.; Xie, H.; Wong, P. K.; Ye, L., Photocatalytic CO2 conversion over single-atom MoN2 sites of covalent organic framework. Applied Catalysis B: Environmental 2021, 291, 120146-120146. https://doi.org/10.1016/j.apcatb.2021.120146

285. Yang, Y.; Lu, Y.; Zhang, H. Y.; Wang, Y.; Tang, H. L.; Sun, X. J.; Zhang, G.; Zhang, F. M., Decoration of Active Sites in Covalent-Organic Framework: An Effective Strategy of Building Efficient Photocatalysis for CO2Reduction. ACS Sustainable Chemistry and Engineering 2021, 9 (39), 13376-13384.
https://doi.org/10.1021/acssuschemeng.1c04994

286. Xu, D.; Lv, H.; Liu, B., Encapsulation of Metal Nanoparticle Catalysts Within Mesoporous Zeolites and Their Enhanced Catalytic Performances: A Review. Frontiers in Chemistry 2018, 6. https://doi.org/10.3389/fchem.2018.00550

287. Schauermann, S.; Nilius, N.; Shaikhutdinov, S.; Freund, H.-J., Nanoparticles for Heterogeneous Catalysis: New Mechanistic Insights. Accounts of Chemical Research 2013, 46 (8), 1673-1681. https://doi.org/10.1021/ar300225s

288. Schmid, G.; Maihack, V.; Lantermann, F.; Peschel, S., Ligand-stabilized metal clusters and colloids: properties and applications. Journal of the

Chemical Society, Dalton Transactions 1996, (5), 589-595. https://doi.org/10.1039/dt9960000589

289. Guo, K.; Zhu, X.; Peng, L.; Fu, Y.; Ma, R.; Lu, X.; Zhang, F.; Zhu, W.; Fan, M., Boosting photocatalytic CO2 reduction over a covalent organic framework decorated with ruthenium nanoparticles. Chemical Engineering Journal 2021, 405, 127011-127011. https://doi.org/10.1016/j.cej.2020.127011

290. Zhao, T.; Niu, Q.; Huang, G.; Chen, Q.; Gao, Y.; Bi, J.; Wu, L., Rational construction of Ni (OH) 2 nanoparticles on covalent triazine-based framework for artificial CO2 reduction. Journal of Colloid and Interface Science 2021, 602, 23-31. https://doi.org/10.1016/j.jcis.2021.05.131

291. Huang, Y.; Du, P.; Shi, W.; Wang, Y.; Yao, S.; Zhang, Z. M.; Lu, T.; Lu, X., Filling COFs with bimetallic nanoclusters for CO2-to-alcohols conversion with H2O oxidation. Applied Catalysis B: Environmental 2021. https://doi.org/10.1016/j.apcatb.2021.120001

292. Li, J.; Liu, P.; Huang, H.; Li, Y.; Tang, Y.; Mei, D.; Zhong, C., Metal-free 2D/2D black phosphorus and covalent triazine framework heterostructure for CO2 photoreduction. ACS Sustainable Chemistry & Engineering 2020, 8 (13), 5175-5183. https://doi.org/10.1021/acssuschemeng.9b07591

293. Gopalakrishnan, V. N.; Nguyen, D.-T.; Becerra, J.; Sakar, M.; Ahad, J. M. E.; Jautzy, J. J.; Mindorff, L. M.; Béland, F.; Do, T.-O., Manifestation of an Enhanced Photoreduction of CO2 to CO over the In Situ Synthesized rGO-Covalent Organic Framework under Visible Light Irradiation. ACS Applied Energy Materials 2021, 4 (6), 6005-6014. https://doi.org/10.1021/acsaem.1c00862

294. Xu, Z.; Cui, Y.; Young, D. J.; Wang, J.; Li, H. Y.; Bian, G. Q.; Li, H. X., Combination of Co2+-immobilized covalent triazine framework and TiO2 by covalent bonds to enhance photoreduction of CO2to CO with H2O. Journal of CO2 Utilization 2021, 49 (101561), 1-9. https://doi.org/10.1016/j.jcou.2021.101561

295. Han, B.; Ou, X.; Zhong, Z.; Liang, S.; Deng, H.; Lin, Z., Rational design of FeNi bimetal modified covalent organic frameworks for photoconversion of anthropogenic CO2 into widely tunable syngas. Small 2020, 16 (38), 2002985-2002985. https://doi.org/10.1002/smll.202002985

296. Pellegrin, Y.; Odobel, F., Sacrificial electron donor reagents for solar fuel production. Comptes Rendus Chimie 2017, 20 (3), 283-295. https://doi.org/10.1016/j.crci.2015.11.026

297. Banerjee, T.; Haase, F.; Savasci, G.; Gottschling, K.; Ochsenfeld, C.; Lotsch, B. V., Single-Site Photocatalytic H2 Evolution from Covalent Organic Frameworks with Molecular Cobaloxime Co-Catalysts. Journal of the American Chemical Society 2017, 139 (45), 16228-16234. https://doi.org/10.1021/jacs.7b07489

298. Global Monitoring Laboratory. https://gml.noaa.gov/ccgg/trends/gl_trend.html.

299. Muratori, M.; Kheshgi, H.; Mignone, B.; Clarke, L.; McJeon, H.; Edmonds, J., Carbon capture and storage across fuels and sectors in energy system transformation pathways. International Journal of Greenhouse Gas Control 2017, 57, 34-41. https://doi.org/10.1016/j.ijggc.2016.11.026

300. Edenhofer, O.; Pichs-Madruga, R.; Sokona, Y.; Kadner, S.; Minx, J. C.; Brunner, S.; Agrawala, S.; Baiocchi, G.; Bashmakov, I. A.; Blanco, G., Technical summary. Climate Change 2014 : Mitigation of Climate Change. IPCC Working Group III Contribution to AR5 2014.

301. Steynberg, A., Introduction to fischer-tropsch technology. In Studies in surface science and catalysis, Elsevier: 2004; Vol. 152, pp 1-63. https://doi.org/10.1016/S0167-2991(04)80458-0

302. Riplinger, C.; Carter, E. A., Influence of Weak Brønsted Acids on Electrocatalytic CO2 Reduction by Manganese and Rhenium Bipyridine Catalysts. ACS Catalysis 2015, 5 (2), 900-908. https://doi.org/10.1021/cs501687n

303. Benson, E. E.; Sampson, M. D.; Grice, K. A.; Smieja, J. M.; Froehlich, J. D.; Friebel, D.; Keith, J. A.; Carter, E. A.; Nilsson, A.; Kubiak, C. P., The electronic states of rhenium bipyridyl electrocatalysts for CO2 reduction as revealed by X-ray absorption spectroscopy and computational quantum chemistry. Angewandte Chemie International Edition 2013, 52 (18), 4841-4. https://doi.org/10.1002/anie.201209911

304. Manbeck, G. F.; Muckerman, J. T.; Szalda, D. J.; Himeda, Y.; Fujita, E., Push or pull? Proton responsive ligand effects in rhenium tricarbonyl CO2 reduction catalysts. The Journal of Physical Chemistry B 2015, 119 (24), 7457-7466.
https://doi.org/10.1021/jp511131x

305. Scheiring, T.; Klein, A.; Kaim, W. J. J. o. t. C. S., Perkin Transactions 2, EPR study of paramagnetic rhenium (I) complexes (bpy>>·>>->>) Re (CO)3X relevant to the mechanism of electrocatalytic CO 2 reduction. Journal of the Chemical Society, Perkin Transactions 1 1997, 12 (12), 2569-2572. https://doi.org/10.1039/a702467c

306. Sampson, M. D.; Nguyen, A. D.; Grice, K. A.; Moore, C. E.; Rheingold, A. L.; Kubiak, C. P., Manganese catalysts with bulky bipyridine ligands for the electrocatalytic reduction of carbon dioxide: Eliminating dimerization and altering catalysis. journal of the American Chemical Society 2014, 136, 5460-5471. https://doi.org/10.1021/ja501252f

307. Qiao, X., Li, Q., Schaugaard, R. N., Noffke, B. W., Liu, Y., Li, D., Li, L. S., Graphite-Conjugated Rhenium Catalysts for Carbon Dioxide Reduction. Journal of the American Chemical Society 2016, 138, 1820-1823. https://doi.org/10.1021/jacs.5b13080

308. Qiao, X., Li, Q., Schaugaard, R. N., Noffke, B. W., Liu, Y., Li, D., ... & Li, L. S., Well-Defined Nanographene-Rhenium Complex as an Efficient Electrocatalyst and Photocatalyst for Selective CO2 Reduction. Journal of the American Chemical Society 2017, 139, 3934-3937. https://doi.org/10.1021/jacs.6b12530

309. Sinha, S.; Sonea, A.; Shen, W.; Hanson, S. S.; Warren, J. J., Heterogeneous Aqueous CO(2) Reduction Using a Pyrene-Modified Rhenium(I) Diimine Complex. Inorganic Chemisty 2019, 58 (16), 10454-10461. https://doi.org/10.1021/acs.inorgchem.9b01060

310. Blakemore, J. D.; Gupta, A.; Warren, J. J.; Brunschwig, B. S.; Gray, H. B., Noncovalent immobilization of electrocatalysts on carbon electrodes for fuel production. Journal of the American Chemical Society 2013, 135 (49), 18288-91.
https://doi.org/10.1021/ja4099609

311. Orchanian, N. M.; Hong, L. E.; Skrainka, J. A.; Esterhuizen, J. A.; Popov, D. A.; Marinescu, S. C. J. A. A. E. M., Surface-immobilized conjugated polymers incorporating rhenium bipyridine motifs for electrocatalytic and photocatalytic CO2 reduction. ACS Applied Energy Materials 2018, 2 (1), 110-123.
https://doi.org/10.1021/acsaem.8b01745

312. Abdellah, M.; El-Zohry, A. M.; Antila, L. J.; Windle, C. D.; Reisner, E.; Hammarström, L., Time-Resolved IR Spectroscopy Reveals a Mechanism with TiO 2 as a Reversible Electron Acceptor in a TiO 2 -Re Catalyst System for CO 2 Photoreduction. Journal of the American Chemical Society 2017, 139 (3),

1226-1232.
https://doi.org/10.1021/jacs.6b11308

313. You, J.; Zhao, Y.; Wang, L.; Bao, W., Recent developments in the photocatalytic applications of covalent organic frameworks: A review. Journal of Cleaner Production 2021, 291, 125822. https://doi.org/10.1016/j.jclepro.2021.125822

314. Pan, Q.; Abdellah, M.; Cao, Y.; Lin, W.; Liu, Y.; Meng, J.; Zhou, Q.; Zhao, Q.; Yan, X.; Li, Z.; Cui, H.; Cao, H.; Fang, W.; Tanner, D. A.; Abdel-Hafiez, M.; Zhou, Y.; Pullerits, T.; Canton, S. E.; Xu, H.; Zheng, K., Ultrafast charge transfer dynamics in 2D covalent organic frameworks/Re-complex hybrid photocatalyst. Nature Communications 2022, 13 (1), 845. https://doi.org/10.1038/s41467-022-28409-2

315. Spies, L.; Carmo, M. E. G.; Doblinger, M.; Xu, Z.; Xue, T.; Hartschuh, A.; Bein, T.; Schneider, J.; Patrocinio, A. O. T., Designing Atomically Precise and Robust COF Hybrids for Efficient Photocatalytic CO(2) Reduction. Small 2025, 21, 2500550. https://doi.org/10.1002/smll.202500550

316. Chen, X.; Huang, N.; Gao, J.; Xu, H.; Xu, F.; Jiang, D., Towards covalent organic frameworks with predesignable and aligned open docking sites. Chemical Communications 2014, 50 (46), 6161-3. https://doi.org/10.1039/C4CC01825G

317. Wu, S.; Li, M.; Phan, H.; Wang, D.; Herng, T. S.; Ding, J.; Lu, Z.; Wu, J., Toward two-dimensional π-conjugated covalent organic radical frameworks. Angewandte Chemie International Edition 2018, 57 (27), 8007-8011. https://doi.org/10.1002/anie.201801998

318. Jin, E.; Geng, K.; Fu, S.; Addicoat, M. A.; Zheng, W.; Xie, S.; Hu, J. S.; Hou, X.; Wu, X.; Jiang, Q., Module-Patterned Polymerization towards Crystalline 2D sp2-Carbon Covalent Organic Framework Semiconductors. Angewandte Chemie International Edition 2022, 61 (9), e202115020. https://doi.org/10.1002/anie.202115020

319. Sharma, S.; Kumar, P.; Chandra, R., Applications of BIOVIA materials studio, LAMMPS, and GROMACS in various fields of science and engineering. In Molecular dynamics simulation of nanocomposites using BIOVIA materials studio, Lammps and Gromacs, 2019; pp 329-341. https://doi.org/10.1016/B978-0-12-816954-4.00007-3

320. Dubed Bandomo, G. C.; Mondal, S. S.; Franco, F.; Bucci, A.; Martin-Diaconescu, V.; Ortuño, M. A.; van Langevelde, P. H.; Shafir, A.; López, N.; Lloret-Fillol, J., Mechanically Constrained Catalytic Mn(CO)3Br Single Sites in a Two-Dimensional Covalent Organic Framework for CO2Electroreduction in

H2O. ACS Catalysis 2021, 11, 7210-7222. https://doi.org/10.1021/acscatal.1c00314

321. Sajid, H., Effect of interlayer slipping on the geometric, thermal and adsorption properties of 2D covalent organic frameworks: a comprehensive review based on computational modelling studies. Physical Chemistry Chemical Physics 2024, 26 (11), 8577-8603. https://doi.org/10.1039/D4CP00094C

322. Spitler, E. L.; Koo, B. T.; Novotney, J. L.; Colson, J. W.; Uribe-Romo, F. J.; Gutierrez, G. D.; Clancy, P.; Dichtel, W. R., A 2D covalent organic framework with 4.7-nm pores and insight into its interlayer stacking. Journal of the American Chemical Society 2011, 133 (48), 19416-21. https://doi.org/10.1021/ja206242v

323. Lukose, B.; Kuc, A.; Heine, T., The structure of layered covalent-organic frameworks. Chemistry - A European Journal 2011, 17 (8), 2388-92. https://doi.org/10.1002/chem.201001290

324. Ying, Y.; Tong, M.; Ning, S.; Ravi, S. K.; Peh, S. B.; Tan, S. C.; Pennycook, S. J.; Zhao, D., Ultrathin Two-Dimensional Membranes Assembled by Ionic Covalent Organic Nanosheets with Reduced Apertures for Gas Separation. Journal of the American Chemical Society 2020, 142 (9), 4472-4480.
https://doi.org/10.1021/jacs.9b13825

325. Zhou, W.; Wu, H.; Yildirim, T., Structural stability and elastic properties of prototypical covalent organic frameworks. Chemical Physics Letters 2010, 499 (1-3), 103-107. https://doi.org/10.1016/j.cplett.2010.09.032

326. Zhan, Z.; Liu, Y.; Wang, W.; Du, G.; Cai, S.; Wang, P., Atomic-level imaging of beam-sensitive COFs and MOFs by low-dose electron microscopy. Nanoscale Horiz 2024, 9 (6), 900-933. https://doi.org/10.1039/D3NH00494E

327. Spies, L.; Carmo, M. E. G.; Marrenjo, G. J.; Reuther, S.; Ganswindt, P.; Patrocinio, A. O. T.; Bein, T.; Lopes, O. F.; Schneider, J., MnI-Functionalized Covalent Organic Framework as Efficient Electrocatalyst for CO2 Reduction in a Catholyte-Free Zero-Gap Electrolyzer. Advanced Functional Materials 2025, 2502953.

328. Tolosana-Moranchel, A.; Pecharromán, C.; Faraldos, M.; Bahamonde, A., Strong effect of light scattering by distribution of TiO2 particle aggregates on photocatalytic efficiency in aqueous suspensions. Chemical Engineering Journal 2021, 403, 126186. https://doi.org/10.1016/j.cej.2020.126186

329. Lin, W.-C.; Jayakumar, J.; Chang, C.-L.; Ting, L.-Y.; Elsayed, M. H.; Abdellah, M.; Zheng, K.; Elewa, A. M.; Lin, Y.-T.; Liu, J.-J.; Wang, W.-S.; Lu, C.-Y.; Chou, H.-H., Effect of energy bandgap and sacrificial agents of cyclopentadithiophene-based polymers for enhanced photocatalytic hydrogen evolution. Applied Catalysis B: Environment and Energy 2021, 298, 120577. https://doi.org/10.1016/j.apcatb.2021.120577

330. Vallejo-Rendón, D.; Ramos-Domínguez, N.; Nava-Diguero, P.; Espinosa-Faller, F.; Caballero-Briones, F., Factors affecting photocatalytic activity. In Graphene-Based Photocatalysts for Hydrogen Production and Environmental Remediation, Springer: 2024; pp 161-180. https://doi.org/10.1007/978-3-031-68464-7_7

331. Choate, J. C.; Silva, I., Jr.; Hsu, P. C.; Tran, K.; Marinescu, S. C., The Positional Effect of an Immobilized Re Tricarbonyl Catalyst for CO(2) Reduction. ACS Applied Materials & Interfaces 2024, 16 (38), 50534-50549. https://doi.org/10.1021/acsami.4c05536

332. Nichols, A. W.; Machan, C. W., Secondary-Sphere Effects in Molecular Electrocatalytic CO(2) Reduction. Frontiers in Chemistry 2019, 7, 397. https://doi.org/10.3389/fchem.2019.00397

333. Nandy, S.; Savant, S. A.; Haussener, S., Prospects and challenges in designing photocatalytic particle suspension reactors for solar fuel processing. Chemical Science 2021, 12 (29), 9866-9884. https://doi.org/10.1039/D1SC01504D

334. Pellegrino, F.; Pellutiè, L.; Sordello, F.; Minero, C.; Ortel, E.; Hodoroaba, V.-D.; Maurino, V., Influence of agglomeration and aggregation on the photocatalytic activity of TiO2 nanoparticles. App. Catal. B, Envirom. 2017, 216, 80-87. https://doi.org/10.1016/j.apcatb.2017.05.046

335. Machan, C. W.; Sampson, M. D.; Chabolla, S. A.; Dang, T.; Kubiak, C. P., Developing a Mechanistic Understanding of Molecular Electrocatalysts for CO2 Reduction using Infrared Spectroelectrochemistry. Organometallics 2014, 33 (18), 4550-4559. https://doi.org/10.1021/om500044a

336. Bard, A. J.; Faulkner, L. R.; White, H. S., Electrochemical methods: fundamentals and applications. John Wiley & Sons: 2022.

337. Santos, E.; Schmickler, W., On the timescale of electrochemical processes. Electrochimica Acta 2024, 498. https://doi.org/10.1016/j.electacta.2024.144659

338. Zheng, W., Seeing Is Not Always Believing: Experimental and Interpretive Traps of In Situ/Operando Electrocatalysis. ACS Electrochemistry 2026, XXX, XXX−XXX. https://doi.org/10.1021/acselectrochem.6c00058

339. Albero, J.; Peng, Y.; García, H., Photocatalytic CO 2 Reduction to C2+ Products. ACS Catalysis 2020, 10 (10), 5734-5749. https://doi.org/10.1021/acscatal.0c00478

340. Karamian, E.; Sharifnia, S., On the general mechanism of photocatalytic reduction of CO2. Journal of CO2 Utilization 2016, 16, 194-203. https://doi.org/10.1016/j.jcou.2016.07.004

341. Qiao, X.; Li, Q.; Schaugaard, R. N.; Noffke, B. W.; Liu, Y.; Li, D.; Liu, L.; Raghavachari, K.; Li, L.-S., Well-Defined Nanographene-Rhenium Complex as an Efficient Electrocatalyst and Photocatalyst for Selective CO2 Reduction. Journal of the American Chemical Society 2017, 139 (11), 3934-3937. https://doi.org/10.1021/jacs.6b12530

342. Kuriki, R.; Sekizawa, K.; Ishitani, O.; Maeda, K., Visible-light-driven CO2 reduction with carbon nitride: enhancing the activity of ruthenium catalysts. Angewandte Chemie International Edition 2015, 54 (8), 2406-2409. https://doi.org/10.1002/anie.201411170

343. Muresan, N. M.; Willkomm, J.; Mersch, D.; Vaynzof, Y.; Reisner, E., Immobilization of a Molecular Cobaloxime Catalyst for Hydrogen Evolution on a Mesoporous Metal Oxide Electrode. Angewandte Chemie International Edition 2012, 124 (51), 12921-12925. https://doi.org/10.1002/ange.201207448

344. Maier, S. E.; Nagel, T.; Turan, M.; Kaya, E.; Frey, W.; Dyballa, M.; Estes, D. P., Comparison of the Catalytic Activity of Surface-Immobilized Copper Complexes with Phosphonate Anchoring Groups for Atom Transfer Radical Cyclizations and Additions. Organometallics 2024, 43 (3), 233-241. https://doi.org/10.1021/acs.organomet.3c00377

345. Lohse, M. S.; Bein, T., Covalent Organic Frameworks: Structures, Synthesis, and Applications. Advanced Functional Materials 2018, 28 (33). https://doi.org/10.1002/adfm.201705553

346. Suleman, S.; Sun, K.; Zhao, Y.; Guan, X.; Lin, Z.; Meng, Z.; Jiang, H.-L., Enhanced Photocatalytic CO 2 Reduction via Linkage Substitution in Porphyrinic Covalent Organic Frameworks. Chinese Chemical Society 2024, 6 (7), 1689-1697. https://doi.org/10.31635/ccschem.023.202303319

347. Haase, F.; Lotsch, B. V., Solving the COF trilemma: towards crystalline, stable and functional covalent organic frameworks. Chem Soc Rev 2020, 49 (23), 8469-8500. https://doi.org/10.1039/D0CS01027H

348. Zhu, X.-Q.; Zhang, M.-T.; Yu, A.; Wang, C.-H.; Cheng, J.-P., Hydride, hydrogen atom, proton, and electron transfer driving forces of various five-membered heterocyclic organic hydrides and their reaction intermediates in acetonitrile. Journal of the American Chemical Society 2008, 130 (8), 2501-2516.
https://doi.org/10.1021/ja075523m

349. Roberge, P. R., Handbook of corrosion engineering. 2013. https://doi.org/10.1002/9781118436707.hmse033

350. Toby, B. H.; Dreele, R. B. v., GSAS-II : the genesis of a modern open-source all purpose crystallography software package. 2013, 46 (2), 544-549.
https://doi.org/10.1107/S0021889813003531

351. Chen, J.; Tao, X.; Tao, L.; Li, H.; Li, C.; Wang, X.; Li, C.; Li, R.; Yang, Q., Novel conjugated organic polymers as candidates for visible-light-driven photocatalytic hydrogen production. Applied Catalysis B: Environmental 2019, 241, 461-470. https://doi.org/10.1016/j.apcatb.2018.09.011

352. Tamaki, Y.; Morimoto, T.; Koike, K.; Ishitani, O., Photocatalytic CO2 reduction with high turnover frequency and selectivity of formic acid formation using Ru(II) multinuclear complexes. Proceedings National Academy of Sciences of USA 2012, 109 (39), 15673-15678. https://doi.org/10.1073/pnas.1118336109

353. Fukuzumi, S.; Koumitsu, S.; Hironaka, K.; Tanaka, T., Energetic comparison between photoinduced electron-transfer reactions from NADH model compounds to organic and inorganic oxidants and hydride-transfer reactions from NADH model compounds to p-benzoquinone derivatives. Journal of the American Chemical Society 1987, 109 (2), 305-316. https://doi.org/10.1021/ja00236a003

354. Schwarze, M.; Stellmach, D.; Schröder, M.; Kailasam, K.; Reske, R.; Thomas, A.; Schomäcker, R., Quantification of photocatalytic hydrogen evolution. Physical Chemistry Chemical Physics 2013, 15 (10), 3466-3472. https://doi.org/10.1039/c3cp50168j

355. Variar, A. G.; Ramyashree, M. S.; Ail, V. U.; Priya, S. S.; Sudhakar, K.; Tahir, M., Influence of various operational parameters in enhancing photocatalytic reduction efficiency of carbon dioxide in a photoreactor: A review.

Journal of Industrial and Engineering Chemistry 2021. https://doi.org/10.1016/j.jiec.2021.04.017

356. Chung, H. Y.; Wong, R. J.; Wu, H.; Gunawan, D.; Amal, R.; Ng, Y. H., Scalable and Integrated Photocatalytic Reactor Systems for Solar-to-Fuel Production: Photoredox and Photoreforming Processes. Advanced Energy Materials 2025, 15 (28). https://doi.org/10.1002/aenm.202404956

357. Sathre, R.; Scown, C. D.; Morrow III, W. R.; Stevens, J. C.; Sharp, I. D.; Ager III, J. W.; Walczak, K.; Houle, F. A.; Greenblatt, J. B., Life-cycle net energy assessment of large-scale hydrogen production via photoelectrochemical water splitting. Energy Environmental Science 2014, 7 (10), 3264-3278. https://doi.org/10.1039/C4EE01019A

358. Weekes, D. M.; Salvatore, D. A.; Reyes, A.; Huang, A.; Berlinguette, C. P., Electrolytic CO(2) Reduction in a Flow Cell. Accounts of Chemical Research 2018, 51 (4), 910-918. https://doi.org/10.1021/acs.accounts.8b00010

359. MASEL, R.; LIU, Z.; ZHAO, D.; CHEN, Q.; LUTZ, D.; NERENG, L., Commercializing Biobased Products: Opportunities, Challenges, Benefits, Risks In CO2 Conversion to Chemicals with Emphasis on using Chemicals Renewable Energy/Resources to Drive the Conversion, 2015; Vol. 43, p 215. https://doi.org/10.1039/9781782622444-00215

360. The Global CO2 Initiative. Global Roadmap for Implementing CO2 Utilization. (accessed 07/13).

361. Zhang, G.; Li, S.; Du, X.; Zhang, Y.; Wang, T.; Zhang, P.; Gong, J., From Molecules to Modules: Pathways toward Scalable Electrochemical CO(2) Reduction. Accounts of Chemical Research 2025, 58 (21), 3223-3234. https://doi.org/10.1021/acs.accounts.5c00416

362. Liang, S.; Altaf, N.; Huang, L.; Gao, Y.; Wang, Q., Electrolytic cell design for electrochemical CO2 reduction. Journal of CO2 Utilization 2020, 35, 90-105. https://doi.org/10.1016/j.jcou.2019.09.007

363. Elgrishi, N.; Rountree, K. J.; McCarthy, B. D.; Rountree, E. S.; Eisenhart, T. T.; Dempsey, J. L., A Practical Beginner's Guide to Cyclic Voltammetry. Journal of Chemical Education 2017, 95 (2), 197-206. https://doi.org/10.1021/acs.jchemed.7b00361

364. Kaim, W.; Fiedler, J., Spectroelectrochemistry: the best of two worlds. Chem Soc Rev 2009, 38 (12), 3373-82. https://doi.org/10.1039/b504286k

365. Fang, W.; Wang, M.; Cai, L.; Xia, B. Y., Fundamental Insights for Practical Electrocatalytic CO2 Reduction. Accounts of Chemical Research 2025, 58 (15), 2365-2378. https://doi.org/10.1021/acs.accounts.5c00154

366. Diamond, L. W.; Akinfiev, N. N., Solubility of CO2 in water from− 1.5 to 100 C and from 0.1 to 100 MPa: evaluation of literature data and thermodynamic modelling. Fluid phase equilibria 2003, 208 (1-2), 265-290. https://doi.org/10.1016/S0378-3812(03)00041-4

367. Ma, D.; Jin, T.; Xie, K.; Huang, H., An overview of flow cell architecture design and optimization for electrochemical CO2reduction. Journal of Materials Chemistry A 2021, 9, 20897-20918. https://doi.org/10.1039/D1TA06101A

368. Overa, S.; Ko, B. H.; Zhao, Y.; Jiao, F., Electrochemical approaches for CO2 conversion to chemicals: a journey toward practical applications. Accounts of chemical research 2022, 55 (5), 638-648. https://doi.org/10.1021/acs.accounts.1c00674

369. Inglis, J. L.; MacLean, B. J.; Pryce, M. T.; Vos, J. G., Electrocatalytic pathways towards sustainable fuel production from water and CO2. Coordination Chemistry Reviews 2012, 256 (21), 2571-2600. https://doi.org/10.1016/j.ccr.2012.05.002

370. Liu, C.; Cundari, T. R.; Wilson, A. K., CO2 Reduction on Transition Metal (Fe, Co, Ni, and Cu) Surfaces: In Comparison with Homogeneous Catalysis. The Journal of Physical Chemistry C 2012, 116 (9), 5681-5688. https://doi.org/10.1021/jp210480c

371. Smieja, J. M.; Sampson, M. D.; Grice, K. A.; Benson, E. E.; Froehlich, J. D.; Kubiak, C. P., Manganese as a substitute for rhenium in CO2 reduction catalysts: The importance of acids. Inorganic Chemistry 2013, 52, 2484-2491.
https://doi.org/10.1021/ic302391u

372. Bourrez, M.; Orio, M.; Molton, F.; Vezin, H.; Duboc, C.; Deronzier, A.; Chardon-Noblat, S., Pulsed-EPR Evidence of a Manganese (II) Hydroxycarbonyl Intermediate in the Electrocatalytic Reduction of Carbon Dioxide by a Manganese Bipyridyl Derivative. Angewandte Chemie International Edition 2014, 53 (1), 240-243. https://doi.org/10.1002/anie.201306750

373. Grills, D. C.; Ertem, M. Z.; McKinnon, M.; Ngo, K. T.; Rochford, J., Mechanistic aspects of CO2 reduction catalysis with manganese-based molecular catalysts. Coordination Chemistry Reviews 2018, 374, 173-217. https://doi.org/10.1016/j.ccr.2018.05.022

374. Rosser, T. E.; Windle, C. D.; Reisner, E., Electrocatalytic and Solar-Driven CO2 Reduction to CO with a Molecular Manganese Catalyst Immobilized on Mesoporous TiO2. Angewandte Chemie International Edition 2016, 55 (26), 7388-7392.
https://doi.org/10.1002/anie.201601038

375. Wang, X.; Thiel, I.; Fedorov, A.; Copéret, C.; Mougel, V.; Fontecave, M., Site-isolated manganese carbonyl on bipyridine-functionalities of periodic mesoporous organosilicas: efficient CO2 photoreduction and detection of key reaction intermediates. Chemical science 2017, 8 (12), 8204-8213. https://doi.org/10.1039/C7SC03512H

376. Rønne, M. H.; Madsen, M. R.; Skrydstrup, T.; Pedersen, S. U.; Daasbjerg, K., Mechanistic Elucidation of Dimer Formation and Strategies for Its Suppression in Electrochemical Reduction of Fac-Mn(bpy)(CO)3Br. ChemElectroChem 2021, 8 (11), 2108-2114. https://doi.org/10.1002/celc.202100279

377. Reuillard, B.; Ly, K. H.; Rosser, T. E.; Kuehnel, M. F.; Zebger, I.; Reisner, E., Tuning Product Selectivity for Aqueous CO(2) Reduction with a Mn(bipyridine)-pyrene Catalyst Immobilized on a Carbon Nanotube Electrode. Journal of the American Chemical Society 2017, 139 (41), 14425-14435. https://doi.org/10.1021/jacs.7b06269

378. Walsh, J. J.; Smith, C. L.; Neri, G.; Whitehead, G. F. S.; Robertson, C. M.; Cowan, A. J., Improving the efficiency of electrochemical CO2 reduction using immobilized manganese complexes. Faraday Discussions 2015, 183, 147-160.
https://doi.org/10.1039/C5FD00071H

379. Sun, Z.; Ma, T.; Tao, H.; Fan, Q.; Han, B., Fundamentals and challenges of electrochemical CO2 reduction using two-dimensional materials. Chem 2017, 3 (4), 560-587. https://doi.org/10.1016/j.chempr.2017.09.009

380. Johnson, D.; Qiao, Z.; Djire, A., Progress and Challenges of Carbon Dioxide Reduction Reaction on Transition Metal Based Electrocatalysts. ACS Applied Energy Materials 2021, 4 (9), 8661-8684. https://doi.org/10.1021/acsaem.1c01624

381. Yu, F.; Deng, K.; Du, M.; Wang, W.; Liu, F.; Liang, D., Electrochemical CO2 reduction: From catalysts to reactive thermodynamics and

kinetics. Carbon Capture Science & Technology 2023, 6, 100081. https://doi.org/10.1016/j.ccst.2022.100081

382. Singh, H. D.; G, M.; Misra, R.; Sarkar, S.; Chakraborty, D.; Nandi, S., Selective electroreduction of CO2 to value-added C1 and C2 products using MOF and COF-based catalysts. Advanced Composites and Hybrid Materials 2024, 7 (6), 209. https://doi.org/10.1007/s42114-024-01016-z

383. López-Magano, A.; Ortín-Rubio, B.; Imaz, I.; Maspoch, D.; Alemán, J.; Mas-Ballesté, R., Photoredox Heterobimetallic Dual Catalysis Using Engineered Covalent Organic Frameworks. ACS catalysis 2021, 11 (19), 12344-12354. https://doi.org/10.1021/acscatal.1c03634

384. López-Magano, A.; Mas-Ballesté, R.; Alemán, J., Predesigned Covalent Organic Frameworks as Effective Platforms for Pd(II) Coordination Enabling Cross-Coupling Reactions under Sustainable Conditions. Advanced Sustainable Systems 2022, 6 (3). https://doi.org/10.1002/adsu.202100409

385. Liu, Y.; Ma, Y.; Zhao, Y.; Sun, X.; Gándara, F.; Furukawa, H.; Liu, Z.; Zhu, H.; Zhu, C.; Suenaga, K.; Oleynikov, P.; Alshammari, A. S.; Zhang, X.; Terasaki, O.; Yaghi, O. M., Weaving of organic threads into a crystalline covalent organic framework. Science 2016, 351 (6271), 365-369. https://doi.org/10.1126/science.aad4011

386. Dubed Bandomo, G. C.; Franco, F.; Liu, C.; Mondal, S. S.; Gallo, A.; Nervi, C.; Lloret-Fillol, J., Toward the Understanding of the Structure-Activity Correlation in Single-Site Mn Covalent Organic Frameworks for Electrocatalytic CO2 Reduction. ACS Applied Energy Materials 2024, 7 (3), 1348-1357. https://doi.org/10.1021/acsaem.3c03117

387. Zou, L.; Chen, Z.-A.; Si, D.-H.; Yang, S.-L.; Gao, W.-Q.; Wang, K.; Huang, Y.-B.; Cao, R., Boosting CO2 Photoreduction via Regulating Charge Transfer Ability in a One-Dimensional Covalent Organic Framework. Angewandte Chemie International Edition 2023, 62 (46), e202309820. https://doi.org/10.1002/anie.202309820

388. Liu, N.; Bartling, S.; Springer, A.; Kubis, C.; Bokareva, O. S.; Salaya, E.; Sun, J.; Zhang, Z.; Wohlrab, S.; Abdel-Mageed, A. M.; Liang, H.-Q.; Francke, R., Heterogenized Molecular Electrocatalyst Based on a Hydroxo-Bridged Binuclear Copper(II) Phenanthroline Compound for Selective Reduction of CO2 to Ethylene. Advanced materials 2024, 36 (6), e2309526. https://doi.org/10.1002/adma.202309526

389. Neyhouse, B. J.; White, T. A., Modifying the steric and electronic character within Re(I)-phenanthroline complexes for electrocatalytic CO 2 reduction. Inorganica Chimica Acta 2018, 479, 49-57. https://doi.org/10.1016/j.ica.2018.04.008

390. Chen, Z.; Li, N.; Zhang, Q., Covalent Organic Frameworks as Promising Platforms for Efficient Electrochemical Reduction of Carbon Dioxide: A Review. Small Structures 2024, 5 (5), 2300495. https://doi.org/10.1002/sstr.202300495

391. Gala, E.; C. Dubed Bandomo, G.; Vettori, M.; Royuela, S.; Martínez-Fernández, M.; Martínez, J. I.; Salagre, E.; Michel, E. G.; Zamora, F.; Lloret-Fillol, J.; Segura, J. L., Post-synthetic modification of covalent organic frameworks with active manganese centers for electrocatalytic CO2 reduction in water. Journal of Materials Chemistry A 2025, 13 (2), 1142-1152. https://doi.org/10.1039/D4TA02807D

392. Haaring, R.; Kang, P. W.; Guo, Z.; Lee, J. W.; Lee, H., Developing Catalysts Integrated in Gas-Diffusion Electrodes for CO2 Electrolyzers. Accounts of Chemical Research 2023, 56 (19), 2595-2605. https://doi.org/10.1021/acs.accounts.3c00349

393. Burdyny, T.; Smith, W. A., CO2 reduction on gas-diffusion electrodes and why catalytic performance must be assessed at commercially-relevant conditions. Energy & Environmental Science 2019, 12 (5), 1442-1453. https://doi.org/10.1039/C8EE03134G

394. Zhang, Q.; Dong, S.; Shao, P.; Zhu, Y.; Mu, Z.; Sheng, D.; Zhang, T.; Jiang, X.; Shao, R.; Ren, Z.; Xie, J.; Feng, X.; Wang, B., Covalent organic framework-based porous ionomers for high-performance fuel cells. Science 2022, 378 (6616), 181-186. https://doi.org/10.1126/science.abm6304

395. Shahbaz, A.; Ahmad, K.; Qureshi, K.; Majeed, H.; Arshad, I.; Tabinda, T.; Iftikhar, T.; Khair, K.-u.; Ashfaq, M.; Shah, H. U. R.; Ahmad, M. Z.; Lee, S.-I., Porous materials: Covalent Organic Frameworks (COFs) as game-changers in practical applications, a review. Reviews in Inorganic Chemistry 2024, 44 (1), 117-133. https://doi.org/10.1515/revic-2023-0018

396. Trasatti, S., The absolute electrode potential: an explanatory note Pure

Applied Chemistry 1986, 58 (7), 955-966. https://doi.org/10.1351/pac198658070955

397. DeLuca, E. E.; Chan, T.; Taylor, J. M.; Lee, B.; Prabhakar, R. R.; Kubiak, C. P., Steric Effects on CO2 Reduction with Substituted Mn (Bpy)(CO) 3X-Type Catalysts on Multiwalled Carbon Nanotubes Reveal Critical Mechanistic Details. ACS Catalysis 2024, 14 (3), 2071-2083. https://doi.org/10.1021/acscatal.3c05771

398. Lee, A. J.; DeLuca, E. E.; Kelly, E. B.; Taylor, J. M.; Weddle, L. R.; Chen, H.; Park, C.; Loeb, C. K.; Chan, T.; Kubiak, C. P., Cambered Bipyridyl Ligand with Extended Aryl System Enables Electrochemical Reduction of Carbon Dioxide and Bicarbonate by Mn (bpy)(CO) 3Br-type Catalyst Immobilized on Carbon Nanotubes. Journal of the American Chemical Society 2025, 147 (9), 7411-7422. https://doi.org/10.1021/jacs.4c15547

399. Eagle, C.; Neri, G.; Piercy, V. L.; Younis, K.; Siritanaratkul, B.; Cowan, A. J., A manganese complex on a gas diffusion electrode for selective CO 2 to CO reduction. Sustainable Energy & Fuels 2023, 7 (9), 2301-2307. https://doi.org/10.1039/D3SE00236E

400. Hosokawa, T.; Tsuji, M.; Tsuchida, K.; Iwase, K.; Harada, T.; Nakanishi, S.; Kamiya, K., Metal-doped bipyridine linked covalent organic framework films as a platform for photoelectrocatalysts. Journal of Materials Chemistry A 2021, 9 (17), 11073-11080. https://doi.org/10.1039/D1TA00396H

401. Tauc, J., Optical properties and electronic structure of amorphous Ge and Si. Materials Research Bulletin 1968, 3 (1), 37-46. https://doi.org/10.1016/0025-5408(68)90023-8

402. Rotter, J. M.; Guntermann, R.; Auth, M.; Mähringer, A.; Sperlich, A.; Dyakonov, V.; Medina, D. D.; Bein, T., Highly conducting Wurster-type twisted covalent organic frameworks. Chemical Science 2020, 11 (47), 12843-12853. https://doi.org/10.1039/D0SC03909H

403. Guntermann, R.; Frey, L.; Biewald, A.; Hartschuh, A.; Clark, T.; Bein, T.; Medina, D. D., Regioisomerism in Thienothiophene-Based Covalent Organic Frameworks—A Tool for Band-Gap Engineering. Journal of the American Chemical Society 2024, 146 (23), 15869-15878. https://doi.org/10.1021/jacs.4c02365

404. Guntermann, R.; Helminger, D.; Frey, L.; Zehetmaier, P. M.; Wangnick, C.; Singh, A.; Xue, T.; Medina, D. D.; Bein, T., Tunable Isometric Donor-Acceptor Wurster-Type Covalent Organic Framework Photocathodes. Angewandte Chemie International Edition 2024, 63 (51), e202407166. https://doi.org/10.1002/anie.202407166

405. Heidary, N.; Morency, M.; Chartrand, D.; Ly, K. H.; Iftimie, R.; Kornienko, N., Electrochemically Triggered Dynamics within a Hybrid Metal-Organic Electrocatalyst. Journal of the American Chemical Society 2020, 142 (28), 12382-12393. https://doi.org/10.1021/jacs.0c04758

406. Sato, S.; Saita, K.; Sekizawa, K.; Maeda, S.; Morikawa, T., Low-Energy Electrocatalytic CO2 Reduction in Water over Mn-Complex Catalyst Electrode Aided by a Nanocarbon Support and K+ Cations. ACS Catalysis 2018, 8 (5), 4452-4458. https://doi.org/10.1021/acscatal.8b01068

407. Sun, C.; Rotundo, L.; Garino, C.; Nencini, L.; Yoon, S. S.; Gobetto, R.; Nervi, C., Electrochemical CO(2) Reduction at Glassy Carbon Electrodes Functionalized by Mn(I) and Re(I) Organometallic Complexes. Chemphyschem 2017, 18 (22), 3219-3229. https://doi.org/10.1002/cphc.201700739

408. Sikdar, N., Electrochemical CO(2) Reduction Reaction: Comprehensive Strategic Approaches to Catalyst Design for Selective Liquid Products Formation. Chemistry 2024, 30 (66), e202402477. https://doi.org/10.1002/chem.202402477

409. Shi, C.; Hansen, H. A.; Lausche, A. C.; Nørskov, J. K., Trends in electrochemical CO2 reduction activity for open and close-packed metal surfaces. Physical Chemistry Chemical Physics 2014, 16 (10), 4720-4727. https://doi.org/10.1039/c3cp54822h

410. Kuhl, K. P.; Hatsukade, T.; Cave, E. R.; Abram, D. N.; Kibsgaard, J.; Jaramillo, T. F., Electrocatalytic conversion of carbon dioxide to methane and methanol on transition metal surfaces. Journal of the American Chemical Society 2014, 136 (40), 14107-13. https://doi.org/10.1021/ja505791r

411. Pedersen, J. K.; Batchelor, T. A. A.; Bagger, A.; Rossmeisl, J., High-Entropy Alloys as Catalysts for the CO2 and CO Reduction Reactions. ACS Catalysis 2020, 10 (3), 2169-2176. https://doi.org/10.1021/acscatal.9b04343

412. Grim, R. G.; Badgett, A.; Braunecker, W. A.; Guarnieri, M. T.; Habas, S. E.; Hahn, C.; Neyerlin, K.; Prajapati, A.; Ruddy, D. A.; Walker, R. Z., The Chemistry of CO(2) Conversion: A Review. Chemical Reviews 2026, 126 (9), 5028-5082. https://doi.org/10.1021/acs.chemrev.5c00361

413. Raciti, D.; Cao, L.; Livi, K. J. T.; Rottmann, P. F.; Tang, X.; Li, C.; Hicks, Z.; Bowen, K. H.; Hemker, K. J.; Mueller, T.; Wang, C., Low-Overpotential

Electroreduction of Carbon Monoxide Using Copper Nanowires. ACS Catalysis 2017, 7 (7), 4467-4472. https://doi.org/10.1021/acscatal.7b01124

414. Ding, J.; Wei, Z.; Li, F.; Zhang, J.; Zhang, Q.; Zhou, J.; Wang, W.; Liu, Y.; Zhang, Z.; Su, X.; Yang, R.; Liu, W.; Su, C.; Yang, H. B.; Huang, Y.; Zhai, Y.; Liu, B., Atomic high-spin cobalt(II) center for highly selective electrochemical CO reduction to CH(3)OH. Nature Communications 2023, 14 (1), 6550. https://doi.org/10.1038/s41467-023-42307-1

415. Müller, A. V.; Ahmad, S.; Sirlin, J. T.; Ertem, M. Z.; Polyansky, D. E.; Grills, D. C.; Meyer, G. J.; Sampaio, R. N.; Concepcion, J. J., Reduction of CO to Methanol with Recyclable Organic Hydrides. Journal of the American Chemical Society 2024, 146 (15), 10524-10536. https://doi.org/10.1021/jacs.3c14605

416. Fogg, D. E.; dos Santos, E. N., Tandem catalysis: a taxonomy and illustrative review. Coordination Chemistry Reviews 2004, 248 (21-24), 2365-2379.
https://doi.org/10.1016/j.ccr.2004.05.012

417. Shi, Q.; Zhang, B.; Wu, Z.; Yang, D.; Wu, H.; Shi, J.; Jiang, Z., Cascade Catalytic Systems for Converting CO(2) into C(2+) Products. ChemSusChem 2025, 18 (7), e202401916. https://doi.org/10.1002/cssc.202401916

418. Cicco, L.; Dilauro, G.; Pulpito, M.; Capriati, V., Recent advances in metal-, organo-, and biocatalyzed one-pot tandem reactions under environmentally responsible conditions. Current Opinion in Green and Sustainable Chemistry 2023, 41. https://doi.org/10.1016/j.cogsc.2023.100799

419. Kracher, D.; Kourist, R., Recent developments in compartmentalization of chemoenzymatic cascade reactions. Current Opinion in Green and Sustainable Chemistry 2021, 32. https://doi.org/10.1016/j.cogsc.2021.100538

420. Zheng, W.; Yang, X.; Li, Z.; Yang, B.; Zhang, Q.; Lei, L.; Hou, Y., Designs of Tandem Catalysts and Cascade Catalytic Systems for CO(2) Upgrading. Angewandte Chemie International Edition 2023, 62 (43), e202307283.
https://doi.org/10.1002/anie.202307283

421. Morales-Guio, C. G.; Cave, E. R.; Nitopi, S. A.; Feaster, J. T.; Wang, L.; Kuhl, K. P.; Jackson, A.; Johnson, N. C.; Abram, D. N.; Hatsukade, T.; Hahn, C.; Jaramillo, T. F., Improved CO2 reduction activity towards C2+ alcohols on a

tandem gold on copper electrocatalyst. Nature Catalysis 2018, 1 (10), 764-771. https://doi.org/10.1038/s41929-018-0139-9

422. O'Mara, P. B.; Wilde, P.; Benedetti, T. M.; Andronescu, C.; Cheong, S.; Gooding, J. J.; Tilley, R. D.; Schuhmann, W., Cascade Reactions in Nanozymes: Spatially Separated Active Sites inside Ag-Core-Porous-Cu-Shell Nanoparticles for Multistep Carbon Dioxide Reduction to Higher Organic Molecules. journal of the American Chemical Society 2019, 141 (36), 14093-14097.
https://doi.org/10.1021/jacs.9b07310

423. Meng, D. L.; Zhang, M. D.; Si, D. H.; Mao, M. J.; Hou, Y.; Huang, Y. B.; Cao, R., Highly Selective Tandem Electroreduction of CO(2) to Ethylene over Atomically Isolated Nickel-Nitrogen Site/Copper Nanoparticle Catalysts. Angewandte Chemie International Edition 2021, 60 (48), 25485-25492. https://doi.org/10.1002/anie.202111136

424. Ishida, H.; Tanaka, K.; Tanaka, T., Electrochemical-CO2-reduction-catalyzed-by-ruthenium-complexes-ru(bpy)2(co)2-2-and-ru(bpy)2(co)cl-effect-of-ph-on-the Formation of CO and HCOO-. Organometallics 1987, 6, 181-186. https://doi.org/10.1021/om00144a033

425. Tanaka, K.; Ooyama, D., Multi-electron reduction of CO2 via Ru-CO2, -C(O)OH, -CO,-CHO, and -CH2OH species. Coordination Chemistry Reviews 2002, 226 211-218. https://doi.org/10.1016/S0010-8545(01)00434-9

426. Nagao, H.; Mizukawa, T.; Tanaka, K., Carbon-carbon bond formation in the electrochemical reduction of carbon dioxide catalyzed by a ruthenium complex. Inorganic Chemistry 1994, 33 (15), 3415-3420. https://doi.org/10.1021/ic00093a033

427. Barakat, M.; Fosu, E. A.; Jakubikova, E., Cobalt(II) Phthalocyanine Substituents Tune the Electrocatalytic CO2 Conversion to Methanol. Inorganic Chemistry 2025, 64 (42), 20896-20906. https://doi.org/10.1021/acs.inorgchem.5c02279

428. Hutchison, P.; Smith, L. E.; Rooney, C. L.; Wang, H.; Hammes-Schiffer, S., Proton-Coupled Electron Transfer Mechanisms for CO2 Reduction to Methanol Catalyzed by Surface-Immobilized Cobalt Phthalocyanine. Journal of the American Chemical Society 2024, 146 (29), 20230-20240. https://doi.org/10.1021/jacs.4c05444

429. Machan, C. W.; Stanton, C. J.; Vandezande, J. E.; Majetich, G. F.; Schaefer, H. F.; Kubiak, C. P.; Agarwal, J., Electrocatalytic Reduction of Carbon Dioxide by Mn(CN)(2,2′-bipyridine)(CO)3: CN Coordination Alters Mechanism.

Inorganic Chemistry 2015, 54, 8849-8856. https://doi.org/10.1021/acs.inorgchem.5b01715

430. Mairegger, T.; Li, H.; Griesser, C.; Winkler, D.; Filser, J.; Hormann, N. G.; Reuter, K.; Kunze-Liebhauser, J., Electroreduction of CO(2) in a Non-aqueous Electrolyte-The Generic Role of Acetonitrile. ACS Catalysis 2023, 13 (9), 5780-5786. https://doi.org/10.1021/acscatal.3c00236

431. Zhu, S.; Li, T.; Cai, W.-B.; Shao, M., CO2 Electrochemical Reduction As Probed through Infrared Spectroscopy. ACS Energy Letters 2019, 4 (3), 682-689. https://doi.org/10.1021/acsenergylett.8b02525

432. Smith, B. J.; Parent, L. R.; Overholts, A. C.; Beaucage, P. A.; Bisbey, R. P.; Chavez, A. D.; Hwang, N.; Park, C.; Evans, A. M.; Gianneschi, N. C.; Dichtel, W. R., Colloidal Covalent Organic Frameworks. ACS Central Science 2017, 3 (1), 58-65. https://doi.org/10.1021/acscentsci.6b00331

433. Yao, L.; Rodriguez-Camargo, A.; Guntermann, R.; Heck, F.; Van Gele, S.; Vignolo-Gonzalez, H.; Duppel, V.; Bein, T.; Lotsch, B. V., Covalent Organic Framework-Carbon Nanotube Core-Shell Nanohybrids for Enhanced Catalytic Site Utilization of Molecular Catalysts in CO(2) Electroreduction. Angewandte Chemie International Edition 2026, e21776. https://doi.org/10.26434/chemrxiv-2025-mtlg9

Appendix A

Supplementary Information for Chapter 2

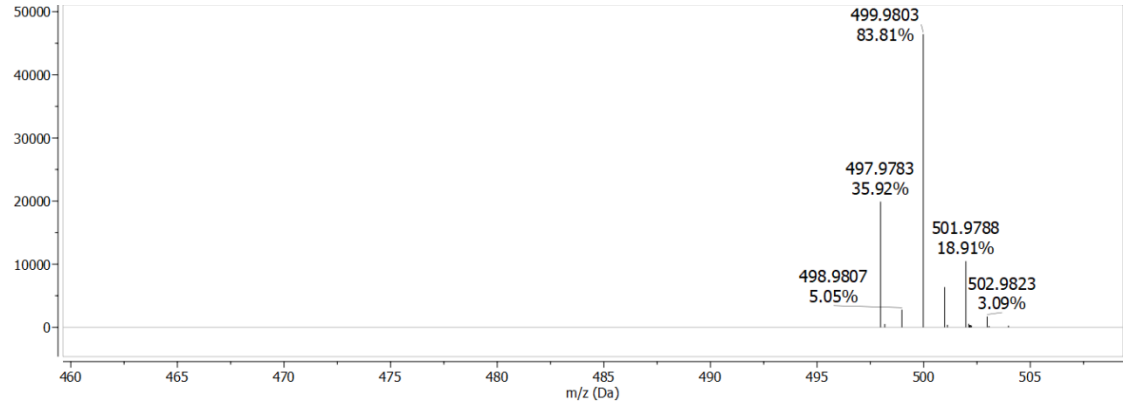


Figure A1. (–)–HRESIMS spectrum of Re-pbiH.

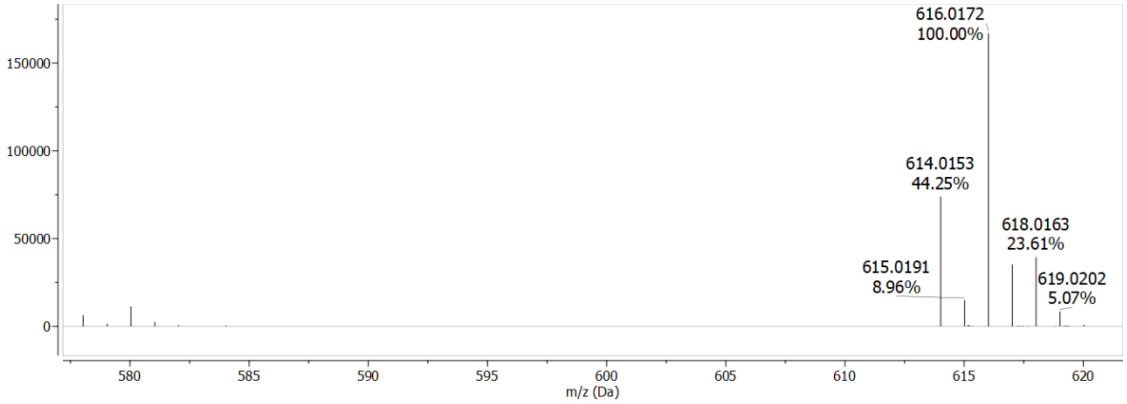


Figure A2. (–)–HRESIMS spectrum of Re-bbzp.

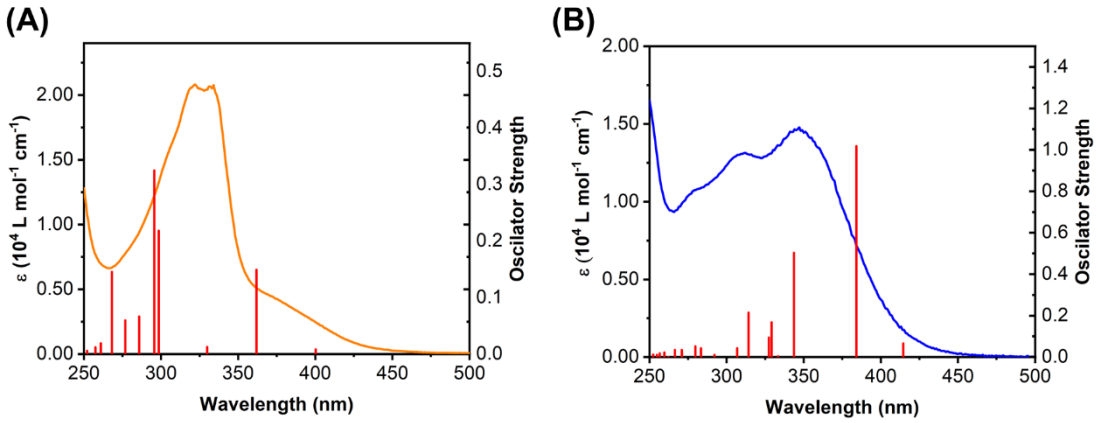


Figure A3. Experimental UV-Vis absorption spectra of Re-pbiH (A) and Re-bbzp (B) complexes compared to the these TD-DFT predicted oscillators strengths (right axis).

Table A1. Lowest energy electronic transitions and their corresponding oscillator strengths for the main UV-Vis transitions found for Re-pbiH.

l nm (eV)	Oscillator strength	Transitions	Nature
400.33 (3.0971)	0.0084	H-1 → L (8.2%) H → L (91.8%)	$MLCT_{Re\rightarrow NN}$
361.81 (3.4268)	0.1494	H-1 → L (92.2%) H → L (7.8%)	$MLCT_{Re\rightarrow NN}$
329.82 (3.7592)	0.0127	H-2 → L (92.1%) H-2 → L+1 (2.8%) H-2 → L+2 (2.8%) H-2 → L+3 (2.2%)	$MLCT_{Re\rightarrow NN}$

Table A2. Lowest energy electronic transitions and their corresponding oscillator strengths for the main UV-Vis transitions found for Re-bbzp.

l nm (eV)	Oscillator strength	Transitions	Nature
359.28 (3.4510)	0.0345	H-1 → L (51.6%) H → L (48.4%)	$MLCT_{Re\rightarrow NN}$
343.44 (3.6101)	0.8567	H-4 → L (4.3%) H-1 → L (41.7%) H → L (54.0%)	$MLCT_{Re\rightarrow NN}$
305.40 (4.0598)	0.6716	H-4 → L+1 (2.6%) H-3 → L (66.1%) H-2 → L (20.5%) H-1 → L (3.7%) H-1 → L+1 (7.0%)	$MLCT_{Re\rightarrow NN}$

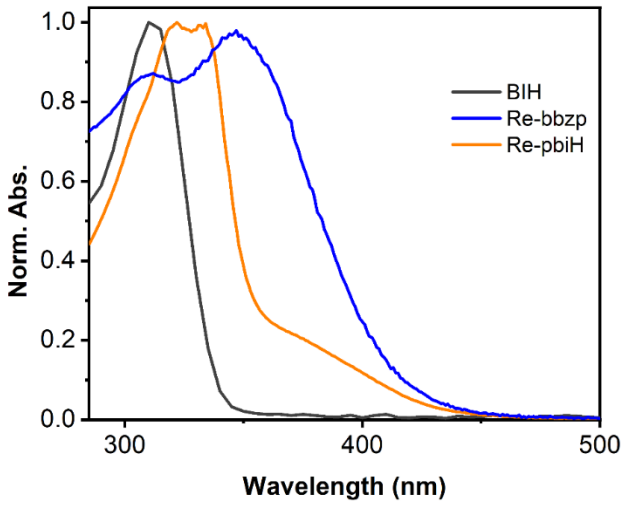


Figure A4. UV-vis spectra of the used electron donor (BIH) and evaluated photocatalysts in acetonitrile at 298 K.

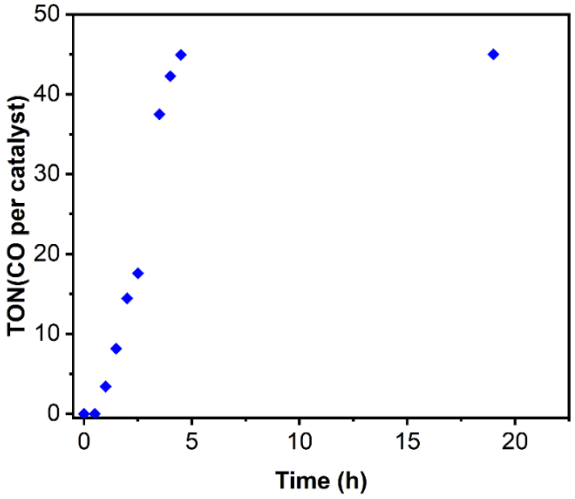


Figure A5. Long-term irradiation time dependence of CO formation photocatalyzed by Re-bbzp complex. Experiments were performed in CO_2-saturated 10 mL CH_3CN solutions containing 6.7 mmol L^{-1} of BIH and 0.03 mmol L^{-1} of photocatalysts (λ > 370 nm).

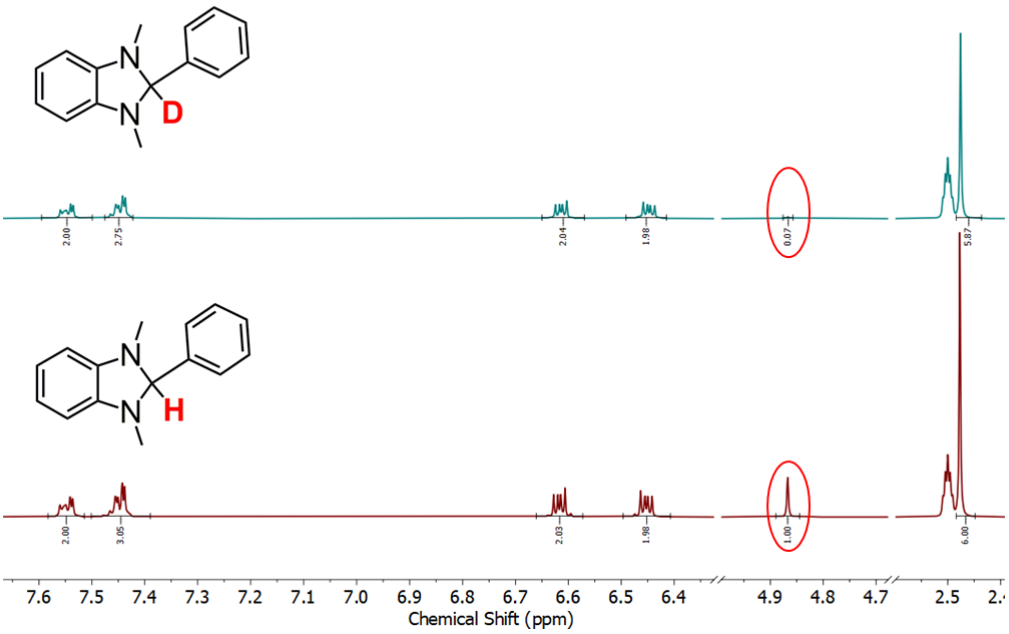


Figure A6. ^{1}H-NMR spectra of the complex BIH (red) and its deuteride form (BID) (blue) in DMSO-d^{6}. The highlighted peak corresponds to the replaced proton on BIH.

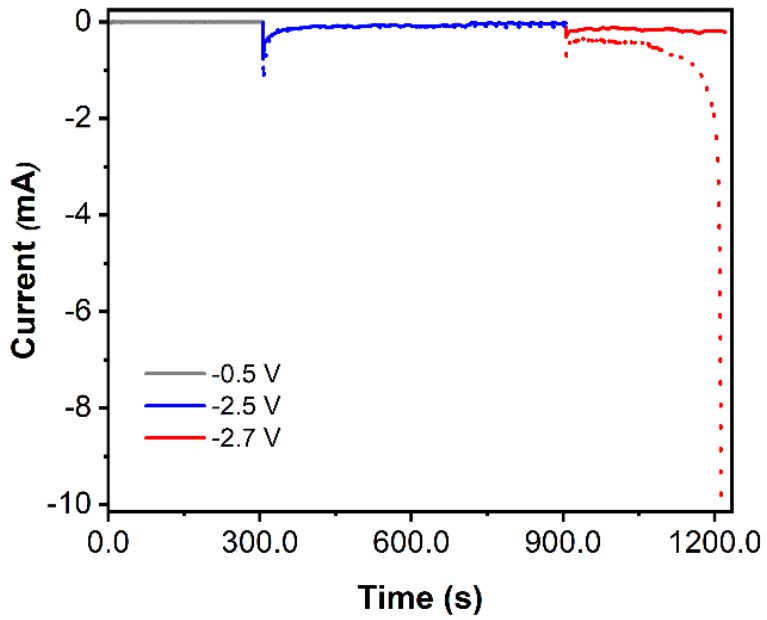


Figure A7. Chronoamperometry measurements of Re-bbzp complex performed for the IR-SEC experiments in acetonitrile with Bu_4NPF_6 electrolyte for the first (E_p = –2.5 V *vs*. Fc^+/Fc) and second (E_p = –2.7 V vs. Fc^+/Fc) electron reduction

process under Ar (solid line) and CO_2 (dotted line) atmosphere. The potential -0.5 V *vs*. Fc^+/Fc did not show changes in the IR spectra as expected.

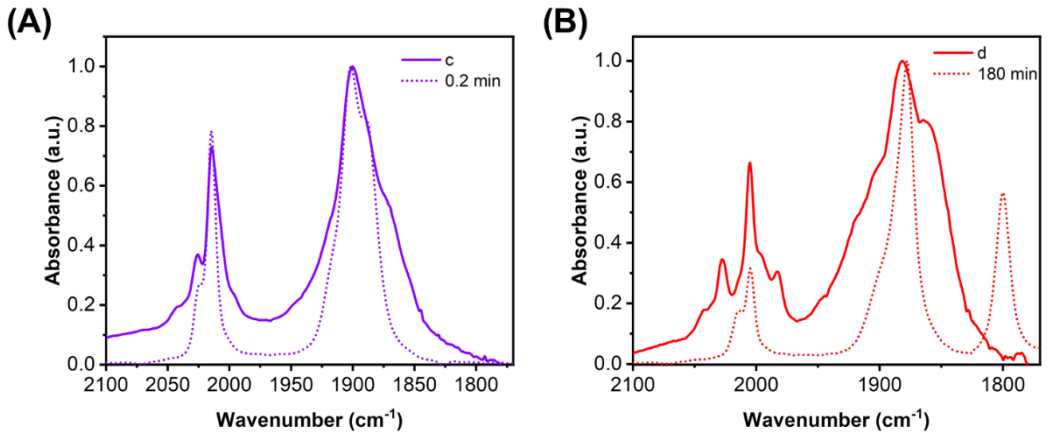


Figure A8. Comparison between the *in-situ* experimental spectra (dotted lines) and the corresponding spectroelectrochemical (SEC) spectra (solid lines) of one- (a) and two- (b) electron reduced species under Ar atmosphere.

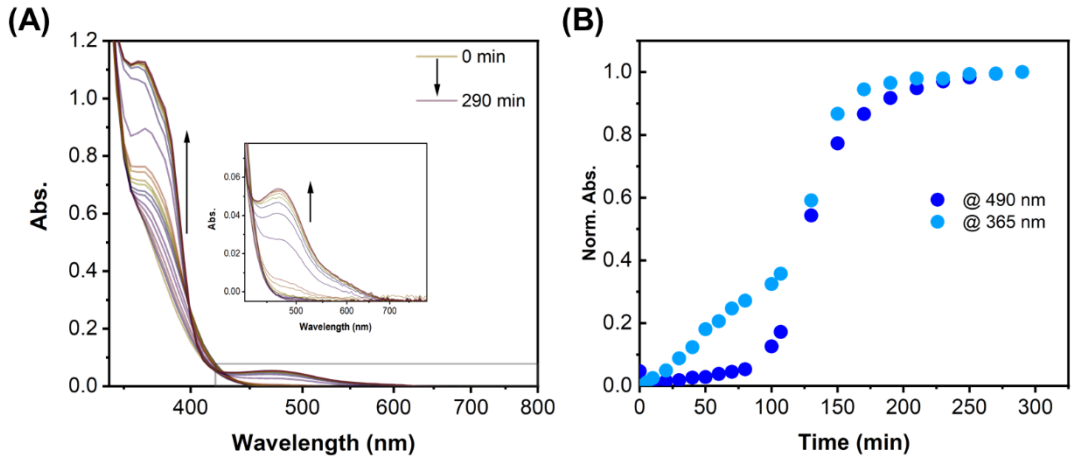


Figure A9. UV−vis spectral changes (a) and the corresponding kinetic traces at selected wavelengths during the photoirradiation for Re-bbzp (0.06 mmol L^{-1}) in Ar-saturated CH_3CN solutions containing excess of BIH (1.40 mmol L^{-1}) (λ_{irr} = 365 nm).

Data for computed stationary points

***fac*-[Re(CO)$_3$(bbzp)]**

Charge: 0 Multiplicity: 2

C	1.32258600	1.99456800	-0.10124300
C	-1.03455700	2.27199000	-0.00792600
C	1.48297100	3.37154900	-0.19771400
C	-0.89574300	3.67006100	-0.08992400
C	0.36132700	4.23038400	-0.22220600
H	2.48343600	3.78582400	-0.19791800
H	-1.77846700	4.29832500	-0.05759900
C	-2.27535600	1.60130900	0.11982500
H	-3.78656500	3.08191800	0.38347600
N	-2.31208600	0.23647300	0.06876900
Re	-0.46747700	-0.70532200	-0.37012300
C	-1.27138000	-2.33733500	-0.97634900
C	1.17311800	-1.20168500	-1.24935200
C	0.09328000	-1.54787200	1.21243100
O	2.16254700	-1.50474900	-1.83291300
O	-1.78881300	-3.33473500	-1.37019200
O	0.42680500	-2.07606800	2.22637900
N	0.06776300	1.39753500	-0.09338200
N	-3.54432600	2.10758000	0.29935900
C	-4.43520000	1.03756500	0.39441400
C	-3.65809300	-0.14186900	0.25588900
C	-4.26399200	-1.39977200	0.33066600
C	-5.81692100	0.99652800	0.59294700
C	-5.64733300	-1.44569500	0.53095600
C	-6.41204500	-0.26716800	0.65757200
H	-3.68489900	-2.30919700	0.23867200
H	-6.40243300	1.90260600	0.69599000
H	-7.48298700	-0.34134700	0.81173600
H	-6.14211500	-2.40873400	0.59325000

C	4.66581200	0.54723900	-0.18918600
H	3.73898300	1.97512900	-1.49863400
C	4.05982800	-0.13902800	0.89892600
C	2.52740300	1.17429800	0.07651400
N	3.67083700	1.38037200	-0.68686600
N	2.72918300	0.27567600	1.04155500
C	4.79807800	-1.06761900	1.64799300
C	5.99706600	0.32628300	-0.56056500
H	6.45367200	0.85021500	-1.39260600
H	4.34125800	-1.59040500	2.48091800
C	6.12584500	-1.28884000	1.28470200
H	6.72326800	-2.00052900	1.84472700
C	6.71529500	-0.60223000	0.19545600
H	7.75151500	-0.80205300	-0.05645600
H	0.49026000	5.30235900	-0.30150900

Zero-point correction= 0.315407 (Hartree/Particle)
Thermal correction to Energy= 0.340083
Thermal correction to Enthalpy= 0.341027
Thermal correction to Gibbs Free Energy= 0.258606
Sum of electronic and zero-point Energies= -1424.172824
Sum of electronic and thermal Energies= -1424.148148
Sum of electronic and thermal Enthalpies= -1424.147204
Sum of electronic and thermal Free Energies= -1424.229625

***fac*-[Re(CO)$_3$(bbzpH)]$^+$**

Charge: 1 Multiplicity: 2

C	-1.40023900	1.92570500	0.23177300
C	0.94648300	2.22540300	-0.01973100
C	-1.54312000	3.28184500	0.53928900
C	0.82187000	3.58590100	0.24670000
C	-0.42463000	4.12403900	0.58424700
H	-2.53476300	3.70143600	0.65856600

H	1.69526800	4.22618800	0.20360500
C	2.18034200	1.57540200	-0.32956300
H	3.61600500	3.09479700	-0.71631000
N	2.24105000	0.21926300	-0.33156000
Re	0.45326100	-0.75127400	0.34979300
C	0.93681000	-0.75161500	2.16062400
C	-1.26371100	-1.48090200	0.85199200
C	1.11122800	-2.55413500	0.16982800
O	-2.30123600	-1.94899800	1.18236400
O	1.26437700	-0.70608900	3.30210100
O	1.51099900	-3.66438000	0.05316500
N	-0.14068200	1.32948000	0.07461200
N	3.40597400	2.11310800	-0.62449700
C	4.30658900	1.06640400	-0.82999700
C	3.56866400	-0.13150700	-0.64253400
C	4.19503800	-1.37569000	-0.78064100
C	5.66445600	1.06187700	-1.15809000
C	5.55316800	-1.38439500	-1.10583800
C	6.27691400	-0.18597300	-1.29228700
H	3.65163700	-2.30094100	-0.64372800
H	6.21745800	1.98273000	-1.30060100
H	7.33023600	-0.23543100	-1.54479100
H	6.06419000	-2.33404600	-1.21901700
C	-4.75320100	0.48997100	-0.12545500
H	-3.97598100	1.84885900	1.34569200
C	-4.06402800	-0.17195100	-1.16467900
C	-2.58802200	1.16558900	-0.08030500
N	-3.80606200	1.29827700	0.51652200
C	-4.70954500	-1.06924300	-2.01777000
C	-6.11347400	0.27811700	0.10464700
H	-6.64157000	0.78512400	0.90253800
H	-4.18220600	-1.57524600	-2.81659900
C	-6.07169100	-1.28001900	-1.79001100

H	-6.61360700	-1.96732500	-2.42923100
C	-6.76022100	-0.62018600	-0.74804700
H	-7.81701800	-0.81466400	-0.60676800
H	-0.53377100	5.17609400	0.81054800
N	-2.73982200	0.27379600	-1.10028100
H	-2.00484700	0.02840200	-1.74789100

Zero-point correction= 0.329355 (Hartree/Particle)
Thermal correction to Energy= 0.354110
Thermal correction to Enthalpy= 0.355055
Thermal correction to Gibbs Free Energy= 0.272549
Sum of electronic and zero-point Energies= -1424.617030
Sum of electronic and thermal Energies= -1424.592274
Sum of electronic and thermal Enthalpies= -1424.591330
Sum of electronic and thermal Free Energies= -1424.673836

$BIH^{\bullet+}$

Charge: 1 Multiplicity: 2

C	1.70972700	0.00000000	-0.23232400
C	2.87955900	0.00000000	-1.00577300
C	1.79661500	0.00000000	1.17053400
C	4.13324500	0.00000000	-0.38116900
H	2.81305100	0.00000100	-2.08961700
C	3.04855100	0.00000000	1.79028200
H	0.89393500	-0.00000100	1.77286000
C	4.21806500	0.00000000	1.01528800
H	5.03502100	0.00000100	-0.98355800
H	3.11367300	-0.00000100	2.87292600
H	5.18849700	0.00000000	1.50012900
C	0.35800700	0.00000000	-0.92485800
H	0.50796700	0.00000000	-2.01526900
C	-1.72353400	0.72016500	-0.12332400
C	-1.72353400	-0.72016500	-0.12332400

C	-2.86066200	1.44267600	0.28411000
C	-2.86066200	-1.44267600	0.28411000
C	-3.97032300	0.71270000	0.68806800
H	-2.87159400	2.52471700	0.27698700
C	-3.97032300	-0.71270000	0.68806800
H	-2.87159500	-2.52471700	0.27698700
H	-4.86359200	1.23639800	1.00742400
H	-4.86359200	-1.23639800	1.00742300
N	-0.50813900	-1.14842900	-0.55927000
N	-0.50813900	1.14842900	-0.55927000
C	-0.10123700	-2.53274600	-0.79198300
H	0.97977900	-2.61264000	-0.67089100
H	-0.58419400	-3.18402200	-0.06211100
H	-0.37626700	-2.85413400	-1.80241800
C	-0.10123700	2.53274600	-0.79198300
H	0.97977900	2.61263900	-0.67089600
H	-0.37627200	2.85413600	-1.80241600
H	-0.58418900	3.18402100	-0.06210700

Zero-point correction= 0.281170 (Hartree/Particle)
Thermal correction to Energy= 0.295104
Thermal correction to Enthalpy= 0.296048
Thermal correction to Gibbs Free Energy= 0.238953
Sum of electronic and zero-point Energies= -690.117486
Sum of electronic and thermal Energies= -690.103551
Sum of electronic and thermal Enthalpies= -690.102607
Sum of electronic and thermal Free Energies= -690.159703

BI•

Charge: 0 Multiplicity: 2

C	1.75137400	-0.00000300	-0.00000200
C	2.50828100	-1.08247900	-0.56729300
C	2.50827600	1.08247700	0.56728900

C	3.89839600	-1.07385100	-0.55827400
H	1.98959600	-1.90133800	-1.05235600
C	3.89839100	1.07385600	0.55827200
H	1.98958600	1.90133500	1.05235200
C	4.61803700	0.00000400	-0.00000100
H	4.43372000	-1.90571800	-1.00816800
H	4.43371100	1.90572600	1.00816500
H	5.70278100	0.00000700	-0.00000100
C	0.32991600	-0.00000400	-0.00000400
C	-1.85807500	0.70704000	-0.02117400
C	-1.85807700	-0.70704500	0.02116900
C	-3.05031900	1.43037700	-0.04505100
C	-3.05032400	-1.43037700	0.04504600
C	-4.25627000	0.69978000	-0.02446800
H	-3.05693300	2.51389800	-0.06610200
C	-4.25627200	-0.69977400	0.02446600
H	-3.05694400	-2.51389700	0.06609500
H	-5.19886300	1.23697300	-0.04268700
H	-5.19886700	-1.23696400	0.04268600
N	-0.52509200	-1.12617800	0.04720700
N	-0.52509100	1.12617000	-0.04721800
C	-0.13161000	-2.48694600	0.40739300
H	0.80664400	-2.46412200	0.96282300
H	-0.90356000	-2.92259600	1.04757400
H	-0.00666000	-3.12598900	-0.47328200
C	-0.13161400	2.48694800	-0.40736900
H	0.80669400	2.46415000	-0.96270600
H	-0.90351300	2.92257600	-1.04762700
H	-0.00676800	3.12599300	0.47332000

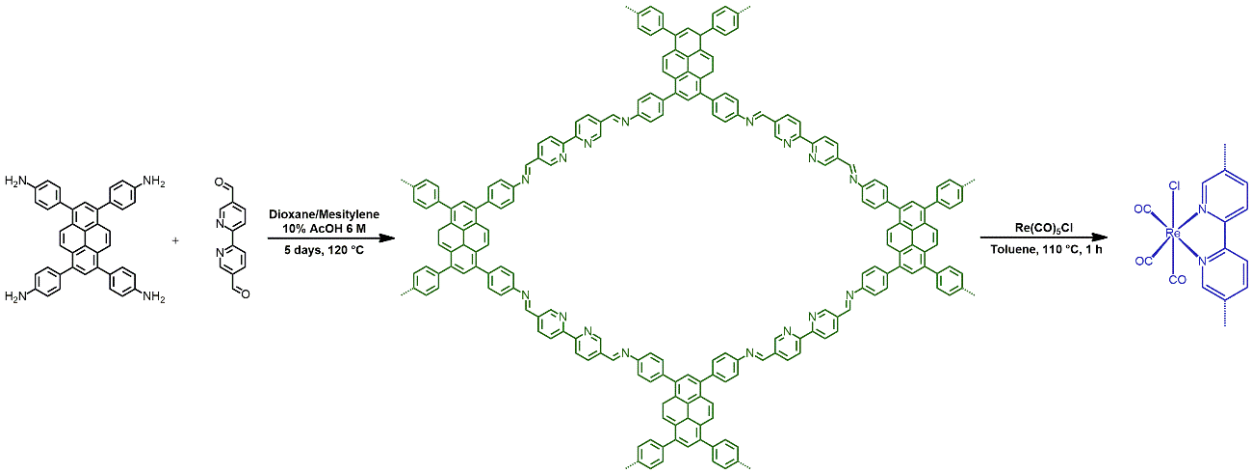
Zero-point correction=	0.268111 (Hartree/Particle)
Thermal correction to Energy=	0.282317
Thermal correction to Enthalpy=	0.283261

Thermal correction to Gibbs Free Energy= 0.226658
Sum of electronic and zero-point Energies= -689.662990
Sum of electronic and thermal Energies= -689.648785
Sum of electronic and thermal Enthalpies= -689.647841
Sum of electronic and thermal Free Energies= -689.704444

Appendix B

Supplementary Information for Chapter 4

Structural Characterization



Scheme B1. Scheme of the synthesis route for **bpyPyr** and **RebpyPyr COFs.**

Table B1. Miller Indices for **bpyPyr COF** obtained though Pawley-refinement considering a triclinic unite cell with a space group P1 (a = 28.201 Å, b = 28.226 Å, c = 7.282 Å, α = 103.2°, β = 104.3°, and γ = 81.7). R_{wp} = 9.66%. R_{wp} (without background) = 7.34%. R_p = 7.37%.

h	k	l	2-theta	Intensity
0	1	0	3.2265	100.000
1	1	0	4.3577	1.664
1	-1	0	4.7851	1.709

2	0	0	6.4918	15.047
3	0	0	9.7442	2.178
3	3	0	13.0986	0.000

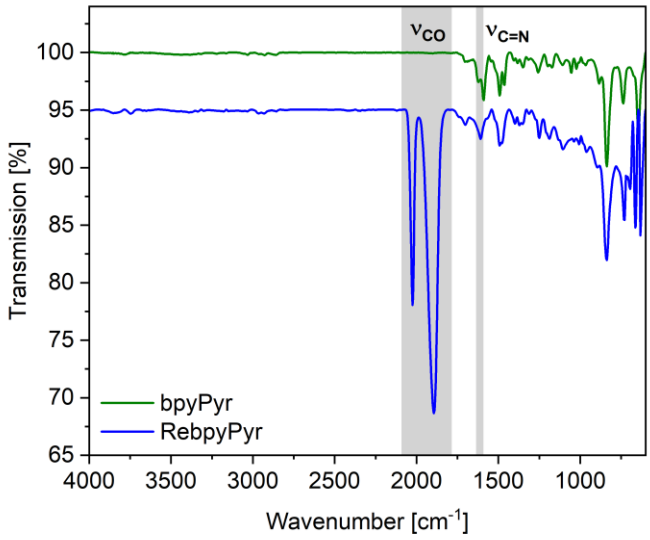


Figure B1. FTIR spectra of **bpyPyr** (green) and **RebpyPyr COFs** (blue) for 42% of covared bpy sites.

Table B2. Miller Indices for **RebpyPyr COF** containing 50% of bpy sites covered by $Re(CO)_3Cl$ units obtained though Pawley-refinement considering a triclinic unite cell with a space group P1 (a = 28.201 Å, b = 28.226 Å, c = 7.282 Å, α = 103.2°, β = 104.3°, and γ = 81.7). R_{wp} = 8.89%. R_{wp} (without background) = 2.94%. R_p = 6.59%.

h	k	l	2-theta	Intensity
0	1	0	3.2265	100.000
1	1	0	4.3577	14.300

1	-1	0	4.7851	10.571
2	0	0	6.4918	19.871
3	0	0	9.7442	0.404
3	3	0	13.0986	6.873

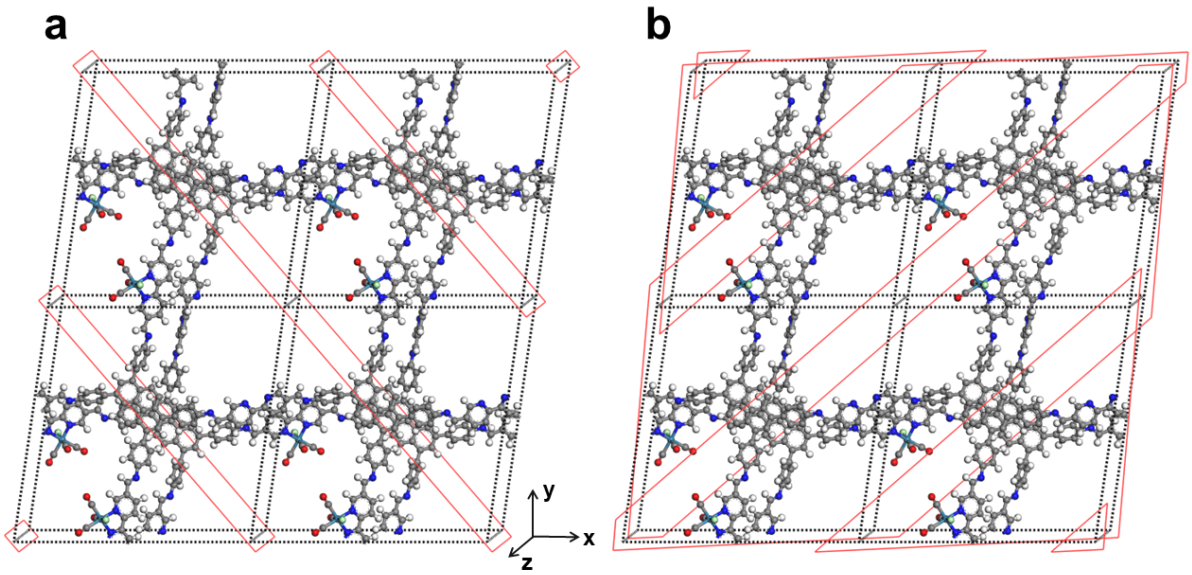


Figure B2. Representation of the Miller planes corresponding to the diffraction peaks emerged post- Re-modification at a) 4.28° and b) 13.0°, assigned to (110) and (330) planes, respectively.

Variation of the rhenium loading

Table B3. Re amount determined by ICP-OES and their corresponding bpy site coverage percentage.

wt% Re ICP OES	bpy sites covered
3.35	9%
1.27	3%
13.1	42%
16.85	57%
19.89	73%
22.35	85%

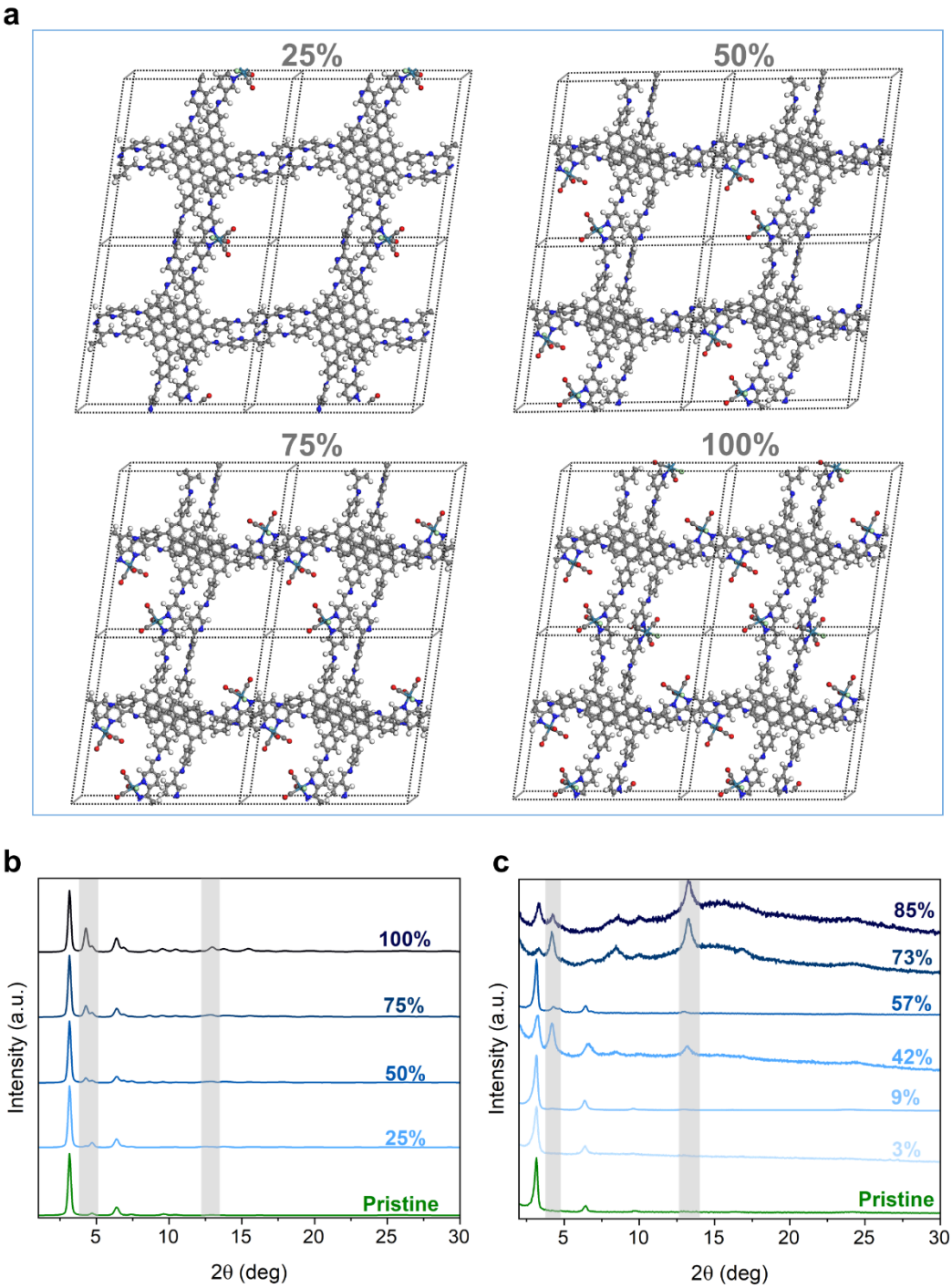


Figure B3. a) Structure models of **RebpyPyr COF** illustrating varying degrees of $Re(CO)_3Cl$ coordination at the bpy sites. (d = lateral offset between adjacent layers) b) Simmulated and c) experimental PXRD patterns of the **bpyPyr COF** at different $Re(CO)_3Cl$ loading (expressed as % bpy occupancy). Highlighted regions indicate the XRD reflections most influenced by the metalation process.

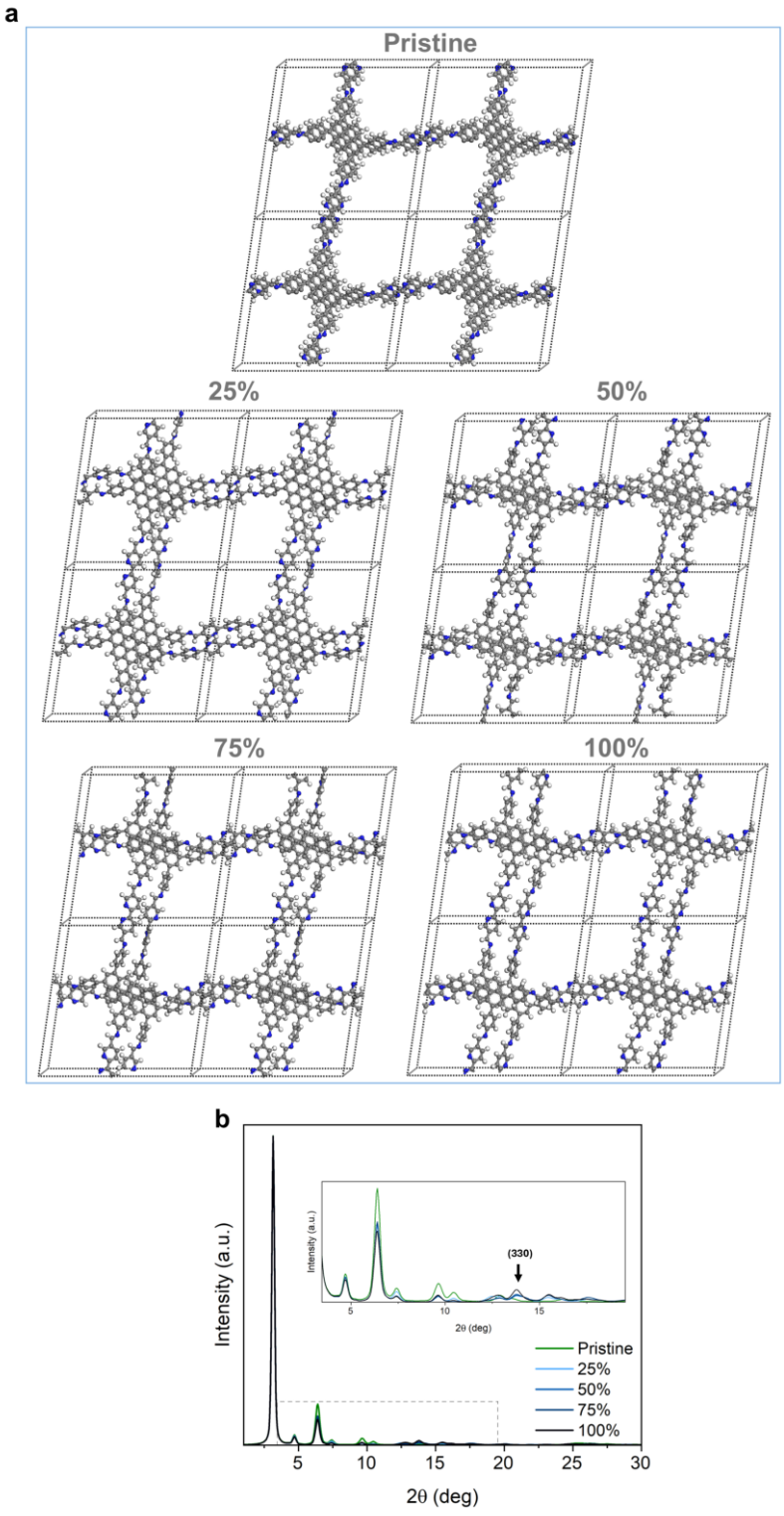


Figure B4. a) Pre-optimized structure models of **RebpyPyr COF** from the **Figure 3** (main text) for different degrees of bpy sites coverage with all the $Re(CO)_3Cl$ removed for generating their b) corresponding PXRD spectra in the absence of

$Re(CO)_3Cl$ units but keeping different layers offset pre-optimized. (the arrow highlights the peak at 2q = 13.0° emerging from the layers offset from the reflection plane (330)).

Morphological characterization

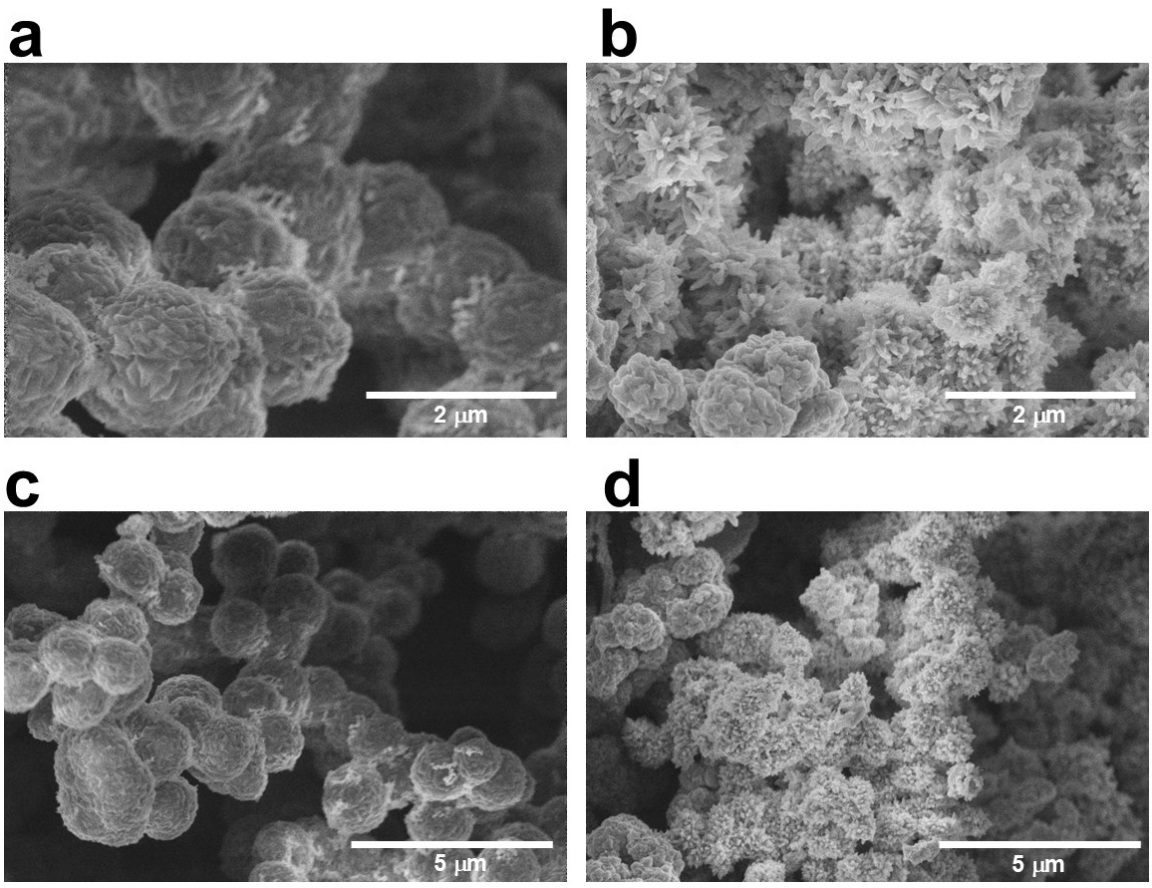


Figure B5. SEM images of the **bpyPyr COF** (a and c) and **Rebpypyr COF** (b and d).

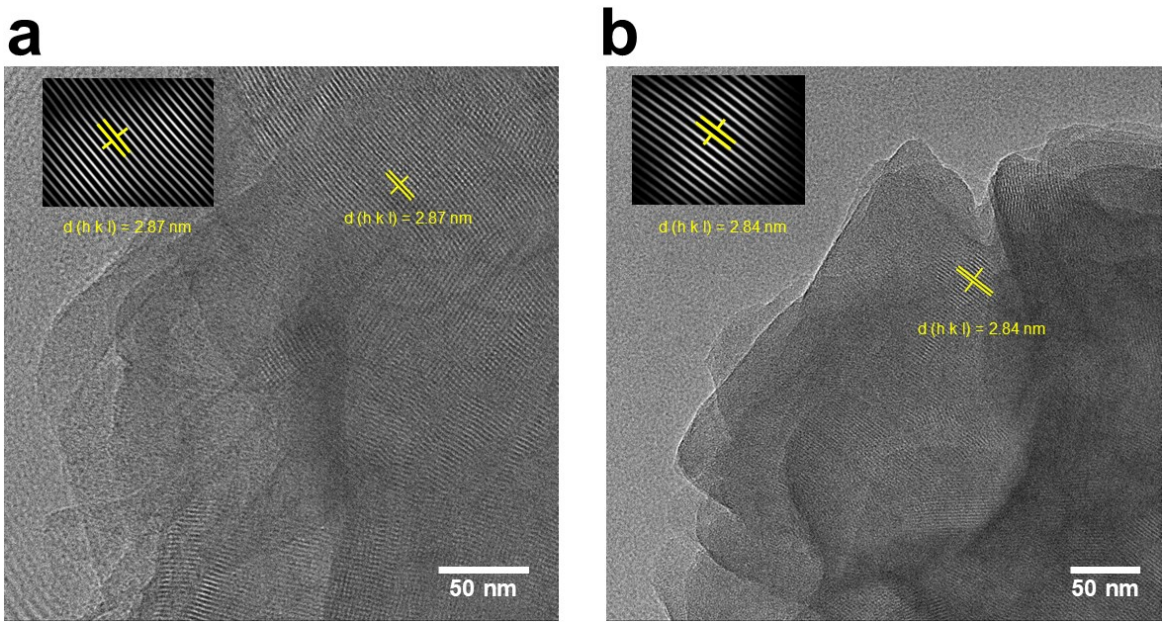


Figure B6. HR-TEM images of the **bpyPyr COF** (a) and **Rebpypyr COF** (b).



Figure B7. Images of bpyPyr COF (pristine) and RebpyPyr (Re-modified COF).

Photocatalytic experiments

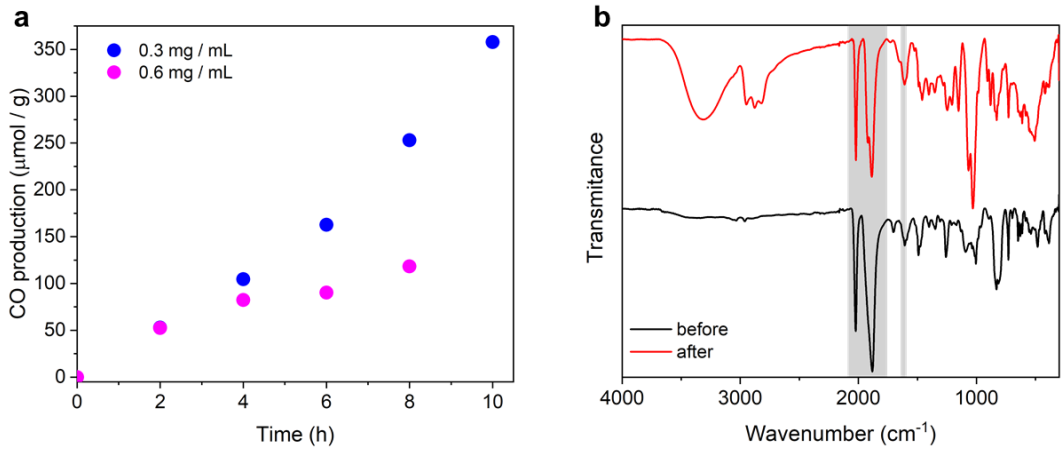


Figure B8. a) CO production using **RebpyPyr COF** under illumination with l > 370 nm and different catalyst concentrations. b) FTIR spectra of the **RebpyPyr COF** before and after photocatalysis under illumination with l > 370 nm.

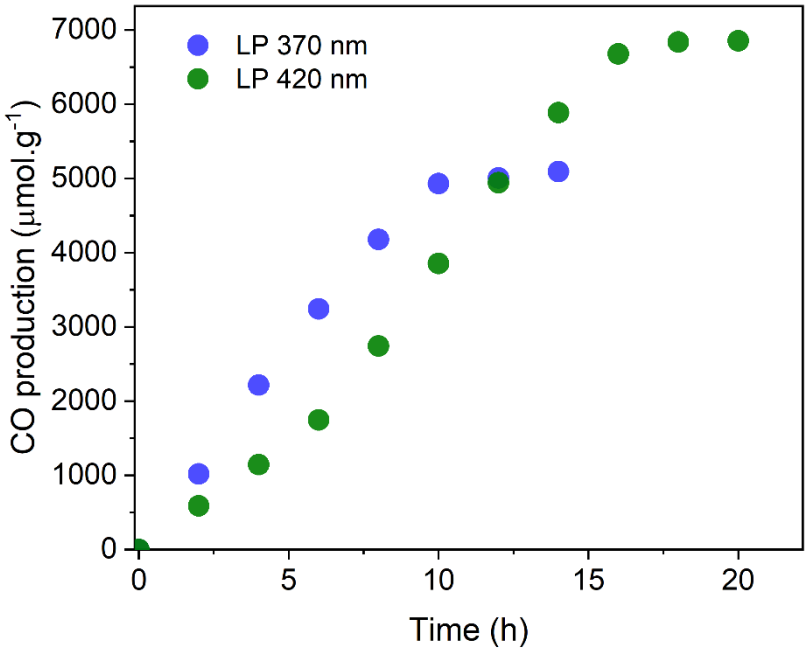


Figure B9. CO evolution by **RebpyPyr COF** under illumination with l > 370 nm (blue) and l > 420 nm (green) using BIH as electron donor.

Table B4. COF-based hybrid Re complexes applied in the photoreduction of CO_2 to CO.

COF	CO production rate [μmol $g^{-1}h^{-1}$]	Sacrificial agent/ solvent	Conc. [mg mL^{-1}]	Amount of Re(I) active sites [μmol]*	TON_{CO}	Light source	Ref.
Re bpyDBC	1160	BIH/CH_3CN	0.3	0.93	35 (24h. after two additional purges with CO_2)	300 W (Xe) >370 nm	[315]
Re-Bpy-sp^2-c-COF	1040 1400[a]	TEOA/CH_3CN	0.2	0.97	18.7 (17.5 h)	300 W (Xe) >420 nm	[68]
Re-COF	750	TEOA/ CH_3CN	0.3	0.27	48	225 W (Xe) >420 nm	[66]
RebpyPyr	765	BIH/CH_3CN-C_6H_5OH	0.3	0.84	2.2 (2.5h)	300 W (Xe) >370 nm	[This work]
RebpyPyr	673	BIH/CH_3CN-H_2O	0.3	0.84	2.0 (2.5h)	300 W (Xe) >370 nm	[This work]
RebpyPyr	525	BIH/CH_3CN-C_6H_5OH	0.3	0.84	7 (16 h)	300 W (Xe) >420 nm	[This work]
Re-TpBpy-COF	282	TEOA/ CH_3CN-H_2O	1.3	21.3	-	200 W (Xe) >390 nm	[280]
Re bpyDBC	180	BIH/CH_3CN	0.3	0.93	7.0 (72 h)	300 W (Xe) >420 nm	[315]

[a] In the presence of a photosensitizer

* The Re(I) content was calculated based on the wt% given by ICP OES.

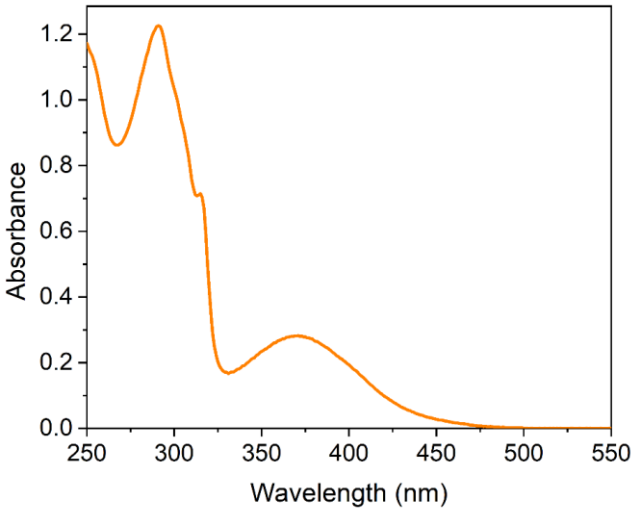


Figure B10. UV-vis spectra of *fac*-$Re(CO)_3(bpy)Cl$ in acetonitrile at 298 K.

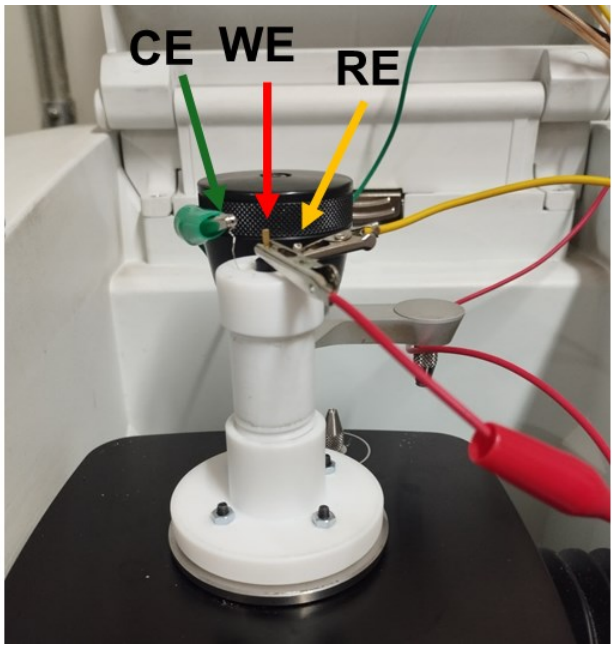


Figure B11. ATR-IR-SEC cell containing a **RebpyPyr COF**/MWNT-modified glassy carbon working electrode, a platinum wire counter electrode, and a silver wire pseudo-reference electrode.

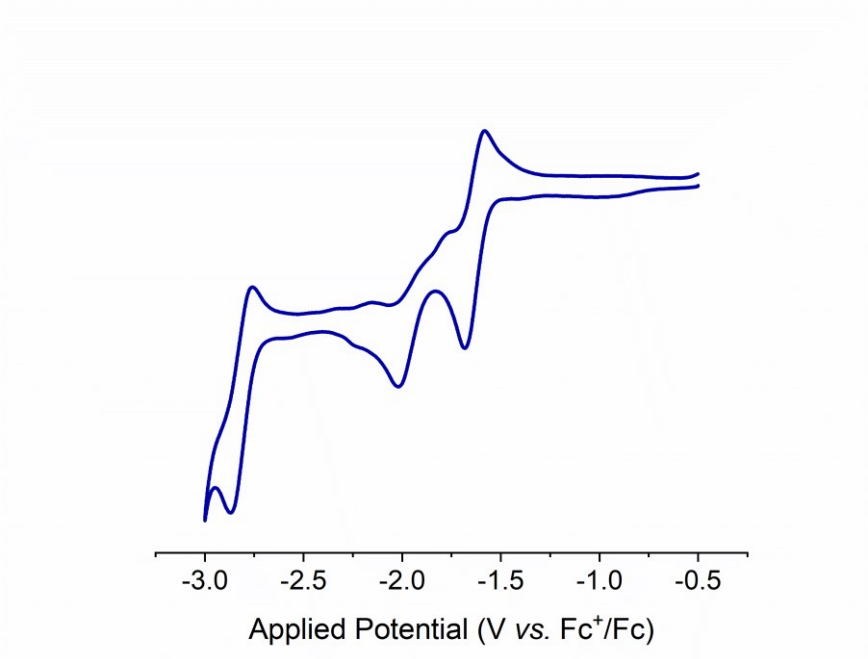


Figure B12. Cyclic voltammogram of *fac*-[Re(CO)$_3$(bpy)Cl] measured with a scan rate of 50 mV s^{-1} in argon-saturated 0.1 M TBAPF$_6$/CH$_3$CN.

Table B5. Fitting parameters obtained from Boltzmann fitting of the initial species during IR-SEC experiments (Nernst analysis).

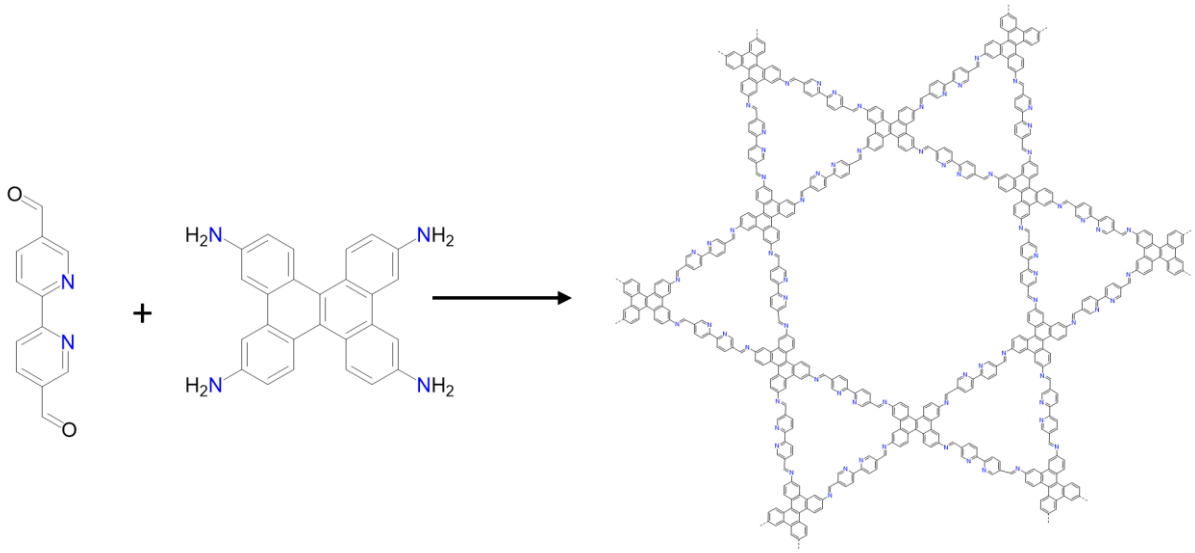
A1	-0.05885 ± 0.02272
A2	1.0025 ± 0.01184
x0	-2.11859 ± 0.01863
dx	0.28655 ± 0.01649
Reduced Chi-Sqr	2.64296E-4
R-Square (COD)	0.99879
Adj. R-Square	0.99827

Table B6. Fitting parameters obtained from Boltzmann fitting of the final species during IR-SEC experiments (Nernst analysis).

A1	1.05529 ± 0.01604
A2	-0.00831 ± 0.01125
x0	-1.94909 ± 0.01504
dx	0.31483 ± 0.01465
Reduced Chi-Sqr	1.7364E-4
R-Square (COD)	0.9992
Adj. R-Square	0.99886

Appendix C

Supplementary Information for Chapter 4



Scheme C1. Scheme of the synthesis route for **bpyDBC** COF.

Electron Microscopy

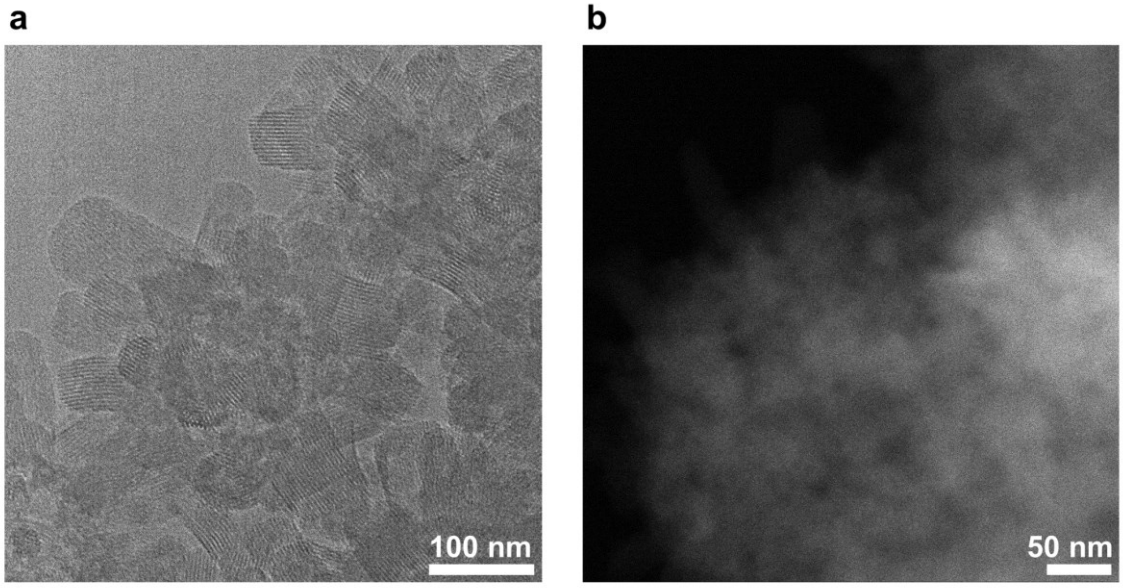


Figure C1. (a) TEM and (b) STEM-HAADF images of the **bpyDBC** COF.

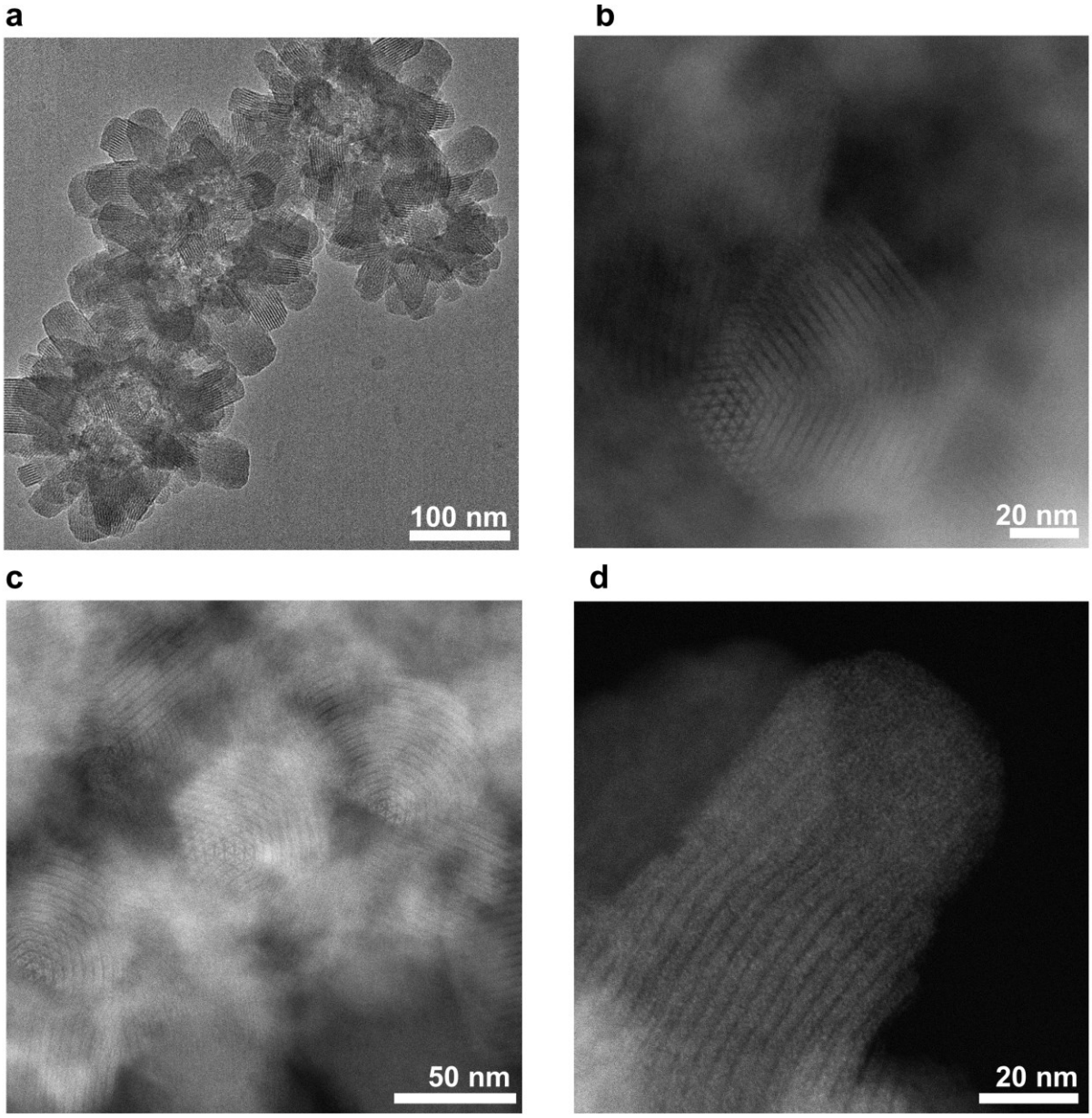


Figure C2. (a) TEM image and (b)-(d) STEM-HAADF images of the **Re bpyDBC** COF taken at different positions and magnifications.

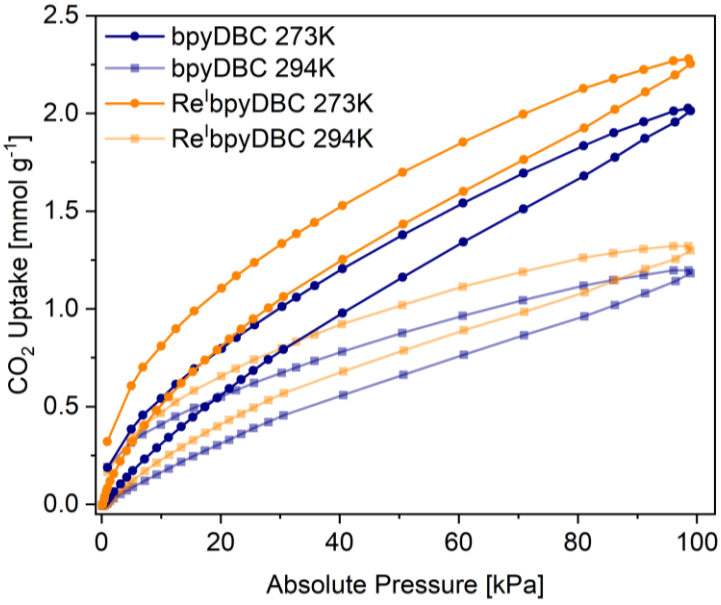


Figure C3. CO_2 adsoption and desorption of both **bpyDBC** and **Re bpyDBC** COF at 273 K and 294 K.

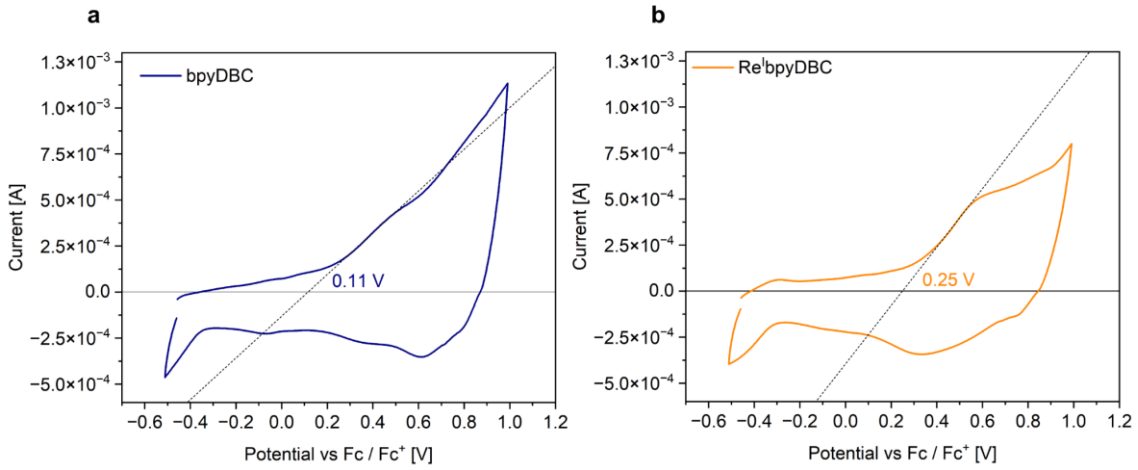


Figure C4. CV curves for both COFs measured against the ferrocene redox couple. The onset of the first oxidation peak reflects the conduction band energy of the material.

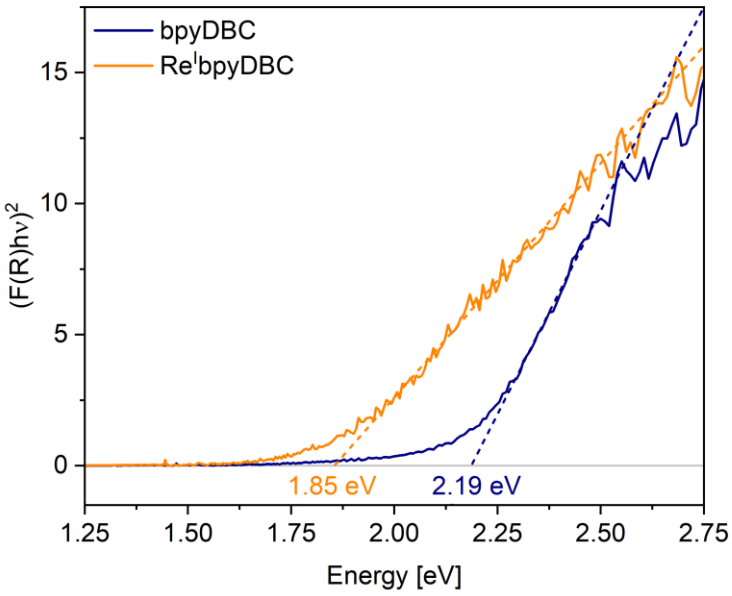


Figure C5. Tauc plot of the two COFs assuming a direct transition. The band gap energy is reduced upon introduction of the Re-complex into the COF structure.

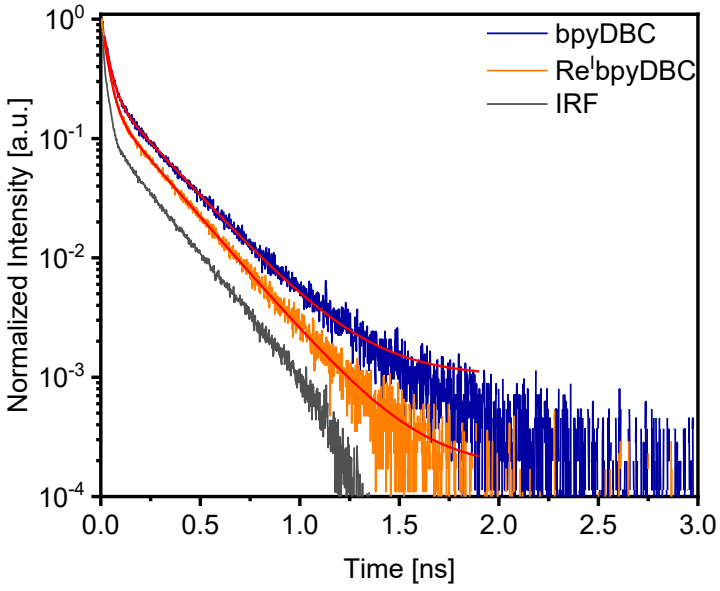


Figure C6. Excited state lifetime of the **bpyDBC** and **Re bpyDBC** COF measured using the TCSPC method (λ_{exc} = 375) and collected at the maximum emission

wavelength. The COFs were measured as dry powders under ambient conditions. The signals were fitted to a double-exponential decay (red lines).

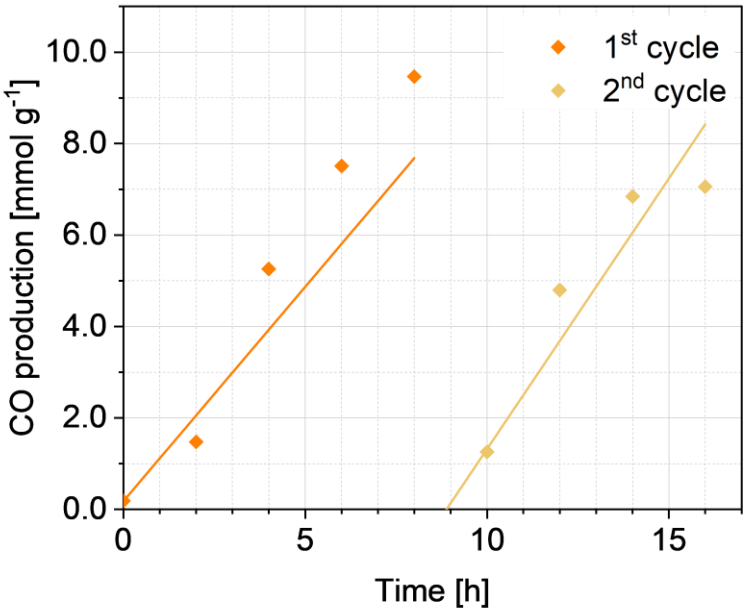


Figure C7. Recycling studies under illumination with λ > 370 nm. Straight lines indicate the linear fitting to extract the CO production rates of 0.94 mmol g^{-1} h^{-1} and 1.18 mmol g^{-1} h^{-1} for the first and second cycle, respectively. The observed plateau in CO production at the end of the second cycle can be attributed to the depletion of BIH, the sacrificial donor.

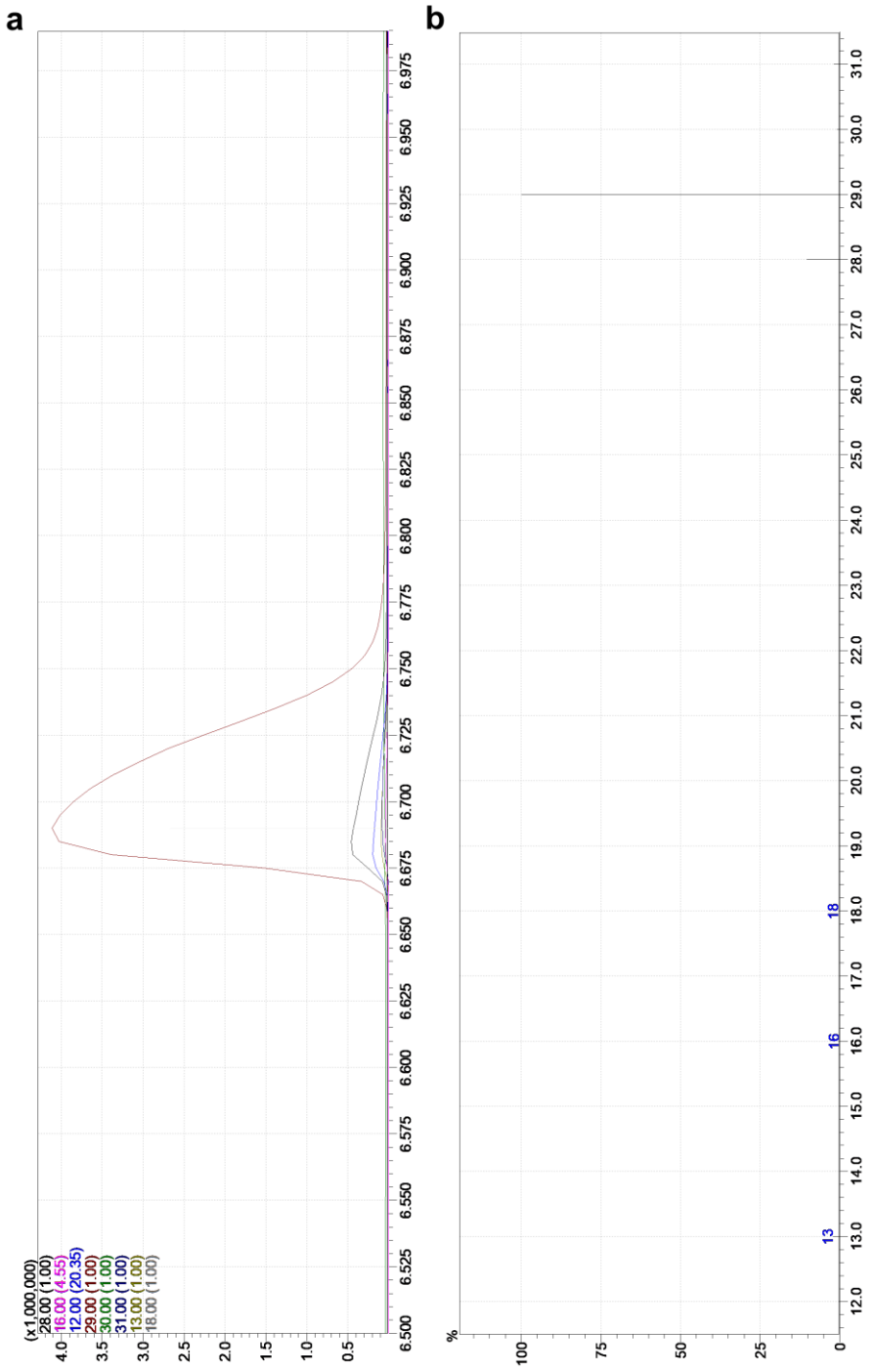


Figure C8. GC-MS analysis of photocatalytic experiments under an illumination of λ > 370 nm using isotopically labelled $^{13}CO_2$. (a) Gas chromatography (GC) data showing the retention time of the detected CO and (b) mass spectrometry (MS) confirming the isotopic signature of ^{13}CO (M = 29 g mol^{-1}), indicating its origin from $^{13}CO_2$.

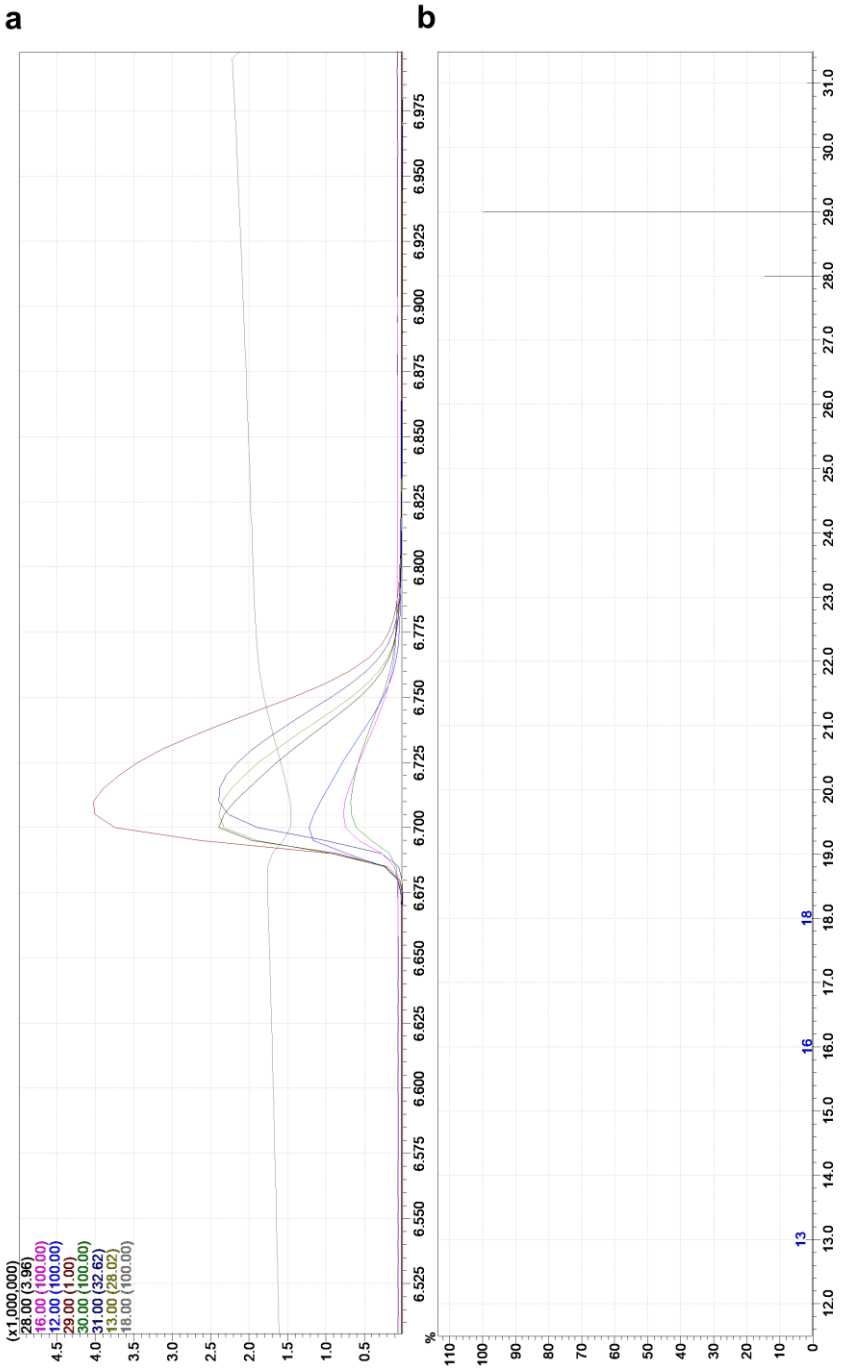


Figure C9. GC-MS analysis of photocatalytic experiments under an illumination of λ > 400 nm using isotopically labelled $^{13}CO_2$. (a) Gas chromatography (GC) data showing the retention time of the detected CO and (b) mass spectrometry (MS) confirming the isotopic signature of ^{13}CO (M = 29 g mol^{-1}), indicating its origin from $^{13}CO_2$.

Appendix D

Supplementary Information for Chapter 7

Table D1. Parameters considered for TON_{CO} calculation.

Catalyst	wt% of Mn (from ICP-OES)	Deposited mass of catalyst [mg]	Number of moles of catalytic centers[a)] [μmol]	Potential [V]	n_{CO}[μmol]	TON_{CO}
fac-$Mn(CO)_3(bpy)Br$	-	~0.5	~1.34	**2.6**	19	14
				2.8	10	7
				3.0	11	8
Mn PhenPy COF	3.29	~1.0	~0.7	**2.6**	189	278
				2.8	222	308
				3.0	128	200

[a)] For details on calculating the moles of Mn in the Mn PhenPy COF catalyst using ICP-OES data, refer to the *Mn-occupation of Phen sites* section below.

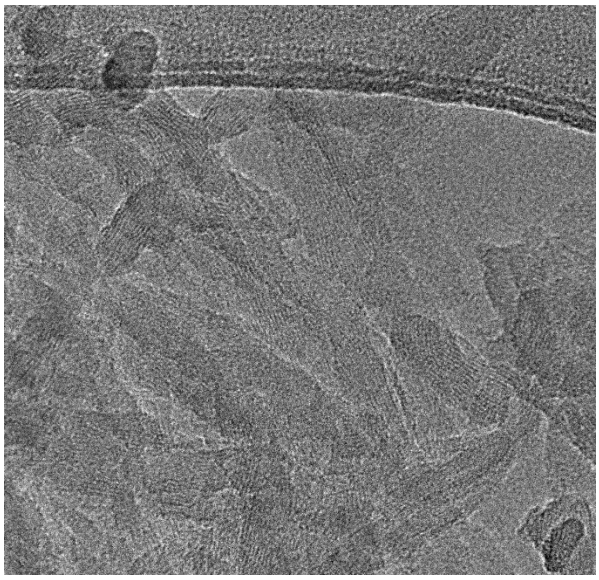


Figure D1. TEM micrograph of the **PhenPy** COF.

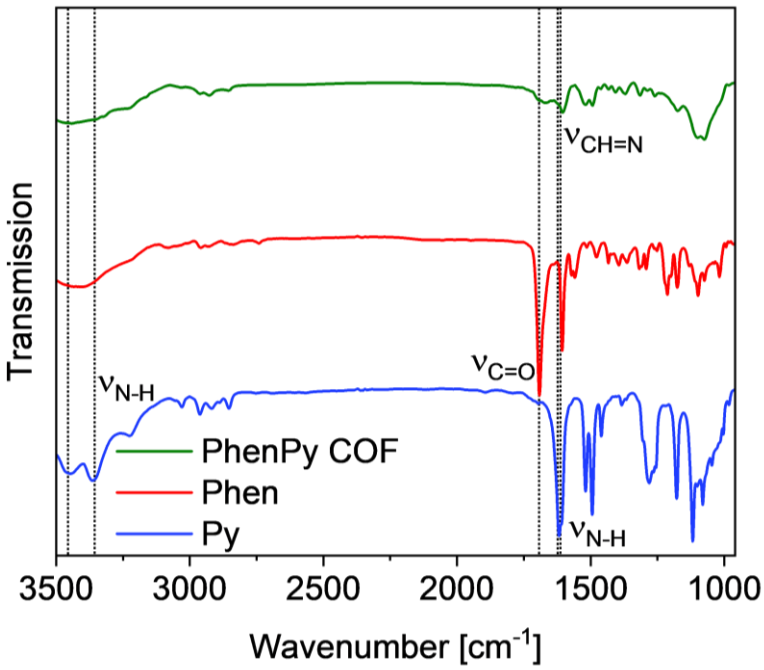


Figure D2. FTIR spectra of the building blocks Phen (red) and Py (blue) together with the spectrum of the synthesized **PhenPy** COF (green). Carbonyl, amine and imine vibrations are indicated by the dotted lines.

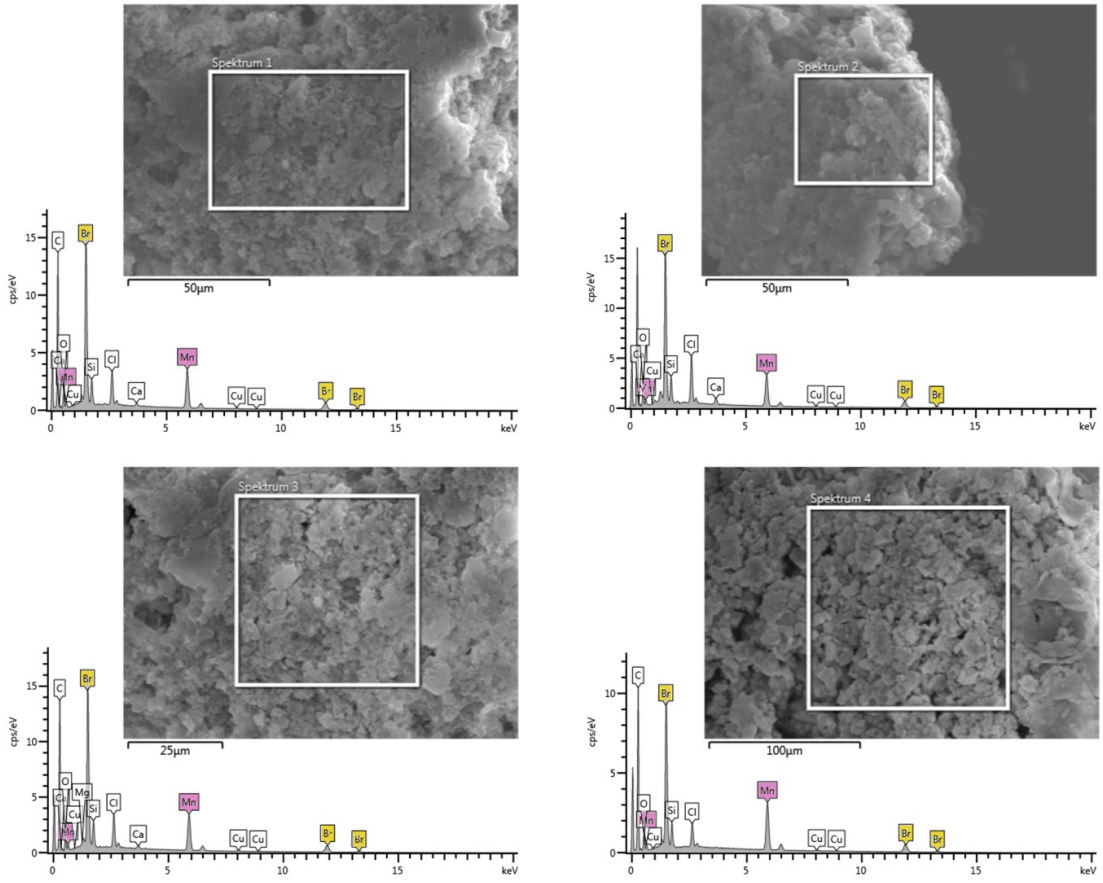


Figure D3. SEM-EDX spectra of **Mn PhenPy** COF powder, collected at the indicated area on the powder's surface.

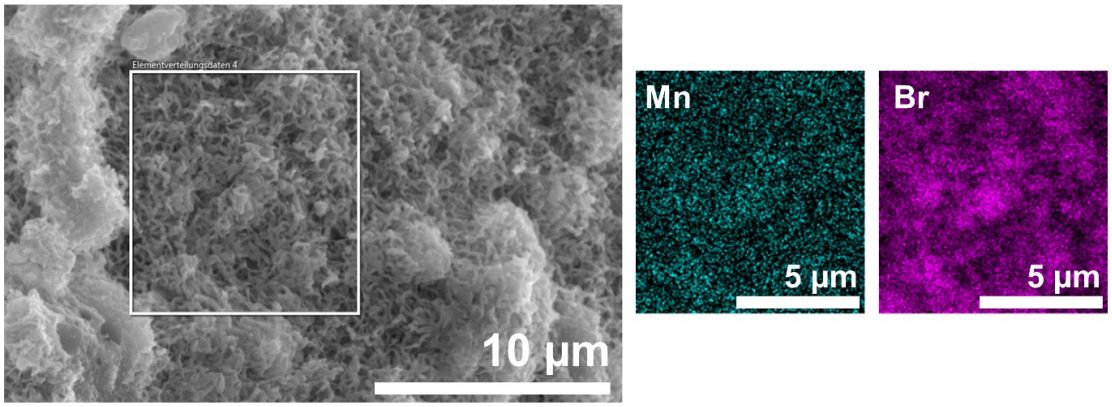


Figure D4. SEM EDX mapping of **Mn PhenPy** COF powder, collected at the indicated area on the powder's surface.

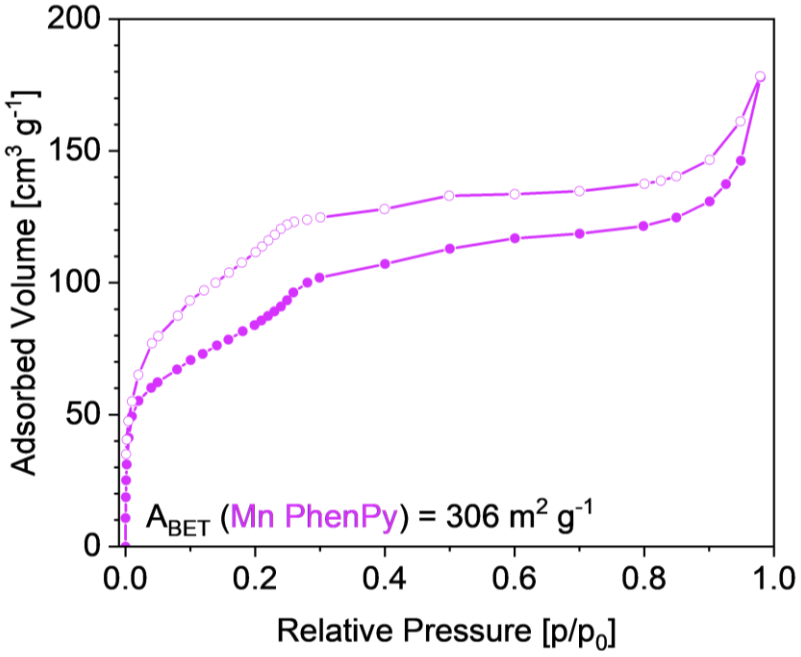


Figure D5. N_2 sorption experiments of the **Mn PhenPy** COF reveal a BET surface area of 306 m^2g^{-1}.

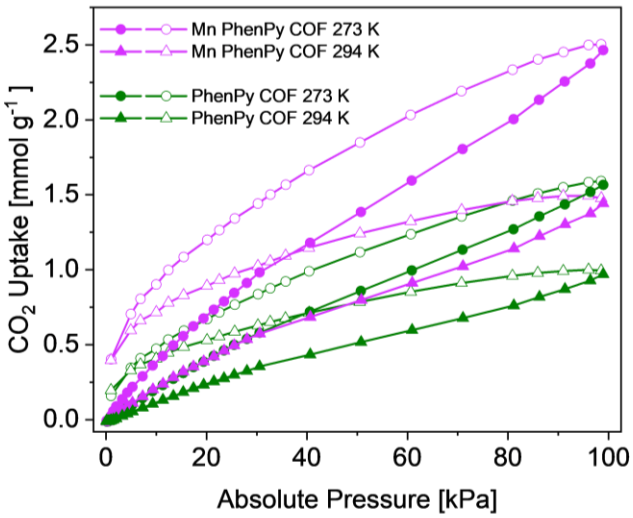


Figure D6. CO_2 Adsorption isotherms of **PhenPy** (green) and **Mn PhenPy** (pink) COFs at 273 K and 294 K.

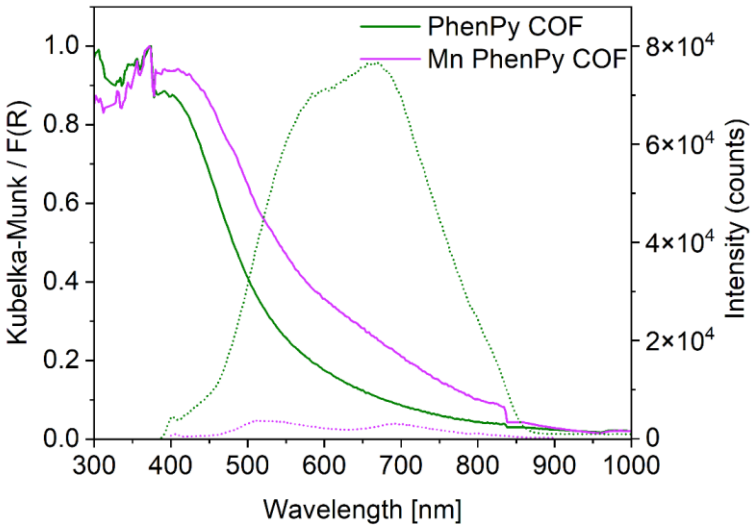


Figure D7. UV-Vis absorption and photoluminescence spectra of both **PhenPy** (green) and **Mn PhenPy** (pink) COFs.

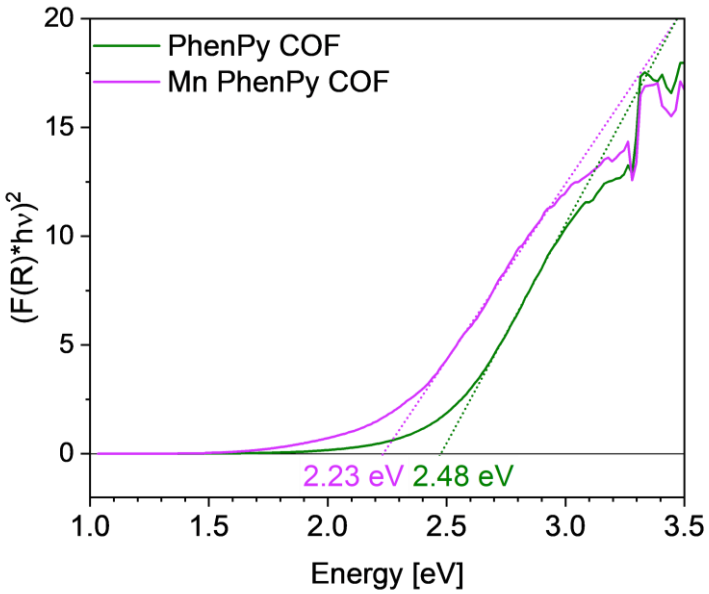


Figure D8. Tauc plots of **PhenPy** (green) and **Mn PhenPy** (pink) COFs assuming a direct transition. The band gap energy is reduced upon introduction of the Mn-complex into the COF structure.

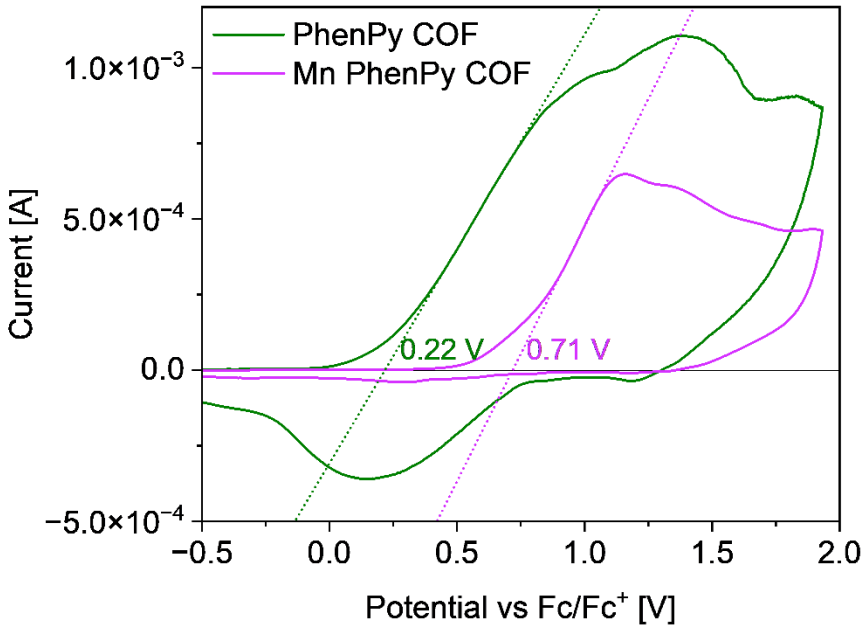
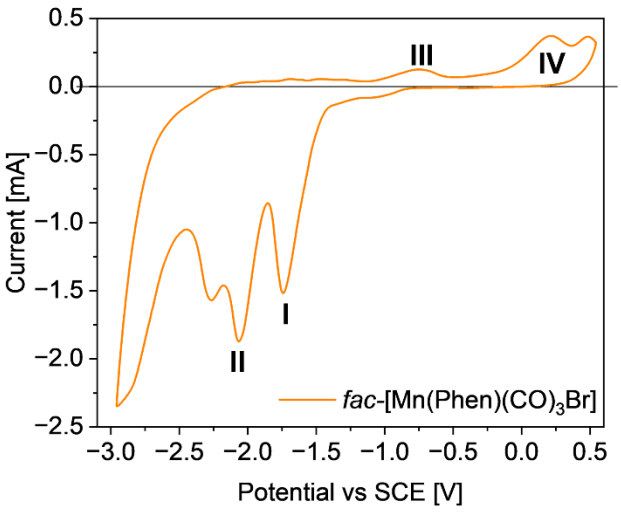


Figure D9. CV curves of **PhenPy** (green) and **Mn PhenPy** (pink) COFs measured against the ferrocene redox couple at a scan rate of 10 mV/s. The onset of the first oxidation peak reflects the conduction band energy of the material.

CV of molecular analog fac-[Mn(Phen)(CO)3Br]



I Dimer Formation

$[Mn(L)(CO)_3Br] + e^- \rightarrow [Mn(L)(CO)_3Br]^-$

$[Mn(L)(CO)_3Br]^- \rightarrow [Mn(L)(CO)_3] + Br^-$

$[Mn(L)(CO)_3] \rightarrow \frac{1}{2}\ \mathbf{[Mn(L)(CO)_3]_2}$

II Dimer Reduction

$[Mn(L)(CO)_3]_2 + 2\ e^- \rightarrow 2\ \mathbf{[Mn(L)(CO)_3]^-}$

III Reoxidation of $[Mn(L)(CO)_3]^-$

IV Reoxidation of $[Mn(L)(CO)_3]_2$

Figure D10. Assignment of the redox features in the CV of the molecular analog *fac*-[Mn(**Phen**)$(CO)_3$Br] according to the literature.[283, 377, 429] The CV was measured in a three-electrode setup in acetonitrile ($TBAPF_6$, 0.1 M), using a Pt

wire as the reference electrode, under Ar at a scan speed of 10 mV s^{-1}. The reduction peaks at -2.25 V and -2.85 V are not discussed in the literature. We therefore tentatively assign them to irreversible reductions of the Phen building block.

Curriculum Vitae

Marcos Eduardo Gomes do Carmo

marcos.go.carmo@gmail.com

Scholar Google | ORCiD

Education

2022 - M.Sc. in Chemistry. Federal University of Uberlândia – UFU, Brazil.

2019 - B.Sc. in Chemistry. Federal University of Goiás – UFG, Brazil.

International Research Internship

Ph. D. Visting Scholar. University of North Carolina at Chapel Hill - UNC, USA. 09/2025 to 05/2026

Activity: Elucidating catalytic mechanisms for rhenium molecular and hybrid catalysts for CO_2RR. Research conducted in alignment with the Center for Hybrid Approaches in Solar Energy to Liquid Fuels (CHASE). Supervised by Prof. Dr. Gerald. Jerry Meyer. Funded by Programa de Doutorado-sanduíche no Exterior (PDSE).

Ph. D. Visting Scholar. Ludwig-Maximilians University of Munich-LMU, Germany. 11/2022 to 01/2023

Activity: Synthesis of Covalent Organic Frameworks containing bipyridine sites as coordinating center for $Re(CO)_3Cl$ immobilization as hybrid catalytic platforms for CO_2RR. Supervised by Dr. Thomas Bien and Dr. Jenny Schneider. Funded by Alexander von Humboldt Foundation.

Funding and Awards

- **2023** - Invited front cover of the Journal of Materials Chemistry A with the article: “From conventional inorganic semiconductors to covalent organic frameworks: advances and opportunities in heterogeneous photocatalytic CO_2 reduction”.
- **2025/2026** - Visiting graduate student fellowship (University of North Carolina at Chapel Hill) though the Programa de Doutorado-sanduíche no Exterior (PDSE), grant 88881.128029/2025-01.
- **2023** – Academic scholarship from Fundação de Amparo à Pesquisa do Estado de Minas Gerais (FAPEMIG), grant 15487.
- **2022/2023** - Visiting graduate student fellowship (Ludwig University of Munich) though the Alexander von Humboldt Foundation, grant 8200625.
- **2022** - Invited front cover of the Journal of the Brazilian Chemical Society with the article: “Temperature Dependent Emission Properties of ReI Tricarbonyl Complexes with Dipyrido-Quinoxaline and Phenazine Ligands”.
- **2020** – Academic scholarship from Fundação de Coordenação de Aperfeiçoamento de Pessoal de Nível Superior, grant 88887.498842/2020-00.

Papers under revision

Carmo, M. E. G. Spies, L. Augusto, K. K. L., Sampaio, R. N., Meyer, G. J., Schneinder. J. Patrocinio, A. O. T. Unlocking CO_2 Photoreduction with Re(I) Single-Site COF-based Catalysts: Structure-Activity Relationships. Journal of Materials Chemistry A.

Publications – Journal Articles

1. **Carmo, M. E. G**., Moreira, G., Silva, V. F., Desordi, J., Gonçalves, P. J., Machado, A. E. H., Sampaio’, R. N., Meyer, G. J., Patrocinio, A. O. T. Mechanistic Insights into CO2-to-CO Photoreduction by Proton-Responsive

Imidazole–Pyridine Re(I) Complexes. Inorg. Chem., 2026, 65 (16), p. 9188–9198.

2. de Matos, P. A., **Carmo, M. E. G.**, Parussulo, A. L. A., Silva, C. M. F., Lino, R. C., Toma, H. E., Beletti, M., Junior, R. J. O., Patrocinio, A. O. T., Matias, T. A., Tsubone, T. M. Ligand Rigidity and π-Surface Modulate Biomolecular Interactions and Cytotoxicity in Ru (II) Polypyridyl Complexes. *Inorganics*, *14*(2), **2026**, 63.
3. Silva, J. N. M., Desordi, J. C., Ducas, E. S. A., Chaves, O. A., **Carmo, M. E. G**., Patrocinio, A. O. T., Bernardo, A. I., Gonçalves, P. J. Insights into bovine serum albumin (BSA) photooxidation mediated by mono-cationic porphyrins with Pd (II), Pt (II), and Ru (II) bipyridyl complexes. *Journal of Photochemistry and Photobiology A: Chemistry*, **2025**, p. 116793.
4. Spies, L., **Carmo, M. E. G**., Marrenjo, G. J., Reuther, S., Ganswindt, P., Patrocinio, A. O. T., Bien, T., Lopes, O. Schneider, J. MnI-Functionalized Covalent Organic Framework as Efficient Electrocatalyst for CO2 Reduction in a Catholyte-Free Zero-Gap Electrolyzer.” Adv. Funct. Mater. **2025**, 2502953.
5. **Carmo, M. E. G.**, Spies, L., Döblinger, M., Xu, Z., Xue, T., Hartschuh, A., Bien, T., Schneider, J., Patrocinio, A. O. T. Designing Atomically Precise and Robust COF Hybrids for Efficient Photocatalytic CO2 Reduction. Small, **2025**, 2500550.
6. **Carmo, M. E. G.**, Matos, P. A., Maia, P. I., Machado, A. E. H., Beletti, M. E., Tsubone, T. M., Patrocinio, A. O. T. The photophysics of Ir (III) cyclometalated complexes containing the 2-(2-pyridyl) benzimidazole ancillary ligand: Protonation effect and their potential as specific lysosome probes in cells." J. Phot. Phot. A. 448, **2024**, p. 115339.
7. Lavor, T. S., Teixeira, M. H. S., Matos, P. A., Lino, R. C., **Carmo, M. E. G**., Beletti, M. E., Patrocinio, A. O. T., Oliveira, R. J., Tsubone, T. M. The impact of biomolecule interactions on the cytotoxic effects of rhenium (I) tricarbonyl complexes. Journal of Inorganic Biochemistry, v. 257, **2024**, p. 112600.
8. **Carmo, M. E. G**., Spies, L., Silva, G. N., Lopes, O. F., Bein, T., Schneider, J., Patrocinio, A. O. T. From conventional inorganic semiconductors to covalent organic frameworks: advances and opportunities in heterogeneous photocatalytic CO2 reduction. J. Mater. Chem. A 11.26, **2023**, p. 13815-13843.

9. RAMOS, C. L., Prado, F. S., **Carmo, M. E. G**., Souza, B., Machado, A. E. O., Patrocinio, A. O. P. Temperature dependent emission properties of ReI tricarbonyl complexes with dipyrido-quinoxaline and phenazine ligands. Journal of the Brazilian Chemical Society, v. 33, n. 05, **2022**, p. 425-436.
10. **Carmo, M**. E., Kunizaki, F. C. D. C., Sousa, N. L. D. S., Romualdo, L. L. Caracterização e Avaliação da Toxicidade de MP10 Presentes na Área Urbana de Catalão–GO Associados a Parâmetros Climatológicos. Revista Processos Químicos, 14(27), **2020**, 37-48.

Oral presentation in scientific meeting

- Covalent Organic Framework as supporting material for Re(I)-hybrid photocatalysts: Understanding the influence of building blocks. International Workshop on Photoactive Materials for Sustainable Energy Conversion. 2025.
- Catalytic Mechanisms of Hybrid-COFs for CO_2 Reduction Using In Situ X-ray Absorption Spectroscopy. São Paulo School of Advanced Science on 4th Generation Synchrotron Techniques (SPSAS SyncLight). 2024.

Abstract in scientific meetings

1. **Marcos E. G. Carmo**, Antonio O. P., Covalent Organic Frameworks Modified With Re(I) And Mn(I) Complexes As Efficient And Robust Platforms For Hybrid CO_2 Catalysts. Inter-American Photochemical Society (IAPs). Águas de Lindóia - SP, Brazil, 2026.
2. **Marcos E. G. Carmo**, Laura Spies, Thomas Bein, Jenny Schinider And Antonio O. T. Patrocinio. Synthesis and characterization of Re(I) modified Covalent Organic Framework for CO2 photoreduction" São Paulo School of Advanced Science on 4^{th} Generation Synchrotron Techniques (SPSAS SyncLight). Campinas-SP, Brazil. 2024.

3. **Marcos E. G. Carmo**, Laura Spies, Thomas Bein, Jenny Schinider And Antonio O. T. Patrocinio. New Re(I)-Modified Covalent Organic Frameworks For CO_2 Photoreduction. XXI Brazilian Meeting on Inorganic Chemistry. Belo Horizonte, MG, Brazil. 2024.
4. Vanessa F. Silva, **Marcos E. G. Carmo**, Antonio O. T. Patrocinio. Synthesis and characterization of a new tricarbonyl Mn(I) complex containing an imidazole-based ligand. XXI Brazilian Meeting on Inorganic Chemistry. Belo Horizonte, MG, Brazil. 2024
5. Gabrielly Moreira, Vanessa F. Silva, **Marcos E. G. Carmo**, Pablo J. Gonçalves, Jaqueline, Antonio E. H. Machado and Antonio O. T. Patrocinio. Photophysical properties of Re(I) complexes containing imidazole ligands: towards the application on CO_2 reduction. XXI Brazilian Meeting on Inorganic Chemistry. Belo Horizonte, MG, Brazil. 2024.
6. Patrícia A. Matos, **Marcos E. G. Carmo**, Antonio O. T. Patrocínio, Tiago A. Matias, Tayana M. Tsubone. Ruthenium Polypyridines As Photosensitizer For Photodynamic Therapy. 51ª Reunião Anual da Sociedade Brasileira de Bioquímica e Biologia Molecular (SBBq). Águas de Lindóia - SP, Brazil. 2022.
7. Lavor, T. S. ; **Carmo, Marcos E. G. Do** ; Estevam, T. O. ; Patrocinio, A. O. T. ; Tsubone, T. M. ; Otaguro, H. . Evaluating Re(I) Complexes As Anticancer Agent. 51ª Reunião Anual da Sociedade Brasileira de Bioquímica e Biologia Molecular (SBBq). Águas de Lindóia - SP, Brazil. 2021.
8. Patrícia A. Matos, **Marcos E. G. Carmo**, Antonio O. T. Patrocínio, Tiago A. Matias, Tayana M. Tsubone. Interaction of ruthenium complex with biomolecules and its outcomes of photodynamic efficiency, 20th International Union for Pure and Applied Biophysics (IUPAB), virtually, 2021.
9. **Marcos E. G. Carmo**, Newton M. B. Neto, Antonio O. T. Patrocinio. Um hidrogênio conta... A influência do sítio de coordenação nas propriedades fotofísicas de complexos de Ir(III). IV workshop de química inorgânica da UFAM, Manaus - AM, Brazil. 2020.
10. Lincoln L. Romualdo, **Marcos E. G. Carmo**, Nara L. S. Sousa, Fugitive emissions analysis from industrial in the urban PM10 using X-ray fluorescence spectrometry. 15th Rio Symposium on Atomic Spectrometry. Mendoza, Argentina. 2019.

11. **Marcos E. G. Carmo**, Lincoln L. Romualdo. Estudo por DFT e DFT-DT de estruturas com efeito push-pull e propriedades espectrais para aplicações fotovoltaicas.. In: 42ª Reunião Anual da Sociedade Brasileira de Química Joinville -SC, Brazil. 2019.
12. Fernanda, C. Kunizaki, **Marcos E. G. Carmo**, Lincoln L. Romualdo. Estudo teórico de novos complexos com bases de Schiff visando obtenção de altos valores de hiperpolarizabilidade (β). 42ª Reunião Anual da Sociedade Brasileira de Química. Joinville – SC, Brazil. 2019.
13. **Marcos E. G. Carmo**, Nara L. S. Sousa, Fernanda, C. Kunizaki, Lincoln L. Romualdo. Concentração e variação da composição elementar das partículas totais em suspensão na cidade de Catalão - GO. IX Semana da Química Prof. Dr. Fernando Petacci UFG/RC. Catalão – GO, Brazil. 2017.

Organization of Scientific events

- International Workshop on Photoactive Materials for Sustainable Energy Conversion. Universidade Federal de Uberlândia, Uberlândia - MG, Brazil. March, 19-21, 2025.
- 2ª Escola Mineira de Eletroquímica. Universidade Federal de Uberlândia, Uberlândia - MG, Brazil. March 10-14, 2025.

Committee member

- LOPES, O. F.; LIMA, R. C.; **CARMO, M. E. G**. Undergraduate Research Defense Committee for João Victor Martins Primo. Síntese, caracterização e aplicação do Nb2O5 na fotodegradação de poluentes orgânicos e produção de H2 verde. 2024. B.Sc. in Industrial Chemistry - Federal University of Uberlândia.

Selected summer schools

- Selected Participant, São Paulo School of Advanced Science on 4th Generation Synchrotron Techniques – SPSAS SyncLight, Brazilian Synchrotron Light Laboratory (LNLS/CNPEM). Campinas, SP, Brazil, October, 14-25, 2024.
- Selected Participant, 17th PTASchool of Electrochemistry & 4th Workshop on Electrochemistry, from Sensing to Energy Conversion and Storage. University of São Paulo. São Paulo, SP, Brazil, December, 3-8, 2023.

Extension project

- Student Research in the project “Monitoring of Atmospheric Air Quality in the City of Catalão,” coordinated by Professor Lincoln Lucílio Romualdo and conducted at the Academic Unit of Chemistry, Federal University of Goiás (Catalão Campus). Served as a, completing a total workload of 176 hours from July 1, 2018, to June 30, 2019.